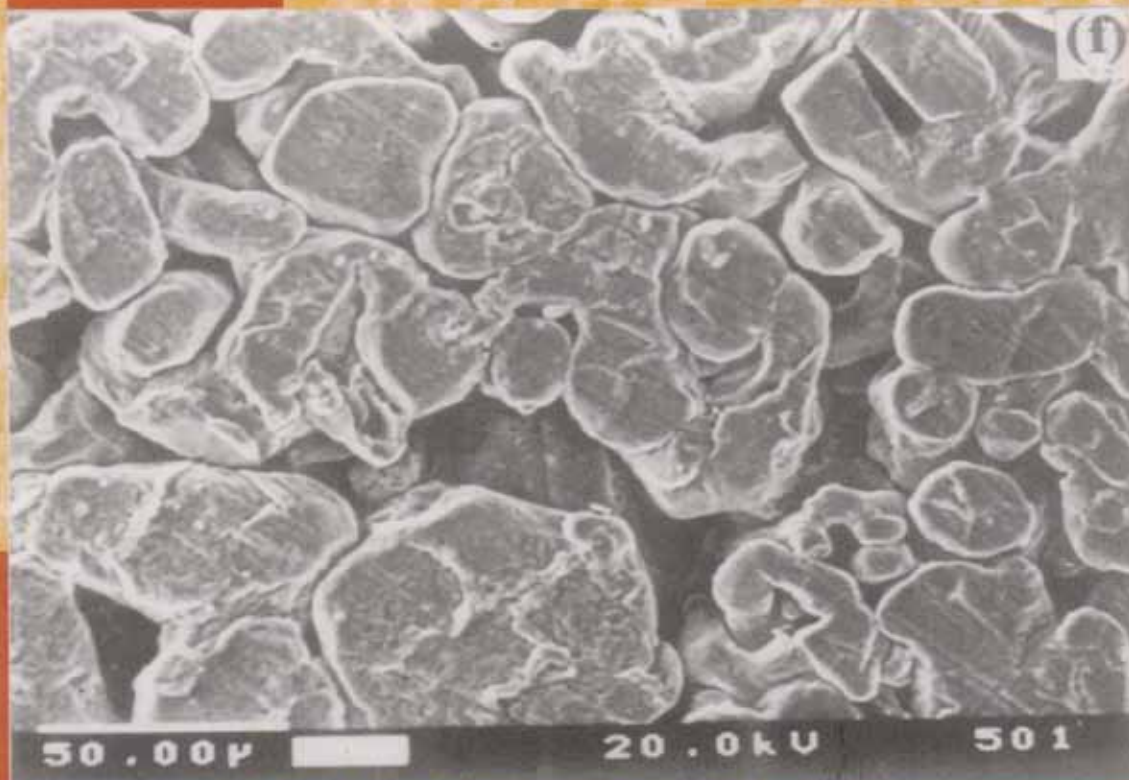


ISSN 0377 - 9416



Volume 28, 2002

# TRANSACTIONS OF POWDER METALLURGY ASSOCIATION OF INDIA



Guest Editors :  
Prof. T. R. Rama Mohan  
Prof. P. Ramakrishnan

**Guest Editors :**  
**Prof. T. R. Rama Mohan**  
**Prof. P. Ramakrishnan**

**Volume 28**  
**December 2002**

**Published by**



**Powder Metallurgy Association of India**  
**Department Of Metallurgical Engineering**  
**and Material Science, I.I.T, Bombay,**  
**Powai, Mumbai - 400 076**

Neither the Powder Metallurgy Association of India nor the editor  
assumes responsibility for opinions expressed by the authors of the papers.

**Cover Photograph : Microstructure of Green Compact of Titanium Powder**

## EDITORIAL

The 28th National Powder Metallurgy Conference was held during January 22-24, 2002 at New Delhi along with the International Conference on Powder Metallurgy in Automotive Applications. The Proceedings of the International Conference, Powder Metallurgy in Automotive applications-II, Edited by T. R. Rama Mohan and P. Ramakrishnan was published in 2002 by Oxford & IBH Publishing Co. Pvt. Ltd., New Delhi. The papers presented at the 28th.ATM covered wide range of topics related to Synthesis and Characterization of Powders, Consolidation and Evaluation of Sintered Properties and are included in this volume of Transaction. The best paper award went to "The effect of attritor milling time on the production of hard metal powders and sintered components " by S. Ramesh Rao et.al., of Widia India Ltd., while the best product was adjudged as a "Gear shift cam drive of a gear box assembly "developed by Mahindra Sintered Products Ltd. The increasing activities of PMAI will provide the dissemination and exchange of information pertaining to Powder Metallurgy and Particulate Materials there by promoting their usage in our country.

T.R.Rama Mohan  
P. Ramakrishnan



**CONTENTS**

**SYNTHESIS AND CHARACTERISATION OF POWDERS**

1. PROCESSING AND MICROSTRUCTURAL ANALYSIS OF RAPIDLY  
SOLIDIFIED WHITE CAST IRON POWDERS  
*B.B. Pani, P.G. Mukunda, O.N. Mohanty* 1
2. PRODUCTION OF POWDER METALLURGY GRADE ATOMIZED  
IRON POWDERS  
*B.B. Pani, B. Ravi Kumar, O.N. Mohanty* 5
3. FERROMAGNETIC COMPOSITE POWDERS – PHOSPHATED IRON  
POWDERS COATED WITH A THERMOSET POLYMER  
*V. Uma and R. Sundaresan* 9
4. IRON BASED POWDER Fe-P FOR SOFT MAGNETIC APPLICATION  
BY A THERMO-CHEMICAL PROCESS  
*K. Malobika, D.N. Fedorov and A. Sivakumar* 22
5. DESIGN AND FABRICATION OF VARIOUS TYPES OF BALL MILLS FOR  
THE SYNTHESIS OF ALUMINUM BASED METAL MATRIX COMPOSITE POWDERS  
*Rajesh Purohit, Pramod Sahu and Rakesh Sagar* 31
6. SYNTHESIS OF COMPOSITE ALUMINA ZIRCONIA NANO-POWDERS BY  
THE SOL GEL PROCESS  
*Thirunavukkarasu, S.K. Malhotra and Paramanand Singh* 43
7. PRODUCTION OF SiC-Al<sub>2</sub>O<sub>3</sub> COMPOSITE POWDERS FROM FLY ASH  
*Sangita Kumari, M.M. Godkhindi, K. Das and P.G. Mukunda* 56
8. THERMODYNAMIC EVALUATION OF REDUCTION OF SILICA IN THE  
PRESENCE OF IRON  
*A.I. Khovavko, D.N. Fedorov and K. Malobika* 64

**CONSOLIDATION**

9. EFFECT ATTRITOR MILLING TIME ON THE PROPERTIES OF HARDMETAL  
POWDERS AND SINTERED COMPONENTS  
*S. Ramesh Rao, Pritish Bhattacharya, A. Shivashankar, R. Rengurajan  
and P.R. Desai* 71
10. SINTERING OF COATED W-Cu ALLOYS  
*Chiradeep Ghosh and Anish Upadhyaya* 84
11. EFFECT OF TRANSITION METAL ADDITIVES ON ACTIVATED SINTERING  
OF TUNGSTEN-BRONZE  
*M. Debata and A. Upadhyaya* 92



12.	EFFECT OF SWAGING ON MICROSTRUCTURE EVOLUTION IN W-Ni-Fe ALLOYS <i>S.K. Rout, A. Upadhyaya, A. Tewari</i>	103
13.	REACTIVE HOT PRESSING OF IRON ALUMINIDES <i>D. Srinivas, M.M. Godkhindi, P.G. Mukunda, and S. Das</i>	117
14.	SYNTHESIS OF TITANIUM NITRIDES BY DIRECT NITRIDATION OF TITANIUM POWDERS <i>V.V. Dabhade, R. Bajjal, T.R. Rama Mohan and P. Ramakrishnan</i>	127
15.	Si <sub>3</sub> N <sub>4</sub> COMPOSITE BY INSITU FORMATION OF MoSi <sub>2</sub> <i>R.V. Krishnarao, J. Subrahmanyam and M. Srinivasarao</i>	136
16.	SYNTHESIS OF SILICON PENTACOORDINATED COMPLEX AS A PRECURSOR FOR PROCESSING GLASS AND GLASS-CERAMICS <i>G.V. Ramana Reddy, Debasis Bera, Anil Anal, B.T. Rao, and T.R. Rama Mohan</i>	141
17.	SYNTHESIS AND CHARACTERIZATION OF YTTRIA FULLY STABILIZED ZIRCONIA POWDERS <i>Nikhil Deo, N.V.N. Ramakrishna, Anil Anal, B.T. Rao, T.R. Rama Mohan, and Ramji Lal</i>	152
18.	SYNTHESIS OF TITANIUM – BIOGLASS COMPOSITES <i>Vivek Mathur, Anil Anal, B.T. Rao, and T.R. Rama Mohan</i>	160

#### EVALUATION OF SINTERED PROPERTIES

19.	EFFECT OF SINTERING TEMPERATURE AND Y <sub>2</sub> O <sub>3</sub> ADDITION ON THE MICROSTRUCTURAL EVOLUTION OF P/M STAINLESS STEELS <i>Shankar. J and A. Upadhyaya</i>	168
20.	CORRELATION BETWEEN THERMAL SHOCK RESISTANCE AND THE SALIENT PARAMETERS OF ALUMINA BASED SELF-FLOW CASTABLES <i>K. Sankaranarayanan and Paramanand Singh</i>	185
21.	STUDY OF PRODUCTION AND PROPERTIES OF COPPER-MICA COMPOSITE BY POWDER METALLURGY TECHNIQUE <i>Vishal Arora, Gaurav Verma, Manisha Taneja, N.C. Upadhyay</i>	200
22.	SYNTHESIS AND MECHANICAL PROPERTY EVALUATION OF YTTRIA PARTIALLY STABILIZED ZIRCONIA CERAMICS <i>Soumen Biswas, Anil Anal, B.T. Rao, T.R. Rama Mohan and Ramji Lal</i>	221
23.	DEVELOPMENT OF INDIRECTLY HEATED FUEL ROD SIMULATOR FOR THERMO HYDRAULIC SAFETY EXPERIMENT <i>S.K. Srivastava, P. Sundara Rajan, S.V. Paibhale, V.G. Date</i>	232
24.	MACHINABILITY OF S.G. IRON WITH ZIRCONIA TOUGHENED ALUMINA CUTTING TOOL <i>T. Sornakumar, R. Krishnamurthy and C.V. Gokularathnam</i>	243
25.	SYNTHESIS AND EVALUATION OF MECHANICAL PROPERTIES OF ZIRCONIA TOUGHENED ALUMINA (ZTA) <i>R. Mehreja, N. Bhargava, Praveen G. Nair, G.V. Prabhu Gaunkar, B.T. Rao T.R. Rama Mohan and Ramji Lal</i>	249

## PROCESSING AND MICROSTRUCTURAL ANALYSIS OF RAPIDLY SOLIDIFIED WHITE CAST IRON POWDERS

B. B. Pani\*

P. G. Mukunda\*\*

O. N. Mohanty\*\*\*

\*Sr. Lecturer, University College of Engineering, Burla – 768 018

\*\*Professor, IIT, Kharagpur-721 302

\*\*\*Director (R&D) Centre TISCO, Jamshedpur-83 1007.

### Abstract :

Rapidly solidified white cast iron powders were produced by water atomization route. By DAS analysis the cooling rate of the as received powders was measured to be  $10^4$  to  $10^5$  K/Sec. The powders were characterized in various ways like chemical analysis, size distribution, SEM, XRD analysis etc. In order to retain the advantages gained by rapid solidification, the powders were hydrogen annealed below  $A_1$  transformation temperature. The annealed powders were encapsulated by a mild steel can and further hot pressed, hot forged and hot rolled with intermediate heating to thin sheets. The entire thermo mechanical processing was carried out below  $750^\circ\text{C}$ . By SEM analysis very fine grained ferrite carbide structure was obtained in the processed material. Because of carbon diffusion from cast iron particles to the mild steel portion this has also been converted to fine grained ferrite carbide structure. This structure is quite good for superplastic deformation to manufacture high strength and wear resistant machine components. The room temperature hardness was found to be 490 VHN.

### Introduction :

White cast irons are not much attractive in industries. The main reason for this is due to presence of massive iron carbides network which are quite brittle and lack machinability. From investigations carried out by researchers[1-11] it reveals that very fine grained ferrite carbide structure can be obtained by following suitable processing techniques. At ambient temperature with controlled strain rate, such structurally modified materials can deform superplastically to manufacture high strength, wear resistance products which are having tremendous potential applications in industries[3].

In the present investigation an attempt has been made to produce rapidly solidified white cast iron powders with suitable composition. During further processing care has been taken to retain advantages gained in materials by rapid solidification. After characterization of powders a simple and industrially feasible thermo-mechanical processing method is adopted to obtain fine grained equiaxed ferrite carbide structure which is suitable for superplastic deformation at ambient temperature.

### Experimental :

#### 1. Powder Production and Characterization :

Wrought iron obtained from arc melting of sponge iron fines was remelted in an induction furnace and water atomized to cast iron powders. During remelting, required amount of ferro-chrome and ferro-silicon were added to get within 1-2% Cr and Si in the powders. The chemical analysis of the powders is given in Table-1. As the cooling rate is high in small sized powders, powder size below -100 mesh size were taken for further processing. From the SEM micrograph (Fig.1) the

cooling rate is analysed using DAS (Dendritic Arm Spacing) technique. The powders were hydrogen annealed at 700°C (below  $A_1$  temperature) for one hour so that the advantages gained during rapid cooling will not be destroyed.

**TABLE-I Chemical analysis of water atomized cast iron powders.**

C	Cr	Si	S	P	Fe
3.51	1.5	1.3	0.012	0.03	Balance

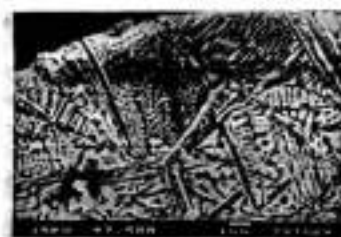


**Fig.1 SEM micrograph of powder showing dendritic as well as Cellular Structure**



**Fig.2 SEM micrograph of the encapsulated thermo-mechanically processed powders**

## **2. Encapsulation and Thermo-mechanical Processing :**

By conventional pressing and sintering it was quite difficult to get high density material from rapidly solidified cast iron powders. Hot Isostatic Pressing (HIP) is the ideal method of good consolidation for this material. Mordike et al[12] used methods like hot extrusion and forging for consolidating such materials. Caligiuri et al [13] used superplastic hot pressing method to get superplastic structure in processed materials. Kazuo et al [14] has found nearly theoretical density by vacuum hot pressing method. A different method called encapsulation thermo mechanical processing (ETMP) was incorporated here. The details of the process are discussed as follows.

Rectangular cans of size 12cm X 4cm X 4cm were made from mild steel sheets of 2mm thickness by gas welding. The surface of the can was properly cleaned by grinding. White cast iron powders which was hydrogen annealed at 700°C was filled in it and finally the can was closed by a mild steel plate and again welded by gas welding process.

The can with powders was first hot pressed at 700°C temperature at 40MPa pressure. The furnace temperature was raised after putting the encapsulated powder-can inside an induction furnace



in argon atmosphere. This facility was fabricated for this investigation. After 20 minutes of hot pressing the material was taken out and put inside a tube furnace which was located near the forging machine and re-heated at 700°C for 20 minutes in argon atmosphere and then forged by a 0.5 ton capacity air hammer which has 110 strokes per minute. Initially the number of strokes was fewer and it was increased with deformation. The forged materials were again reheated in an electric resistance furnace. The material was heated for 25 minutes at 750°C and rolled by a 2 and 4 high rolling mill. The reheating and rolling continued for several times with a 10 to 12 percent reduction in a pass till the material was rolled to 2mm thick sheet. SEM micrographs were obtained after 5% nital etched condition (Fig.2).

### Results and Discussions :

Figure 1 shows the microstructure of a medium size particle (around 40µm) where the structure shows that it is mostly dendritic and cellular in nature. From DAS analysis the cooling rate is found to be  $10^4$  to  $10^5$  K/Sec.

Cr and Si both are present in cast iron powders (Table-1). Addition of Cr within 1-2% suppresses graphitization and also increases the volume fraction of carbides. During thermo-mechanical processing these carbides resist grain growth. Silicon addition of around 1-2%, however, increases the  $A_1$  transformation temperature up to 800°C and increases ferrite stability range.

Figure 2 shows the microstructure of the rolled material in 5% nital etched condition. Here it is marked that very fine equiaxed iron carbide grains (0.5-1µm) are nicely distributed in ferrite matrix. The average ferrite grain size is 1-2 µm. It is very important to note here that the mild steel region has also been converted to fine grain structure as in the cast iron powder portion. This conversion is possibly due to diffusion of carbon from white cast iron powder materials to mild steel region.

The microstructure obtained here looks good for superplastic deformation at ambient temperature with controlled strain rate to manufacture various types of complex shaped articles. As reported by Sherby[3] such structure can give very good strength and room temperature ductility. The room temperature hardness was found to be 490 VHN.

### Conclusion :

It is quite possible to obtain fine grained superplastic structure by encapsulation thermo-mechanical processing of micro alloyed rapidly solidified white cast iron powders which were produced by water atomization. Such materials are having potential application in industries.

### Acknowledgement :

The authors would like to express their sincere thanks to AICTE, New Delhi for financial assistance for this work.

## References :

1. O.D. Sherby, "Ultra High Carbon Steels, Damascus Steels and Ancient Blacksmiths", *Iron and Steel Institute of Japan International*, Vol.39, No.7, pp 637-648, (1999)
2. J. Perttula, "Reproduced Wootz Damascus Steel", *Scandinavian J. of Metallurgy*, 30, pp65-68 (2001).
3. D. R. Lesuer, C. K. Syn, A. Goldberg, J. Wadsworth and O.D. Sherby, "The Case for Ultra High Carbon Steels as Structural Materials", *JOM*, 8, pp 40-46, (1993)
4. B. B. Pani, *Ph.D. Thesis*(Submitted), IIT, Kharagpur, India, (2001).
5. N. K. Das, C. S. Sivaramakrishnan and O. N. Mohanty, "Rapid Solidification of Cast Iron-Some New Observations", *Key Engineering Materials*, Vol. 38 & 39, pp 65-82, (1989)
6. A.Bose, P.G.Mukunda, "Self Lubricating Iron Copper Bearing From Cast Iron Powder", *Trans. of P/M Association of India*, pp.76-82, 12 Sept., (1985).
7. B. B. Pani, P.G.Mukunda, O.N.Mohanty, "Manufacturing Low Cost Composites by Synthesizing Cast Iron and Iron Powders", *Proc. of Nat. Sem. on Special Materials : Processing and characterizing*, RRL, Bhubaneswar, 17-18 Jan. (2001).
8. A.A. Zhukov, O.N. Mohanty, P.G. Mukunda, B.B. Pani, "White and Stable Mottled Alloyed Irons Regarded as In-Situ Composites", *Nat. Sem. On Composite Materials*, IGIT, Sarang, Orissa, March 18-19,(1994).
9. P. Ramachandra Rao, "Rapid Solidification of Steels", *Bul. of Mat. Science*, Indian Academy of Science, Vol.15, No.6, Dec.(1992).
10. O. A. Ruano, L.E. Eiselstein and O.D. Sherby, "Room Temperature Strength and Ductility of Rapidly Solidified White Cast Iron", *Powder Metallurgy* 26, pp155-160, (1983)
11. L. E Eiselstein et. al., "Microstructure and Mech. Properties of Rapidly Solidified White Cast Iron Powders", *Proceedings of 3rd Int. Conference of Rapid solidification Processing Gatherburg*, D. National Bureau of Standards, pp.245-251, 6-8 December (1982)
12. D. Burchands, K.V. Kainer, B. L. Mordike, "Consolidation of Rapidly Solidified High Carbon Iron Base Alloys", *Int. Conf. on Strength of Metals*, pp.1645-1650, (1983)
13. R.D.Caligiuri, R. J. Whalen, O.D.Sherby, "Superplastic Hot Pressing of White Cast Irons", *Int. J. of Powder Met. and Powder Tech.*, Vol.12, No.1, (1976)
14. Kazuo Isonashi, M. Tokizane, "Superplastic Deformation of P/M Ultra High Carbon Steel", *Int. J. of Powder Met.*, Vol.25, No.3, (1989).

## PRODUCTION OF POWDER METALLURGY GRADE ATOMIZED IRON POWDERS

B. B. Pani\*

B. Ravi Kumar\*\*

O. N. Mohanty\*\*\*

\*Sr. Lecturer, University College of Engineering, Burla-768018.

\*\* Scientist, NML, Jamshedpur-831 007

\*\*\*Director (R&D) Centre TISCO, Jamshedpur-831007.

### Abstract :

Indian sponge irons are free from manganese and many other undesirable foreign elements. In the same time, because of its high affinity to oxygen, presence of manganese is not desirable in iron powders to manufacture sintered products. Keeping in view of this, sponge iron fines, processed at NML, Jamshedpur was taken as raw material to produce wrought iron by arc furnace. This wrought iron again was re-melted by an induction furnace with requisite amount of additives and then water atomized to iron powders. These powders were characterized and tested in various ways like chemical analysis, SEM, XRD analysis, particle shape, size, size distribution analysis, apparent density, flow rate, compaction and sintering studies etc. It was finally found that this powder is quite suitable for manufacturing ferrous based P/M products.

### Introduction :

The automotive industries are growing very fast in India and hence there is potential demand for impurity free cost effective iron powders in the country. For manufacturing quality iron powders the source material play a very significant role. In this context sponge irons which are plentifully available from various sources in the country are chemically very much consistent and low cost. In the ancient time the famous Indian "Wootz", materials were also produced from such sponge fines[1]. In the present investigation an attempt has been made to use Indian sponge irons as source material to produce gangue free water atomized powder metallurgy grade iron powders.

### Experimental :

#### 1. Sponge Iron Melting :

Sponge iron fines which were processed at NML, Jamshedpur, were chemically analysed (Table-1) and then melted in an arc furnace with requisite amount of additives. After proper removal of slags the molten metal was cast to iron ingot. The chemical analysis of the iron ingot is presented in Table-2.



TABLE-1:Chemical analysis of sponge iron fines.

Elements	% mass content
Fe	89.00
C	0.20
S	0.02
P	0.05
FeO	6.50
Al <sub>2</sub> O <sub>3</sub>	2.50
SiO <sub>2</sub>	2.40

TABLE-2:Chemical analysis of iron produced after arc melting of sponge fines.

Elements	% mass content
C	0.3
S	0.014
P	0.03
Si	0.002
Fe	Balance

## 2. Powder Production :

The iron ingot was cut to pieces and then remelted in an induction furnace with requisite amount of additives. During melting the slags were removed. The molten metal then poured to a preheated tundish and then passed through a nozzle of the water atomizer having four number of high velocity water jets. The water mixed iron powders were collected at the bottom of the tank with the help of a filter and then vacuum dried. Powders greater than 80 mesh size were sieved out and below this were taken for further investigation.

## 3. Characterisation :

The chemical analysis of the above powders was carried out which is in presented Table-3. Particle size and size distribution analysis were carried out by a SA-CP<sub>2</sub> Shimadzu centrifugal particle size analyzer. The XRD analysis was done by a Siemen's model X-Ray diffractometer (Fig.1). The apparent density and flow rate of the powders were carried out by Hall Flowmeter and Density Cup. The other physico-mechanical characteristics are presented in Table-4.

TABLE-3:Chemical analysis of water atomized iron powders.

Elements %	Unannealed	Annealed
C	0.3	0.021
S	0.01	0.01
P	0.026	0.026
Fe	Balance	Balance

TABLE-4:Physico-mechanical characteristics of water atomized iron powders.

Median particle size $\mu\text{m}$	78.48
Surface area $\text{m}^2/\text{g}$	0.011
Apparent density $\text{g}/\text{cm}^3$	2.9
Flow rate $\text{Sec}/50\text{g}$	25

#### 4. Consolidation and Sintering :

The annealed powders were properly blended with 1% zinc stearate and then cold compacted by double action die compaction process. Here an universal testing machine of 50T capacity was used. The mass of the compacts were determined by a microbalance and green densities were measured by metric method.

The compacts were sintered in a platinum resistance tube furnace at 1100°C for 30 minutes in hydrogen atmosphere. The sintered densities were recorded in the same way as green densities. The compaction and sintering data are presented in Fig.2.

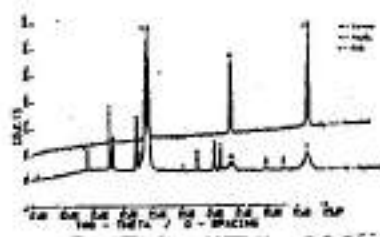


Fig.1 XRD analysis of water atomized powders

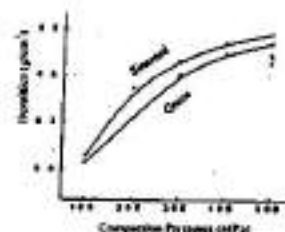


Fig.2 Density vs compaction pressure of water atomized iron powders

#### Results and Discussions :

From Table-1 it shows that the sponge irons are free from Cr and Mn and hence the powders produced from this is free from these elements (Table-3). Because of high affinity to oxygen these elements are not desired in iron powders for manufacturing sintered powder metallurgy products. Some FeO and Fe<sub>3</sub>O<sub>4</sub> which were detected in as atomized stage by XRD analysis (Fig.1) were removed after hydrogen annealing.

From the chemical analysis of as atomized and annealed powders it reveals that carbon content which was 0.3% in as received stage came down to 0.021% after hydrogen annealing. 0.01% P and 0.026% S received in the powders are comparable with P/M grade iron powders for making good quality P/M components[2].

From Table-4 it reveals that the median particle size and computed surface area for these powders are 78.48  $\mu\text{m}$  and 0.011  $\text{m}^2/\text{g}$  respectively. The flow rate is 25 Sec./50g. The apparent density for the present powders is 2.9g/cm<sup>3</sup> which is quite good for making P/M components[2]. From Fig.2 it shows that the compressibility of these powders is very good. Green density of 6.75g/cm<sup>3</sup> which was obtained by compacting at 414 MPa pressure is comparable with powders produced by many reputed firms in India and abroad[2]. As expected the sintered densities are higher than the green densities.

**Conclusion :**

The characteristics of the above produced iron powders are quite good for manufacturing high performance P/M components. This technology can be best exploited by Indian P/M industries.

**Reference :**

1. O.D.Sherby “, Ultra High Carbon Steels, Damascus Steels and Ancient Blacksmiths”, *Iron and Steel Institute of Japan International*, Vol.39, No.7, pp637-648 (1999).
2. I. M. Fedorochenko Ed., *Materiali, Tekhnologia, Sboistva, Primenenia, Spravochnik*, Kiev, Naukova Dumka (1985).
3. B.B.Pani, Ph.D. Thesis, IIT, Kharagpur, (2001).
4. R. M. German, *Powder Metallurgy of Iron and Steel*, A Wiley Interscience Publication, John Wiley of Sons, Ins. USA, (1998).
5. K. K. Rao, “Iron Powder Production in India”, *Powder Metallurgy Association of India News Letter*, 14,6, pp 7-10, (1988).
6. P. Lindskog, P. Arbstedt, “Iron Powder Manufacturing Techniques, A Brief Review”, *Powder Metallurgy*, 21, 1, pp 14-19 (1986).
7. B. B. Agarwal, K.K.Prasad, G.I.S. Chauhan, P.K.Choudhury, “Growth of Sponge Iron in India and its Prospects”, *Journal of Minerals and Metals Review*, 4, pp 25-30 (1992).
8. B. M. Sarangi, “Sponge Iron-A Case Study Based on Market Conditioons”, *Proc. of one day Workshop on Sponge Iron*, Organized by IPITATA Sponge Iron Ltd. and Bureau of Indian Standards, Jamshedpur, India, May 4, pp 18-32 (1993).
9. V. B. Akimenko, “Powder Metallurgy-Results and Problems”, *STAL*, 12, pp 55-59 (1985).



## **FERROMAGNETIC COMPOSITE POWDERS –PHOSPHATED IRON POWDERS COATED WITH A THERMOSET POLYMER**

**V. Uma and R. Sundaresan**

**International Advanced Research Centre for Powder Metallurgy and New Materials,  
Balapur P.O, RCI Road, Hyderabad-500 005**

### **ABSTRACT**

Ferromagnetic composite powders offer flexibility for electrical machine design beyond the range of laminates. The flexibility is created by isotropic magnetic properties exhibited by these materials. Since the soft magnets from these powders are processed in PM route, it is possible to produce high volumes in near net shape resulting in material saving and ultimate cost reduction.

Usually, composite powders are produced by obtaining a thin coating of a dielectric material on iron powder particles. A process has been established at ARCI to obtain phosphated iron powders on which dielectric coating is created. A high curing temperature thermoset is used as the dielectric. Resistivity, DC and AC magnetic properties are measured and reported.

### **INTRODUCTION:**

In Europe, two different concepts of material structures for soft magnetic cores were first proposed in the 1880's with the aim of reducing core losses. The first, the laminated sheet approach described by Edison in 1880, proposed thin iron sheets, stacked together with insulators separating them to be utilized as a soft magnetic core [1].

In 1886, Fritts disclosed a composite iron material as an alternate approach to the laminated sheet stack. It was composed of iron powder with an insulating layer on iron particles. When this composite powder was formed into a solid core, the core would have similar electromagnetic properties as the laminated core [2]. But, Fritts's idea could not find application because P/M technology was virtually non-existent then.

Laminates are only good for medium performance, low frequency applications. They exhibit higher core losses at higher frequencies and are restricted to 'rectangular' geometries with flux in the plane of sheet [3]. The thinner the individual sheet, the lower the eddy current losses and better the performance. This, however, raises the cost [4]. Further, the limitations of square/rectangular cross-section of laminates, in which the lines of magnetic flux are flat curves parallel to each other, are imposed on the application design [5].

These limitations can be overcome by PM processing (based on Fritts's idea) of cores from pure iron powders suitably insulated from one another, because, they, in principle, could exhibit isotropic magnetic properties with low eddy current losses even at high frequencies; PM processing could facilitate high production rates of net shapes with good tolerance and surface finish [6]. Presently, numerous attempts are being made to perfect the technique of coating the dielectric materials on iron powder particles [7]. Warm compaction technique to deliver high dense, cured product was also perfected. As a result, General Motors successfully produced P/M moulded core for ICE ignition coil replacing laminated cores with less losses which had been in production since 1990s [8].

Although there are many claims of success for producing dielectric coatings on iron powders, only a few are commercially viable. These techniques involve either a discrete encapsulation or coating performed prior to compaction [9,10,11,12,13], or in-situ, during warm compaction and/or curing step [14].

Commercially suitable organic materials can be of two categories: thermoplastics and thermosets. Thermoplastics have a softening range that can sometimes be exploited during coating and compaction steps. Thermosets generally require a thermal treatment (curing) after the compaction step, and once cured, these systems generally exhibit excellent elevated temperature stability, both magnetically and mechanically [12].

## THEORETICAL

The design considerations when using soft magnetic materials for rotating machines or transformers have to take hysteresis and eddy current losses into consideration.

### Hysteresis loss

Figure 1 shows the effect within ferromagnetic materials known as *hysteresis*.

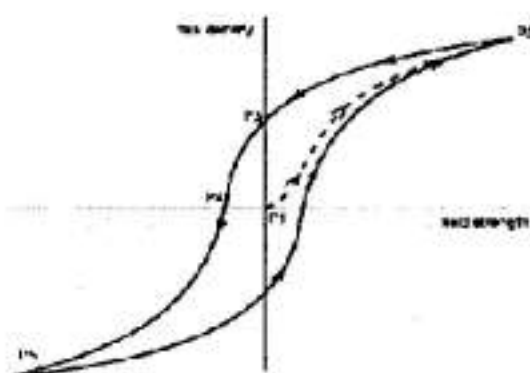


Fig. 1: Hysteresis loop

Starting with an unmagnetized sample at the origin (P1) where both field strength and flux density are zero, the field strength is increased in the positive direction as the flux begins to grow along the dotted path until P2 is reached. If the field strength is now relaxed, then, instead of retracing the initial magnetization curve, the flux falls more slowly. In fact, even when the applied field is returned to zero there will still be a remaining (remnant) flux density at P3. To force the flux to go back to zero, it is required to reverse the applied field (P4). The field strength here is called the coercivity. P5 is reached with further reversal of the field. This type of magnetization curve is called a hysteresis loop. Hysteresis constitutes a loss because it is required to expend energy in order to set up the remnant flux. This is explained in the Fig. II. The area (shown shaded) between the B-H curve and the B axis represents the work done (per unit volume of material);  $W = \oint H dB \text{ J m}^{-3}$  [15]

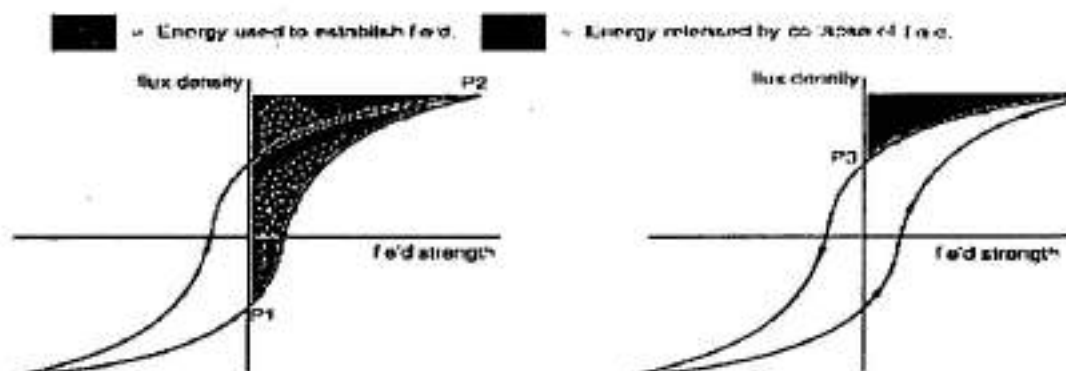


Fig. II: Pictorial representation of work done in a hysteresis cycle



It is clear that the energy required to magnetize the core by moving from P1 to P2 is more than that which it returns when going from P2 to P3. It is possible to picture it as 'back emf' which opposed the initial increase in coil current. The 'emf' generated is always proportional to the change in flux; but the flux changes less on the 'way down' than it does going up [15].

In other words, when a ferromagnetic material is magnetized, some of the domains are driven beyond the point at which the changes are reversible. Then, when the imposed field intensity is decreased to zero, the material retains some degree of magnetization. The total power lost over one complete cycle is proportional to the area within the hysteresis loop. Because this effect is related to an area, hysteresis loss is roughly proportional to the square of the working flux density; for transformer iron (iron-silicon steel), this about  $B^{1.6}$ . The particular value for a given material is called the *Steinmetz exponent*,  $n$  [16].

Because a hysteresis loss is incurred each time the core cycles, from positive to negative values of  $B$ , the loss rate (watts) is directly proportional to the frequency of operation,  $f$  (Hz). These proportionalities can be combined in a single formula for the hysteresis loss is  $P_h = K_h \times f \times B^n$  watts  $m^{-3}$  where  $K_h$  also depends on the particular core material [15].

### Magnetic Saturation

The hysteresis loop is complete only when the material being magnetized reaches magnetic saturation. The material being magnetized contains domains of aligned atoms such that each domain has a net dipole moment. Application of a magnetic field to these materials will cause these domains to rotate, and the walls between different domains to move such that the macroscopic dipole moment increases in the direction of the applied magnetic field. This in turn increases the magnetic flux density in the material above what would exist in a vacuum. In soft magnetic materials this net flux density is approximately linear to the magnetic field over a certain field range, and so it can be assumed that the material has a large constant magnetic permeability. At some field level, however, all of the magnetic dipoles in the material will be aligned, and the material will magnetically 'saturate' at a prescribed flux density. At this point, increasing the magnetic field in the material will not increase its flux density. Thus, the proportionality between hysteresis loss and the area under the hysteresis loop would hold good only when tracing of the loop takes magnetic saturation into consideration [16].

Magnetic saturation can be affected by residual stress in the material. Thus, in order to saturate the magnetically material, it is required to anneal the material before subjecting it to magnetization. Certain alloying additions like boron/boron compounds help in reducing the

residual stresses[17] which are sometimes an inevitable result of processing steps of the material.

The phenomena of magnetic hysteresis is very complex, and it is not yet fully understood, despite the attempts made to develop mathematical models of it. Stoner & Wohlfarth postulated a theory based on the rotation of the magnetic moments of single-domain particles with respect to their easy axes. Jiles and Atherton developed a theory in which pinning sites (i.e. inclusions, voids, crystal boundaries and lattice defects, etc.) inhibit domain wall motion. Another competing mathematical description is the Preisach model which assumes a ferromagnet to consist of many small magnetic domains, each with its own characteristic hysteresis loop [16].

### Eddy current loss

Eddy current losses occur whenever the core material is electrically conductive. The magnetic field is contained within a circuit formed by the periphery of the core in the same way as it is contained within a turn on the windings. Thus, around that periphery of the core, a current will be induced in the same way as it is in an ordinary turn which is shorted at its ends. In any resistive circuit the power is proportional to the square of the applied voltage. The induced voltage is itself proportional to  $f \times B$  and so the eddy losses are proportional to  $f^2 B^2$ .

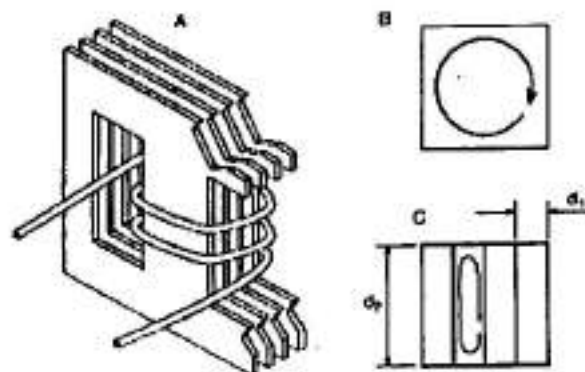


Fig. III: Eddy current in a laminated stack

Figure III shows how the idea of laminations is used to reduce eddy current losses. Using a solid iron core (as in cross-section B) results in a large circulating current. So, instead, the

core is made up of a stack of thin sheets (cross section C). The lines of magnetic flux can still run around the core within the plane of the laminations. However, the situation for the eddy currents is different. The surface of each sheet carries an insulating oxide layer formed during heat treatment. This prevents current from circulating from one lamination across to its neighbours.

It is obvious that, the current in each lamination will be less than the very large current within the solid core; but there are more of these small currents. Yet, they won't add up to the current produced in the solid core because of the following reasons:

Eddy current loss is proportional to the square of induced voltage. Induced voltage is proportional to the rate of change of flux, and each of the laminations carries one quarter of the flux. So, if the voltage in each of our four laminations is one quarter of what it was in the solid core then the power dissipated in each lamination is one-sixteenth the previous value.

Considering the long thin path that the eddy current takes to travel round the lamination, if the laminations were twice as thin (half of  $d_1$ ), the path length of the current would still be about  $2 \times d_2$ . However, the width of the path has halved and therefore **its resistance will double** and so the current will be halved. In other words, eddy current loss is inversely proportional to the square of the number of laminations [15].

If the laminations are brought down the size of a single particle, the eddy current losses will reduce further. However, as mentioned earlier, there are processing difficulties in obtaining good densities. In general, increase in density results in decrease in resistivity and thus increase in eddy current losses. It is necessary to add certain alloying elements to the iron powder, one of them being phosphorous, to increase the resistivity.

Increase in density also means more work hardening of the particles because of the higher compaction loads used to obtain higher densities. It is again necessary to add certain alloying elements like boron based compounds to the iron powder that will help reduce the work hardening [17] at higher compaction loads.

## EXPERIMENTAL

A method is being developed at ARCI by which P and B layers are created on iron powder particles followed by a thermoset layer to address the problems of resistivity, density and strain hardening during compaction. Preliminary results are reported in this paper. Atomized powder was selected for coating. The characteristics of the powder are shown in Table I.

In the first stage, chemicals containing surface alloying elements, suitably diluted with distilled water, were used to obtain coating on iron powders. To facilitate uniform coating of surface alloying elements and the thermoset polymer, a surfactant and small quantities of a hard phase were added. To prevent rusting of iron powder, an antirust agent was also added. By repeated experimentation, the quantities of all the additives were optimised.

TABLE I

Properties of Iron Powder

S.No	Properties	Atomized
1	Hydrogen loss	0.17
2	Carbon (wt %)	<0.02
3	Apparent density(g/cc)	2.66
4	Flow rate (sec)	32
5	<u>Sieve analysis</u> + 212 $\mu\text{m}$ -212 +150 $\mu\text{m}$ -150 $\mu\text{m}$ + 45 $\mu\text{m}$ -45 $\mu\text{m}$	Nil 7-15% Balance 15-25%

500 g of Fe powder was added to 50 ml of the above solution (with optimised constituents) and mixed well in a pot mill. The mix was removed and dried and crushed to obtain iron powder coated with alloying elements.

The powder was chemically analysed and also subjected to SEM and EDAX analysis. The analysis is shown in Annexure-I

1, 2 and 3% of a thermoset resin were added to the dried powder from the first stage and the three compositions were independently pot milled. The milled powders from were compacted at 520MPa to obtain toroids of 50 mm OD, 41 mm ID and 5 mm thick for magnetic measurements. Two samples for each composition were compacted. The compacts were then cured at temperature appropriate to the thermoset resin.

23 X 11x 6 mm samples were made for resistivity measurements; the same processing conditions as for toroids were followed.

From literature survey [6 to 14], it is clear that the compaction loads of 650 to 800 MPa are commonly used in addition to warm compaction. This is to be expected because density plays an important role in reducing hysteresis losses.

But, because of limitations of compaction press, it was necessary to restrict the compaction loads to 520 MPa. Thus, the studies were conducted on samples with relatively low densities. Hence, the actual values of different magnetic properties cannot be compared to those reported in literature. However, the efficacy of the coating process can be studied by various trends exhibited by magnetic properties.

Densities of cured toroids were measured by measuring their respective weights and calculating their volumes.

DC Magnetic properties were measured using a Walker fluxmeter. AC magnetic properties at low frequencies upto 400 Hz were measured using a Walkers hysteresis loop tracer.

## RESULTS AND DISCUSSION:

Chemical analysis of phosphated powder showed P content of 0.12 to 0.17%. EDAX analysis on particles confirmed presence of P and the thermoset in every particle scanned.

The densities of cured samples – toroids and specimens for resistivity measurement – are shown in Table 2.

TABLE 2  
DENSITIES OF CURED SAMPLES

S. No	% of thermoset	Density, g/cc
1	1	6.03
2	2	6.00
3	3	6.2



As a first step resistivity measurement was taken up. Fig. IV shows increase in resistivity with increase in the percentage the thermoset added. There is a substantial increase in resistivity with

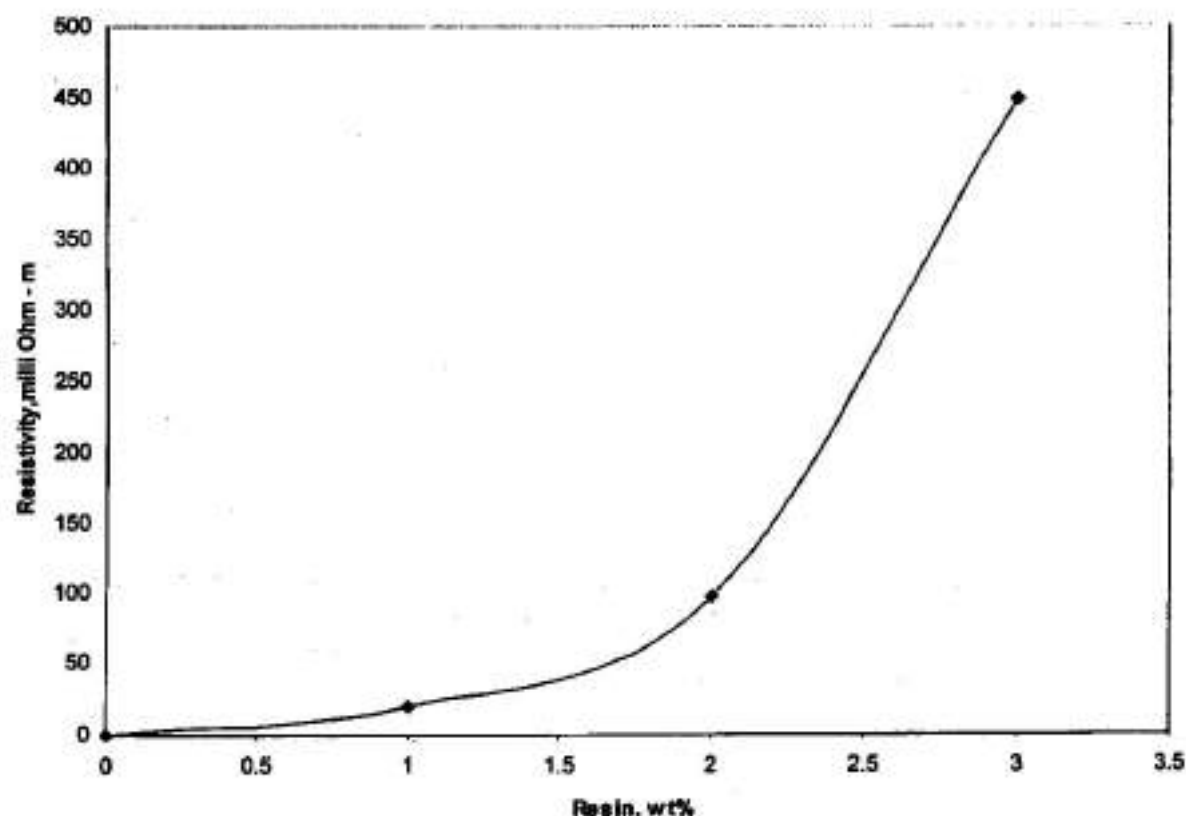


Fig. IV: Resistivity Vs % of thermoset

the increase in thermoset content of from 2 to 3%. The average particle size of the iron powder is about 120  $\mu\text{m}$ . Assuming the particles to be spherical the average surface area of a particles was calculated. A rough estimation of coating thicknesses with 1,2 and 3% of thermoset work out to be 0.6, 1.4 and 2.4  $\mu\text{m}$ . Thus, on a 120  $\mu\text{m}$  particle, a thermoset coating of 2.4  $\mu\text{m}$  showed.

Theoretically, a thorough dielectric coating should, in fact, increase the resistivity to infinity. This never happens because during compaction, rupture of the coated layers is inevitable at certain points. This is true for all coating techniques reported in literature [9 to 14].

Next, DC magnetic properties were measured and the results are plotted in Fig.V. Fe-P-3% thermoset resin was selected for this study.

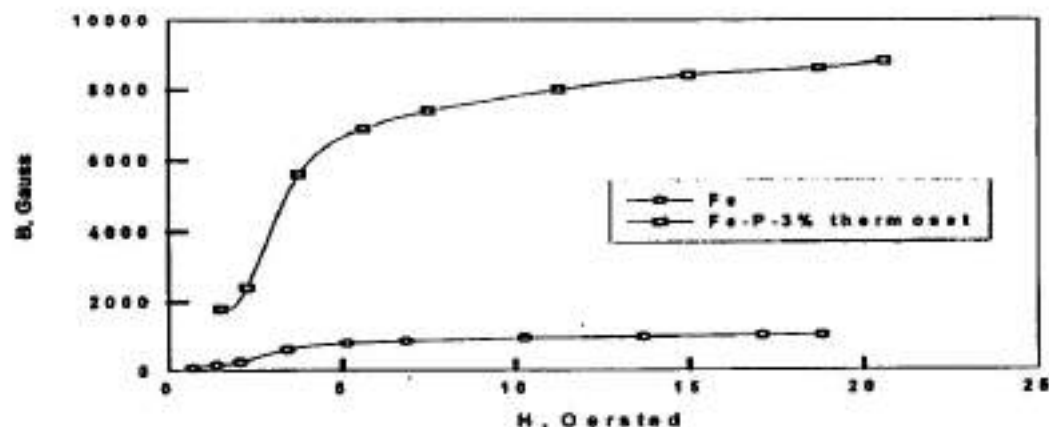


Fig V B-H curves for Fe-P with 3% thermoset resin

Fig. V shows 'B Vs 'H' plot for iron and the coated iron. It is clear from the plot that, pure iron sample saturates about 5 Oe, the induced field levelling off at about 1000 gauss. The coated samples show considerable increase in the B value, reaching 8000 gauss, the saturation starting from 7 Oe of 'H'.

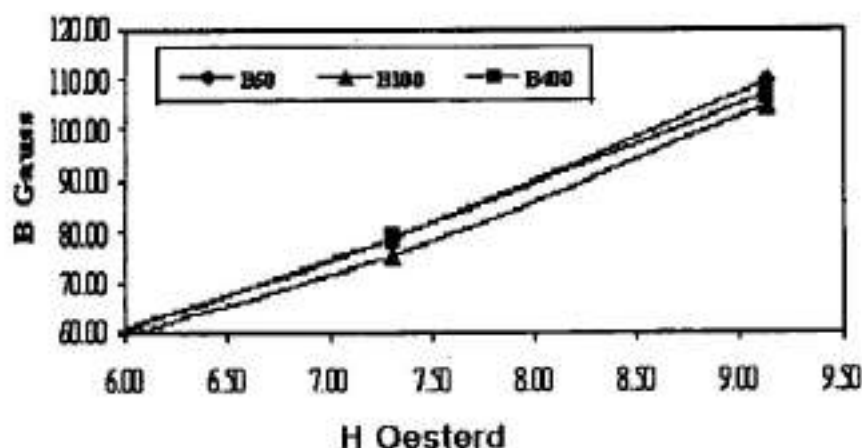


Fig. VI: H Vs B at low frequencies for Fe-P-3% thermoset

A similar study by Matt Persson was done and published in MPR Nov-2000, with coated samples with 7.34 g/cc density showed a B of 12 kG at a H of 0.65 Oe. The same values from Fig. V are 0.7 kG at about 5 Oe respectively, the density of the sample being 6.20 g/cc. As a second step, magnetic properties of coated samples (Fe-P-3% thermoset) at different frequencies (50, 100 and 400 Hz) were measured. The results are shown in Fig. VI.

It is clear from fig. VI that the samples cannot be tested at low frequencies unless there is a possibility to increase the field. From literature [1], it is known that, fields required to saturate a soft magnetic material are usually three times the DC saturation fields. This meant that, to saturate the samples a minimum H of 21 Oe is required.

Since there was no access to equipment that can generate such high H, it was decided to study the effect of higher frequencies. Figs. VII shows the effect of frequency on permeability.

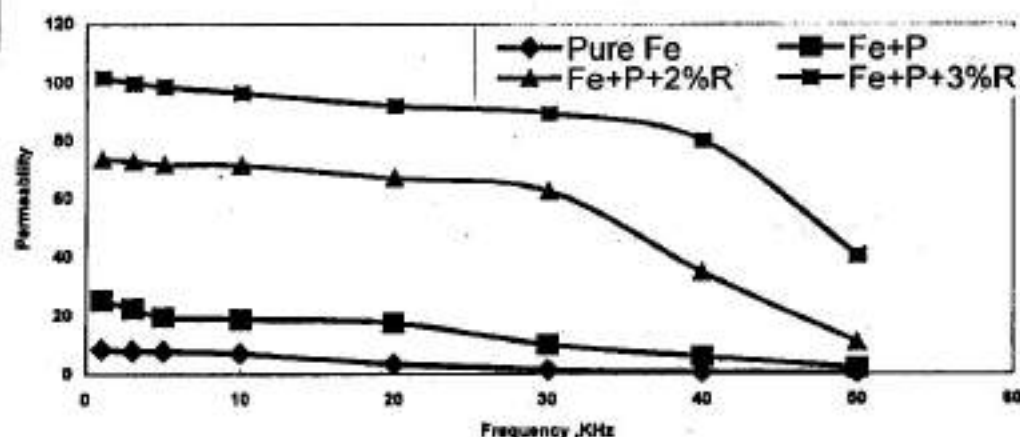


Fig. VII: Effect of frequency on permeability

This data was generated at a H value of 2.6 Oe. This H value was chosen because one of the samples saturated at that value.

The low permeability values for pure iron (almost nil at 30 KHz) are to be expected. The best permeability values (on comparative basis only) are shown by Fe-P-3% thermoset. Only

after 40 KHz, there is a drastic fall in permeability. Till that frequency the permeability sustains in a narrow range. From this it can be inferred that both hysteresis and eddy current losses are reduced.

## CONCLUSIONS:

1. A simple method of coating phosphorous, boron and thermoset polymer has been developed.
2. SEM and EDAX analysis shows P and the thermoset are coated on all the particles scanned.
3. DC magnetic properties are comparable with the values reported in literature.
4. The material shows sustained permeability at high frequencies
5. The material developed by the present method reduces the total core losses
6. Only preliminary studies have been conducted. A thorough study of magnetic properties at different frequencies with samples having different densities (unto 7.2 g/cc) has to be undertaken.

## REFERENCES

1. A. Kordeccki, B. Weglinski and J. Kaczmar: "Properties and Applications of Soft Magnetic Powder Composites" Powder Metallurgy, 1982, vol.25, no.4, p 201
2. M. Alakula, T. Codell, M. Persson and L. Sjoberg, "An Iron Composite Based Switched Reluctance Machine"; Industrial Electrical Engineering and Automation; STP EM 09-07-0636, 1995, p 251
3. T.A. Soileu and L.W. Speaker, "Powder Iron Core Magnetic devices", US patent No. 4,601,765.
4. R. Ward, R. Cambell and w. Boys, "Stator Assembly for an Alternating Current Generator"; US patent No. 4,947,065.
5. David E. Gay, 'High performance micro-encapsulated powders for various P/M applications' ; 'The International Journal of Powder Metallurgy - PM<sup>2</sup>TEC'95. p13

6. Exploitation of soft magnetic composites for electrical machines", by Dr. A.G. Jack, Special interest Seminar, 1998 PM World congress.
7. M. Tusovac and L. Baum, "Magnetic Properties of Metal Injection Moulded (MIM) Materials", Advances in Powder Metallurgy and Particulate Materials, Vol. 5, 1993, compiled by A. Lawley and A. Swanson, Metal Powder Industries Federation, Princeton, NJ, p 189
8. David E. Gay, 'High performance micro-encapsulated powders for various P/M applications' ; 'The International Journal of Powder Metallurgy – PM<sup>2</sup>TEC'95. p25
9. Dr. C. Gelinac, "Applications for ferromagnetic Composite Materials"; 1998 PM World Congress, Special Interest Seminar
10. R. JA. Bas, J. Puig and CB Molins, "Soft magnetic materis in P/M – current applications and state-of-the-art"; AMES S.A., Barcelona, Spain.
11. A/C challenges, Francis Hanejko (Hoganas corporations, New Jersy); Metal Powder Report vol 53 N7/8 1998.
12. Review by Joseph M. Capus " PM Soft magnetics Gaining Ground", Claude Gelines ( QMP & IMI- NRCC Canada), Potential applications for cured iron- resint composites) by Sylvian pelltier ( IMI- NRCC ) Metal Powder Report 1998 VOL 53 N7/8.
13. Patricia Jansson "Soft Magnetic Composites- from DC to 1MHz with Iron Powder"; 1998 PM World Congress, Special Interest Seminar
14. Joseph H. Bulzarik, Robert. F. Krause & Harold. R. Kokal " Accucore extends PM's magnetic reach"; Metal Powder Report, vol53, N7/8 1998, pp38-42
15. R. Clarke "Physics tutorials for undergraduates". Source: Internet.
16. Heath F. Hofmann, 1999-12-12. Source: Inrernet
17. B. D. Cullity, "Introduction to Magnetic Materials", Addison Wesley, 1972. Source: Internet



## IRON BASED ALLOY POWDER Fe-P FOR SOFT MAGNETIC APPLICATION BY A THERMO-CHEMICAL PROCESS

**K. Malobika, D.N. Fedorov\*, and A. Sivakumar.**

**International Advanced Research Centre for Powder Metallurgy and  
New Materials, Opp Balapur village, Hyderabad-500 005**

**\*Gas Institute of National Academy of Sciences, Degtriavska, St 39,  
Kyiv-113, Ukraine**

### ABSTRACT

The Fe-P system is a highly favoured soft magnetic material for AC applications because addition of P decreases the coercive force and increases the resistivity. Conventional wrought metallurgy route for Fe-P systems has limited magnetic applications because of hot-shortness encountered during hot rolling into laminates. Hence, PM is preferred for this alloy system. To obtain Fe-P system through PM route, the raw materials are Fe and Fe<sub>3</sub>P powders. The simplest production method involves mixing the constituents followed by compaction and sintering. However, this method does not ensure uniform and homogeneous distribution of the constituents. Partial-alloying and pre-alloying of the constituents are the usual methods followed to ensure the required distribution.

In the present case, a new chemical based method for P addition for more uniform distribution of P in the matrix has been developed. The resistance and magnetic properties of Fe-P compositions developed thus with P content ranging from 0.25 to 2% are presented and compared with available data on conventionally produced Fe-P systems.

### INTRODUCTION

The iron-phosphorous (Fe-P) system is being promoted commercially as a new soft magnetic material with claims to replace virtually all other high performance soft magnetic P/M materials [1]. The properties of P/M soft magnetic alloys are determined by alloy composition, processing conditions, microstructure, porosity and morphology of the pores. In soft magnetic components, density influences the magnetic properties; as porosity reduces, the flux density, remnant magnetization and maximum permeability increase markedly, whereas coercive force, which is a structure sensitive property, increases marginally. Alloying additions like Si, P, Ni increase the resistivity and decrease the coercivity. However, the manner in which the alloying additions are constituted has a significant effect on the porosity and microstructure[2].

The conventional methods for production of alloy powders of ferrous based P/M materials can be categorized as blended elemental powders, partial or diffusion alloyed powders and prealloyed powders. The process of blending involves mixing of iron powders with alloying additions and

lubricants in blenders. Typical alloying additions include copper, nickel, carbon in the form of graphite, and phosphorus in the form of ferrophosphorus,  $\text{Fe}_3\text{P}$ . However, this method does not always ensure uniform distribution of alloying elements in the matrix [3].

Partial or diffusion alloying is a pyrometallurgical process and may involve chemical and/or metallurgical reactions in addition to bonding. This method improves the inherent compositional homogeneity of the resultant powder without adverse effect to its other processing characteristics, especially, compressibility[4]. However, components made from diffusion bonded Fe-P powders produced using ferrophosphorous show heterogeneous microstructures and do not exhibit uniform hardness unless they are sintered at very high temperatures for long times, sometimes as high as 24 hrs [5].

Prealloyed powders are generally produced by water atomization of liquid alloy steel in which all the alloying elements are homogeneously distributed. These powders are characterized by dense particles with regular shape. With prealloyed powders, no further homogenization is necessary and components produced from these powders have a homogeneous microstructure with greater hardenability. However, these powders are generally less compressible than pure iron powder because of the solid solution strengthening effect of the alloying elements. Despite this limitation, these powders are used to produce soft magnetic components [6].

In the present paper a different method – thermochemical method - of production Fe-P powders is discussed.

## THEORETICAL CONSIDERATION

Conventional wrought metallurgy route for Fe-P systems has limited magnetic applications because of hot-shortness encountered during hot rolling into laminates [7]. Hence, PM is preferred for this alloy system. To obtain Fe-P system through PM route, the raw materials used are Fe and  $\text{Fe}_3\text{P}$  powders. Studies [2,3,4] have shown that the element P stabilizes the more open  $\alpha$ -phase and forms a liquid phase above  $1050^\circ\text{C}$ . Thus, it enables liquid phase sintering at the conventionally used temperatures of  $1120^\circ\text{C}$ . While reasonable magnetic properties are achieved by sintering at  $1120^\circ\text{C}$ , marked improvement is realized by sintering at higher temperatures and longer times[6,8]. High performance soft magnetic materials should magnetize and demagnetize easily; hence, applied field ( $H_c$ ) should be small, while maximum permeability after saturation ( $\mu_m$ ) and maximum induced field after saturation ( $B_m$ ) should be as large as possible for A.C or pulsed D.C applications. Further, resistivity  $\rho$  should be as high as possible in order to minimize the eddy current losses  $E_E$  according to Steinmetz equation[1].

$$E_E = K f^2 B^2 t^2 / \rho \quad (1)$$

where K is a proportionality constant, f is the frequency in hertz, B is the flux density in tesla, t is the sample thickness in meters and  $\rho$  is the resistivity in ohm-meters.

The total losses ' $E_T$ ' are given by

$$E_T = E_H + E_E \quad \dots \quad (2)$$

where  $E_H$  is the hysteresis loss.

Considering the importance of Fe-P system for soft magnetic applications, a new method of in-situ formation of Fe-P system with different percentages of phosphorous has been developed which ensures uniform distribution of the alloying element, minimising the time required for diffusion bonding process of alloying. To produce iron powder alloyed with phosphorus, a phosphated salt is reacted with iron powder. The process involves [9] mixing of Fe powder with P containing salt in solid or liquid form and converting the solid or liquid phase into gaseous phase by treating the mixture under hydrogen atmosphere for the required time and temperature. This results in deposition of phosphorus from gaseous phase onto surface of the solid iron particles ensuring its uniform distribution in Fe matrix and also intimate contact with Fe particles resulting in its diffusion into the iron matrix.

#### EXPERIMENTAL PROCEDURE:

In-house produced iron powder from hydrogen reduction of blue dust, (whose properties are given in table 1) and the salt were taken in the required proportions and mixed thoroughly. Theoretically calculation were done to estimate the quantity of salt to be added to the iron powder to obtain specific P content.

Table 1: Iron Powder characteristics.

Chemical composition:	
Fe	99.50 %
O	0.10 %
C	0.004 %
Si, Al, S, P,	traces
Ca, Mg, Mn	traces
Sieve Analysis:	
+ 180 $\mu$ m	2-3%
- 180 + 150 $\mu$ m	5% max.
- 150 + 45 $\mu$ m	balance
- 45	25% min.
A.D, g/cc	2.4
Compressibility at 4.2 T/cm <sup>2</sup> , g/cc	6.45

100 g of the blended mix thus obtained was thermally treated in a tubular furnace and crushed into powder. All powders were subsequently pressed and compacted at 7 T/cm<sup>2</sup> for rectangular specimens of size 25mmx 6mmx12mm and at 6.5 T/cm<sup>2</sup> for toroidal specimens of 40 mm I.D

and 50 mm O.D with 5 mm thickness. The powders were chemically analyzed before compaction and sintering. The green compacts were sintered at 1260°C for one hour under vacuum ( $10^{-4}$  torr). Sintered densities of the samples were calculated from their weights and dimensions. Resistivity measurements on sintered samples were carried out using micro-ohm meter by four-probe method. For studying the effect of P on resistivity and density, rectangular specimens with P contents of 0.24, 0.31, 0.43 and 0.48 were compacted at 6 and 7 T/cm<sup>2</sup> respectively and sintered under similar sintering conditions.

The powders were also studied using SEM. The powder as well as sintered samples were subjected to XRD analysis.

For one of the compositions, Fe-0.40P, measurement of induced magnetism 'B' for different applied fields 'H' was done at different frequencies. Values of initial magnetic permeability at different frequencies were calculated using the equation:

$$\mu = B/H, \quad \dots \quad (3)$$

where B is the induced magnetism in kilogauss and H is the field in Oersteds.

## RESULTS AND DISCUSSION

The chemical composition and average sintered densities of samples are shown in Table 2. The results of the chemical analysis indicate that varied phosphorous contents ranging from 0.24 to 2.32% have been achieved using the new method. These results are in conformity with the theoretical calculations. They also indicate that P content can be controlled very precisely.

TABLE 2: Iron – Phosphorous Compositions.

Sample No	Phosphorous, %	Sintered density, g/cc ( Average )
A	0.00	7.04
B	0.24	6.79
C	0.30	6.60
D	0.31	6.90
E	0.40	6.92
F	0.43	7.23
G	0.48	7.40
H	0.63	6.74
I	1.05	7.0
J	2.10	---
K	2.32	---

SEM micrograph of Fe-0.40P powder in Fig I shows that the powders retain their spongy nature.

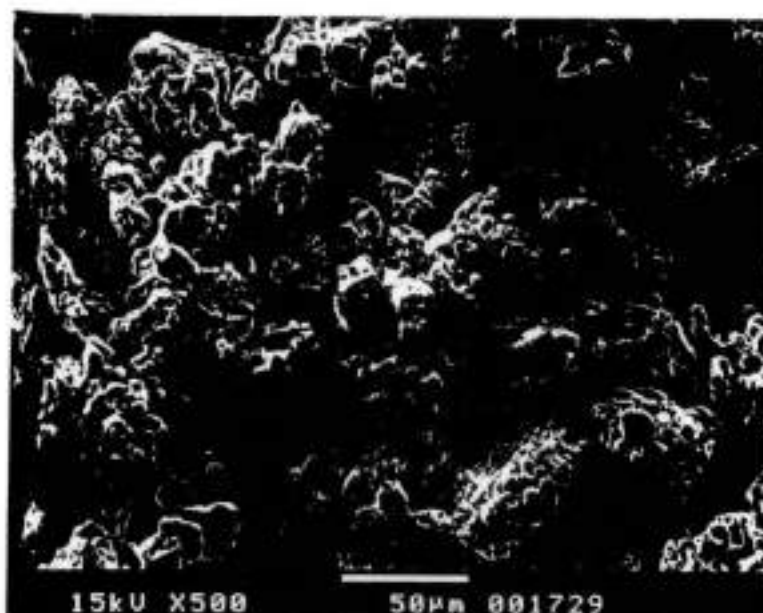


Fig I: SEM of Fe-0.40 P powder

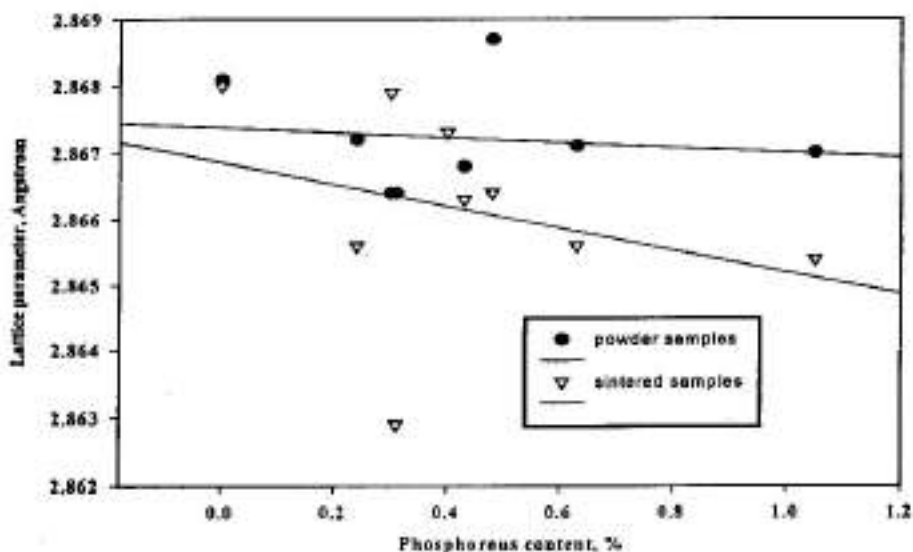


Fig .II: Lattice parameter Vs Phosphorous content



XRD studies show no phosphorous in elemental or combined form. This supports the idea that the process ensures homogeneous distribution of the alloying element (even in small quantities) into the iron matrix. From XRD patterns, lattice parameters were calculated and plotted against P content in Fig. II.

From the figure it is observed that with increasing P content, the lattice parameter is decreasing. The effect is more pronounced in case of the sintered samples than in the case of powders. This change in the lattice parameter confirms diffusion of P atoms into iron lattice.

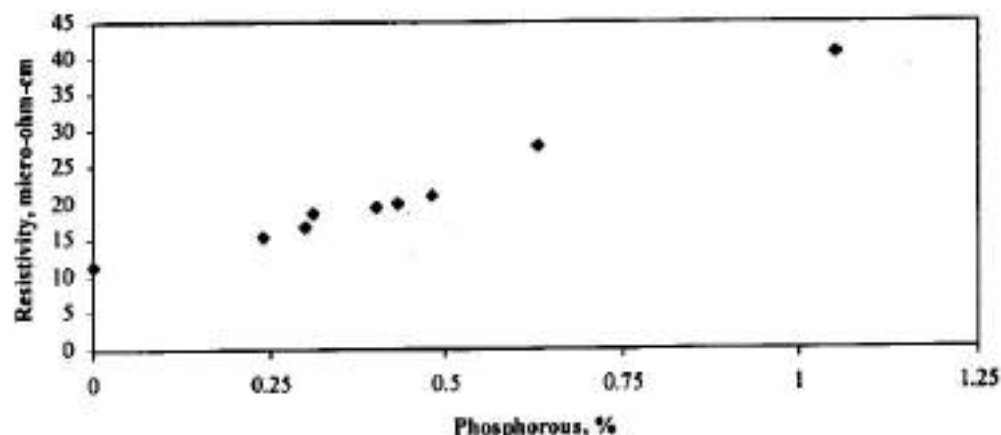


Figure III: Graph of Phosphorous content Vs Resistivity

Fig III shows the graph between phosphorous content and electrical resistivity which indicates increasing resistivity with increase in P content. The resistivity values from literature for Fe-0.45P [9] (starting material, prealloyed powders) range from 20 to 23 micro ohm-cm for different densities, whereas the values range from 19.34 to 23.2 micro ohm-cm for the same density and similar compositions for the samples tested.

Test specimens were produced with different phosphorous contents at two different compaction pressures of 6 and 7 T/cm<sup>2</sup> respectively. Green compacts were sintered at 1260°C and compositions at densities ranging from 6.40 to 6.50, 6.80 to 7.00, 7.20 to 7.30 and 7.35 to 7.40 g/cc.

Average resistivity versus densities for different P contents are shown in Fig. IV. Density has an important bearing on soft magnetic properties of iron. Increase in density reduces resistivity thus increasing the eddy current losses. At the same time increase in density decreases coercivity and hence the hysteresis loss. In order to reduce the total core losses, it is necessary to increase resistivity without compromising on density. This is achieved by addition of P in the required

percentage. Fig. IV shows that the effect of phosphorous content in increasing resistivity is more than that in decreasing density. The best results were obtained in samples containing 0.48% P.

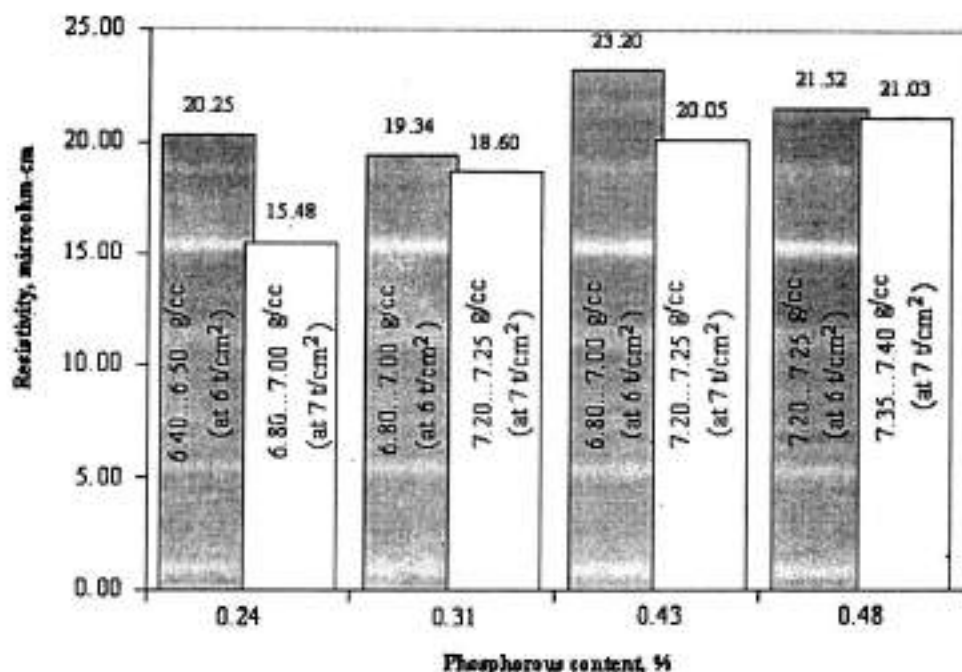


Fig.IV: Resistivity at different density ranges vs Phosphorous contents.

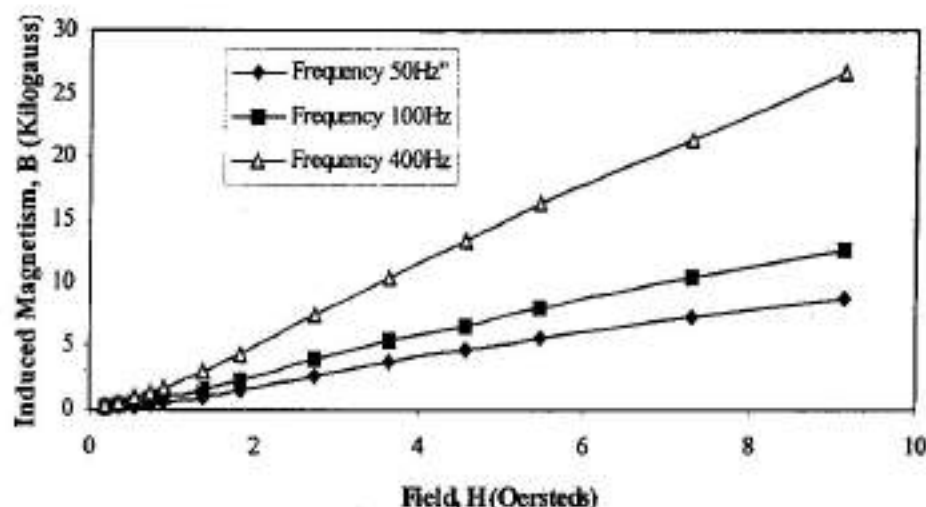


Fig. V: Graph between Field and Induced Magnetism

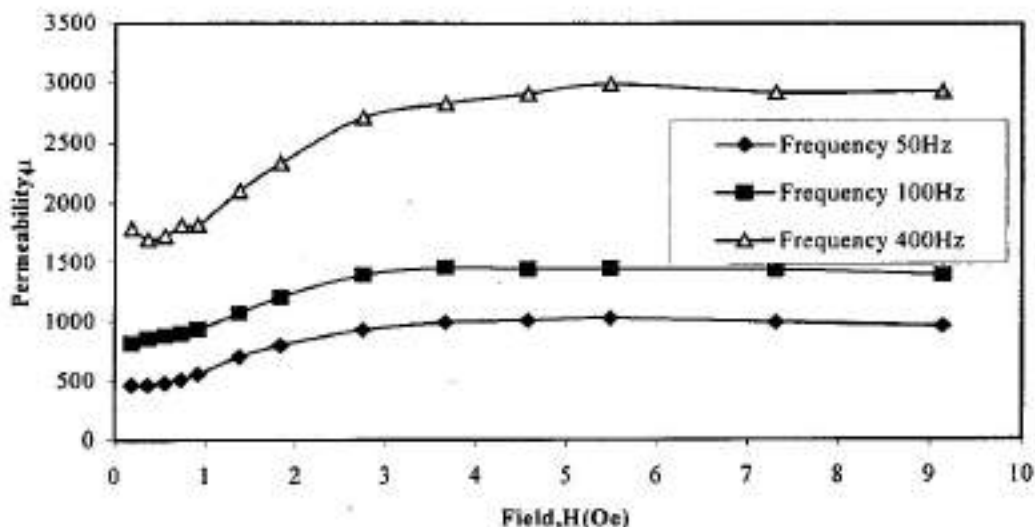


Fig. VI: Graph between field and permeability at different frequencies

The graph of ' $B$  Vs  $H$ ' and ' $\mu$  Vs  $H$ ' have been shown in Fig V and VI respectively for Fe-0.40P. These values have been measured at 50, 100 and Hz. Due to limitations of the equipment, measurement at higher frequencies was not done. It is clear that as  $H$  and frequency increase,  $B$  increases, while  $\mu$  increases upto a particular value of  $H$  beyond which it levels off. The  $\mu$  value obtained by us was a maximum of 3000 for an applied field of 9.5Oe. The standard values reported in literature are 4800 for field of 25Oe[1]. However, there is a clear indication of possibility of increase in  $\mu$  with further increase in  $H$  and even with increase in frequency.

## CONCLUSIONS

1. The addition of phosphorous by this thermochemical method enables to achieve close control over the composition.
2. Homogeneous distribution of P in Fe is obtained in this process.
3. The Fe-P powder obtained by this alloying method retains its spongy nature (compressibility) for PM processing.
4. The increase in the resistivity with increasing content of phosphorous can help in reducing eddy current losses.
5. With addition of phosphorous, it is possible to obtain higher densification, thus reducing hysteresis losses and hence the total core losses.

6. The resistivity values and the magnetic properties are comparable to those measured on samples produced from prealloyed powders.
7. Further measurements at higher frequencies are required to know when the samples get saturated and find out  $\mu_m$ . Further measurements are also required at higher H values to find out how much increase is possible for both B and  $\mu$  values

## REFERENCES

- 1) Howard I. Sanderow, "High temperature sintering", "New perspectives in powder metallurgy", Vol 9, MPIF, Princeton, New Jersey, pp168 ( 1990).
- 2) Lindskog, J. Tengzelius, and S.A.Kvist, "Phosphorous as an alloying element in Ferrous P/M", Modern developments in Powder Metallurgy, Vol.10, Metal Powder Industries Federation, Princeton, NJ, pp.133-151(1984).
- 3) P.Lindskog, J. Tengzelius, and S.A.Kvist, "Phosphorous as an alloying element in Ferrous P/M", Internal Report 76-2, Hoganas A.B, Sweden(1976).
- 4) B. Weglinski and J. Kaczmar, Powder Metallurgy, Vol 23, No.4, pp210-216(1980).
- 5) W. Brian James, "High performance Ferrous p/m materials for automotive applications", Metal powder report 46,(9), New Jersey, USA (1991).
- 6) K.H. Moyer, M.J. McDermott, M.J. Topolski and D.F.Kearney, "Magnetic Properties of Iron Alloys, Magnetic and Electrical P/M Technology", Metal Powder Industries Federation, Princeton, NJ, pp.37(1980).
- 7) Chaman Lall, 'Soft magnetism', "Fundamentals for powder metallurgy and metal injection moulding", Metal Powder Industries Federation, Princeton, NJ, pp.53-62(1992).
- 8) J.M. Capus and K. Hajmrle, " How Sintering atmosphere affect magnetic properties", Annual powder metallurgy Conf,(1982).
- 9) Stepanchuk A. N, Bilyk I.I, Boiko P.A, "Technology of the Powder Metallurgy", Kyiv, Vysha Shkola, pp 415( 1989).

## DESIGN AND FABRICATION OF VARIOUS TYPES OF BALL MILLS FOR THE SYNTHESIS OF ALUMINUM BASED METAL MATRIX COMPOSITE POWDERS

Rajesh Purohit, Pramod Sahu and Rakesh Sagar

Mechanical Engineering Department, Indian Institute of Technology, Delhi-110016

### ABSTRACT

Mechanical alloying is a viable processing route for the manufacture of ductile and brittle particulates of different alloys or composite systems. It consists of repeated welding, fracturing and re-welding of powder particles in a high energy ball charge. In the present work, three different types of ball mills namely tumbler ball mill, attrition mill and planetary ball mill have been designed and fabricated for the mechanical alloying of aluminum based metal matrix composite powders. The mixture of aluminum and 15 weight % SiC powder was mechanically alloyed using tumbler ball mill. The mechanical alloying was achieved in 15 hours of milling. Powder samples were taken out at each 5 hours interval in order to study the change in morphology of composite powder structures using scanning electron microscopy (SEM). The mechanism of milling has also been discussed. The critical rotational speed of the horizontal ball mill was determined. The temperature rise during milling was also measured.

**Keywords:** Mechanical alloying, aluminum powders, SiC particulates, ball mill, scanning electron microscope and critical rotational speed.

### 1. INTRODUCTION

Global competition has forced manufacturers to shift towards innovative ideas, newer manufacturing processes and substitution of conventional materials by new kind of materials to achieve a better quality of product. Automobile, aircraft and other industries are now shifting towards powder metallurgy process. The reason is that the products made by this process offer excellent properties like, high strength to weight ratio, high stiffness, corrosion resistance, wear resistance, low co-efficient of thermal expansion, closer dimensional tolerances, self lubricating properties and versatility to designer. The powder metallurgy process offers a number of advantages over the other manufacturing processes such as:

1. Reduction in manufacturing cost because of high material utilization, reduced machining and low energy consumption.
2. Improved performance because of fine-grained structure and chemical homogeneity.
3. Flexibility to the designer in material selection that allows the production of engineering components with optimized mechanical and physical properties.
4. Enables processing of materials having poor workability such as ceramics and carbides.



Due to the above benefits of powder metallurgy process it is a constant endeavor on the part of researchers to study each step of the process. The benefits obtained by the products made by this process almost depend upon the quality and homogeneity of the powder mixtures. The blending and mixing provide a mechanical mixture of two or more types of powder particles without any evidence of atomic bonding between them. For last few decades the mechanical alloying (MA) has been evolved as a newer powder processing technique to achieve mixing at molecular level. MA is a high energy, dry ball milling technique that produces composite metal powders with sub-micron and macro homogeneity. MA is being employed increasingly in the development of metal matrix composites (MMCs) because it leads to a relatively uniform distribution of the metal powders.

Mechanical alloying is a non-equilibrium powder processing technique and is widely used for the preparation of magnetic materials, alloys and inter-metallic compounds. The main advantages of MA are that the reactions, which occur at high temperature, are made to occur at low temperatures. Since the pioneering work by Benjamin and co-workers [1,2], considerable effort has been made at extending the range of materials that can effectively be processed by MA.

The process of MA starts with blending of individual powder constituents where the diameter of the particles can range from 1 to 500  $\mu\text{m}$ . During MA, the largest number of collisions are of the ball-powder-ball type in which the powders are deformed between the colliding balls as shown in Fig. 1 and Fig. 2. A single collision between two balls results in either coalescence or fracture of the entrapped material. The velocity of colliding balls, the kinetic shock energy and kinetic shock frequency are the important parameters that determine the mechanics of mechanical alloying [3]. By mechanical alloying process hard and fragile component is fractured and incorporated, at the same time, in the soft and ductile component. The powder particle size is changed during the entire process and some intermetallic compounds may also occur between the respective components.

In a ductile metal like aluminum, the powders cold weld easily and thus it becomes difficult to control MA. To reduce the tendency for cold welding, organic surfactants known as process control agents (PCA) have been added in small amounts e.g. 1-3 weight % of the total powder charge. The PCA delays cold welding and allows the material to work harden sufficiently to fracture. During sintering, the organic compounds decompose and the carbon is absorbed to form carbides [3]. Mechanical alloying is a complex process and hence involves optimization of a number of variables to achieve the desired product phase and/or microstructure. The effect of various process parameters such as mill type, material of milling container, speed, grinding medium, ball to powder weight ratio, extent of filling of vial etc. on the final milling product are discussed in detail by C. Suryanarayana [4]. All these process variables are not completely independent. For example, optimum milling time depends on the type of mill, size of the grinding medium, temperature of milling, ball to powder weight ratio etc.



Fig. 1 Effect of Impact

(a) Brittle single particle, (b) Ductile single spherical particle

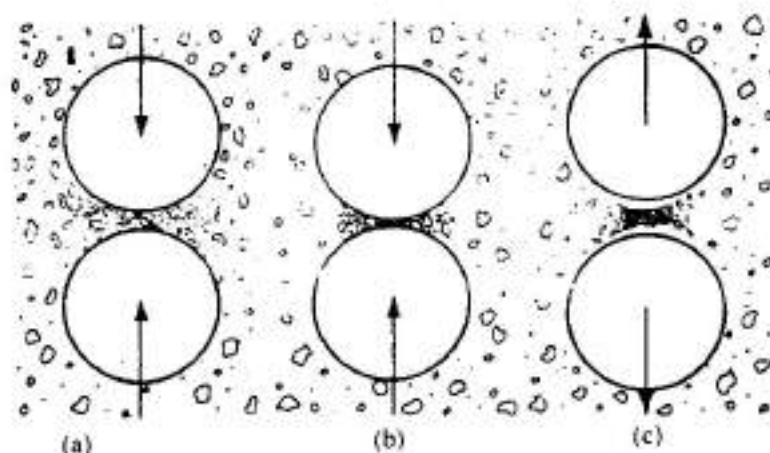


Fig. 2 Process of trapping an incremental volume of powder between two balls in a randomly agitated charge of balls and powder

## 2. MECHANISM OF ALLOYING

The mechanical alloying mechanism consists of an initial microforging stage in which particles are deformed in the absence of agglomeration by welding and fracture. Eventually, particles become so severely deformed and embrittled by cold work that they enter a secondary stage, during which the particles fracture by a fatigue failure mechanism and/or by the fragmentation of fragile flakes. Fragments generated by this mechanism may continue to reduce in size in the absence of strong agglomerating forces by alternate microforging and fracture. When fracture dominates and the role of microforging is negligible in the absence of welding agglomeration, flakes continue to become smaller until molecular interaction occurs. As particles (particularly flakes) become finer, coupling forces tend to become greater and agglomerates become stronger. Eventually, milling forces that deagglomerate the particles reach equilibrium with the coupling forces present, and an equilibrium agglomerate particle size results [5].

When cold welding between particles occurs, the initial process is microforging. This is followed by secondary process of fracture, microforging and agglomeration. After a period of time, cold welding and fracturing attain steady state equilibrium. Average particle size obtained at this stage depends on the relative ease with which agglomerate can be formed by welding,

fatigue and fracture strength of composite particles, and resistance of particles to deformation. Particle size distribution is narrow, because particles larger than average are reduced in size at the same rate that fragments smaller than average grow through accretion of smaller particles and wear debris produced by attrition [5].

The milling mechanism varies according to different combination of metals and alloys to be milled: (i) ductile-ductile, (ii) ductile-brittle, (iii) brittle-brittle systems [4,6].

#### Ductile-ductile system:

A large number of elemental blends that are mechanically alloyed so far fall in this category. The mechanism of alloying when both components of blends are ductile was first given by Benjamin and Volin [2] and was further dealt with in detail by Benjamin. The mechanical alloying occurs progressively in five stages. In the first stage, the equiaxed ductile particles are flattened by microforging resulting in flaky and plate like particles. Increased surface area of the particles results in extensive cold welding of powder components on further milling (second-stage) resulting in composite lamellae structure associated with an increase in average particle size. Meanwhile a small quantity of the powder, usually one or two-particle thickness, also gets welded on to the ball surfaces. This coating of the powder on the grinding medium is advantageous since it prevents excessive wear of the grinding medium; additionally the wear of the grinding medium does not contaminate the powder.

On further milling the aspect ratio of composite lamellae reduces due to fracturing and the plate like coarse particles becomes equiaxed. The increase in hardness and brittleness due to strain hardening is the reason of fracturing to dominate in this stage.

In the fourth stage, the welding orientations in the composite particles become random and convoluted. Alloying begins to occur at this stage due to the combination of decreased diffusion distances (interlamellar spacing), increased lattice defect density and the heating effect that may have occurred during the milling operation. The final stage is characterized by a narrow particle size distribution and the composition becomes more uniform. A saturation level of the hardness of the particles is attained in this steady state processing stage and all the particles get heavily cold worked. At this stage the individual lamellae cannot be resolved in an optical microscope. The completion of the MA process and attainment of the homogeneous structure is characterized by the ease in removal of powder from the grinding medium.

#### Ductile-brittle system:

The early work of Benjamin and his group [1,2,4,6] on the ODS alloys is a typical example of a ductile-brittle system. In such a system, the ductile metallic particles such as Ni or Al are flattened and welded to each other during milling, while the brittle phase such as oxide particles is fragmented/comminuted. These brittle particles are then entrapped along the cold welded interfaces in the layers of the ductile phase. As milling proceeds, the layers of the ductile phase come closer and ultimately become unresolved while the brittle phase is uniformly distributed as fine particles in the matrix of the ductile phase.

#### Brittle-brittle system:

During milling of brittle-brittle component system, the harder (more brittle) component gets fragmented and embedded in the softer (less brittle) component. Material transfer in these systems is thought to be due to diffusion caused by rise in temperature during milling. This may

be due to the enhanced diffusion paths in these systems caused by deformation induced defects which are expected to be insignificant in brittle-brittle systems [6].

### 3. FABRICATION OF BALL MILLS

Three different types of ball mills namely tumbler ball mill, attrition mill and a planetary ball mill have been fabricated for the mechanical alloying of various alloys and composite systems. The motion of milling medium and charge varies between different types of mill, with respect to movement and trajectories of individual balls, and the degree of energy applied to impact, shear, attrition, and compression forces acting on powder particles.

#### 3.1 Tumbler ball mill:

A tumbler ball mill (also called horizontal ball mill) has been fabricated for mechanical alloying of aluminum and SiC particulates. The tumbler ball mill consists of a cylindrical container (with 300mm diameter and 100mm width) with horizontal axis and supported by two axial shafts, which are mounted on two self-aligning ball bearings. The mill rotates at 80 rpm through a single-phase geared motor. The rpm of geared motor is 173, which is reduced to 80 rpm using pulley and belt drive.

The mill is filled with balls and powder charge up to about 20 to 35 % of its total volume and the milling is done for required period of time (12 to 15 hours). The balls either roll (cascade) down the surface of the charge or fall down (cataract) through free space on the material. Due to the combined action of centrifugal force and the friction between balls and container wall, the balls move together with the container wall until the gravitational force is balanced by the centrifugal force, and subsequently fall down in free space causing an impact with the powder particles.

As the mill is used for mechanical alloying of aluminum and SiC particulates, the container is made of the same material i.e. Al-15 weight % SiC<sub>p</sub> composites (through casting and further machining operations), to prevent contamination of powders from the container walls. The container is made leak-proof so that inert gas (argon) can be filled in it to prevent contamination from atmospheric oxygen. An opening for filling the powder and balls is provided with a rubber seal. To fill the argon gas the mill is equipped with two non-return valves.

#### 3.2 Attrition mill:

An attrition mill has also been fabricated, which consists of a water-jacketed stationary cylindrical container (300 mm diameter and 450 mm height) with a centrally mounted vertical shaft with a number of impellers radiating from it at different angles (Fig. 4). The impellers are mounted helically to obtain a complex motion of balls and powders in axial, radial and circumferential directions and hence to achieve a homogeneous mixing of powder particles. The shaft rotates at different speeds via a belt and pulley drive through a 1.5 Hp three-phase AC motor. The speed of the impeller shaft can be varied from 100 to 1000 rpm by changing the speed ratio of the belt and pulley drive. The mill is filled with powder and ball charge up to 35 % of its total volume. The rotation of central shaft with impellers causes a stirring action and differential movement between the balls and the material being milled. This provides a



substantially higher degree of surface contacts between the powder particles and the balls than any other ball mill.

Milling is accomplished by impact and shear forces. The rotating charges of balls and powder form a vortex at the upper end of the stirring shaft, into which the milling product and balls are drawn. The powder particles are impacted by balls travelling in various trajectories that collide within the dilated charge of balls and powder. Attrition mills are high-energy mills in which large quantities of powder (from 0.5 to 40 kg) can be milled in relatively shorter period of time (about 1 to 15 hours). High heat is generated during milling in attrition mill, which rose the temperature to high values. Therefore the mill is surrounded with a cooling jacket in which water is continuously circulated to carry away the heat generated and thus maintains the temperature to about 40 to 50 °C.

While the other ball mills use large mediums, normally 12.7 mm (0.5 in.) or larger, and run at low rotational speeds of 10 to 50 rpm, the attrition mill agitator rotates at speeds ranging from 60 rpm to 300 rpm and uses medium that ranges from 3 mm to 6 mm. The power input to attrition mill is used to agitate the medium and not to rotate or vibrate the heavy milling container. Product output is relatively low with attrition mills, compared to large tumbler and vibratory ball mills. Consequently, tumbler ball mills usually are used for production runs of 135 to 180 kg per day.

**Mechanism of attrition mills:** The central rotating shaft of an attrition mill, equipped with several arms (Fig. 5) exerts sufficient stirring action to tumble the grinding medium randomly through the entire chamber volume, causing irregular movement by:

- Impact action on the medium
- Rotational force on the medium
- Tumbling force as medium fills in the void left by the arms

For fine grinding, both impact and shearing forces must be present. In attrition mills, impact is caused by constant impinging of the grinding medium, due to irregular movement. Shearing action is produced by random movement of the balls in different rotational directions, which exerts shearing forces on the adjacent slurry. The strongest agitation occurs at a point located two thirds of the way from the center. Grinding does not occur against the chamber walls, which serves as a container rather than a grinding surface. Minimal wear of chamber walls ensures long service life.

In attrition mill, grinding time is related to medium diameter and agitator speeds, within given limits, as:

$$t = \frac{kd}{\sqrt{n}} \quad \dots\dots\dots (1)$$

where, 't' is grinding time required to reach a certain median particle size; 'k' is a constant that varies with the slurry being processed and the type of medium and mill being used; 'd' is the diameter of the medium; and 'n' is the speed of the shaft, in rpm.

### 3.3 Planetary ball mill:

Planetary ball mill is a high-energy mill because it gives large impact and attrition forces to the particulate materials. It consists of a number of cylindrical containers called vials attached at the periphery of a circular plate, whose axis is vertical (Fig.8). The vials contain metal powders and ball charge. The plate rotates about its axis, while the vials rotate about their

own axes as well as revolve about the center of the circular plate in the opposite direction, resulting in a planet like motion of the vials. Due to this counter rotation high impact and high attrition forces are generated. The angular velocity of the support plate of radius ' $R$ ' is represented by ' $\Omega$ ' and the angular velocity of vials of radii ' $r$ ' is represented by ' $\omega$ '. For a typical planetary ball mill which has ' $r/R$ ' between 0.1 to 0.3, the optimum setting of ' $\omega/\Omega$ ' is between -3.25 and -2.25 (negative sign indicates opposite sense of motion).

A planetary ball mill with four vials arranged along the periphery of an aluminum support plate has been fabricated as shown in Fig.6. The specifications of the mill are as follows:

Radius of vials: 67.5 mm

Height of vials: 200 mm

Radius of circular plate: 225 mm

Motor rating: 2 HP, 3 phase, 440 V, 925 rpm.

The motor rotates the support plate through a v-belt drive. The speed of the plate can be varied from 100 to 500 rpm using pulleys of different diameters. The drive for individual vials is also taken from the shaft of the support plate using v-belt and pulleys of different diameters. The critical rotational velocity of the mill is calculated by using the formula [3]:

$$\dot{w}_{crit} = -1 - \sqrt{(R/r)}$$

Where

$\dot{w}_{crit} = \omega/\Omega$  = critical ratio of vial speed to plate speed

$R$  = radius of support plate, 225 mm

$r$  = radius of vial, 100 mm.

Using above values of the parameters, the critical ratio of the vials to plate speed, ' $\dot{w}_{crit}$ ' was calculated to be -2.825. For optimum energy transfer from balls to powder during impact the ratio of vial speed to plate speed is kept about 80 % of the critical value [7]. Therefore the ratio of the angular velocity of vial to the angular velocity of plate is taken as -2.25.

The vials are filled (25 to 35 % of their total volume) with the grinding balls and the powder charge to be milled. The vials and the plate rotate in opposite directions and therefore the centrifugal forces on the balls alternately act in like and opposite directions. This causes the grinding balls to run down towards the central axis of the support plate.

To prevent contamination from vial walls the vials are made of the same material as the powder to be milled i.e. Al- 15 weight % SiC<sub>p</sub> composite (through casting and further machining process). To prevent contamination from atmospheric oxygen, the vials are made perfectly leak proof and the top cover plate is provided with rubber seal. Two non-return valves are provided in each vial for filling argon gas.

For mechanical alloying, the mixture of Al and SiC particulates in required proportions along with the steel balls are filled in the vials with about 25 to 35 % of their total volume and the cover plate with the rubber seal are screwed tightly. Then the argon is passed in the vials to escape the air and create inert atmosphere in the vials to prevent contamination. The mill is run for the required period of time (12 to 15 hours) until a steady state is reached when the composition of each powder particle becomes same as the proportion of the elements in the starting powder mix.





Fig. 3 Tumbler ball mill

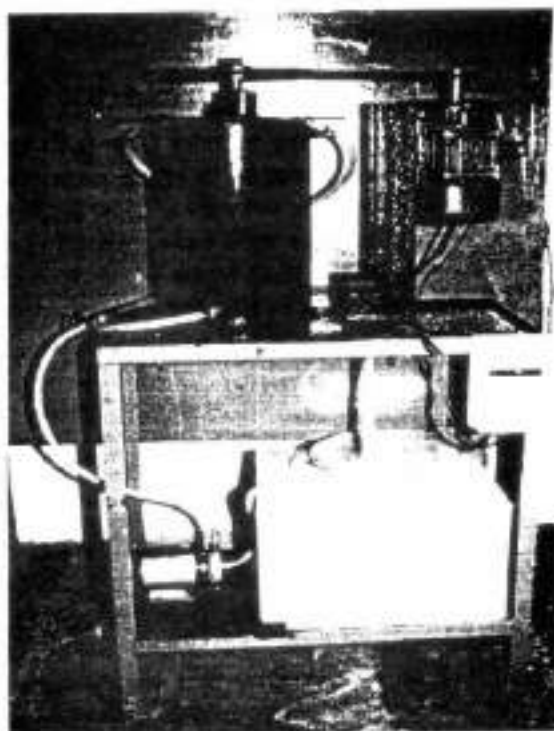
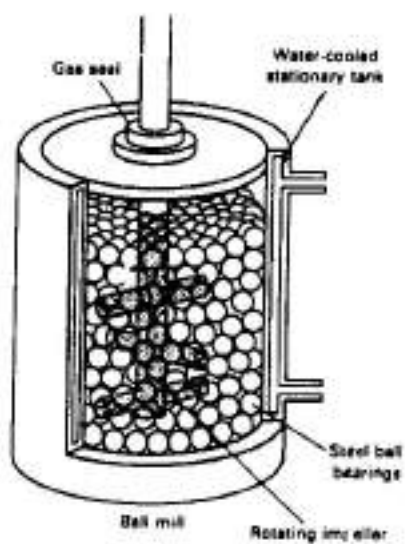


Fig. 4 Attrition mill



**Fig. 5 Inside view of an attrition mill**



**Fig. 6 Planetary ball mill**

#### 4. SYNTHESIS OF Al-15 WEIGHT % SiC COMPOSITE POWDERS BY MECHANICAL ALLOYING:

The mixture of aluminum with 15 weight % SiC particulates was ball milled using horizontal ball mill in argon atmosphere. The parameters used for mechanical alloying are shown in Table 1. Steel balls with ball to powder weight ratio of ten were used as grinding media. In order to minimize the extreme tendency of aluminum to get it self welded during milling, 2 weight % of stearic acid was added as a process control agent. Powder samples were taken from the mill at each 5 hours interval of milling. The scanning electron micrographs of the powder samples were taken to study the change in powder particle morphology during milling. The maximum temperature rise during milling was also measured.

TABLE 1 Horizontal ball milling parameters

S. No.	Parameters	Value
1.	Mill capacity	4500 cm <sup>3</sup>
2.	Container material	Al-15 weight % SiC composite (Cast)
3.	Speed of ball mill	84 rpm
4.	Ball diameter	9 mm( 50 %), 10.5 mm (50 %)
5.	Ball to powder weight ratio	10:1
6.	Weight of powder charge	500 gm
7.	Weight of the balls	5 Kg
8.	Percentage filling of ball mill	30 % (by volume)
9.	Process control agent	2 wt. % stearic acid
10.	Milling atmosphere	Argon

#### 5. RESULTS AND DISCUSSION

The powder particle morphology of Al-15 weight % SiC<sub>p</sub> composite powders at various stages of milling is shown in Fig. 7. Figure 7 (a) shows irregular, morphology of Al-15 weight % SiC<sub>p</sub> composite powders before mechanical alloying. Figure 7 (b) shows that after 5 hours of milling the equiaxed ductile aluminum particles are flattened due to microforging resulting in flat plate like structures while the SiC particulates were fragmented. Figure 7(c) shows a cluster type of powder particle morphology. The increased surface area of aluminum particles results in cold welding of powder components while the SiC particulates were entrapped along the cold welded interfaces of Al powder particles. In the final stage of mechanical alloying, as shown in Fig 7 (d), a fine homogeneous equiaxed composite structure is obtained due to fracturing of composite lamellae structure and their random welding orientation. Due to inert gas atmosphere the newly fractured surfaces were prevented from oxidation and than the shear forces result in welding of powder particles. The individual lamellae were unresolved in an optical microscope. The size distribution revealed that a homogeneous equiaxed powder particle structure with average powder particle size of 3  $\mu$ m was obtained after 15 hours of milling.

It has been observed that if the mechanical alloying is incomplete, it is very difficult to remove the powder from the balls and the inner walls of milling container while after

completion of the mechanical alloying the composite powder can easily be taken off from the balls as well as the walls of the milling container.

The temperature rise measured during milling of aluminum and 15 weight % SiC particulates was 95°C. The high value of temperature rise is due to exothermic reaction between aluminum and oxygen. The critical rotational speed of the horizontal ball mill, measured at 30 % volume filling of mill with the balls and powder charge was 110 rpm (see appendix).



Fig. 7 Scanning electron micrographs of the Al-15 weight % SiC<sub>p</sub> composite ball milled for (a) 0 hours, irregular particles; (b) 5 hours, flat lamellaer; (c) 10 hours cluster; (d) 15 hours, equiaxed.

## REFERENCES

1. Benjamin J. S., "Dispersion strengthened superalloys by mechanical alloying", *Metallurgical Transactions*, Vol.1, pp. 2943-2951 (1970)
2. Benjamin J. S. and Volin T. E., "The mechanism of mechanical alloying", *Metallurgical Transactions*, Vol. 5, pp. 1929-1934 (1974).
3. Kunal Ghosh, Tom Troczynski and Ashok C. Chakrader, "Processing of composite Al/SiC powders for plasma spraying", *The Int. J. of Powder metallurgy*, Vol. 35, No. 2, pp 27-35 (1999).
4. Suryanarayana C., "Mechanical alloying and milling", *Progress in Materials Science*, Vol. 46, pp 1-184, (2001)
5. William E. Kuhn, "Milling of Brittle and Ductile Materials", revised by Carl C. Koch, ASM Handbook, Vol. 7, Powder Metal Technologies and Applications, pp 56-70 (1998).
6. Murty B. S. and Ranganathan S., "Novel materials synthesis by mechanical alloying/milling", *International Materials Reviews*, Vol. 43, No. 3, pp 101-141 (1998).
7. Hiroshi Watanabe, "Critical rotational speed for ball-milling", *Powder Technology*, Vol.104, pp 95-99 (1999).

## Appendix

## Critical rotational speed:

An increase in milling speed increases the energy input into the powder and hence decreases the time required for milling. But depending upon the mill design there are certain limitations to the maximum speed that could be employed. The critical rotational speed of a ball mill is the speed at which balls just start to stick with inner surface of the milling container. The outermost layer of balls occurs when the trajectory of the balls coincides with inner wall of the jar. Above the critical speed, the balls will be pinning to the inner walls of the vial and do not fall down to exert any impact force. Therefore the maximum speed should be just below this critical value so that the balls fall down from the maximum height to produce maximum collision energy. The critical rotational speed ( $N_c$ ) of a ball mill is given by the formula [7]:

$$N_c = \frac{1}{2\pi} \sqrt{\frac{g}{R\sqrt{1-\beta}}} \text{-----(2)}$$

Where 'g' is gravitational acceleration, 'R' is radius of the milling container and 'β' is ball containing fraction, which is defined as the ratio of the volume of the charge (balls and powder) to the volume of the milling container.

## **SYNTHESIS OF COMPOSITE ALUMINA ZIRCONIA NANOPOWDERS BY THE SOL GEL PROCESS**

**A.Thirunavukkarasu, S.K.Malhotra and Paramanand Singh\***

**Composites Technology Center, IIT, Madras, Chennai – 600 036, India**

**\*Department of Metallurgical Engineering, IIT, Madras, Chennai – 600 036, India**

### **ABSTRACT**

Nanopowders of composite alumina zirconia were synthesized by the solgel process. This was carried out using the organometallic precursors aluminium secondary butoxide and zirconium isopropoxide. These were reacted in a medium of alcohol with continuous stirring at a particular temperature. Water was added to cause hydrolysis at pre-selected time intervals. The sol obtained was dried in an oven to cause gelation and further to produce powder.

The experimental parameters like temperature, concentration, pH and solvent type were varied to get higher yield of nanopowders. The temperature increase leads to enhanced hydrolysis and hydrolysis rates. The concentration controls the availability and level of aluminium hydroxide in the reaction liquid, which in turn affects the condensation process that nucleates and grows nanoparticles.

The pH affects the nucleophilic reactivity of water, which is necessary for the hydrolysis of the precursors. The solvent has different aspects such as dielectric constant and hydrogen bonding which influence the synthesis. The powder so produced were characterized using BET and TEM.

The present study deals with the effects of different parameters on the yield of nanopowders and characterizes the powder so produced using BET and TEM study.



## Introduction

Nanocomposites are a special class of composites. They are defined as composites of more than one solid phase where atleast one of the phases shows dimensions in the nanometer range [1]. Nanocomposites are divided into several subclasses based on composition: metal-based nanocomposites (e.g., metal/metal, metal/ceramic, metal/intermetallics and metal/glass), ceramic based nanocomposites (e.g., oxide/oxide including glass ceramics, oxide/nonoxide and nonoxide/nonoxide) and polymer based nanocomposites (e.g., polymer/glass, polymer/ceramic and polymer/metal)[2].

Nanocomposites can also be classified based on the microstructure. Niihara classified nanocomposites into four categories: intragranular, intergranular, hybrid and nano/nano composites. Alternatively, the connectivity concept proposed by Newnham [2] in defining microstructures of large dimensions in composites can also be extended to nanocrystalline size. The connectivity is described as 0-3, 1-3, 2-2, etc., with numbers denoting dimensions- the former signify the second phase and the latter represent the matrix (e.g., 2-2 means an interpenetrating two-dimensional microstructure).

Nanocomposites can be synthesized by any method capable of producing very fine grain size. The important feature of the successful processes is that they enable the crystalline phases to nucleate but suppress the growth of the nuclei.

Plasma phase synthesis is one of the processes used to synthesize nanocomposites. It requires the presence of plasma or a highly ionized form of gas called the fourth state of matter.

Another method is CVD Chemical Vapor Deposition in which gaseous reactants produce a deposit on a substrate. Nanocomposites have also been produced by sputtering which is a cold evaporation technique that employs pure metals, alloys and compounds to deposit a layer of material onto a suitable substrate.

The solgel method of synthesis involves the transformation of a homogeneous solution to a phase where the molecular structure is no longer reversible. In Intercalation, ion exchange is carried out with layered materials to produce a nanocomposite. Organometallic pyrolysis in which organometallic precursors are pyrolyzed to produce ceramic materials is also a successful method. Ignition of precursor solutions for producing nanocrystalline ceramics is called combustion synthesis or auto-ignition.

Yet another process is mechanical alloying which is a solid state process involving welding, fracture and rewelding of elemental or prealloyed powders in a high energy ball mill.

In the present work, the sol gel process has been chosen to produce nanocrystalline Alumina Zirconia composite powder. The sol gel process offers the possibility of being scaled up and also requires minimal facilities for its implementation.

Nanopowders can be processed to successfully obtain nano/nano composites which have properties that cannot be obtained with conventional materials. They have much higher strength and enhanced fracture toughness. They also have higher hardness. The elastic modulus of these materials is also higher. They also exhibit superplasticity. These composites show good strength retention at elevated temperatures. Once, one system has been studied, it can easily extended to

other systems.

Nanopowders of composite Alumina-Zirconia have been synthesized by the sol gel process. All the experiments spanning a wide spectrum of conditions lead to the formation of nanopowders. But there is also considerable variation in the results. These results point to the significance of synthesis parameters in determining the nature of the endproduct. While very high surface area powders are reported in the literature the variations therein and the parameters which may cause the same are not studied. An elucidation of some of the parameters and a verification of their significance is outlined.

### Synthesis of Nanopowder

Nanopowders of composite alumina zirconia have been synthesized by the sol gel process. This has been carried out using the organometallic precursors aluminium secondary butoxide and zirconium isopropoxide.

Aluminium secondary butoxide is dissolved in solvent containing acetyl acetone. The solution is raised to appropriate temperature and pH additives incorporated. This is hydrolysed by addition of distilled water/solvent mixture (distilled water + anhydrous solvent) and stirred for 1 hour in ambient environment. Subsequently zirconium n-propoxide is added and stirred for two hours. Finally water/solvent mixture containing water is added in a continuous stream under vigorous stirring [3]. This leads to the formation of a clear yellowish sol.

The experimental parameters like temperature, concentration, pH and solvent type were varied to get higher yield of nanopowders.

The sol obtained was dried in an oven at 110°C for four or more hours to cause gellation and then further to dry the gel.

The dried gel was calcined at 500°C for two hours to produce powder. The organic residues decompose and burn at a minimum temperature of 500°C hence the choice of this temperature for calcination.

The calcined powder was then milled in a planetary mill to break the lumps of powder. The milling was carried out for 5 hours at 100rpm.

#### **Characterization of nanopowders**

The maximum limit of powder that can be realized was calculated for a given amount of precursors. This was then compared with amount powder actually obtained and the yield was calculated. The yield was about 95%.

X-Ray diffraction was carried out to confirm the presence of both alumina and zirconia phases. The XRD was implemented in a Philips PW1710 instrument that had a diffractometer. CuK $\alpha$  radiation of wavelength 1.542 Angstroms was used to obtain the powder pattern. Since the powders from the sol gel process were amorphous, they were calcined at 1200°C for four hours before XRD characterization. The results showed the presence of alumina and zirconia in the material.

The powders were studied by the BET method to find the surface area per unit mass.

The BET procedure was carried out using a Sorptomatic 1990 instrument. The initial and final  $P/P_0$  was between 0.05 and 0.33. The relation for the surface area per unit mass was [5]:

$$S = X_m N_0 A_0 / (wM)$$

Where

$M$  = Molecular weight of adsorbate

$A_0$  = Average occupational area of an adsorbate molecule

$N_0$  = Avogadro's number

$w$  = sample weight

$X_m = (A+B)^{-1}$

$A$  and  $B$  are obtained from the variation of gas volume adsorbed ( $X$ ) with pressure  $P$  in the equation:

$$P/[X(P_0 - P)] = B + A (P/P_0)$$

where  $A$  is the slope and  $B$  is the intercept of the plot.

The BET surface area was then used to calculate the average particle size.

The relation between surface area and particle size is [5]:

$$d = K_s / (S\rho)$$

$d$  = particle size

$K_s$  = shape factor = 1

$S$  = surface area (in  $\text{m}^2/\text{gm}$ )

$\rho$  = density

TEM study of the powders was carried out using a Philips CM12 120 KV instrument at magnifications between 45,000 and 1,00,000. The powders were ultrasonicated in an Schoeller and Co. ultrasonic agitator in acetone medium. The frequency of the instrument was 30 KHz. A drop of the suspension was placed on a carbon coated grid. This was then allowed to dry and observed in the TEM.

## RESULTS AND DISCUSSION

The XRD spectrum is shown in Fig. 1.

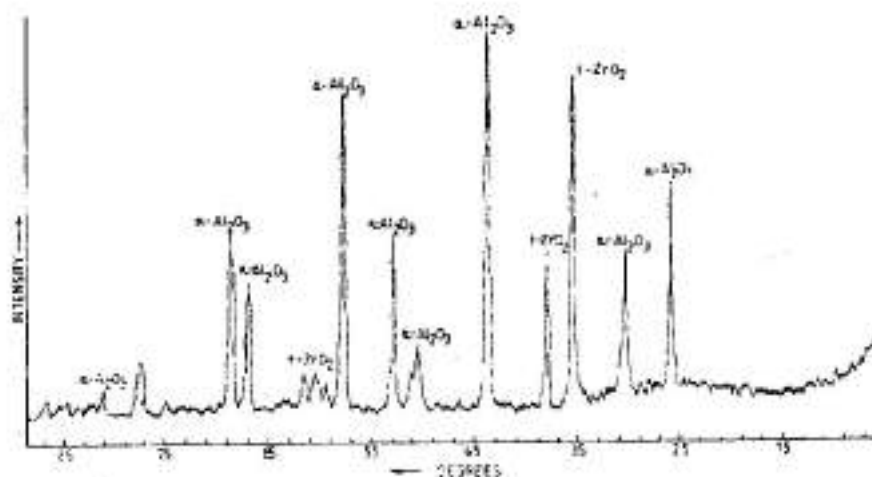


Fig. 1 XRD Spectrum of DebsiM powder.

The results shown the presence of both Alumina and Zirconia in the powder.



A typical BET plot for the old T4P powder is shown in Fig. 2.

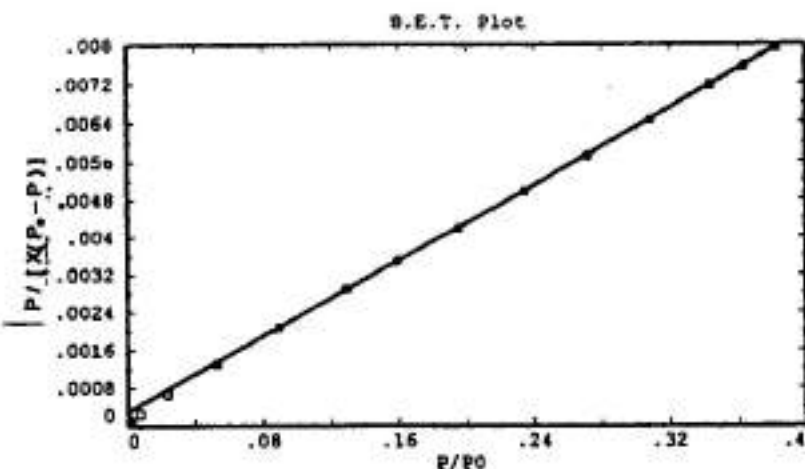


Fig. 2.

The experiments and BET results are shown in Table 1.

Sample name	Solvent	Concentration	R/H	Temperature	pH	Water/Alkoxide	BET Surface Area	d (nm)
OldT0	Eth	0.381	2	44	7	1	170.88	1.408
OldT2	40eth +60 acet	0.76	5	37	7	1	204.63	1.175
OldT3	70Eth+30 Acet	0.381	10	45	9	1	212.55	1.132
OldT4P	25 Eth + 75Acet	1.523	5	37	9	1.5	214.23	1.123
OldT6	90 Eth + 10 Acet	0.381	2	30	7	1	183.12	1.314
T19	10 Eth + 90 Acet	0.76	5	30	2	1	150.81	1.595
DebsiM	Butanol	1.52	2	30	7	1	243.41	0.988

ETH - Ethanol, ACET - Acetone

The TEM Photographs are shown in Fig. 3 and Fig. 4.



Fig. 3 TEM photograph of old TiO powder at 1,00,000 X.

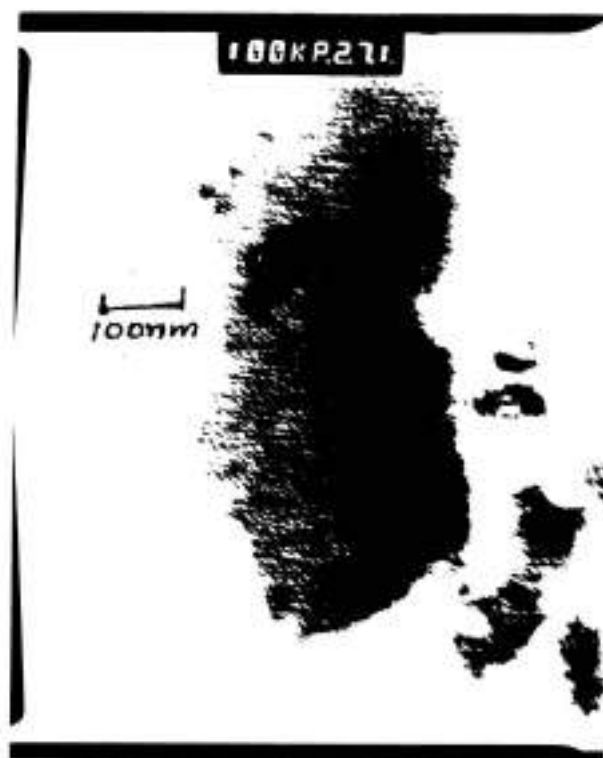


Fig. 4 TEM photograph of old T4P at 1,00,000 X.

The temperature increase leads to enhanced hydrolysis and hydrolysis rates. It also influences the rate and extent of diffusion of molecular species in the reaction liquid. The concentration controls the availability and level of aluminium hydroxide in the reaction liquid, which in turn affects the condensation process that nucleates and grows nanoparticles. The concentration also includes water which is a reactant (water concentration can be reduced by addition of ethanol)[4].

The pH affects the hydrolysis and condensation processes that take place during the synthesis reaction [6,7]. The solvent has different aspects such as dielectric constant [4] and hydrogen bonding which influence the synthesis. The dielectric constant reflects the insulation ability of the solvent which means that the electromagnetic van der Waals potential is used to polarize the solvent rather than attract neighboring particles. This means that a high dielectric constant leads to good separation and dispersion of the nanoparticles as soon as they are formed preventing agglomeration while also ensuring that they do not coalesce to form micropowders.

The second aspect of the solvent effect is that the solvent ethanol molecules hydrogen bond among themselves and they can also hydrogen bond with aluminium hydroxide molecules. This would lead to speedy and enhanced transport of the molecular species over longer diffusion lengths leading to coarsening of the nuclei. This would lead to coarse micropowders.

## CONCLUSIONS

- (i) By varying the process parameters (Temperature, concentration, pH and solvent type) it is possible to obtain optimum yield, particle size and particle size distribution.

- (ii) In the present work, it was observed that basic pH gives best results regarding particle size and size distribution.
- (iii) Effect of other process parameters is also being studied.

#### 4. REFERENCES

1. Sternitzke, Martin, Review: Structural Ceramic Nanocomposites, J. Eur. Ceram. Soc., Vol.17, No.9, pp1061 – 82 (1997).
2. Bhaduri & S.B.Bhaduri, Recent developments in Ceramic Nanocomposites, JOM, Vol.50, No. 1, pp 44-51, (1998).
3. M. Balasubramanian, Ph.D Thesis, Processing and Characterization of alumina-zirconia powders and composites, May 1996, IIT, Madras.
4. L.Gao, W.Li, J.Wang and J.K.Guo, Influence of some parameters on the synthesis of  $ZrO_2$  nanoparticles by heating of alcohol-aqueous salt solutions, Journal of Nanoparticle Research, Vol.1, No.1, pp349-352, (1999).
5. German, Randall M., Powder Metallurgy Science, Metal Powder Industries Federation, 2<sup>nd</sup> Edition, 1994.
6. Prabhu. G.B., Bourell, D. L., Abnormal grain growth in alumina-zirconia nanocomposites. Nanostructured Materials, Vol.5, No.6, pp 727-732, (1995).
7. Hench, Larry.L., West, Jon K., The Sol-Gel Process, Chemical Reviews, Vol.90, No.1, pp33-72, (1990).

## PRODUCTION OF SiC-Al<sub>2</sub>O<sub>3</sub> COMPOSITE POWDERS FROM FLY ASH

Sangita Kumari, M.M. Godkhindi, K. Das and P.G. Mukunda  
Department of Metallurgical and Materials Engineering  
I.I.T. Kharagpur 721302 (India)

### Abstract

Silicon Carbide is emerging as an important structural material both in monolithic and composite form. It is produced mainly through the carbothermal reduction of silica. Fly ash produced in very large quantities by thermal power plants is an industrial waste and is considered a serious pollutant affecting the fertility of the soil and quality of ground water. Fly ash however contains upto 60% finely divided silica particles. Present work attempts to investigate the possibility of converting the SiO<sub>2</sub> in the fly ash into silicon carbide and thus produce SiC-Al<sub>2</sub>O<sub>3</sub> composite mixtures by eliminating other undesirable ingredients.

### 1. INTRODUCTION

Nearly 73% of India's total installed power generation capacity is thermal, of which coal-based generation is 90%. The 85 utility thermal power stations besides the several captive power plants use bituminous and sub-bituminous coal and produce large quantities of fly ash. High ash content of Indian coal (30-50%) contributes to these large volumes of fly ash [1]. According to "The financial Express 3<sup>rd</sup> Jan. 1999," India generates 100 million tonnes of fly ash per year.

Fly ash is the finely divided coal combustion by product collected by electrostatic precipitators from the flue gases. The condition of the particle surface is initially reducing. As combustion proceeds, relatively non-volatile elements trapped in organic metallic species are transformed into gaseous phases along with the mineral matter in their more volatile form. [2]

Fly ash is a serious source of air pollution, since it remains air borne for long period and causes health hazards. It lowers the soil fertility and contaminates surface and sub-surface water, clogs natural drainage and reduces the P<sub>H</sub> of water.

The fly ash contains SiO<sub>2</sub>, Al<sub>2</sub>O<sub>3</sub>, Fe<sub>2</sub>O<sub>3</sub> and several other oxides all in the crystalline form with an average particle size of ~200 mesh. The present work attempts to convert the SiO<sub>2</sub> in the fly ash into SiC whiskers and by eliminating the undesirable oxides to produce Al<sub>2</sub>O<sub>3</sub>-SiC (w) composite mixtures.

### 2. THEORETICAL BACKGROUND

#### Thermo chemistry of carbide formation

A large majority of oxides such as silica, alumina and TiO<sub>2</sub> would undergo reduction to carbides, when heated to an elevated temperature in presence of carbon and a reducing atmosphere. The free energy of formation of SiC, Al<sub>2</sub>O<sub>3</sub>, and TiC can be calculated from the free energy data available [3]. The relevant relations are



----[1]

$$\Delta G_f = 148200 - 1.3T \log T - 117.08T \text{ Cal. } [298\text{K}-1686\text{K}]$$



$$\Delta G_T = 147200 - 2.73T \log T - 111.86T \text{ Cal. } [1686\text{K}-2000\text{K}]$$



$$\Delta G_T = 587620 + 3.75T \log T - 737.41T \text{ Cal.}$$



$$\Delta G_T = -94783.33 - 50.23T \text{ Cal.}$$

During the pyrolysis, reductions of these oxides take place, giving rise to following weight changes.

**Table 1: Stoichiometry of reactions**

Constituent (g)	Carbon (g)	Carbide (g)
$\text{SiO}_2$ (1g)	0.600	$\text{SiC}$ (0.667g)
$\text{Al}_2\text{O}_3$ (1g)	0.529	$\text{Al}_4\text{C}_3$ (0.706g)
$\text{TiO}_2$ (1g)	0.456	$\text{TiC}$ (0.747g)

Further  $\text{Al}_2\text{O}_3$ - $\text{SiO}_2$  phase system indicates a eutectic formation occurs at  $1587^\circ\text{C}$  with 95-mole%  $\text{SiO}_2$  and 5-mole%  $\text{Al}_2\text{O}_3$ . Heating of finely divided mixture of  $\text{Al}_2\text{O}_3$  and  $\text{SiO}_2$  particles may also produce certain glassy phases in the presence of other impurity oxides.

### 3.EXPERIMENTAL PROCEDURE:

#### Raw Materials

The fly ash used in the present investigation was obtained from the thermal power station at Kolaghat in West Bengal. Fly ash particles are composed of several major oxides:

**Table 2 Chemical Composition of fly ash**

Comp.	Weight percent of the comp.	Average Weight % of the Comp.
$\text{SiO}_2$	53.5-60.05	56.77
$\text{Al}_2\text{O}_3$	13.08-21.25	17.16
$\text{Fe}_2\text{O}_3$	5.79-21.25	13.52
$\text{MgO}$	0.96-1.43	1.19
$\text{TiO}_2$	0.86-2.00	1.43
$\text{K}_2\text{O}$	1.01-1.62	1.31
$\text{CaO}$	0.83-1.26	1.04
$\text{MnO}$	0.06-0.24	0.15
$\text{P}_2\text{O}_5$	0.42-0.76	0.52
LOI	2.49-6.74	4.61

### Pretreatment of raw materials and preparation of mixtures

The as-obtained fly ash was first boiled in distilled water for one hour and decanted mass was boiled in sufficient quantities of dilute HCl to remove various undesirable oxides. After acid boiling the contents were washed again in distilled water and dried. There was about 23.6% wt loss observed after this treatment. It may be noted that there is considerable fluctuation in the weight loss in individual experiments indicating the inhomogeneous nature of the fly ash. For further calculations, it was assumed that this fly ash when heated in bulk and for sufficient length of time would lose all oxides, leaving  $\text{SiO}_2$ ,  $\text{Al}_2\text{O}_3$  and  $\text{TiO}_2$  in the approximate ratio of 75:23:2. The trace of transition element oxides ( $\text{Fe}_2\text{O}_3$ ,  $\text{MnO}$  etc) may in fact have beneficial effect in term of providing a catalyst for the reaction (see table 3).

Table 3 Fly ash treatment

S.No.	Water Treatment				Dilute HCl Treatment				% Loss
	Initial Wt (g)	Final Wt (g)	Wt Loss (g)	% Loss	Initial Wt (g)	Final Wt (g)	Wt Loss (g)	% Loss	
01	4.03	3.57	0.46	11.4	3.39	3.00	0.39	11.5	21.6
02	4.07	3.57	0.50	12.3	3.39	3.03	0.36	10.6	21.6
03	4.10	3.92	0.18	4.40	3.64	2.35	1.29	35.44	38.3
04	4.10	3.76	0.34	8.30	3.52	3.34	0.18	05.11	12.9

Three different varieties of carbon source were used for the present investigation, viz, carbon black, charcoal powder and graphite powder. For the purpose of estimating the stoichiometric requirements, all the three carbon samples were heated to  $1200^\circ\text{C}$  in a vacuum furnace and the weight losses after holding for 1 hr were recorded and are listed in Table 4. It was observed that upto  $1200^\circ\text{C}$  all the volatile matter was removed and useful residue left. It was found that carbon black showed 7.3%, charcoal 55.4% and graphite 3.57% weight loss.

**Table. 4** Estimation of volatiles for different carbon sources

Powder	Wt before treatment (g)	Wt after treatment (g)	Wt loss (g)	% Loss	Average Wt Loss (%)
Carbon Black	2.30	2.13	0.17	7.40	7.30
	1.67	1.55	0.12	7.19	
Graphite	1.95	1.87	0.08	4.10	3.67
	1.32	1.28	0.04	3.03	
Charcoal	1.23	0.52	0.71	57.72	55.34
	1.30	0.61	0.69	53.08	

So for one gram of fly ash 0.644 g of carbon black, 0.932 g of charcoal and 0.621 g of graphite were mixed in terms of stoichiometric requirements.

### Mixing

The fly ash powder was next mixed with carbon black, graphite and charcoal powder separately in different ratios (fly ash: carbon=1:0.6 and 1: 1.2) and mixed thoroughly in a laboratory mixer. The mixer was operated at speed of 92 revolutions per minute and time duration for each mixing was about 15-20 minutes.

### Pyrolysis

The resultant mixture was pyrolysed over a temperature range of 1250-1600°C under  $10^{-2}$  Pa vacuum, with the heating rate of 15-18°C/min. The furnace used in the present pyrolysis was an Astro carbon resistance furnace.

### Post- pyrolysis Treatment

The pyrolysed product was first heated in a muffle furnace at a temperature of 700°C for 3 hr to remove excess carbon. Then it was boiled in NaOH solutions for 30 min. to remove unreacted  $\text{SiO}_2$ . The samples were finally subjected to X-ray diffraction analysis and SEM -EDS studies. XRD analysis was carried out on Philips PW 1840 X-ray diffractometer coupled with PW 1729 X-ray generator. The generator settings were 220V, 3.5 KVA and 50-60Hz.  $\text{CuK}\alpha$  radiations with Nickel filter was the choice in all of the experiments performed. SEM equipment of model no. JSM 5800 made by JEOL, was used. The samples were examined at three different magnifications. EDS analysis was used to identify the constituents.

## 4. RESULTS

**Table 5:** Estimated percentage loss observed during pyrolysis of fly ash and carbon mixture (1:0.6)

Temp. (°C)	Wt. Change during Pyrolysis		Wt. Change during Post-Pyrolysis Treatment	
	Initial Wt. of mixture (g)	Final Wt. of mixture (g)	Wt. after Carbon removal (g)	Wt after NaOH boil (g)
1250	1.601	1.245	0.81	0.69
1300	1.786	1.113	0.82	0.73
1350	1.870	1.048	0.81	0.67
1400	1.407	0.704	0.58	0.49
1450	1.522	0.739	0.58	0.50
1500	1.525	0.784	0.64	0.63
1550	1.652	0.755	0.63	0.58

**Table 6:** Estimated chemical composition of the pyrolysis product

Temp (°C)	Analysis before pyrolysis			Analysis after post pyrolysis treatment					
	Wt of SiO <sub>2</sub> (g)	Wt of Al <sub>2</sub> O <sub>3</sub>	Wt of TiO <sub>2</sub> (g)	Wt of SiC (g)	Wt of Al <sub>2</sub> O <sub>3</sub> (g)	Wt of TiC (g)	% SiC	% Al <sub>2</sub> O <sub>3</sub>	% TiC
1250	0.751	0.230	0.020	0.417	0.230	0.015	63.0	34.7	2.3
1300	0.837	0.257	0.022	0.479	0.257	0.016	63.7	34.2	2.1
1350	0.877	0.269	0.023	0.489	0.269	0.017	63.1	34.7	2.2
1400	0.659	0.202	0.018	0.370	0.202	0.013	63.3	34.5	2.2
1450	0.713	0.219	0.019	0.406	0.219	0.014	63.5	34.3	2.2
1500	0.715	0.219	0.019	0.429	0.219	0.014	64.8	33.1	2.1
1550	0.775	0.238	0.020	0.456	0.238	0.015	64.3	33.6	2.1

**Table 7:** Conversion efficiency during pyrolysis (fly ash: carbon black = 1:0.6)

Temperature (°C)	Theoretical Yield of SiC (g)	Exp. Yield of SiC (g)	$\eta$
1250	0.500	0.417	83.4
1300	0.558	0.479	85.8
1350	0.585	0.489	83.6
1400	0.440	0.370	84.1
1450	0.476	0.406	85.3
1500	0.477	0.429	89.9
1550	0.517	0.456	88.2

Table 8: Comparative efficiency of various form of carbon

Temp (°C)	Efficiency, $\eta$ (%)					
	Fly ash & carbon black mixture		Fly ash & charcoal mixture		Fly ash & graphite mixture	
	1: 0.6	1:1.2	1:0.6	1:1.2	1:0.6	1:1.2
1250	83.4	86.0	83.1	86.7	85.0	86.5
1300	85.8	85.3	85.4	81.2	87.2	87.9
1350	83.6	79.9	87.5	90.4	84.4	83.1
1400	84.1	83.0	87.1	82.6	78.0	71.3
1450	85.3	82.4	80.9	82.8	79.9	81.5
1500	89.9	84.4	84.0	90.2	84.8	87.8
1550	88.2	86.0	88.8	86.7	81.8	86.5

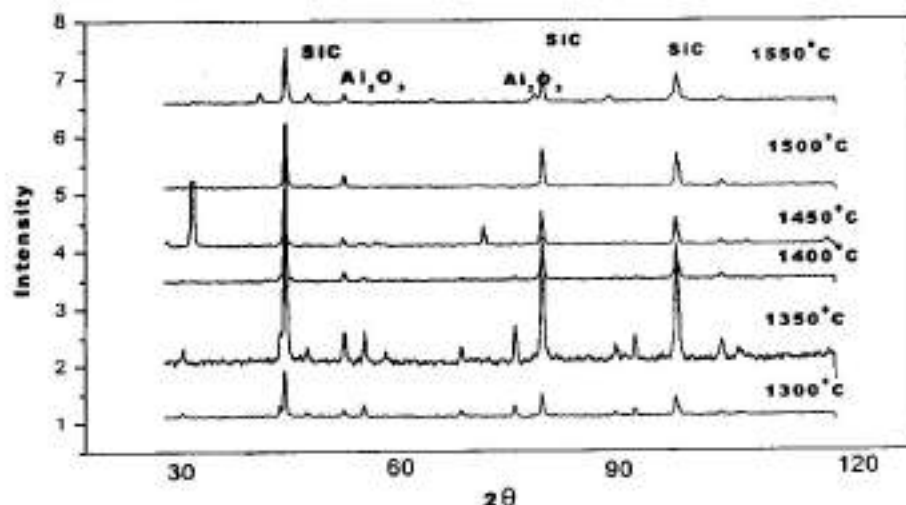
XRD and SEM Analysis

Fig. 1 XRD patterns of final product of fly ash and carbon (fly mixture pyrolysed at different temperature)

XRD pattern of pyrolysis products is shown in Fig 1. XRD data indicates that SiC was formed in both  $\alpha$  and  $\beta$  varieties. Scanning electron micrographs of SiC formed for different carbon varieties utilized is shown in Fig2, Fig3, and Fig4. The scanning studies clearly indicated that SiC formed has three morphology, thin long whiskers type of  $\beta$ -SiC, particulate form of  $\alpha$ -SiC and honeycomb type SiC. It was observed that very large amount of SiC whiskers and rod like  $Al_2O_3$  are distributed throughout the matrix in case of carbon black.

But in case of charcoal SiC formed has a typical honeycomb type. No whiskers are seen. Interestingly tape like structures with major constituents as  $Al_2O_3$  is seen in different parts of matrix in fly ash and charcoal mixture. This could possible be due to some kind of a liquid formation involving  $Al_2O_3-Al_4C_3$  eutectic or  $Al_2O_3-SiO_2$  type of eutectic. But when concentration of charcoal is increased, then SiC-whiskers are observed. In case of graphite sample, whiskers as well as particle type SiC is observed. The formation of large quantity of elongated whiskers in considerable quantity is exciting finding and this process may prove an interacting way of producing important composite mixtures from a harmful industrial waste.

SEM and EDS studies have revealed the formation of  $Al_2O_3$ -SiC composite with varying  $Al_2O_3$ : SiC content. The conversion product consists of mainly 63-64% SiC (w) and 33-35%  $Al_2O_3$  with 1-2% TiC with conversion efficiency of approximately 80%, (Table 7). However  $Al_2O_3$  formed has quite different morphology as compared to the starting material. This has important bearing on the usefulness of the final product as  $Al_2O_3$ -SiC composite mixture. The efficiency remains the same for all type of carbon; only the quality of the product makes the difference among various carbons tried. As the nature of source affects both the reactivity of carbon and by providing suitable substrate affects the morphology of the carbide produced. For the present investigation three different carbon sources were used viz, industrial carbon black, charcoal and graphite powder. Carbon black results whiskers, graphite results whiskers and particle and charcoal results honeycomb type morphology.

## 5.CONCLUSIONS

- Fly ash silica is successfully converted into Silicon carbide and SiC- $Al_2O_3$  (33.1-35.7%  $Al_2O_3$ ) composite powder.
- Silicon Carbide whiskers in very large quantities could be produced through pyrolysis of fly ash.
- The efficiency of the conversion is approximately 80% for all type of carbon tried. The difference arises only in to the quality of product. A lot of elongated whiskers were observed in case of carbon black samples. Graphite showed both the whiskers and particle type SiC. Charcoal showed honeycomb type SiC but with increasing the charcoal concentration whiskers were seen even in the fly ash charcoal mixture.

## 6. REFERENCES

1. The Business Line, 22 December 1999.
2. Fischer et al, (1976): Physical and morphological studies of size classified coal fly ash, Environmental Science and technology, vol. 12, No. 4, pp447-451.
3. O.Kubaschewski, E.L.Evans and C.B.Alcock, "Metallurgical Thermo chemistry" Fourth Edition, Pergamon Press Ltd, Headington Hill Hall, Oxford 4 & 5 Fitzray square, London (1967).





Fig. 2 SEM of final product of fly ash and graphite sample pyrolysed at 1400°C

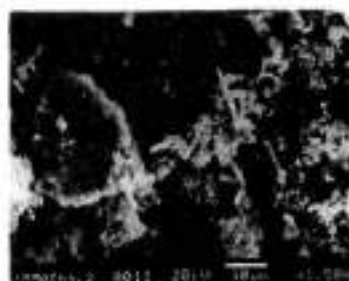


Fig. 3 SEM of final product of fly ash and charcoal sample pyrolysed at 1550°C

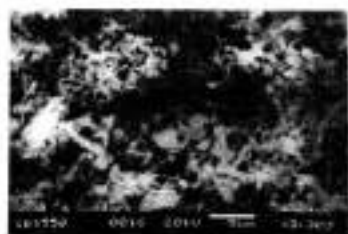


Fig. 4 SEM of final product of fly ash and carbon sample pyrolysed at 1550°C



Fig. 5 SEM of final product of fly ash and charcoal sample pyrolysed at 1400°C

## THERMODYNAMIC EVALUATION OF REDUCTION OF SILICA IN THE PRESENCE OF IRON

A.I. Khovavko, D.N. Fedorov\* and K. Malobika\*\*

\*Gas Institute of National Academy of Sciences, Degtriavska, St 39, Kyiv-113, Ukraine

\*\*International Advanced Research Centre for Powder Metallurgy and New Materials,  
Balapur P.O, RCI Road, Hyderabad-500 005

### ABSTRACT

SiO<sub>2</sub>, an inevitable impurity in iron ore (Fe<sub>2</sub>O<sub>3</sub>), has adverse effects on iron powders produced by reduction of the oxide. It is possible to beneficiate the ore by physical separation methods and reduce the content of SiO<sub>2</sub> upto 0.35%. Further decrease entails costly beneficiation techniques increasing the price of the ore and thus the price of the iron powder.

In general, it is difficult to reduce the highly stable SiO<sub>2</sub> to Si. High temperatures and low dew points, together with high hydrogen contents are required. However, when Fe<sub>2</sub>O<sub>3</sub>, containing SiO<sub>2</sub> as impurity, is reduced in hydrogen, there is a thermodynamic possibility of SiO<sub>2</sub> getting reduced such that Si dissolves in freshly reduced iron, thus reducing the activity of Si. This can happen at the conditions required for reduction of haematite to iron. The theoretical calculations to prove this possibility have been presented here.

### INTRODUCTION

Silicon is an important alloying addition to iron used for soft magnetic applications. Its addition increases electric resistance and decreases coercive force, hysteresis and eddy current losses. [1]

One of the methods of obtaining Fe-Si alloy is to mix iron powder with required amount of ferro-silicon powder with particle size less than 40 µm and thermally treat the mix for 10 to 20 hours. Another method is diffusion bonding from point sources. Both methods are complicated and costly.

Si can alloy with iron in any ratio according to the reaction[2]



where,

[Si]<sub>Fe</sub> denotes silicon dissolved in iron matrix, and, ΔG is given in cal/mol

Reduction of silica to silicon is usually done at high temperatures in electric arc furnaces using carbon as reduction agent.



$\Delta G = 168000 - 87T$ . Reaction (2) starts above 1930°K



$\Delta G = 141000 - 78T$ . Reaction (3) starts above 1810°K

In presence of iron, temperature of reduction decreases significantly as depicted in the following reaction:



$\Delta G = 141300 - 86T$ . Reaction (4) starts above 1640°K. The activity of Si reduces due to its dissolution in Fe, thus reducing the temperature required for carbothermic reduction.

#### IRON POWDER PRODUCTION FROM BLUE DUST ( $\text{Fe}_2\text{O}_3$ ):

$\text{SiO}_2$ , an inevitable impurity in iron ore ( $\text{Fe}_2\text{O}_3$ ), has adverse effect on iron powder produced by reduction of the oxide. It is possible to concentrate the ore by physical separation methods and reduce the content of  $\text{SiO}_2$  down to 0.35%. Further decrease entails costly beneficiation techniques because silica possibly exists in intimate contact with iron oxide below 0.35%. Thus, blue dust concentrate may be considered as naturally alloyed raw material with respect to silica. In conventional temperature range of iron oxide reduction (700 to 1000°C) it is practically impossible to reduce  $\text{SiO}_2$ . As a matter of fact, silicon has the potential to oxidize to silica even under hydrogen atmosphere having dew point of -70°C or better [3,4]. But, due to presence of highly active, freshly reduced iron particles the condition for dissolving Si into Fe is created. Due to dissolution in Fe, the activity of Si is decreased. This creates conditions under which reduction of  $\text{SiO}_2$  becomes possible.

#### THEORETICAL CONSIDERATIONS

Bulanov and Ukhov [5] had shown the possibility to reduce stable oxides ( $\text{SiO}_2$ ,  $\text{Al}_2\text{O}_3$ , etc., or, in general,  $\text{MeO}$ ) in presence of freshly reduced iron particles. The thermodynamic possibility of the process described by them is based on dissolving the reaction product [Me] in iron matrix.

In a reduction process for Me from naturally alloyed raw material by hydrogen at 700 to 1200 °C, the solid and gas phases in equilibrium are  $\text{MeO}$ ,  $\text{MeFeO}$ ,  $\text{FeO}$ ,  $\text{Fe}$ ,  $(\text{H}_2 + \text{H}_2\text{O})$ . Thus, this is a four-component system consisting of  $\text{Fe} - \text{Me} - \text{O} - \text{H}$ .

Using Gibbs phase rule, the degrees of freedom  $f$  are,

$$f = c - p + 2 = 6 - p \quad \dots \quad (5)$$

where,

$c$  denotes the number of components – 4 - in the system and  $p$  denotes the number of phases – 2 - in the system. From equation (5) it follows that in the case of non-variant system ( $f = 0$ ) there can be six phases simultaneously in equilibrium; in case of the monovariant system ( $P =$

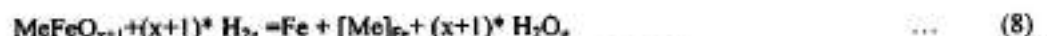
constant), five phases can be in equilibrium, while, four phases can be in equilibrium in case of bivariant system ( $P = \text{constant}$ ,  $T = \text{constant}$ ). In such a system, the possible chemical reactions and their respective equilibrium constants are given below:



$$K_{(6)} = (P_{\text{H}_2\text{O}}/P_{\text{H}_2})^{*a_{\text{Me}}} = F_1(T) \quad \dots \quad (6a)$$



$$K_{(7)} = P_{\text{H}_2\text{O}}^{*a_{\text{Me}}}/P_{\text{H}_2}^{*a_{\text{MeO}}} = F_2(T) \quad \dots \quad (7a)$$



$$K_{(8)} = (P_{\text{H}_2\text{O}}^{x+1}/P_{\text{H}_2}^{x+1})^{*a_{\text{Me}}} = F_3(T) \quad \dots \quad (8a)$$



$$K_{(9)} = P_{\text{H}_2\text{O}}/P_{\text{H}_2} = F_4(T) \quad \dots \quad (9a)$$

The system condition is completely defined by the parameters  $P$ ,  $T$ ,  $P_{\text{H}_2}$ ,  $P_{\text{H}_2\text{O}}$ ,  $[\text{Me}]_{\text{Fe}}$  and  $(\text{MeO})_{\text{FeO}}$ . Since reduction is conducted usually at  $P = 1 \text{ atm}$ ,

$$P_{\text{H}_2} + P_{\text{H}_2\text{O}} = 1 \quad \dots \quad (10)$$

Considering partial pressures of hydrogen and moisture as corresponding volume parts,

$$\text{H}_2 + \text{H}_2\text{O} = 1 \quad \dots \quad (11)$$

Now, we can write the functional connection that defines the problems as follows:

$$F_3(T, P_{\text{H}_2}, [\text{Me}]_{\text{Fe}}) = 0 \quad \dots \quad (12)$$

Applying this analysis to silica, it can be said that in the presence of freshly reduced iron powder with high surface, dissolution of Si into Fe-matrix can take place as per the equation,



where,

$\text{H}_2$ ,  $\text{H}_2\text{O}$  are hydrogen and moisture contents in equilibrium with Si dissolved in Fe.

The equilibrium constant of equation (13) will be:

$$K_{(13)} = a_{\text{Si}} \cdot (\text{H}_2\text{O})^2 / a_{\text{SiO}_2} \cdot (\text{H}_2)^2 \quad \dots \quad (13a)$$

where,

$a_{\text{SiO}_2}$  and  $a_{\text{Si}}$  – activities of silica and silicon, respectively, in Fe

Since  $a_{\text{SiO}_2} = 1$  and  $a_{\text{Si}} = \gamma_{\text{Si}} \cdot N_{\text{Si}}$ , where  $\gamma_{\text{Si}}$  denotes the activity coefficient and  $N_{\text{Si}}$  is the molar part of Si. Also, since Si content is low, it is possible to assume that  $\gamma_{\text{Si}} = 1$  and hence  $a_{\text{Si}} = N_{\text{Si}}$ .

Thus equation (13a) can be written as:

$$K_p = (\text{H}_2\text{O})^2 / (\text{H}_2)^2 \cdot N_{\text{Si}} \quad \dots \quad (14)$$

Bulanov and Ukhov [5] proposed the following equations to calculate equilibrium constant in this case.

$$\log K_p = -15786/T + 3.716 - \log N_{\text{Si}} \quad \dots \quad (15)$$

where,

$K_p$  is equilibrium constant;  $T$  is temperature in Kelvin.

Based on the above analysis, we can conclude that the system is defined by three equations, namely (11), (14) and (15) with the values of  $H_2O$ ,  $H_2$ ,  $K_p$  to be calculated.

It is possible to calculate moisture content and compare it with actual condition during reduction of  $Fe_2O_3$ .

$$H_2O = \sqrt{(K_p/N_{Si})} / (1 + \sqrt{(K_p/N_{Si})}) \quad \dots \quad (17)$$

## EXPERIMENTAL PROCEDURE

Reduction of  $Fe_2O_3$  was undertaken in pilot scale pusher type furnace at ARCI. Following were the reduction parameters:

Time of soaking	5 hours
Average furnace temperature	950°C
Cracked ammonia (dew point -50°C)	Reducing agent
Height of powder bed	12mm

The reduced cake was crushed, milled, separated into different fractions and then blended to obtain the required properties. The powder was characterized with following characteristics (See Table 2).

TABLE 1: Characteristics of the dust concentrate

Chemical composition:	
$Fe_2O_3$	99.45%
Carbon	trace
$SiO_2$	0.35 %
Others	traces
Size fraction	-200 $\mu m$

TABLE 2: Characteristics of the reduced powder:

Carbon content	0.005%
Oxygen content	0.300%
Si (total, ICP-AES)	0.228%
$SiO_2$ (wet chemical analysis)	0.200%
Green strength (at 6.5 $g/cm^3$ ), $N/mm^2$	65.80
Compressibility (at 7 Mpa), $g/cm^3$	6.84

## RESULTS AND DISCUSSION

The moisture content calculations were carried out using Excel software for different silicon contents and different temperatures. Depending on the assumed temperatures, equilibrium constants were calculated using equation (15). Thereafter based on silicon contents molar part of silicon  $N_{Si}$  were calculated using equation (3):

$$N_{Si} = A_{Si} / (\%Si) / (A_{Si} / (\%Si) + A_{Fe} / (\%Fe)) \quad \dots \quad (18)$$

where,

$A_{Si}$  - molecular weight of silicon, 28.086

$A_{Fe}$  - molecular weight of iron, 55.85

%Si - assumed content of silicon, %

%Fe - content of iron, %.

Then using equation (17) a moisture content that is in equilibrium with assumed silicon content dissolved in iron matrix was calculated.

A sample result has been shown in Table 3 for 0.2% silicon content. Based on the calculated results, a graph is plotted showing relationship between Si content, temperature and equilibrium moisture content. The plot is shown in Fig 1. One can see from Table 2 and Fig.1 that it is possible to reduce  $SiO_2$  during reduction of Hematite  $Fe_2O_3$  upto a Silicon content of 1.0%.

TABLE 3: Equilibrium condition for 0.2% Si dissolved in Fe

Temperature, °C	Equilibrium constant, $K_p$	Moisture content, %	Dewpoint of $H_2$ , °C
850	1.14240E-08	0.16888	-15.0
900	4.53949E-08	0.336082	- 9.0
950	1.61140E-07	0.631328	0.0
1000	5.17821E-07	1.126095	+ 9.0
1050	1.52347E-06	1.916104	+ 9.5
1100	4.14340E-06	3.121127	+25.0
1150	1.05000E-05	4.879225	+33.0
1200	2.50000E-05	7.332985	+40.5



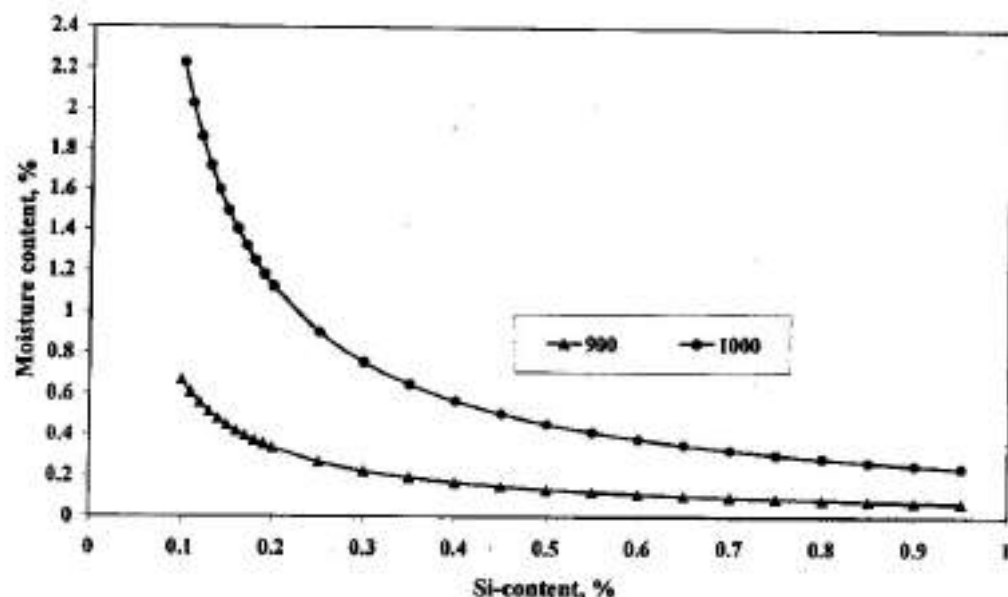


Fig.1. Moisture content Vs silicon content

The results of our experiment confirm the theoretical assumption (See Table 2). The percentage of silicon in silica is approx 46.7% by weight. Thus 0.2% of  $\text{SiO}_2$  contains 0.093% of Si. The balance i.e., 0.135% ( $0.228 - 0.093$ ) is reduced Si dissolved into iron. Thus around 60% of Si has been reduced during reduction of hematite.

## CONCLUSIONS

1. Conventionally, reduction of Si from its oxide takes place under high temperature using carbon as reduction agent.
2. Thermodynamically it is possible to reduce Si at temperature range 800...1000°C under hydrogen atmosphere if dissolution of Si in fresh reduced iron particles takes place.
3. Theoretical calculations have been done which show the possibility to reduce  $\text{SiO}_2$  during reduction of hematite.
4. Our experimental result confirms that it is possible to obtain iron powder alloyed with Si during reduction of iron ore concentrate containing silica.

## REFERENCES

1. Stepanchuk A.N, Bilyk I.I, Boiko P.A, "Technology of the Powder Metallurgy", Kyiv, Vysha Shkola, pp 415 (1989).
2. Kramarov A. D, Sokolov A.N, "Electrometallurgy of steel and ferroalloys", Moscow Metallurgy, pp 376 ( 1976).
3. Robert H. Perry, Don Green, "Perry's Chemical Engineers' Handbook", Kosadido Printing. Co. Ltd, Japan (1987)
4. Trusov B. G, "ASTRA software", Bauman Institute, Moscow.
5. Bulanov V.Ya., Ukhov V.F, "Production of iron powder from naturally-alloyed raw, Moscow, "Nauka", pp152 (1978)

## EFFECT OF ATTRITOR MILLING TIME ON THE PROPERTIES OF HARDMETAL POWDERS AND SINTERED COMPONENTS

**Authors:** S. Ramesh Rao, Pritish Bhattacharya, A. Shivashankar,  
R. Rengarajan and P.R.Desai  
Widia India Limited, Bangalore

### Abstract

One of the most important unit operation in manufacturing of hardmetal powders is wet milling of powders with binder. The particle size is very fine and is of the order of 10 $\mu$ , which calls for a prolonged, milling for uniform mixing of the constituents. Since milling is carried out in presence of stainless steel or tungsten carbide balls particle size reduction also takes place during milling. So milling time has a profound influence on the various properties of the hardmetal powders like average grain size, grain size distribution, carbon and adsorbed gases content. This in turn influences the properties of the sintered components like hardness, toughness, wear resistance and fracture toughness. Hence optimization of milling time is a very important step in processing of hardmetal powders. In the present work the effect of attritor milling time on the properties of hardmetal powders and sintered sample was studied. Two different grades of powder were taken for this purpose. The dry powders and the sintered samples made out of these powders were analyzed for their properties. Milling time was optimized for these two grades of powder on the basis on this analysis.

### INTRODUCTION

Milling of hardmetal powder with binder is carried out in either in a conventional ball mill or attritor mill. Both of these processes have their own processing advantages and disadvantages [1]. Apart from particle size reduction the main objective of the milling is to ensure that every carbide particle is thoroughly coated with binder. During milling the weighed amount of hardmetal powder and binder are fed as charge into the mill. The milling operation is carried out in the presence of an organic solvent like acetone or n-heptane to prevent oxidation of the constituent particles. Conventionally hardmetal powders are milled in ball mills where the energy for milling is obtained by the movement of the milling balls under gravity. But off late attritor mills have taken lead over the ball mills as the equipment widely used for milling of hardmetal powders. Attritor mills are high energy mills where mixing of constituents takes place due to high energy obtained by the movement of balls and agitator. Attritor milling of powders efficiently causes irregular movement of the grinding media and not group movement. There would be no impact from the grinding media on the particles if both media and slurry (solids in the medium) move together [2]. The Milling operation has profound influence on various characteristics of graded hardmetal powders like average particle size, particle size distribution, size, shape of particles, bulk density and tap density [3,4,5]. Milling also alters the chemistry of hardmetal powders by changing its carbon and adsorbed gas content. The oxygen content in the powders is high during attritor milling as the powder absorbs lot of atmospheric gases. The properties attained in dry powders after milling influences subsequent compaction and sintering operation. While powder characteristics like particle shape, particle size

distribution, tap density and bulk density has a say on the compaction behavior of powders, the particle size and chemistry of hardmetal powders exercise a great degree of control over sintered properties like hardness, toughness, magnetic coercivity ( $H_c$ ) and specific magnetic saturation ( $4\pi\sigma$ ). The hardmetal powder has a tendency to absorb large amount of energy especially during attritor milling which when compared to ball mill is an energy intensive process. The energy adsorbed during milling manifests itself in the form of a distorted lattice structure. Powder having higher energy content will have a more distorted lattice structure, which will hasten recrystallization and grain growth tendency during subsequent sintering.

During preparation of a graded hardmetal powder optimization of its milling time is of prime importance to exercise a control over the final properties of sintered compacts. An overmilled powder has the tendency of undergoing abnormal grain growth during sintering while an undermilled powder will not give optimum set of mechanical and physical properties in the sintered parts. An optimum milling time not only gives the requisite set of properties to the sintered compacts but it also standardizes various process variables and process parameters involved in the whole operation of making a sintered hardmetal compact, right from carburizing stage to sintering stage.

#### EXPERIMENTAL PROCEDURE

The present work is primarily aimed at optimizing attritor-milling time for hardmetal powders. Two different hardmetal grades with the specifications given in Table-I were chosen for this purpose. Grade-A is a straight grade and having two phase  $\alpha$  (WC) and  $\beta$  (binder) structure whereas Grade-B is an alloy grade and has three phases  $\alpha$ ,  $\beta$  and  $\gamma$  (cubic carbide).

TABLE I Composition of Grades

S.No.	Grade	ISO application group	Composition, Wt %		
			WC	Co	Cubic Carbide
1.	Grade-A	K20	94.0	6.0	0.0
2.	Grade-B	P30	78.5	11.5	10.0

The carbide was milled with cobalt in an attritor mill with acetone as the milling medium. Hardmetal powder samples in the form of slurry were collected from the attritor mill for this purpose. The sample collection was started for a milling time of 7 hrs for Grade A and 4 hrs for Grade B and they were collected at regular intervals of one hour till the completion of milling operation. Samples were collected in a glass beaker for two powder batches for each of these grades. Nearly 500gms of sample in the form of slurry was collected randomly from five different locations of the attritor mill. The slurry samples were dried in a dessicator to remove acetone. After drying, a part of the dry powder was analyzed for particle size distribution, oxygen and nitrogen content. The remaining dry powder was pressed in a conventional direct press to form the green compact. Green compacts from different milling time samples were then sintered in one batch to form the sintered compacts (will be now referred as dry test samples). The dry test samples were then analyzed for sintered properties like coercivity, specific magnetic saturation, hardness, and fracture toughness. Palmqvist's method [6,7] was used to measure fracture toughness of dry test samples. The fracture toughness and hardness measurement was done at five different locations in the sample and its average value was taken.

into consideration. The dry test samples were then examined to study the microstructural features like porosity, binder distribution, grain size and grain size distribution.

## RESULTS AND DISCUSSIONS

The results of the analysis performed on dry powders and dry test samples for the two powder batches of two grades namely Grade A and Grade B are given below.

### Dry Powder Characteristics

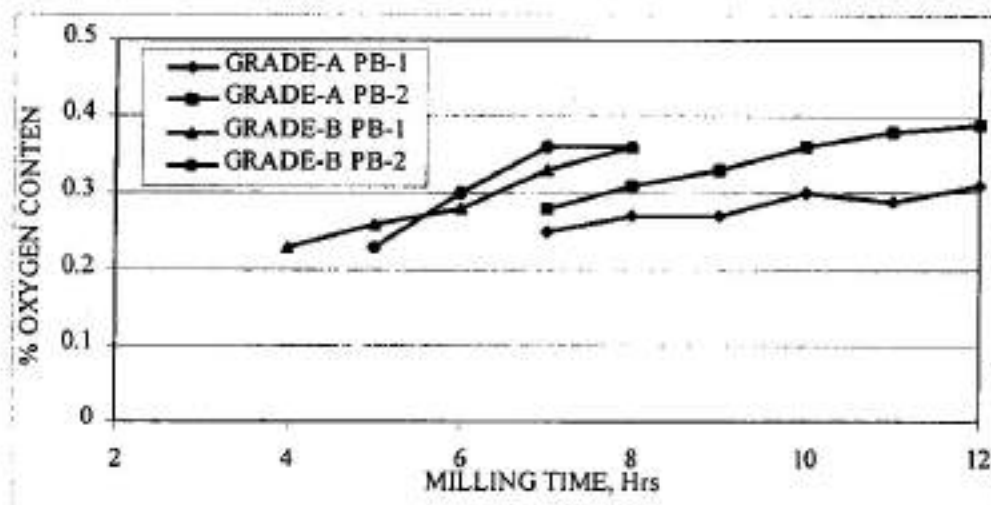


Fig 1 Variation in Oxygen absorption of dry powder with milling time

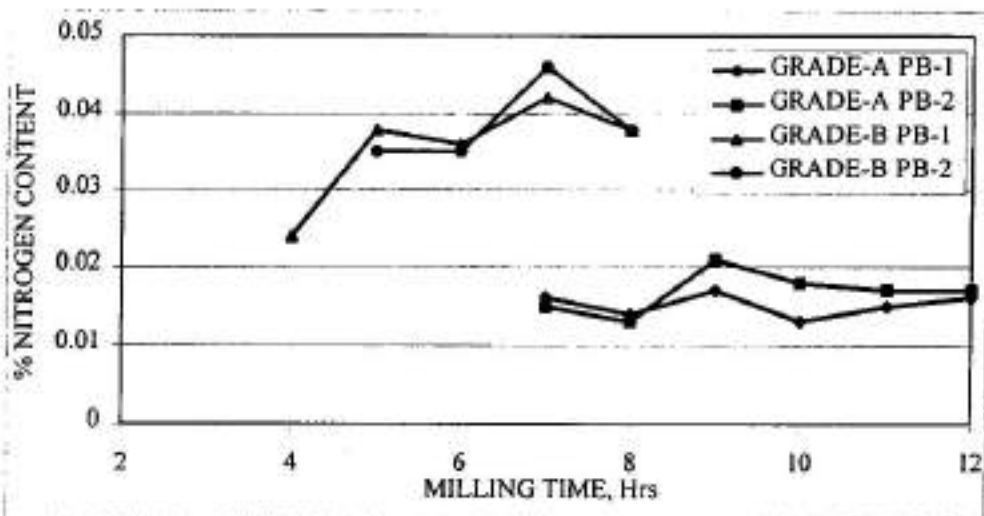


Fig 2 Variation in Nitrogen absorption of dry powder with milling time.

From chemical analysis of the dry powders it is clear that the adsorbed oxygen content increases with an increase in milling time for both the grades of powder as shown in Fig 1. This can be attributed to the increased surface area of particles by size reduction as the milling progresses. The increased surface area increases the quantum of oxygen adsorption. Also nitrogen gas adsorption increases with increase in milling time for Grade-B while it is almost constant for Grade-A as shown in Fig 2. It was observed that Grade-B powder has a greater tendency to absorb atmospheric gases than Grade-A powder. The reason behind this is the presence of cubic carbides like TiC and TaC in Grade-B, which are more susceptible towards reaction with atmospheric gases especially oxygen and nitrogen when compared to hexagonal WC.

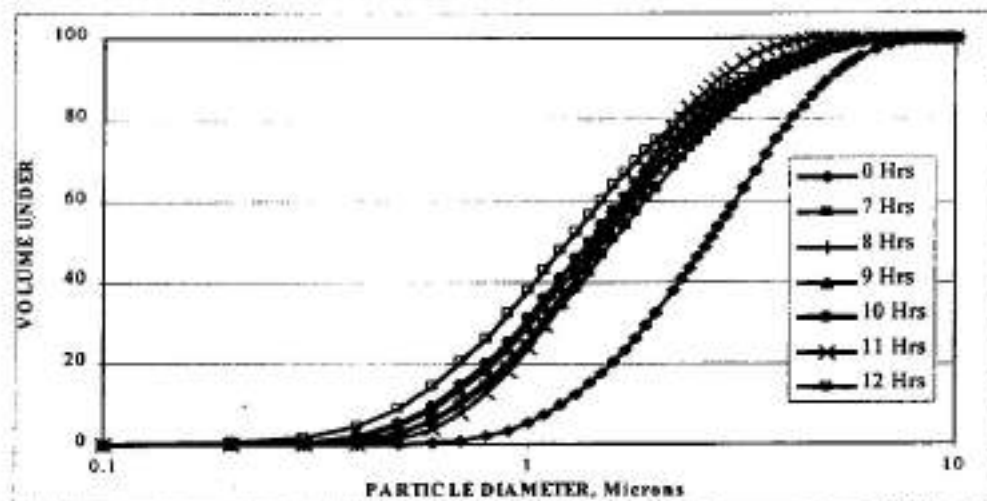


Fig 3 Particle size distribution at different Milling time for Grade-A

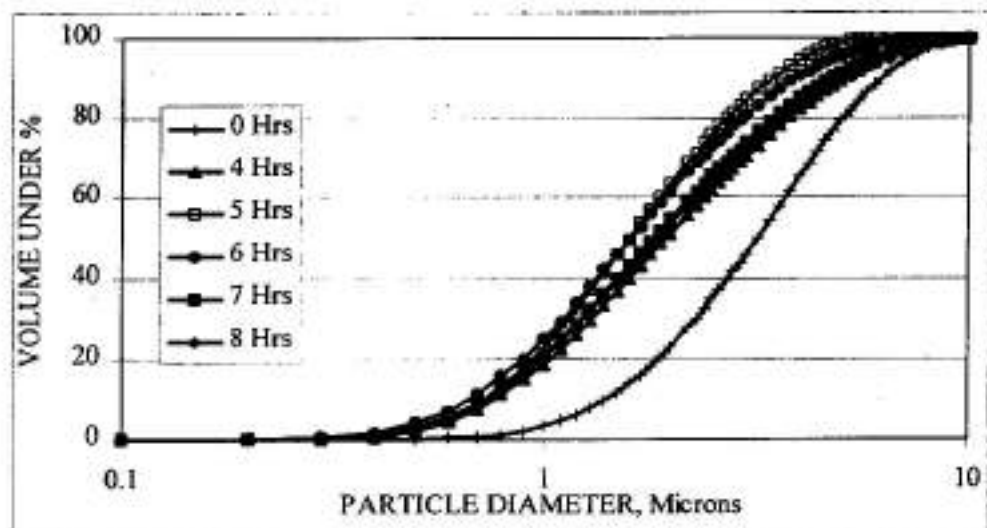


Fig 4 Particle size distribution at different Milling time for Grade-B



Figure 3 and 4 shows the particle size distribution of Grade-A and Grade-B dry powder at different milling time. For Grade-A powder it is clear that particle size reduction takes place with increasing milling time upto 10 hrs after which a bimodal distribution emerges as observed at 11 and 12 hrs of milling. This indicates that over-milling leads to agglomeration of fine particles. For Grade-B size reduction taking place upto 5 hrs and further milling resulted in coalescence of particles as fine particles get agglomerated.

#### Sintered Sample Characteristics

##### **(1) Binder ( $\beta$ ) Distribution**

The microstructural investigation of the dry test sample from both the powder batches of either grade shows that microporosity level of the sample is independent of the milling time beyond 7hrs for Grade-A and 4hrs for Grade-B. However generally there is a decrease in macroporosity levels with an increase in milling time, which also gets reflected in the slight increase in specific gravity of sintered components at higher milling time. On the other hand it was observed that milling time has a pronounced influence on the binder distribution of dry test samples.

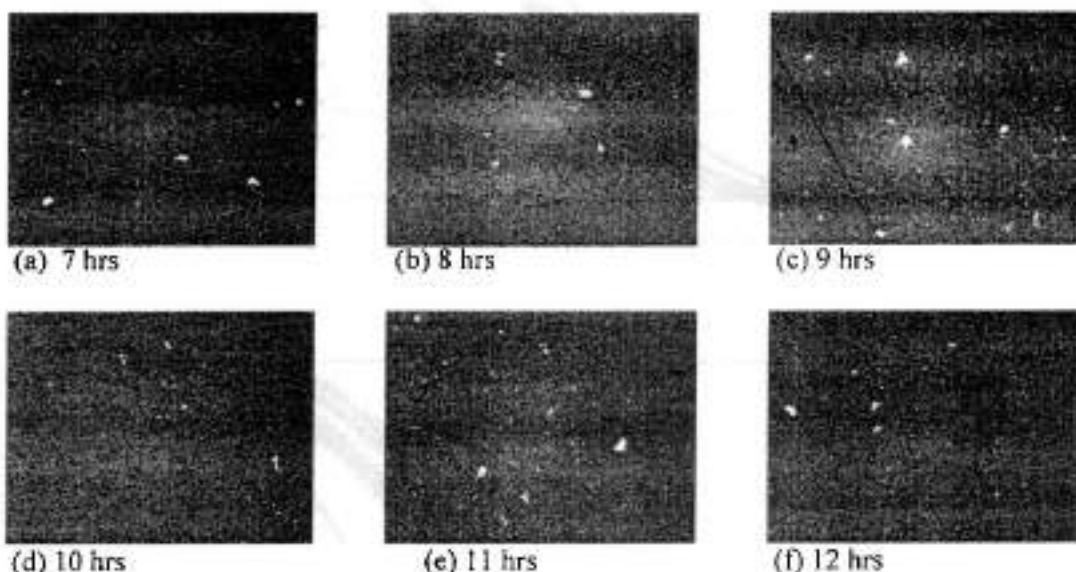


Fig 5 Binder distribution of Grade-A at different milling time (1000X).

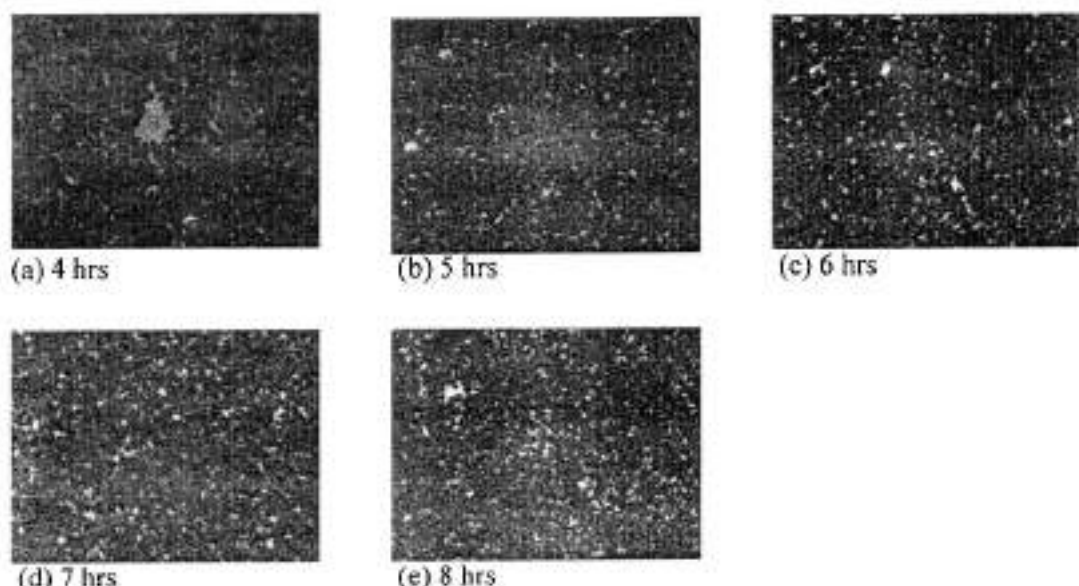
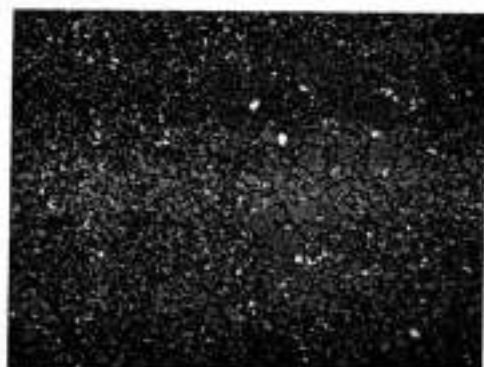


Fig 6 Binder distribution in Grade-B at different milling time (1000X).

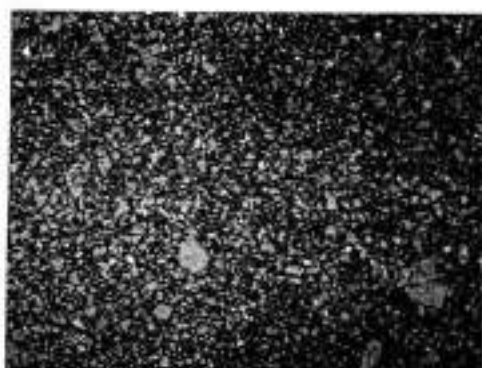
Initially when the powder is undermilled as shown in Fig 5 (a), (b), (c) for Grade-A and Fig 6 (a), (b), (c) for Grade-B the binder distribution is not uniform. As milling progresses binder distribution becomes uniform and the most uniform binder distribution was observed in 10 hrs sample for Grade A and 7 hrs sample for Grade B as illustrated in Fig 5(d) and Fig 6(d) respectively. This observation was same for both the powder batches, which were analysed for these grades. The binder distribution shows such a pattern because when the powder is undermilled the hard phase particles are not uniformly coated with binder as well the size of Cobalt particles is large. As the milling progresses the hard phase particles gets thoroughly coated with binder and the binder particles gets crushed due to the effect of milling. However overmilling of the powders results in deformation and flattening of soft binder particles, which manifests itself in the form of binder lakes in the sintered samples. As a result there is emergence of binder lakes if Grade-A powder is milled beyond 10 hrs as shown in Fig 5 (e), (f) and Grade-B powder is milled beyond 7 hrs as shown in Fig 6 (e).

**(2) Microstructure ( $\alpha$  distribution)**

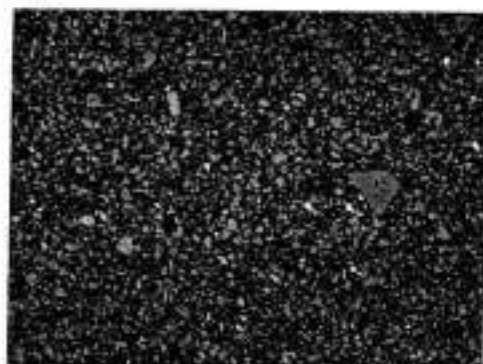
The average carbide grain size reduces with increasing milling time.



(a) 7 hrs



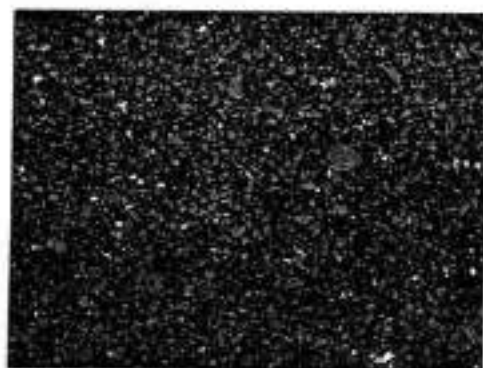
(b) 8 hrs



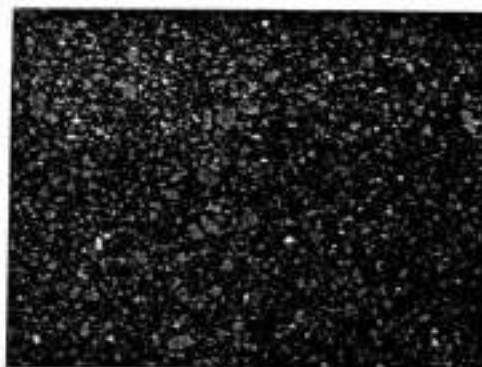
(c) 9 hrs



(d) 10 hrs

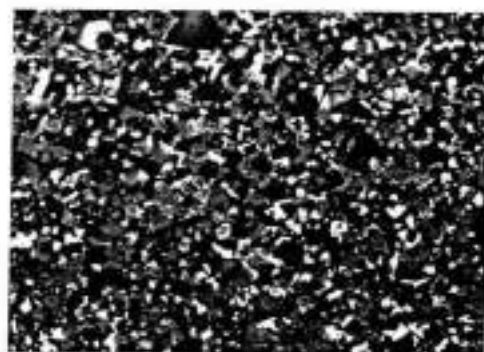


(e) 11 hrs

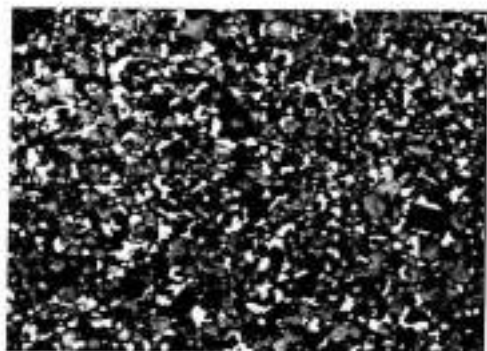


(f) 12 hrs

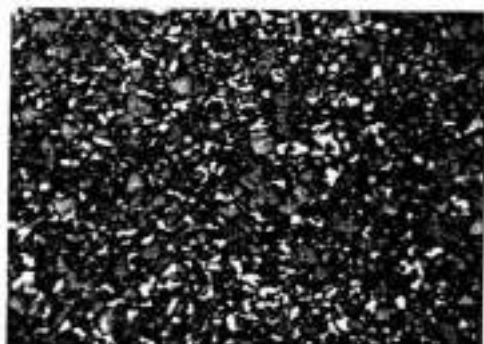
Fig 7 Microstructure of Grade-A samples at different milling time (1000X).



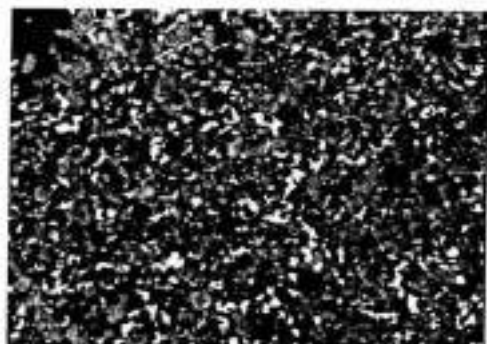
(a) 4 hrs



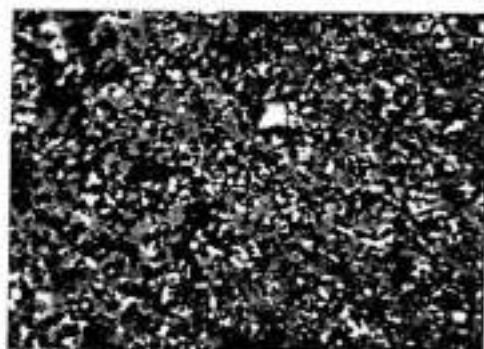
(b) 5 hrs



(c) 6 hrs



(d) 7 hrs



(e) 8 hrs

Fig 8 Microstructure of Grade-B samples at different milling time (1000X).

This can be seen in Fig 7 (a)-(f) and Fig 8 (a)-(e) which shows microstructure of sintered samples at different milling time for Grade-A and Grade-B respectively. During milling the powder particles experience impact and shearing forces. Impact takes place by the constant

impingement of the grinding media due to its irregular movement, which is caused by the movement of agitator arms. On the other hand random movement, rotation and spinning of the balls (media) exerts shearing forces on the adjacent slurry. The combined effect of shearing and impact forces is particle size reduction and good dispersion. It was observed that the distribution of  $\alpha$  phase keeps improving with increasing milling time. This indicates that undermilling results in nonuniform distribution of  $\alpha$  phase, while overmilling introduces additional energy into the powder by impact and shearing action of grinding media, which gets relieved during sintering. Hence grain growth and Ostwald ripening phenomena was conspicuous and a bimodal grain size distribution pattern also emerges as milling is carried out beyond 10 hrs in Grade-A and 7 hrs in Grade-B. This is shown in Fig 7 (e), (f) and Fig 8 (c) respectively.

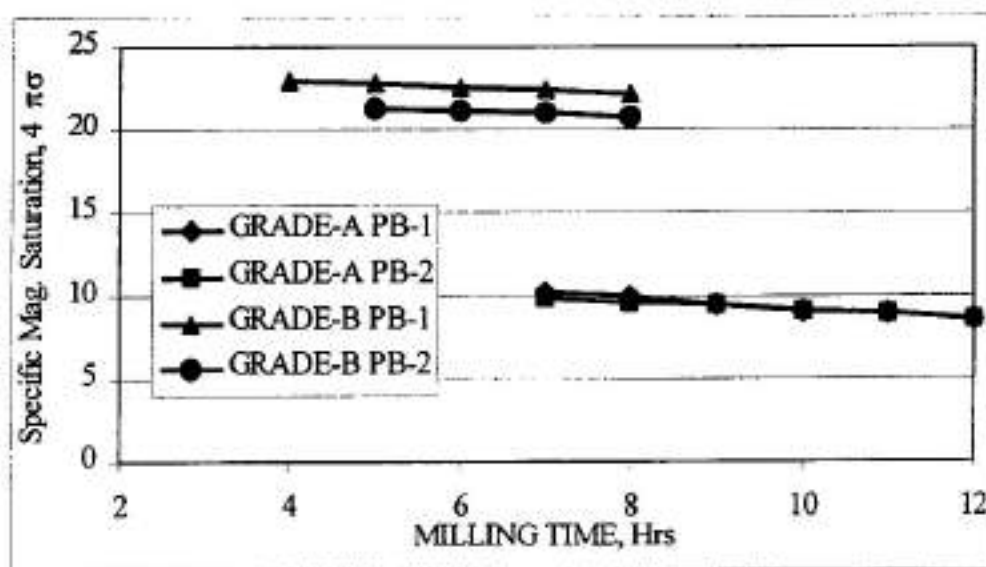


Fig 9 Variation in Specific Magnetic Saturation ( $4\pi\sigma$ ) with Milling Time

Specific magnetic saturation ( $4\pi\sigma$ ) and Coercivity ( $H_c$ ) are the sintered properties for hardmetals. Specific magnetic saturation, which is a measure of purity of the binder phase, decreases with an increase in milling time for both the grades as shown in Fig 9. The powders tend to adsorb oxygen during milling, which gets released in the form of  $CO_2$  and  $CO$  during sintering resulting in carbon loss from the compact. This enhances the dissolution of tungsten in binder thereby reducing the purity of ferromagnetic binder. As seen earlier there is an increase in oxygen adsorption with milling time which contributes towards more carbon loss and reduction in specific magnetic saturation.

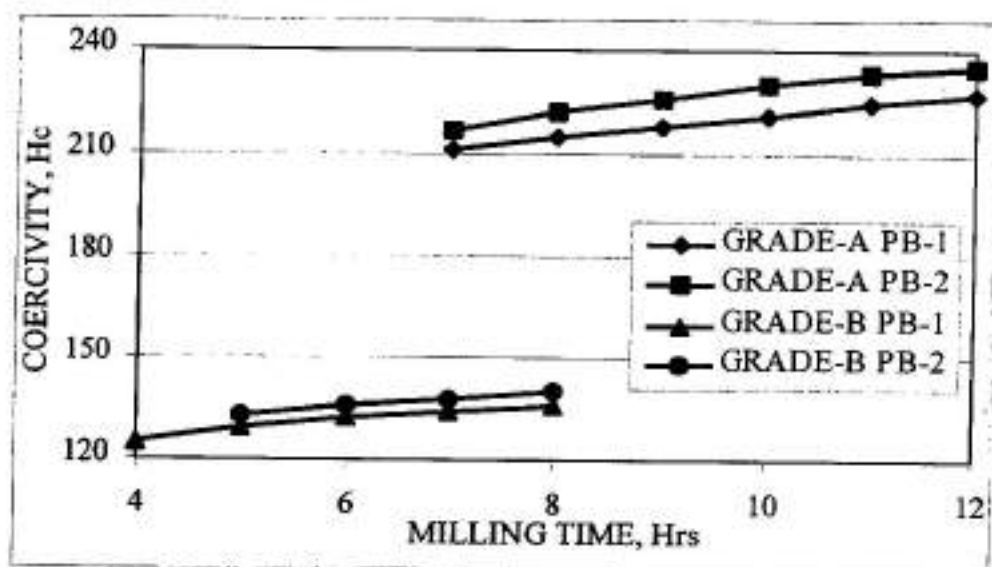


Fig 10 Variation in Coercivity ( $H_c$ ) with Milling Time

Coercivity is a measure of the average carbide grain size and hardness of the sintered components. Carbide grain size and its distribution depends on the particle size before sintering, binder content and sintering conditions. The Coercivity monotonically increases with milling time due to reduction in average carbide grains size and specific magnetic saturation for both grades A and B as shown in Fig 10.

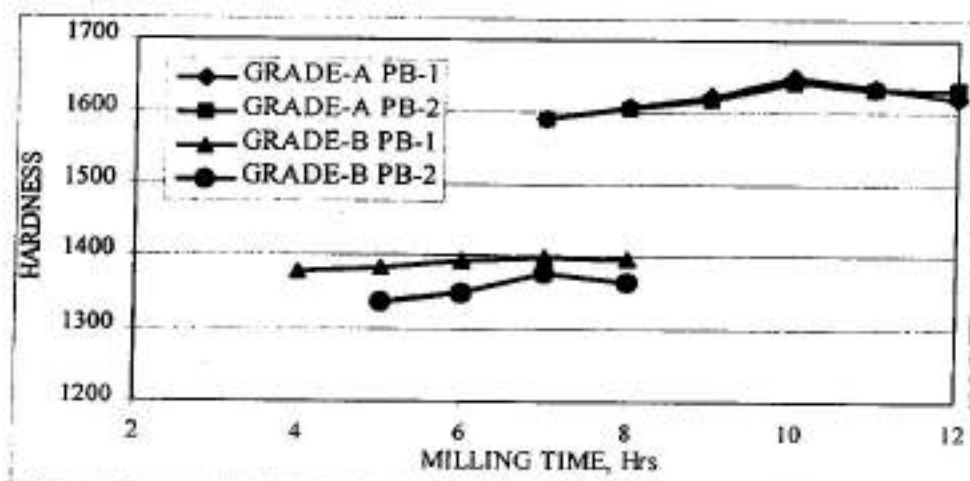


Fig 11 Variation in Hardness ( $H_v30$ ) with Milling Time



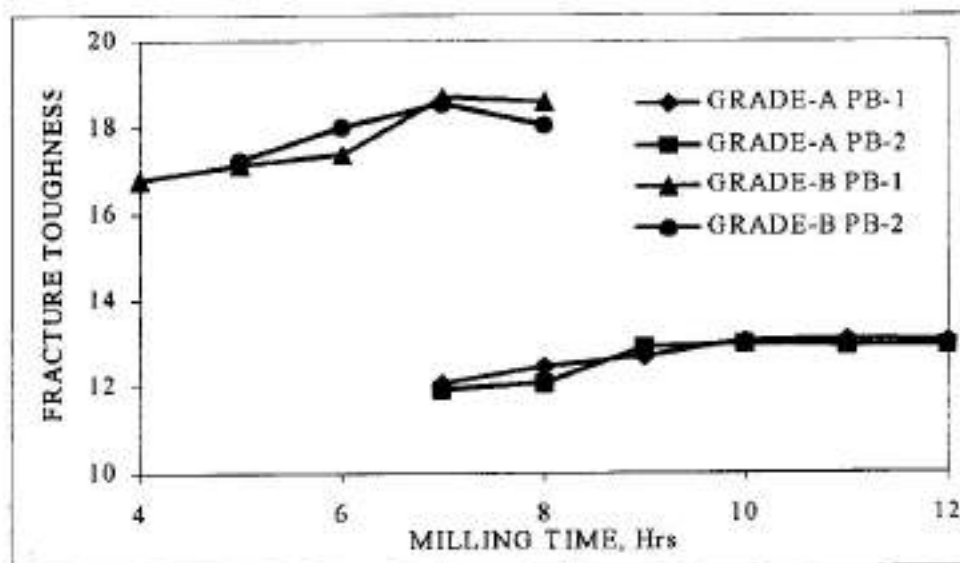


Fig 12 Variation in Fracture Toughness ( $K_{1C}$ ) in  $\text{MPa m}^{1/2}$  with Milling Time

From the dry test sample analysis it was observed that the mechanical properties like hardness and fracture toughness increase with an increase in milling time till 10 hrs of milling for Grade-A and 7hrs of milling for Grade-B as shown in Fig 11 and 12 respectively. After this stage as the milling progresses the hardness value shows a declining trend. This trend was observed in both the powder batches of either grade, which were collected for the present analysis. The drop in hardness value of sintered samples after certain hours of milling is primarily due to grain growth, oswald ripening of grains and emergence of bimodal grain size distribution. However the fracture toughness value stabilizes itself after a particular milling time for both the grades. On one hand there is a reduction in average grain size, which increases the area of grain boundaries. Hence there is an increased probability of formation of a intergranular crack over transgranular crack. The propagation of crack in intergranular fracture mode is relatively easy when compared to transgranular fracture mode. As fracture toughness is an indication of the resistance of material to crack propagation, the reduction in average grain size tends to reduce the fracture toughness. While on other hand increased dissolution of tungsten in binder due to loss of carbon at higher milling time improves the strength of the binder, which contributes towards an increase in fracture toughness value. The overall effect of these two contradictory factors stabilizes the fracture toughness value beyond certain milling time.

## CONCLUSIONS

1. Attritor milling time alters the chemistry of dry powders. The adsorbed atmospheric gases like oxygen and nitrogen content in graded hardmetal powder increases with an

- increase in milling time. The tendency of adsorption of these gases is more pronounced in alloyed grade hardmetal powder when compared to straight grade hardmetal powder.
2. The average particle size and particle size distribution pattern of dry powders changes with an increasing attritor milling time. Initially the particle size reduction results in narrowing of particle size distribution. Prolonged milling powders results in emergence of extra coarse and fine particles, which makes the particle size distribution broader.
  3. Mechanical properties of sintered components depend on the milling time. Hardness increases with increases in milling time till certain level after which it drops. The fracture toughness value stabilizes after certain milling time.
  4. Attritor milling beyond certain limit does not alter the microporosity significantly whereas marginal increase in specific gravity values of sintered components was observed.
  5. Attritor milling time has a major influence on microstructural features of sintered components like binder distribution, average grain size and distribution of hard phases.
  6. Attritor milling time influences the binder distribution of sintered components. If the powder is undermilled the binder distribution is not uniform whereas there is an emergence of binder lakes if the powder is overmilled. An optimum binder distribution is attained at a particular milling time.
  7. Attritor milling induces lot of energy to the powder mixture. The amount of energy input is a function of milling time. Excessive energy input results in phenomenon like ostwald ripening and grain growth during sintering.
  8. Milling time of graded hardmetal powder can be optimized by optimizing grain size distribution, sintered properties and microstructural features for a particular milling time.
  9. The best set of physical and mechanical properties as well as good microstructural features can be obtained at 10 hrs for straight grade with 6% cobalt and 7 hrs for alloyed grade with 11.5% cobalt.

## SCOPE FOR FUTURE WORK

- (1) Further studies can be carried out to know the effect of milling time on
  - (a) Tap and Green density
  - (b) Compaction behaviour
  - (c) Shrinkage and weight loss after sintering
  - (d) Sintered properties like Transverse Rupture Strength, Compressive strength
  - (e) Tool life evaluation
- (2) Study on the effect of attritor mill design parameters on powder characteristics and sintered properties can be done.
- (3) Similar studies can be performed to study the effect of ball milling time on the properties of graded hardmetal powder and sintered components. A comparison can be drawn between ball milling and attritor milling on the properties of milled powder and sintered samples.

**References:**

1. R. Vasudevan, K. Sadananda, "Influence of Attritor milling on the sintered properties of hardmetals", PMAI Newsletter, Vol. 11, No.1, pp 11-14 (1985).
2. "Processing of Tugsten Carbide Powder with the Q (Circulation) Attritor", MPR, (December 1986)
3. S. J. Mashl, D. W. Smith, G. H. Becking and T. E. Hale, "Attritor milling of WC+6% Co: Effect on Powder Characteristics and Compaction Behaviour", RM & HM, , pp 32-40 (March 1989).
4. Hans kolaska, Powder Metallurgy of Hardmetals, Published as lecture series by Association of Powder Metallurgical Industries.
5. Kenneth J. Brookes, World Directory and Handbook of Hardmetals, Fourth edition, International Carbide Data.
6. Y. Torres, D. Casellas, M.Anglada, L.Llanes, "Fracture toughness evaluation of hardmetals: influence of testing procedure", International journal of Refractory metals and Hard materials,19, pp 27-34, (2001).
7. Ponton C.B, Rawlings R.D, "Vickers indentation fracture toughness, part 1: test review of literature and formulation of standardized indentation toughness equations, master Sci Technol, pp 865-872, (1989).

## SINTERING OF COATED W-Cu ALLOYS

Chiradeep Ghosh\* and Anish Upadhyaya\*\*

\* Post-Graduate Student

\*\* Assistant Professor

Materials & Metallurgical Engineering  
Indian Institute of Technology, Kanpur 208016, INDIA

### Abstract

This study investigates the effect of Ni and Co addition on the sintering of W-Cu alloys sintered at temperatures ranging from 900 to 1400°C. Tungsten-copper alloys containing 10, 25, and 40% copper were prepared by mixing and by coating route. Owing to lack of solubility of tungsten in copper, it is very difficult to achieve full density during sintering in W-Cu alloys having starting W powder size greater than 4  $\mu\text{m}$ . The role of transition metal elements Ni and Co in activating the densification during sintering has been critically examined *vis à vis* the solubility effects.

### Introduction

In recent years, considerable attention is being directed to the thermal management materials for microelectronic applications [1-3]. The requirement for such high performance materials is necessitated due to the miniaturization of the semiconductor devices, which imposes restriction on convective cooling media. The high heat generated in the limited cross-section area requires the heat dissipation in a predominantly conductive mode through the surrounding thermal management device. Thus, for better heat dissipation, materials that offer a combination of high thermal conductivity ( $>200 \text{ W/mK}$ ) and low thermal expansion coefficient ( $<7 \text{ ppm/K}$ ) matching that of the Si-chip are required. It is very difficult to achieve this combination through monolithic materials and therefore composite/alloy design is desired. Tungsten-copper alloys are one such candidate materials for these applications wherein the high thermal conductivity of Cu dissipates heat and the low thermal expansion coefficient of W-skeletal structure provides the hermetic sealing between the microelectronic circuitry and the heat sink[2].

Because of the refractory nature of tungsten (m.p. 3420°C), W-Cu alloys are fabricated by powder metallurgical processing, typically through liquid phase sintering. The relatively lower fusion temperature of copper (1083°C) coupled with its good wetting behaviour with W makes W-Cu alloys amenable to liquid phase sintering. Conventionally, rearrangement and solution-precipitation processes are predominant mechanisms that lead to densification during liquid phase sintering. However, as there is no intersolubility between tungsten and Cu in both solid and liquid-state, hence, solution-precipitation is non-existent in W-Cu alloys. This puts constraint on achieving full density in W-Cu system. To circumvent this problem, W-Cu alloys are either milled or very small W particle size is used to enhance the solid-state densification, and thereby achieving full density.

For optimum properties, W-Cu must contain about 20 to 60 (vol.%) of copper [4]. A high volume fraction of Cu in turn restricts rearrangement, which further limits densification. This study aims at investigating the processing of W-Cu alloys containing varying Cu contents. To enhance densification, Cu was coated on to tungsten. The sintering of these coated alloys were compared to that of W-Cu alloy prepared by mixing route. In addition, the sintering response both uncoated and coated W-Cu alloys was also investigated in presence of Ni and Co additions.

### Experimental Procedure

In the present study W-Cu alloys containing 10%, 25% and 40% (wt.%) were investigated. In one set of experiment, the compositions were prepared by mixing the constituent powders in requisite proportion for 30 min in Turbula mixer. In the second set, the same composition powders were prepared by chemically coating copper in the same

proportion on to the tungsten powders so as to yield the same composition. The powders were compacted at 200 MPa using a 20-ton uniaxial hydraulic press (Apex Construction Ltd., UK). Both the coated and the coated compositions resulted in similar green density. In a separate set of experiment, Ni and Co were added to both the coated and the uncoated powders. The activator amount was restricted to 1 wt.%. The green compacts were sintered at 1000°C, corresponding to solid-state sintering and at 1200°C and 1400°C, respectively corresponding to liquid phase sintering. Sintering was done in hydrogen. The heating rate was 5°C/min and the samples were held at the sintering temperatures for 60 min. The sintered samples were subsequently quantified for density.

## Result

### *Densification without Activator Addition*

Figures 1a to 1c show the variation in sintered density with varying Cu content in W-Cu alloys sintered at 1000°C, 1200°C and 1400°C, respectively. From the figures it is obvious that an increase in the copper content and an increasing sintering temperature enhances the sintered density of W-Cu alloys. In addition, for both solid-state (1000°C) as well as liquid phase sintering conditions (1200 and 1400°C), coated powders give marginally higher densification during sintering.

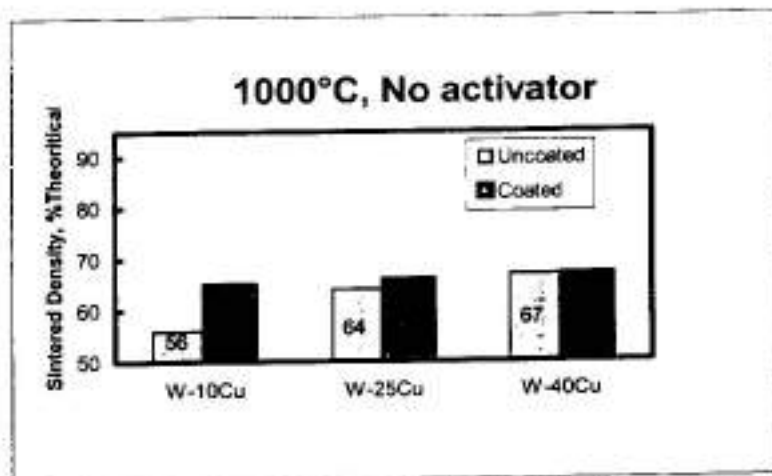


Figure 1a. Effect of Cu content on the sintered density in W-Cu alloys at 1000°C.

### *Densification with Ni and Co Addition*

Table 1 summarizes the effect of Co addition on the sintered density of W-Cu alloys at 1000, 1200, and 1400°C. From the table, one can infer that Co enhanced the densification in W-Cu alloys. The density enhancement is more in coated samples and increases with increasing Cu content and increasing temperature. It is also remarkable to note that in solid-state sintering, cobalt has limited role in densification enhancement. However, in liquid phase sintering, cobalt acts as a potent activator.

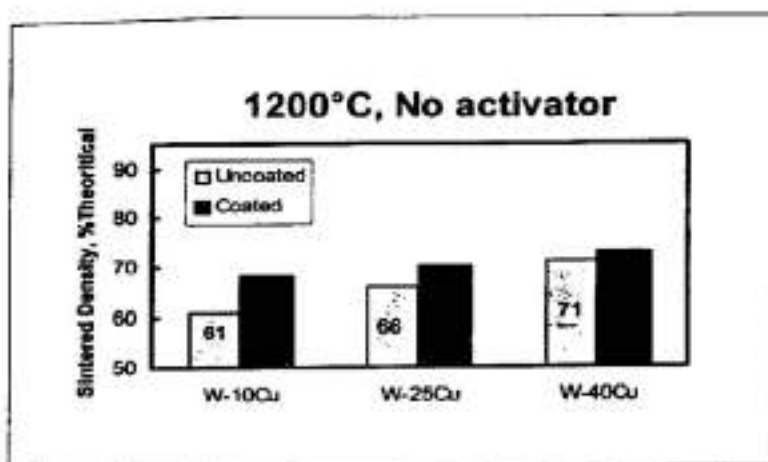


Figure 1b. Effect of Cu content on the sintered density in W-Cu alloys at 1200°C.

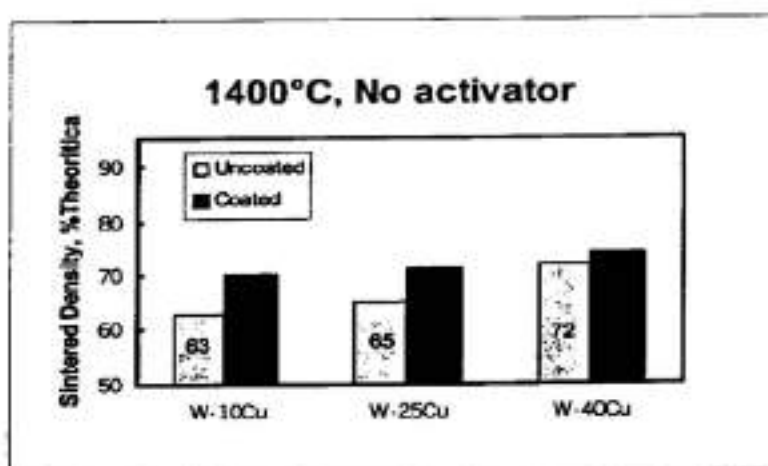


Figure 1c. Effect of Cu content on the sintered density in W-Cu alloys at 1400°C.

Table 1. Effect of sintering temperature on the sintered density of coated and uncoated W-Cu alloys with Co activator.

Composition	state*	sintering temperature, °C		
		1000°C	1200°C	1400°C
W-10Cu	UC	64.7	70.9	82.8
	C	66.9	76.5	85.3
W-25Cu	UC	65.2	74.3	86.7
	C	66.9	80.1	89.7
W-40Cu	UC	65.3	75.4	88.3
	C	67.4	82.9	92.6

UC: uncoated; C: Cu-coated W

Figures 2a to 2c summarize the effect of Ni addition on the sintered density of W-Cu alloys at 1000, 1200, and 1400°C, respectively. As in the previous case, Ni too enhances the sintered density in W-Cu alloys irrespective of the Cu content. Also, Ni-added coated W-Cu alloys undergo higher densification during sintering as compared to the uncoated samples.

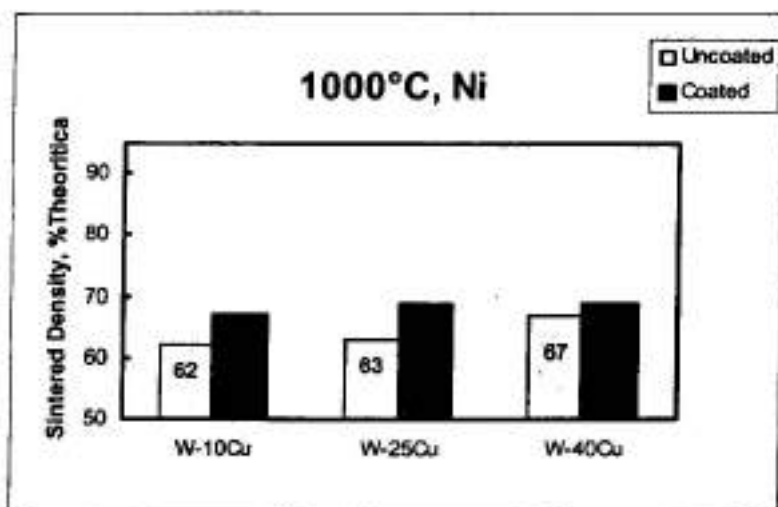


Figure 2a. Effect of Ni addition on the sintered density of coated and uncoated W-Cu alloys at 1000°C.

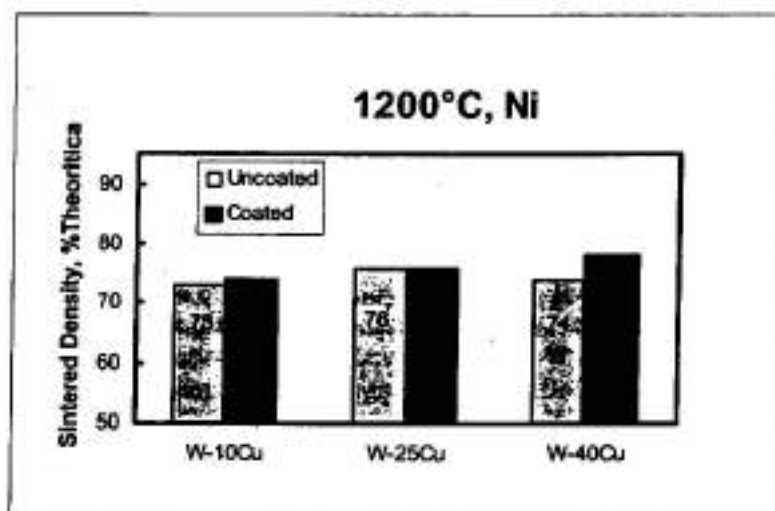
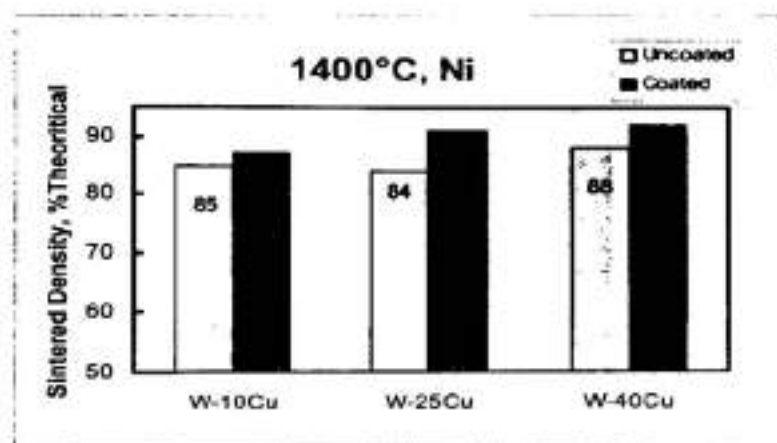


Figure 2b. Effect of Ni addition on the sintered density of coated and uncoated W-Cu alloys at 1200°C.





**Figure 2c.** Effect of Ni addition on the sintered density of coated and uncoated W-Cu alloys at 1400°C.

### Discussion

The average tungsten powder size used for the present investigation varied between 5-10  $\mu\text{m}$ . For such sizes, the W-Cu compacts normally do not undergo much densification in either coated or uncoated forms, even when sintered up to 1400°C. In fact, there is not much difference in the sintered density of W-Cu compacts when sintered at solid-state (1000°C) and liquid phase (1200 and 1400°C) conditions. This underscores that densification in W-Cu alloys is predominantly through skeletal sintering of W-W grains. This is in line with the reported observations in the literature [5,6]. The negligible solubility of tungsten in copper obviates solution-precipitation as densification mechanism. Hence, densification occurs predominantly by solid-state sintering and capillary-induced rearrangement of tungsten grains during liquid phase sintering [7]. The rearrangement will be more in case of coated alloys because of homogeneous melt formation. Hence, coated W-Cu samples always yield higher sintered density as compared to their uncoated counterparts [8]. Furthermore, irrespective of the copper content, the coated W-Cu alloys yield higher density even with Ni and Co activator additions.

As shown in Fig 3, in case of W-10Cu alloys sintered at 1000°C, the coated samples give higher sintered density as compared to uncoated ones. However, Ni and Co addition do not have any appreciable contribution towards densification in W-10 alloys at 1000°C. In contrast, the uncoated W-10Cu samples show significant densification enhancement by Ni and Co addition. This can be inferred by the interaction mechanism of Ni and Co with the W-Cu system. Cobalt has no solubility in Cu. Cobalt enhances the density of tungsten compacts by segregating at the W-W interface and by forming an intermetallic phase which provides a short-circuit diffusion path. However, in case of coated samples, cobalt does not come in contact with tungsten and has therefore no effect on densification. Nickel on the other hand has complete solid solubility with copper. Because of this, in case of W-Cu compacts, Ni goes into solid solution with Cu before it can segregate to the W-W interface. In case of uncoated samples, there is likelihood that there are some W-Co and W-Ni contact surfaces to start with which can contribute to some densification enhancement. Of course, as the sintering progresses, Ni dissolves into Cu, whereas Co does remain segregated. This explains the higher sintered density with Co addition in uncoated W-10Cu as compared to Ni addition.

Once the Cu content increases, the probability of W-Ni or W-Co contacts reduces. Consequently, at 1000°C, there is no significant effect on either activators in both coated as well as uncoated compacts as shown clearly in Fig 4.

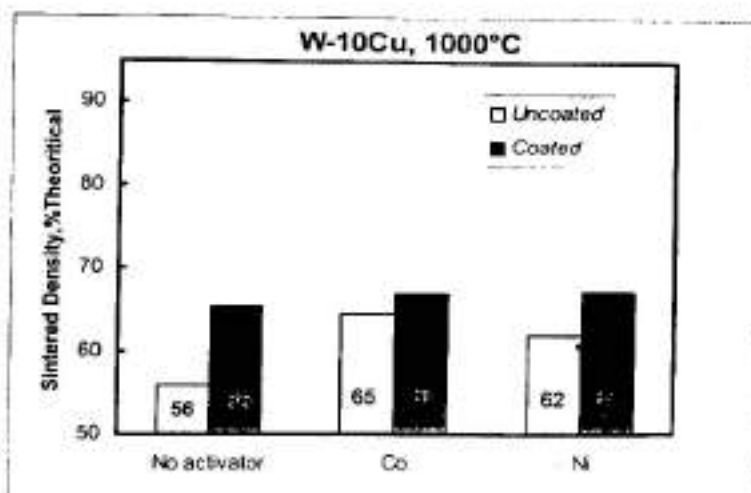


**Figure 3.** Effect of Ni and Co activator on the sintered density of coated and uncoated W-10Cu alloys solid-state sintered at 1000°C.

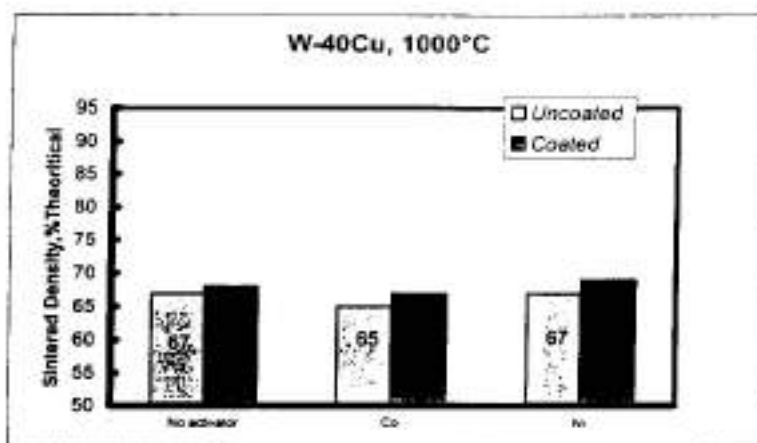


**Figure 4.** Effect of Ni and Co activator on the sintered density of coated and uncoated W-40Cu alloys solid-state sintered at 1000°C.

As shown in Fig 5a, when the W-10 compacts are liquid phase sintered at 1200°C, Ni and Co significantly enhance densification in both uncoated as well as coated compacts. The same composition of W and Cu when sintered at 1200°C with Ni and Co activators enhanced the sintered density for both coated as well as uncoated samples. For coated W-Cu, Co is a better activator and for uncoated Ni addition leads to better densification enhancement at 1200°C. At 1400°C, the potency of both the activators becomes even more with Ni being a better activator in both coated as well as uncoated conditions (Fig 5b). During liquid phase sintering, Cu having a high dihedral angle with respect to W (~ 80-95°), has to attain an equilibrium condition. The Cu-coated tungsten powders correspond to a zero dihedral angle configuration and as soon as the melt formation occurs, Cu will retract from the tungsten and

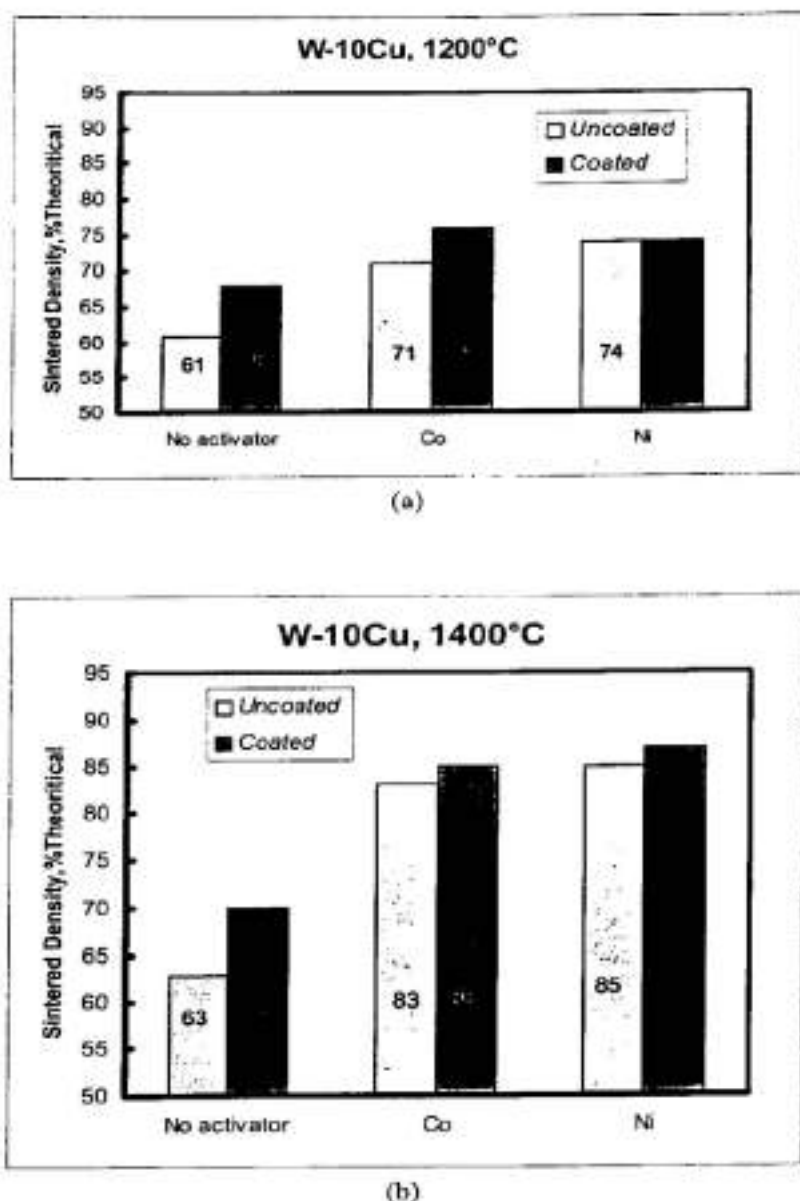


**Figure 5.** Effect of Ni and Co activator on the sintered density of coated and uncoated W-10Cu alloys liquid phase sintered at (a) 1200°C and (b) 1400°C.

will reduce the surface coverage, thereby promoting more W-W contact formation. This condition results in similar response of both the coated and the uncoated compacts towards activator addition.

### Conclusion

This study shows that densification in W-Cu alloys increases with increasing copper content and with powder modification by coating copper on to tungsten. The W-Cu system sinters predominantly by solid-state sintering and there is not much density enhancement

(over the alloys solid-state sintered at 1000°C) even when these alloys are liquid phase sintered at 1200 and 1400°C. For all cases, the coated W-Cu alloys yield higher sintered density than the uncoated ones. Significant densification enhancement occurs with the addition of Ni and Co activators. The choice of activator depends on the Cu content, state of the powder (coated vs. uncoated) and the sintering temperature.

## References

1. R.M. German, K.F. Hens, and J.L. Johnson, "Powder Metallurgy Processing of Thermal Management Materials for Microelectronic Applications," *International Journal of Powder Metallurgy*, 1994, v. 30, n. 2, pp. 205-214.
2. T.W.Kirk, S.G. Caldwell, and J.J. Oakes, "Mo-Cu Composites for Electronic Packaging Applications," *Advances in Powder Metallurgy and Particulate Materials*, Metal Powder Industries Federation, Princeton, NJ, USA, 1992, v. 9, pp. 115-122.
3. R.M. German, *Powder Injection Molding*, Metal Powder Industries Federation, Princeton, NJ, USA, 1990.
4. J.L. Johnson, "Densification, Microstructural Evolution and Thermal Properties of Liquid Phase Sintered Composites," *Ph.D. Thesis*, The Pennsylvania State University, University Park, PA, USA, 1994.
5. I.H. Moon, and J.S. Lee, "Activated Sintering of W-Cu Contact Materials," *Powder Metallurgy*, 1979, v. 22, n. 1, pp. 5-7.
6. J.L. Johnson, and R.M. German, "The Solubility Criterion for Liquid Phase Sintering," *Advances in Powder Metallurgy and Particulate Materials*, Metal Powder Industries Federation, Princeton, NJ, USA, 1994, v. 3, pp. 267-280.
7. A. Upadhyaya, and R.M. German, "Densification and Dilation of Sintered W-Cu Alloys," *International Journal of Powder Metallurgy*, 1998, v. 34, n. 2, pp. 43-55.
8. B. Özkal, A. Upadhyaya, M.L. Ovecoglu, and R.M. German, "Comparative Effects of Coated Powders on the Sintering Behavior of W-Cu Alloys," *Proceedings 2<sup>nd</sup> Turkish National Powder Metallurgy Conference*, S. Saritas (ed.), Türk Toz Metalurjisi Derneği, Ankara, Turkey, 2000, pp. 185-191.

## EFFECT OF TRASITION METAL ADDITIVES ON ACTIVATED SINTERING OF TUNGSTEN-BRONZE

M. Debata\* and A. Upadhyaya\*\*

\*Post Graduate Student

\*\* Assistant Professor

Department of Materials & Metallurgical Engg.  
Indian Institute of Technology, Kanpur

### Abstract

This study investigates the sintering behavior of tungsten-bronze with the addition of different activators. In classic liquid phase sintering densification occurs only due to rearrangement and solution re-precipitation. Systems such as W-Cu, which have negligible solubility of W in Cu, are therefore difficult to densify and are often sintered to full density using small amounts of transition metal activators. Thus, in activated liquid phase sintering, densification enhancement occurs due to rapid diffusion through the segregated activator layer at the grain boundaries. In this study, W-bronze alloys were prepared and sintered at temperatures ranging from 900 to 1400°C. The bronze matrix composition selected was Cu-12Sn, which was prepared by premix as well as prealloyed route. For enhancing liquid phase sintering, both Co and Ni were used as activators.

### Introduction

Tungsten owing to its very high melting point (3420°C) requires a high sintering temperature can be compacted to full density at a sintering temperature of 1400°C by transition metal additions such as Pd and Ni of less than 1 % as opposed to a sintering temperature of 2800°C to get a comparably density part without addition of any additive. Most of the investigations have been carried out by various authors on activated sintering of tungsten. Hayden and Brophy [1] found that the amount of additive required to promote low temperature sintering is equivalent to one monolayer on the powder surface and there is an optimum level content which has beneficial effect on the activation process. This level corresponds to four monolayer. The vastly differing mutual solubility between Ni and W was cited as the reason for directional mass flow of tungsten into nickel. German and Munir [2] studied the temperature sensitivity in activated sintering of tungsten with a number of activators keeping the activator concentration on W surface fixed in each case, which was four monolayers thick. Some of the models have been advanced by many authors in explaining the activated sintering. Solution re-precipitation model by Brophy *et al.* [3] led to the conclusion that the solid Ni layer on tungsten is acting only as a mass transfer medium for it. Panichkina *et al.* [4] suggested a plastic flow mechanism for mass transport. Samsonov and Yakovlev [5-8] introduced the concept of activated sintering in terms of different d-electron structures of activators. Most of the investigators have suggested a diffusional model of mass transport for activated sintering. Ylassary and Tikkanen [9] by their study on the distribution of Ni in the sintered tungsten by electron micro probe

equipment reported that nearly all of the nickel was situated along the grain boundaries. Tooth and Lockington [10] and Gessinger and Fischmeister [11] also demonstrated the same result. The above mentioned conclusions on solid state activated sintering of tungsten being arrived by various authors give the fact that the presence of activator as a grain boundary layer provides a short circuit mass transport path through which the diffusion of tungsten becomes easier and this leads to higher shrinkage rate and enhanced densification. Enhanced densification may also occur in liquid phase sintering. One of the classic examples of activated liquid phase sintering is the W-Cu system. The achievement of higher densification for W-Cu alloys in spite of negligible solubility between W and Cu by addition of transition elements such as Co, Ni, Fe and Pd. Co and Fe in comparison to Ni appears to be much better activator in liquid phase sintering of W-Cu. Johnson and German [12] have reported that the effectiveness of activators for sintering enhancement follows the sequence  $\text{Pd} \rightarrow \text{Ni} \rightarrow \text{Fe} \rightarrow \text{Co}$  with Ni being much less effective than Co or Fe, and Pd showing a very little effect. This sequence of increasing activator effectiveness does not follow the same trend for solid state activated sintering of W ( $\text{Fe} \rightarrow \text{Co} \rightarrow \text{Ni} \rightarrow \text{Pd}$ ). The substantial contribution of enhanced densification and higher shrinkage rate for activated liquid phase sintering is due to rapid diffusion through the segregated layer at the grain boundaries. Many of the applications of activated sintered W based alloys include high temperature stability combined with good mechanical properties, thermal management application that exploit their low coefficient of thermal expansion. Processing by activated sintering is beneficial because of high density possible and least machining operation needed due to near net shape of the sintered product [13].

The present work focuses on processing of novel W-Bronze alloys and study of end properties.

### Experimental Procedure

The experimental variables are given in Table 1. After completion of powder characterization, tungsten-bronze alloys of different compositions were mixed by the help of turbular mixer for 30 mins. Cylindrical green compacts of 12.7 mm diameter and approximately 3mm to 6 mm height were made by a single acting hydraulic press with an applied pressure of 200 MPa. The theoretical densities for different compositions were calculated using the inverse rule of mixing.

Sintering was carried out in two different furnaces, SiC-heated horizontal tubular furnace which can go up to temperature of 1350°C and MoSi<sub>2</sub>-heated one for use at the temperature more than 1300°C. The furnace tube was made up of doubly recrystallized alumina. Commercially pure hydrogen was taken as the sintering atmosphere. Different temperatures such as 950, 1100, 1200, 1300 and 1400°C were selected for the tungsten alloys containing no activator. For the tungsten alloys containing activator, the sintering was performed only at 1200 and 1400°C. The holding time at the sintering temperature for all the cases was 60 min. Due care was taken while programming for the heating rates during the sintering. The sintering cycle at 1400°C is shown in Fig 1. Densities of green and sintered compacts were calculated from the mass and the physical dimension measurements of the sample. Densification parameter ( $\psi$ ), which is a measure of the amount of densification taken place after sintering, was calculated using the following expression;



$$\psi = (SD - GD) / (TD - GD)$$

SD = Sintered Density

GD = Green Density

TD = Theoretical Density

TABLE 1: Experimental Variables

Alloys	W-10 wt. % Bronze W-20 wt. % Bronze
Matrix Composition (Bronze)	Cu-12 wt. % Sn
Matrix Powder Preparation Route	Premix Prealloy
Activator	Ni and Co
Activator Amount	1 wt. %

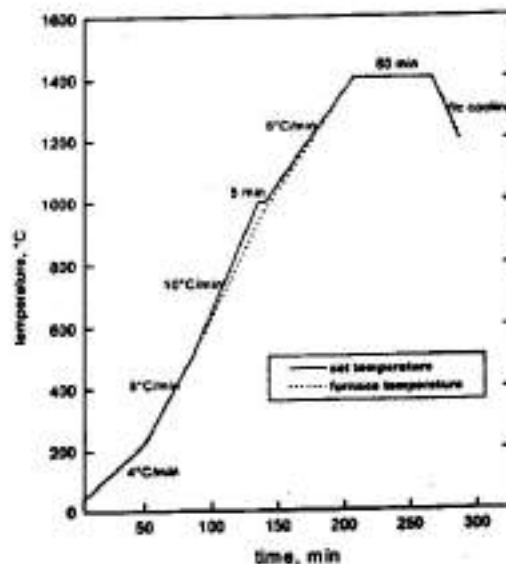




Fig 1: Sintering cycle at 1400°C

The microstructures of the samples were obtained using JEOL, JSM-840A scanning electron microscope.

## Results

### *Variation in sintered density with temperature*

Figure 2 summarizes the results obtained from the sintering of tungsten alloys without any activator at different temperatures. W-20(Cu-Sn) samples show higher sintered density (% theoretical) as compared to W-10(Cu-Sn). Except premix W-10(Cu-Sn) sample rest three samples resulted in maximum densification at 1400°C.

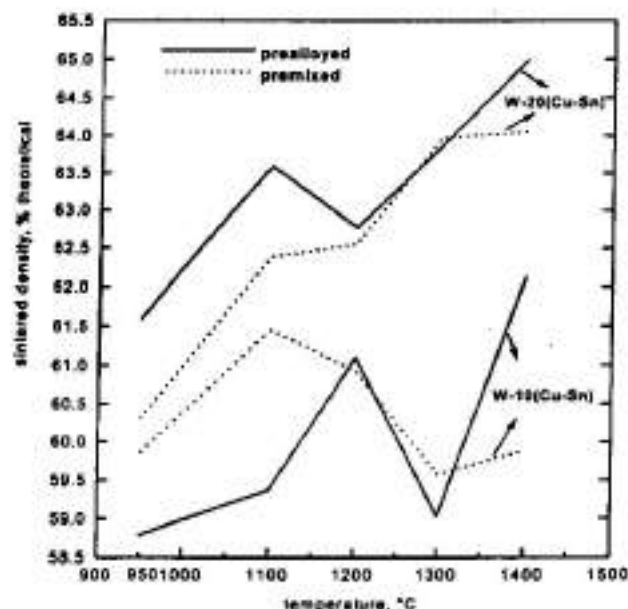


Fig 2: Variation in sintered density with temperature for tungsten-bronze alloys of different composition

### *Variation in sintered density and densification parameter with activator*

Figure 3 and Fig 4 show the effect of activators Ni, and Co on sintered density and densification parameter for the tungsten alloys at 1200°C. Figure 5 and Fig 6 show this effect at 1400°C. At both temperatures, the alloys behave similarly. There occurred maximum densification for samples containing Co, followed by Ni. The samples with no

activator give less densification values. In most of the cases premixed and prealloyed W-20 (Cu-Sn) samples show higher densification than the W-10(Cu-Sn). All the samples with activators Ni and Co at 1400°C give high values for sintered density and densification parameter.

### Scanning Electron Microscopy

Figure 7 and Fig 8 compare the characteristic features between the green as well as sintered premixed W-20(Cu-Sn) sample, sintered at 1400°C. In Fig 7, small pores in the microstructure of green sample at  $\times 1000$  are visible, while the sintered sample shows only the big pores. In Fig 8, the first two micrographs were taken in SE mode and the remaining two in back-scattered mode.

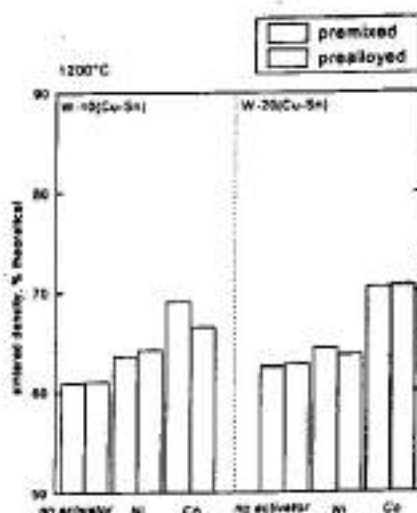


Fig 3: Variation in sintered density with activator Ni and Co at 1200°C

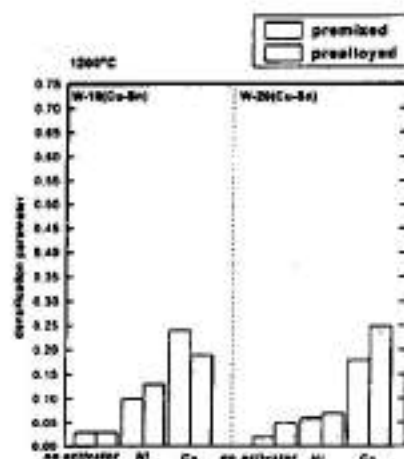


Fig 4: Change in densification parameter with activators Ni and Co at 1200°C

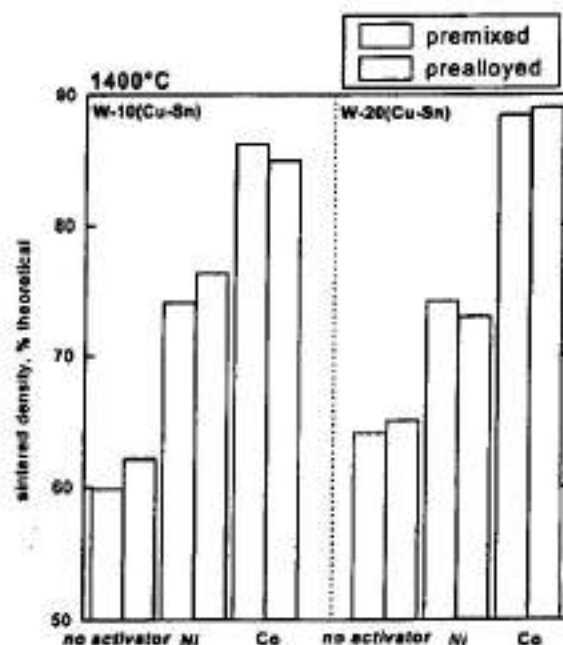


Fig 5: Variation in sintered density with activator Ni and Co at 1400°C

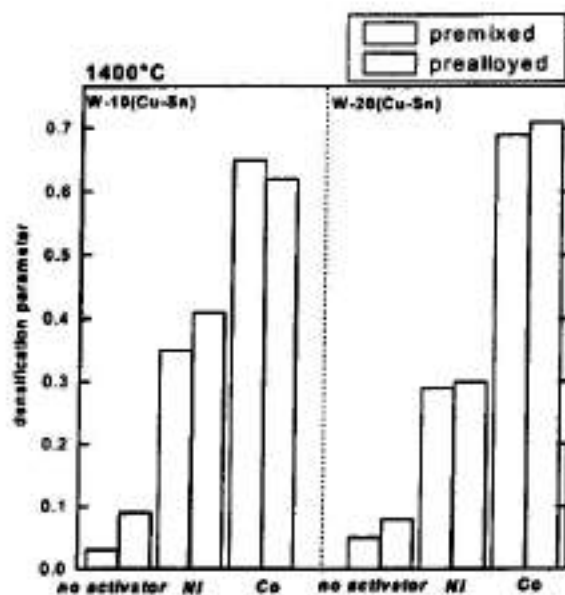


Fig 6: Change in densification parameter with activators Ni and Co at 1400°C

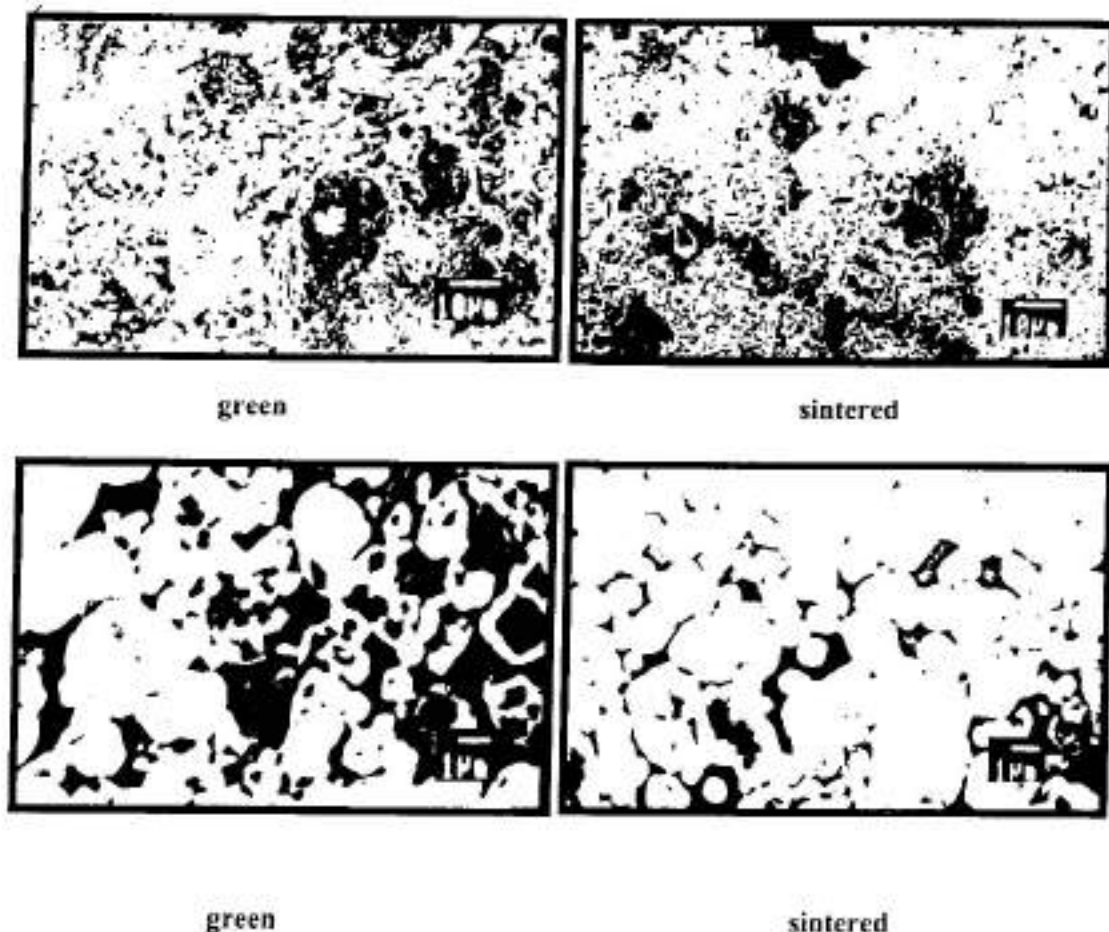


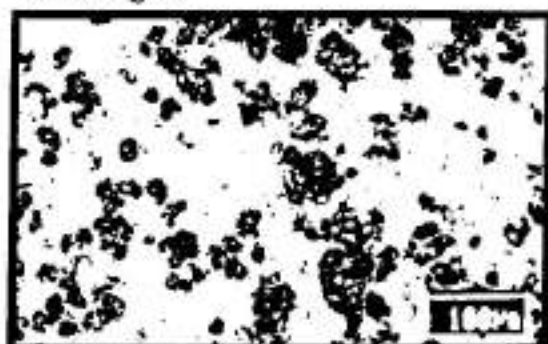
Fig 7: Scanning micrographs of green and sintered premixed W-20(Cu-Sn) samples at low and high magnifications. The samples were sintered at 1400°C for 1h. The SEM images were captured in secondary-electron (SE) imaging mode. The green compact was 62% dense whereas the sintered compact had about 64% of the theoretical density.

*SE Images*

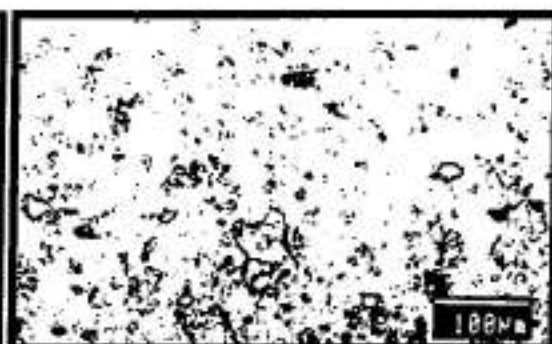
green



sintered

*BSE Images*

green



sintered

Fig 8: Scanning micrographs of green and sintered (1400°C) premixed W-20(Cu-Sn) samples. The SEM images were captured in secondary-electron (SE) and back-scattered electron (BSE) imaging mode.

## Discussion

At 950°C, prealloyed W-Bronze alloys will undergo supersolidus liquid phase with solid + liquid mixture of bronze. This will behave as a slurry with high viscosity, and hence very little densification of compact will occur at this temperature. In the premixed bronze, by the time the temperature reaches 950°C, the tin diffuses into Cu. Thus, at 950°C, the premixed bronze matrix behaves similar to the prealloyed one. At and above 1000°C, the temperature is above the liquidus temperature for the Cu-12Sn composition. Thus, W-bronze system sintered at 1000°C and above undergo classic liquid phase sintering and thereby result in higher densification as compared to alloys sintered at 950°C.

With addition of activators Ni or Co, it is seen that the densification increases, as quite evident from Figs 3,4,5 and 6. Considering first the effect of Ni as an activator for the W-bronze alloys, Ni dissolves completely in liquid Cu and is no longer segregated to grain boundaries and densification proceeds through solution re-precipitation. It is because of this that the efficacy of Ni as an activator in W-Cu compacts is less as compared to its effect on W compacts [12]. In case of W-bronze alloys, some Ni may remain at the grain boundaries due to presence of 12 wt. % Sn, which will enhance the densification even further. For W-bronze with Co as the activator, due to the tendency to form intermetallic with tungsten and the limited solubility of Co in Cu, Co will remain segregated to grain boundaries thereby resulting higher densification than Ni. It is observed that bronze powders prepared by both premixed and prealloyed method result in similar sintered density in both W-10bronze and W-20bronze alloys. This is attributed to the fact that at the sintering temperatures used for this study, the Sn in premixed samples would have completely diffused into copper and therefore its behaviour will be similar to that of prealloyed Cu-Sn powder.

The scanning micrographs shown in Fig 7 and Fig 8 are those for the premixed W-20(Cu-Sn). The Cu present in the green sample will be distributed evenly over the small pores during the process of liquid phase sintering leaving behind big pores in some portions. Due to presence of these big pores in the sintered compact, in the SE mode topographical contrast will be produced. But in BSE mode due to presence of Cu in the green sample, the atomic mass contrast will take place. Microstructural evolution on all these W-bronze alloys followed by the mechanical properties will play a vital role in understanding their behaviour.

## Conclusions

Premixed and prealloyed W-bronze alloys give similar behaviour at 950°C. These alloys undergo liquid phase sintering above 1000°C which results in higher densification. On comparing the activated sintering behaviour, the alloys containing Co activator resulted in better density than the alloy containing Ni activator. The maximum sintered density, percent theoretical, achieved by the W-bronze alloys during the present investigation was about 90 percent, Co being the activator.



## References

1. H.W. Hayden and J.H. Brophy, "The Activated Sintering of Tungsten with Group VIII Elements", *Journal of the Electrochemical Society*, Vol. 110, No. 7, pp 805-810 (1963).
2. R.M. German and Z.A. Munir, "Enhanced Low-Temperature Sintering of Tungsten", *Metallurgical Transactions A*, Vol. 7A, pp 1873-1877(1976).
3. J.H. Brophy, L.A. Shepard and J. Wulff, *Powder Metallurgy*, Interscience Publishers, London, pp 113-135 (1961).
4. V.V. Panichkina, V.V. Skorohod and A.F. Khrienko, *Soviet Powder Metallurgy Metal Ceramics*, Vol. 6, pp 558 (1967).
5. G.V. Samsonov and V.I. Yakovlev, *Soviet Powder Metallurgy Metal Ceramics*, Vol. 6, pp 548 (1967).
6. G.V. Samsonov and V.I. Yakovlev, *Soviet Powder Metallurgy Metal Ceramics*, Vol. 6, pp 607 (1967).
7. G.V. Samsonov and V.I. Yakovlev, *Soviet Powder Metallurgy Metal Ceramics*, Vol. 9, pp 30 (1970).
8. G.V. Samsonov and V.I. Yakovlev, *Soviet Powder Metallurgy Metal Ceramics*, Vol. 8, pp 804 (1969).
9. S. Ylassary and M.H. Tikkanen, "On the Sintering Kinetics of Nickel Activated Tungsten", *Physics of Sintering*, Vol. 7, No. 1, pp 47-54 (1971).
10. I.J. Tooth and N.A. Lockington, *Journal of Less Common Metals*, Vol. 12, pp 353 (1967).
11. Gessinger and Fischmeister, *Journal of Less Common Metals*, Vol. 27, pp129 (1972).
12. J.L. Johnson and R.M. German, *Advances in Powder Metallurgy and Particulate Materials*, Metal Powder Industries Federation, NJ, pp 35-46 (1992).
13. R.M. German, "Activated Sintering of Refractory Metals by Transition Metal Additions", *Reviews on Powder Metallurgy and Physical Ceramics*, Vol. 2, No.1, pp 9-43 (1982).

## EFFECT OF SWAGING ON MICROSTRUCTURE EVOLUTION IN W-Ni-Fe Alloys

S.K.Rout.\* A. Upadhyaya.\*\* A. Tewari.\*\*

\* Graduate Student

\*\* Assistant Professor

*Materials and Metallurgical engineering  
Indian institute of technology, Kanpur, INDIA*

### Abstract

Tungsten based alloys because of their high temperature strength, hardness, good machinability and thermal conductivity is used in various kinds of applications such as radiation shielding, high momentum penetrators. These alloys normally exhibit a dual phase microstructure consisting of rounded tungsten grains embedded in Ni-Fe matrix. As far as the penetrator application is concerned these materials need to have better mechanical strength as they are subjected to high temperature deformations. One of the ways to improve the mechanical properties of these alloys (such as toughness and strength) is by combination of different amount of deformations with heat treatment, also called thermo-mechanical treatment. Evolution of properties are determined from quantitative microstructure analysis, which involves contiguity of the microstructure surfaces, surface area per unit volume ( $S_v$ ) of the W-matrix interfaces through line intercept methods. However the present research involves the room temperature swaging of 90W-7Ni-3Fe alloys to a large deformations levels of 96% and further heat treatment at 500, 900, 1400°C. Finally the micro structural surfaces were quantified and correlated with the properties.

### Introduction

Tungsten heavy alloys have been linked to powder metallurgy processing since 1930's. Tungsten Heavy alloys are a class of material that contains 80-90 wt% W. They generally exhibit a dual phase microstructure, where principal phase being mainly pure tungsten in association with a binder phase containing transition metals (Ni, Fe, Cu, Co) plus dissolved tungsten. In fact the tungsten grain it self is brittle and addition of transition metals make these alloys ductile in nature. The basic advantage of these alloys is that they have high density, high UTS, moderate ductility, good machinability, good corrosion resistance and thermal conductivity. Application of these alloys includes radiation shielding, mass balancing, inertial systems and high momentum penetrators [1]. In fact tungsten heavy alloys have a range of mechanical property variation, especially hardness, UTS, ductility. Here the main focus has been kept on W-Ni-Fe alloys. These heavy alloy microstructures comprise of two phases, the refractory tungsten phase (B.C.C) and other lower melting matrix phase (F.C.C). Liquid phase sintering is the only mechanism to produce these heavy alloys. However in order to get the desired properties of the as sintered alloy one should control the sintering temperature, sintering atmosphere depending upon composition [2,3,4,5]. The properties of these alloys are very much sensitive to processing and are degraded by residual porosity, impurity segregation, interfacial embrittlement and inter-metallic phase formation [6]. Nickel to iron ratio also is an important factor for deciding the mechanical property [7,8]. However the mechanical property of W-Ni-Fe alloy can be improved through thermo-mechanical processing in such a way that this alloy is the best alloy to be used for application mentioned above. The change in mechanical property is interdependent on various factors like, powder characteristics, sintering time, temperature, atmosphere, chemistry and post

cycle treatments. Few researches have been carried out on post-sintering treatment like quenching of the sintered alloy in some way can improve % of elongation and UTS [9,10]. This can be reasoned in a way that during quenching the interfacial segregation of impurity element can be reduced, as compared to annealed and sintered parts. Vacuum treatment has also been suggested for improving the mechanical property as it avoids the occurrence of hydrogen embrittlement.

Different thermo-mechanical treatment has been discussed in various literatures. One of the ways to improve the UTS and yield strength is through cold working and annealing, but hardness value has often-negative effect of this treatment. The heavy alloy when solid state sintered after cold working show better mechanical property, but not that much better as compared to the material liquid phase sintered after mechanical working. The liquid phase sintered material shows better mechanical property due to refined microstructure through recrystallization, stress induced boundary migration and melt penetration into the fine-grained material. Also few research have been performed on primary reduction by extrusion followed by multiple secondary reduction by swaging with intermediate anneals and introduction of intermediate cold swaging to hot rolled and hot swaged specimen [11,12,13,14]. Some time aging treatment of this alloy partially improves the hardness value over a certain range of temperatures due to the precipitation within the W grains, but above a certain temperature the negative effect takes place. The tungsten content has a marked effect on tensile properties of these alloys. The maximum UTS was obtained at 93% W. As far as the penetrator application is concerned, the high momentum penetrator desires high toughness in combination with ductility and strength as they are subjected to high temperature and high strain rate [15,16,17]. DU and WHAs have been successfully used for this application. Though the penetrator performance of DU alloys is more efficient than the WHAs, but due to its environment hazards they are of limited use. Research has been carried out on failure mechanisms of these materials under dynamic compression tests [18,19].

Based on the introductory remarks, the processing route to optimal properties has become evidence. However there are several observation, which are unexplained. This paper addresses the relative importance of amount of deformation and subsequent heat treatment temperatures on the hardness of material on bulk and micro analysis point of view and the contiguity (the average fraction of surface area shared by one W-W grain) of the micro structural surfaces. In addition to that the role of surface area per unit volume ( $S_v$ ) of the W-matrix interfaces plays an important role in determining the kinetics of flow of W-matrix interfaces at different deformation levels and variation of grain size at different heat treatment temperatures. Experiments relating to different heat treatment temperature guides us in deciding which material at what deformation is best suitable to obtain better combination of mechanical properties. As a consequence room temperature swaging to high deformation levels and further heat treatment at different temperatures has been developed for quantifying the most suitable methods to reach the best processing routes for W-Ni-Fe alloys.

## Experimental Approach

The materials used for investigations were W-Ni-Fe alloys of rod shaped in nature consisting of 90 wt% W and rest Nickel and iron in the ratio of 7:3. The diameter of rod

was 0.52 inch. The samples of 5mm in thickness were cut and metallographic techniques used for the preparation of these alloys were sectioning, mounting, and polishing. Abrasive cutter was used for sectioning the specimens so as to get the crosssection of the samples of thickness around 5 mm. Then the samples from three compositions were hot mounted. Care must be taken during hot mounting so as to avoid the loosening of the material inside the mounting base. Generally resins crystals were used for hot mounting. Grinding is one of the steps, which includes considerable relief in the matrix or results in a dual phase microstructure. In other words; the two phase of the material being processed will be of different levels. This is attributed to the fact that the emery paper used quickly grinds away the Ni-Fe matrix while leaving the hard W particles untouched. Hence emery papers were used from coarse to fine grit only for primary removal of scratches. It is very difficult to avoid any relief, but can be minimized. Finally the samples were cloth polished to obtain the typical liquid phase sintered microstructures of 90W-7Ni-3Fe alloy. Figure 1 shows the microstructure of as-received 90W-7Ni-3Fe alloy.

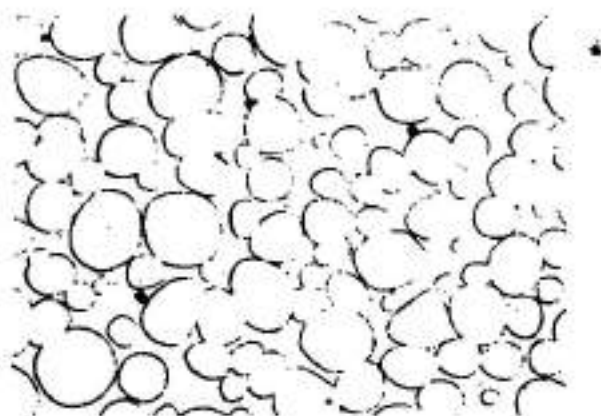


Fig 1: Typical LPS microstructure of 90W-7Ni-3Fe.

Room temperature swaging was carried out by rotary swaging machine. The heavy alloy rod (20 cm in length) was swaged to different deformation levels such as 35, 70, 90, 96% reductions in area. Rotary swaging is the operation where the two dies, which are free to move radially, are held in a spindle which rotates simultaneously. The work is fed between the dies continuously and for every rotation. Rotary swaging is able to produce external surfaces, which are axi-symmetric. Samples of 5-mm thickness were sectioned from the swaged samples of each deformation levels. A diamond wheel was used for sectioning the swaged and heat-treated samples. The wheel was used at a very slow speed in order to avoid any particle pullouts or damage in the sample. The transverse sections and longitudinal sections were mounted and polished. Figure 2 (a), (b), (c), (d) represents the longitudinal sectioned microstructure of swaged samples at 200 magnifications.



Heat treatment of swaged samples was performed in a tubular furnace in hydrogen atmosphere for one hour. The heating rate was 8 °C/ minute. For the present research the three heat treatment temperatures were selected such as: 500, 900 and 1400°C. Finally the samples were sectioned and polished as cited above. Figure 3 (a), (b), (c) represents the micrographs of as-received heat treated samples.

Bulk hardness and micro hardness test were performed on all the samples. MHP 160 Micro-Hardness ( $H_v$ ) was used to perform the micro-hardness tests. Microhardness was performed only on the matrix phase. The load used for indentation was 40 gm. A diamond pyramid indenter was used. The load was applied for a short period of 3-4 seconds. The indentation was square shaped. The length of the two diagonals was measured and their mean was taken.

Quantitative microstructural analysis involves the surface area per unit volume ( $S_v$ ) of the W-matrix interfaces. The  $S_v$  measurements were made on the microstructural surfaces by line intercept methods where the lines are oriented at an angle of 22.5°. The orientation characteristics of the microstructural surfaces were studied from 0 to 90°

## RESULTS:

In this study bulk hardness of the as received sample is less as compared to swaged samples. Hardness of 96% swaged samples is highest at 500°C. Figure 6 shows that hardness decreases with increases in temperatures.

Micro hardness of the matrix phase shows a decreasing trend with heat treatment temperatures as like bulk hardness ( Fig 7).

Surface area per unit volume ( $S_v$ ) of the W-matrix interface for as received samples does not have that much effect with respect to orientations.

Figure 9 shows the variation of  $S_v$  with respect to orientations for 35% swaged samples.

## DISCUSSIONS:

our study involves the bulk hardness measurements, micro hardness measurements of the matrix and surface area per unit volume of the W-matrix interfaces for as-received and 35% swaged samples.

Bulk hardness measurements for 96% swaged samples is more at 500°C. As the heat treatment temperatures increases the hardness decreases due to coarsening of grain at high temperatures which is 1400°C. For the matrix the same phenomenon occurs. Basically the hardness of a material depends upon the nature of chemical composition and dislocation density imparted to the material. In case of swaged samples the hardness is greater for them which were subjected to high deformation levels. But heat treating at high temperatures the amount of dislocation density decreases there by causing decrease in hardness.

Considering same volume fraction, the surface area per unit volume of finer particles is greater as compared to bigger particles. As far as the surface area per unit volume of the W-matrix interface is concerned the graph for as-received samples is same for all orientations.  $S_v$  is more for as received specimen as compared to swaged and heat treated samples. So  $S_v$  does not have any effect with respect to heat treatment temperatures. But for 35% swaged samples  $S_v$  goes on increasing with respect to orientations depicting finer grains at 90° orientations. If we compare the the only swaged sample with heat treated samples, incase of heat treated samples grain coarsening occurs at higher temperatures there by causing lower  $S_v$  values at 900 and 1400°C.

## SUMMARY:

- A practical processing route has been developed for the production of fibrous microstructures in 90W-7Ni-3Fe alloy by imparting high deformation levels i.e., to about 90% and 96% without fracture.
- Micro hardness measurements of matrix decreases with increase in heat treatment temperatures
- Quantitative stereo logical measurements gave an appropriate estimate of the surface area per unit volume of the W-matrix interface.
- For as-received sample  $S_v$  remains almost same with increase in heat treatment temperatures showing no orientations
- For 35% swaged samples the  $S_v$  decreases as we go on increasing the temperatures
- To further enhance the mechanical properties future research should be focussed on taking advantage of hot-deformation processing where a combination of stress and temperature simultaneously applied.

## References

1. S. G. Caldwell, "Tungsten Heavy Alloys," ASM Hand Book, P.W. Lee and R. Lacocca (eds.), Powder Metal Technologies and Applications, Materials Park, Ohio, USA, Vol. 7, pp. 914-921(1998).
2. R.M German, A. Bose and S.S. Mani, "Sintering time and Atmosphere influences on the Microstructure and Mechanical Properties of Tungsten Heavy Alloy," *Metallurgical Transaction A*, Vol. 23, pp. 211-219 (1992).
3. R.M. German and K.S. Churn, "Sintering Atmosphere Effects on the Ductility of W-Ni-Fe Heavy Metals," *Metallurgical Transaction A*, Vol. 15, pp. 747-754 (1984).
4. C. Lea, B.C. Muddle and D.V. Edmonds, "Segregation to Inter Phase Boundaries in Liquid Phase Sintered Tungsten Alloys," *Metallurgical Transaction*, Vol. 14, pp. 667-677 (1983).
5. D.V. Edmonds and P.N. Jones, "Interfacial Embrittlement Liquid Phase Sintered Tungsten Heavy Alloys," *Metallurgical Transactions A*, Vol. 10, pp. 289-295 (1979).
6. L.L. Bourguignon and R.M German, "Sintering Temperature Effects on a Tungsten Heavy Alloy," *The International Journal of Powder Metallurgy*, Vol. 2, n. 2, pp. 115-121 (1988).
7. S.G. Caldwell, "Variation of Ni to Fe Ratio in W-Ni-Fe Alloys: A current Perspective," Tungsten and Tungsten Alloys -1992, A. Bose and R.J. Dowding (eds.), Metal Powder Industries Federation, NJ, USA, pp. 89-96 (1992).
8. J.R. Spencer, "The Effect of Nickel:Iron Ratios on the mechanical properties, Microstructure and Processing of W-Ni-Fe Alloys," Tungsten and Tungsten Alloys -1992, A. Bose and R.J. Dowding (eds.), Metal Powder Industries Federation, NJ, USA, pp. 111-117 (1992).
9. T. Kohno and O. Mayama, "Effects of Sintering and Post Sintering Heat treatment on the Mechanical Properties of W-Ni-Fe Heavy Alloys," International Conference on Powder Metallurgy, Institute of Metals, London, Vol. 1, pp. 324-331 (1990).



10. H.K. Yoon, S.H. Lee, S.J.L. Kang, D.N. Yoon, "Effect of Vacuum Treatment on Mechanical Properties of W-Ni-Fe Heavy Alloy," *Journal of Materials Science*, Vol. 18, pp. 1374-1380 (1983).
11. V. Srikanth and G.S. Upadhyaya, "Effect of Cold Work and Annealing on the Mechanical Properties of 90W-7Ni-3Fe Heavy Alloy," *Journal of Materials Science Letters*, Vol. 7, pp. 195-197 (1988).
12. W. Leonard and L. Magness jr, "Improving Mechanical properties of Tungsten Heavy Alloy Composites through Thermo-Mechanical Processing," Tungsten and Tungsten Alloys -1992, A. Bose and R.J. Dowding (eds.), Metal Powder Industries Federation, Princeton, NJ, pp. 127-135 (1992).
13. M.H Hong, S. Lee, J.N. Noh and Y.W. Kim, "The Effect of Thermo-Mechanical Treatment on the Microstructure and Failure Behavior of Sintered Tungsten Heavy Alloy," Advances in Powder Metallurgy and Particulate Materials-1994, A. Lawley and A. Swanson (eds.), Metal Powder Industries Federation, Princeton, NJ, USA, Vol. 5, pp. 279-288 (1994).
14. A. Bose, D. Sims and R.M. German, "Test Temperature and Strain Rate Effects on the Properties of a Tungsten Heavy Alloy," *Metallurgical Transaction A*, Vol. 19, pp. 487-494 (1988).
15. K.O. Zamora, J.G. Sevillano and M.F. Perez, "Flow Stress and Ductility of Tungsten Heavy Metal Alloys," Tungsten and Tungsten Alloys -1992, A. Bose and R.J. Dowding (eds.), Metal Powder Industries Federation, Princeton, NJ, pp. 281-288 (1992).
16. S.P Doepker, J.A. Mullendore and J.R. Spencer, "A Comparison of W- Ni-Fe and W-Ni-Co Alloys," Tungsten and Tungsten Alloys -1992, A. Bose and R.J. Dowding (eds.), Metal Powder Industries Federation, Princeton, NJ, USA, pp. 273-281 (1992).
17. A. Bose, J. Lankford jr and H. Couque, "Dynamic Compressive Properties of Tungsten Heavy Alloys with varying Grain Sizes," Advances in Powder Metallurgy and Particulate Materials -1994, A. Lawley and A. Swanson (eds.),

- Metal Powder Industries Federation, Princeton, NJ, USA, Vol. 4, pp. 227-238 (1994).
18. C. Lea, B.C. Muddle and D.V. Edmonds, "Segregation to Inter Phase Boundaries in Liquid Phase Sintered Tungsten Alloys," *Metallurgical Transaction*, Vol. 14, pp. 667-677 (1983).
19. M.C. Hogwood and A.R. Bentley, "The Development of High Strength and Toughness Fibrous Microstructures in Tungsten-Nickel-Iron Alloys for Kinetic Energy Penetrator Application," *Tungsten and Refractory Metals*, A. Bose and R.J. Dowding (eds.), Defence Research Agency, Kent, England, pp. 37-45 (1994).

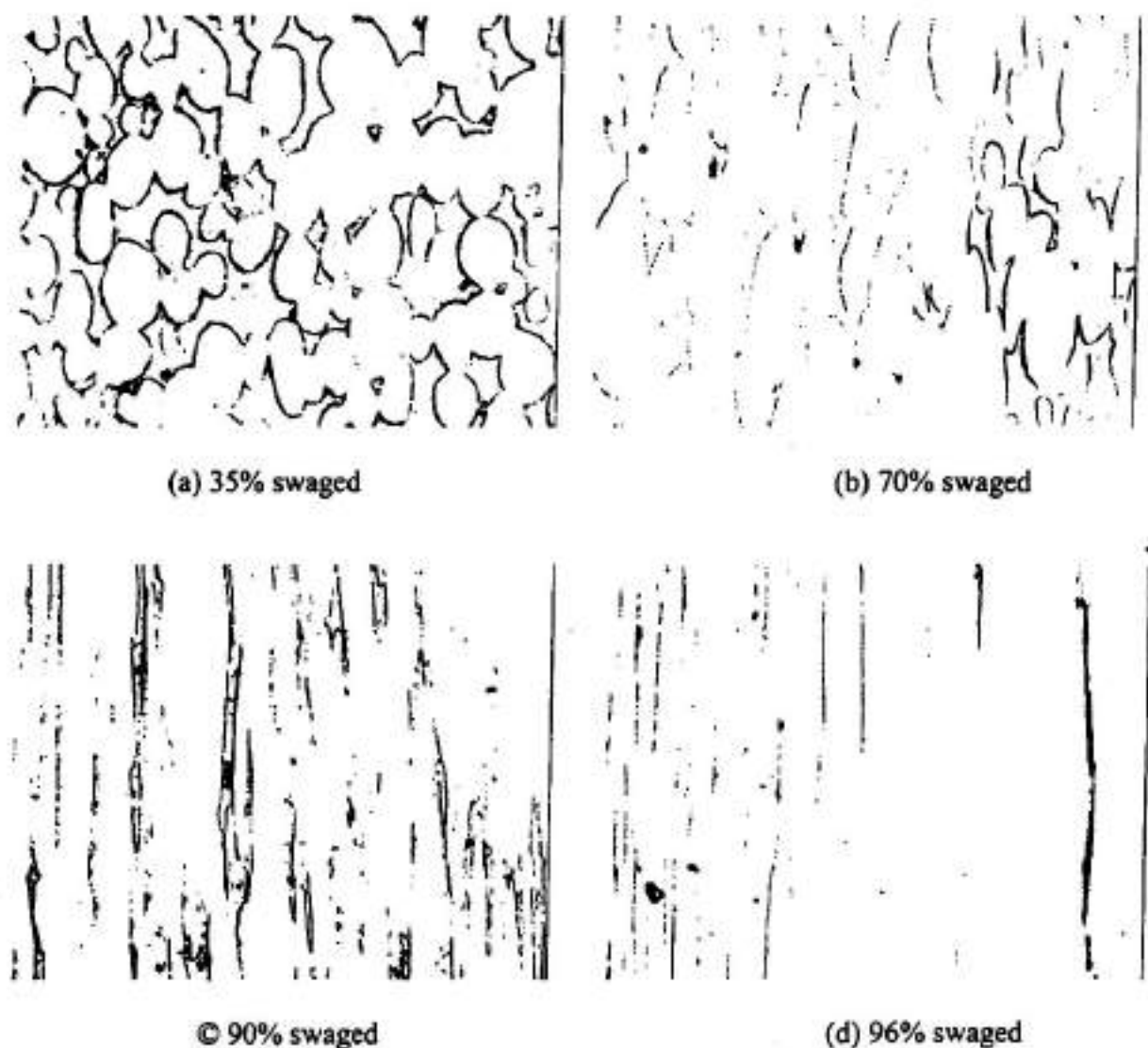
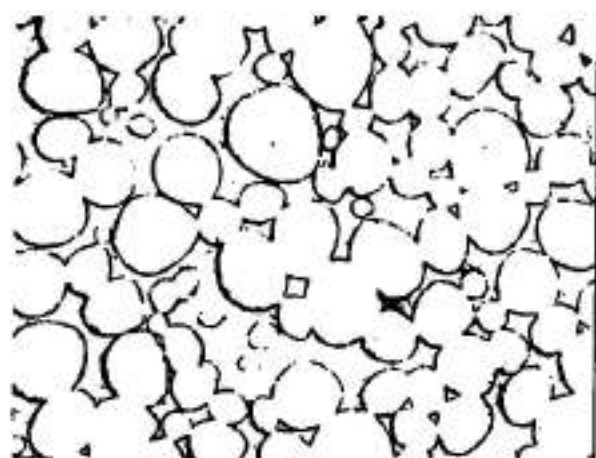


Fig 2. Microstructure of swaged 90W-7Ni-3Fe (a) 35% (b) 70% (c) 90% (d) 96%.



(a) 500°C

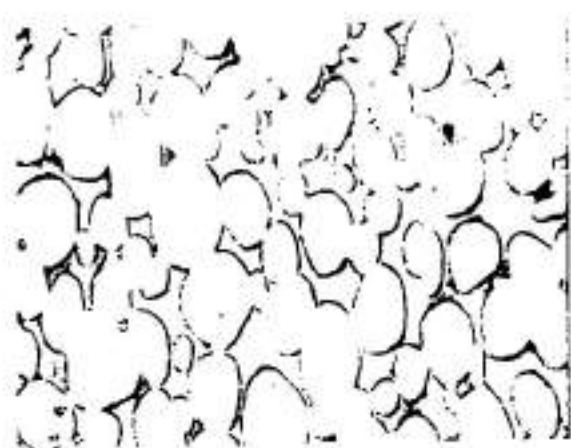


(b) 900°C

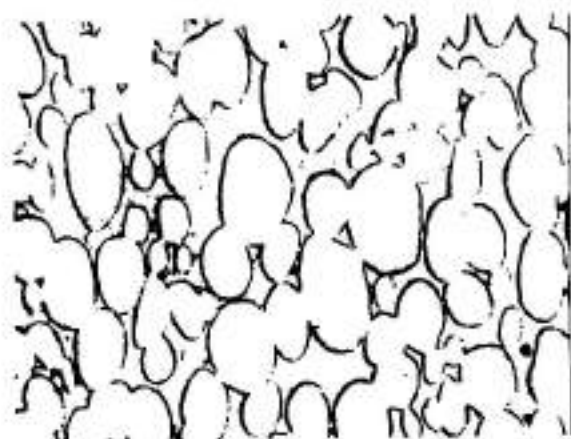


(c) 1400°C

Fig 3. Heat treated as-received 90W-7Ni-3Fe (a) 500°C (b) 900°C (c) 1400°C.



(a) 500°C

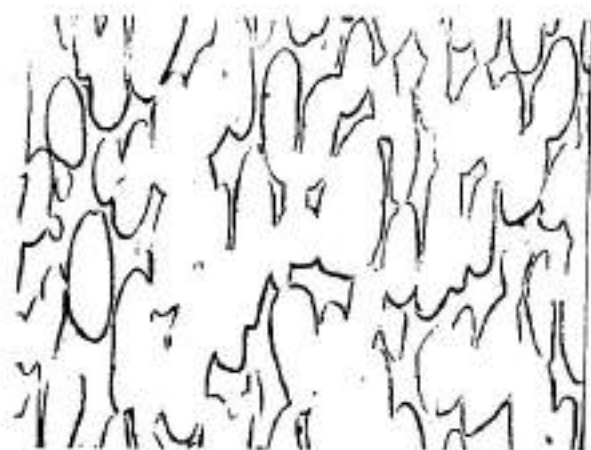


(b) 900°C



(c) 1400°C

Fig 4. Heat treated 38% swaged 90W-7Ni-3Fe (a) 500°C (b) 900°C (c) 1400°C.



(a) 500°C



(b) 900°C



(c) 1400°C

Fig 5. Heat treated swaged microstructure of 90W-7Ni-3Fe (a) 500°C (b) 900°C (c) 1400°C.

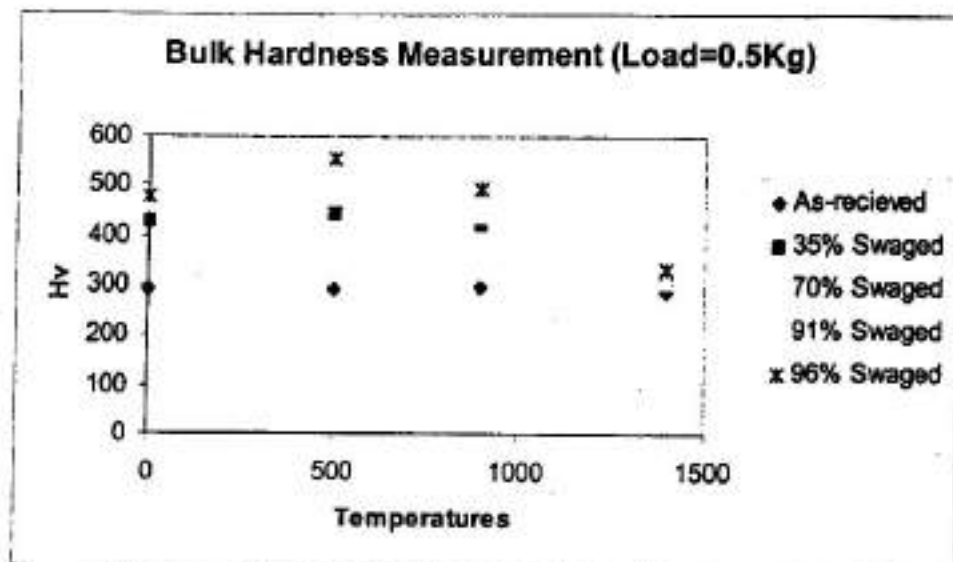


Fig 6. Data showing bulk hardness variation with heat treatment temperatures of 90W-7Ni-3Fe alloy.

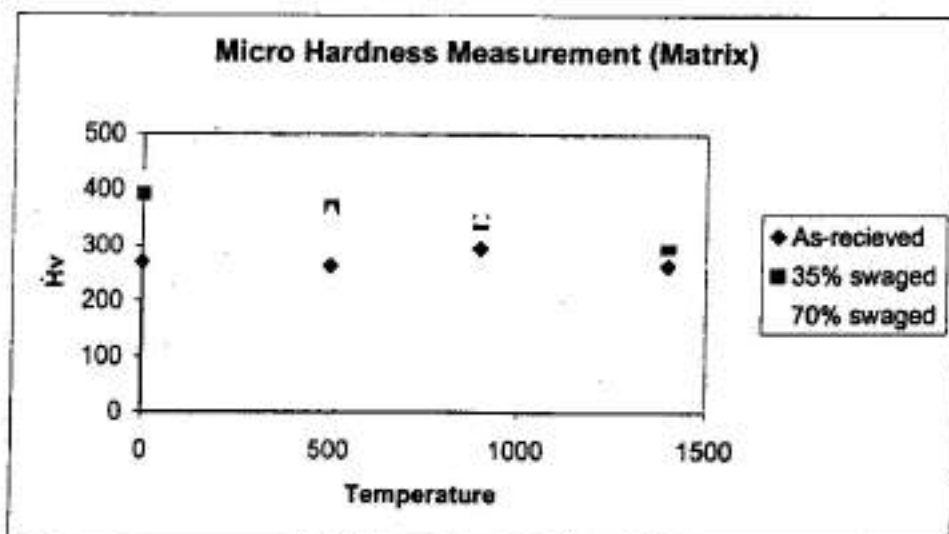


Fig 7. Data showing micro hardness variation of matrix with respect to temperatures for 90W-7Ni-3Fe.



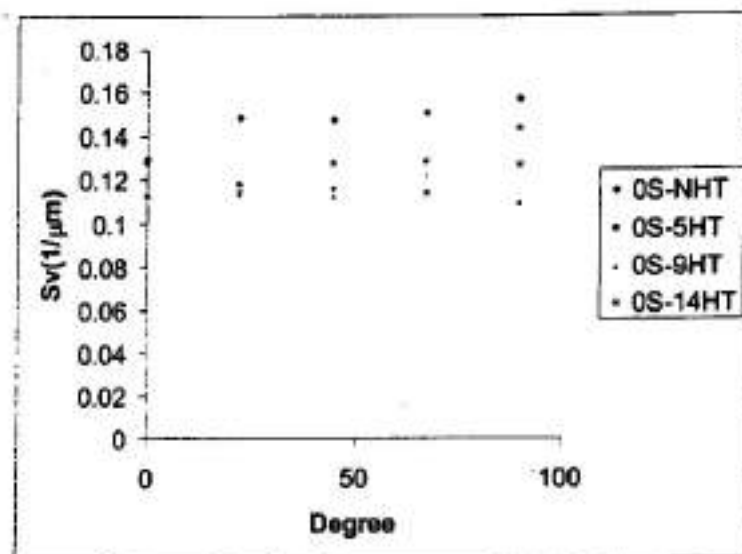


Fig 8. Data showing  $S_v$  variation of as-received 90W-7Ni-3Fe with respect to Orientations.

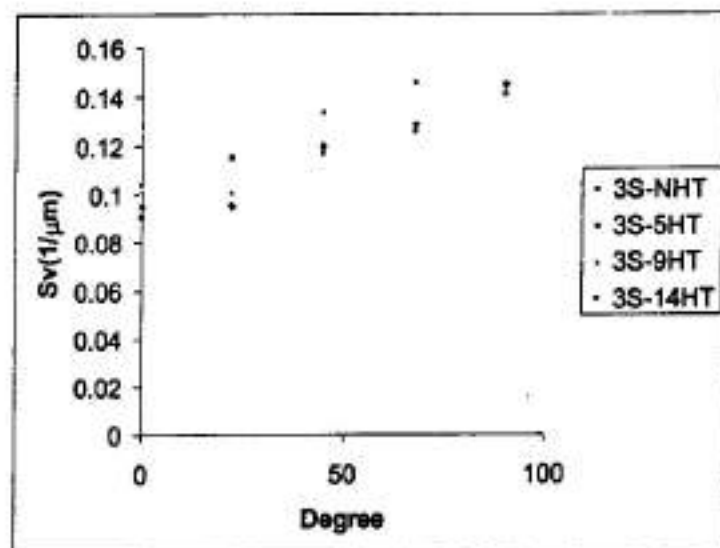


Fig 9. Data showing variation of  $S_v$  with respect to orientations for 90W-7Ni-3Fe.

## REACTIVE HOT PRESSING OF IRON ALUMINIDES

D. Srinivas, M.M Godkhindi, P.G Mukunda, S. Das

Department of Metallurgical and Materials Engineering, IIT Kharagpur.

**Abstract:** Iron Aluminides are attractive materials for high temperature applications because of the combination of the low cost, conservation of strategic elements (Example Cr), low density and remarkable corrosion resistance. Near net shape processing methods are likely to be better routes due to the inherent brittleness of these products. Attempts have been made to produce dense ordered  $Fe_3Al$  intermetallics through reactive hot pressing method. Effect of the addition of nickel as a reaction aid, has been studied. Optimization of process parameters to obtain complete densification and homogeneous microstructure has been attempted. The present work indicates that dense  $Fe_3Al$  samples with excellent properties can be produced by this route.

**Keywords:** Iron aluminides; reactive hot pressing;  $Fe_3Al$  intermetallics; combustion synthesis.

### 1. INTRODUCTION

Intermetallic compounds based on aluminum, such as  $Fe_3Al$ , have attractive combination of low density, high strength that even improves with temperature, good corrosion and oxidation resistance, and use of non-strategic elements. The use of aluminides as a material for dies for the hot forging process has been found to improve the quality of variety of products such as automobile parts, components of electricity generation plants and different tools etc [1].

Currently Iron aluminides ( $Fe_3Al$ ) are being produced through two processes

1. Liquid metal route
2. Conventional Powder metallurgy route.

The drawbacks of the cast route are the susceptibility of the castings for cracking during the machining and the final finishing operations. This problem is mainly due to the intrinsic brittleness of these materials at room temperature. Utmost care has to be taken during casting to prevent the absorption of hydrogen from the atmospheric moisture.

In the conventional Powder Metallurgy route, the prealloyed iron aluminide powders are used for the production of the component. But as the powder is brittle in nature, it is difficult to compact. And this process involves long sintering cycles and high sintering temperatures.

Reactive hot pressing (RHP) involves the simultaneous combustion reaction and uniaxial hot pressing of the green compact. Considerable amount of heat released due to the reaction combined with pressure can help in generating dense pore free product. This technique has been successfully used for the production of  $Ni_3Al$  fasteners from the elemental Ni and Al powders [2]. This process is reported to be energy-efficient and produces a compound that is purer than that

resulting from conventional production methods. The present investigation is an effort to explore the possibility of production of iron aluminides through this process.

The Fe-Al system forms 7 different phases including 2 metastable phases. Table 1 shows the crystal structural data and heats of formation of different compounds formed in this system. From the data it is evident that the heat of formation of  $\text{Fe}_3\text{Al}$  is very low (compared to the heat of formation of  $\text{Ni}_3\text{Al}$  i.e., 42.9 kJ/mol). It is, therefore, expected that addition of varying amounts of Ni/Al mixture may aid the sintering process for  $\text{Fe}_3\text{Al}$ . In an earlier work [3], the effect of Ni addition on the densification has been discussed, and the addition of Ni up to 8.6 wt % significantly yielded better results (sintered density increased from 4.66 g/cc to 4.99 g/cc). Porosity in the product was reduced by the addition of the Ni/Al powders. Addition of the Ni decreases the grain size of the samples.

TABLE 1 Crystal structural data of Fe-Al system. [5]

Phases	Composition		Crystal structure	Heat of formation kJ/mol ( $\Delta H$ ) at 298 K
	at % Al	Wt % Al		
FeAl	23.3 – 55.0	12.8 – 37.0	BCC	-26.23
$\text{Fe}_3\text{Al}$	23.0 – 34.0	13.0 – 20.0	BCC (ordered)	-16.34
$\text{FeAl}_2$	66.0 – 66.9	48.0 – 49.4	Rhombohedral	-27.95
$\text{Fe}_2\text{Al}_3$	70.0 – 73.0	53.0 – 57.0	Monoclinic	-27.52
$\text{FeAl}_3$	74.5 – 76.6	58.5 – 61.3	Monoclinic	-28.81
Metastable phases				
$\text{Fe}_2\text{Al}_4$	81.8	68.5	-----	-----
$\text{FeAl}_4$	85.7	74.3	-----	-----

## 2. EXPERIMENTAL

Hoganas iron powder (SC 100.29) screened to -325 mesh, was subjected to hydrogen reduction at 650°C to reduce the surface oxide layers. Aluminum powder (particle size -325 mesh) and nickel powder (~3  $\mu\text{m}$ ) were used in the as received condition. Two compositions were selected for making the green compacts, as shown in the Table 2. An indigenously designed ball mill using hardened steel balls was used for mixing the powders. Before mixing the container was flushed

with argon gas to avoid any possible oxidation of powder surface during mixing. The time of mixing was found to be 1 hr for optimized results. The mixed powder was compacted into a cylindrical compact of 12.75 mm diameter with the help of a hydraulic press at a compacting pressure of 500MPa. Three alternative routes of densification were investigated as indicated in Table 3.

TABLE 2 Wt. fraction of  $\text{Ni}_3\text{Al}$  in the  $\text{Fe}_3\text{Al}$  mix

$\text{Fe}_3\text{Al}$ : $\text{Ni}_3\text{Al}$	Weight fraction (wt %)		
	%Fe	%Al	%Ni
100:0	86.13	13.87	---
90:10	77.7	13.7	8.6

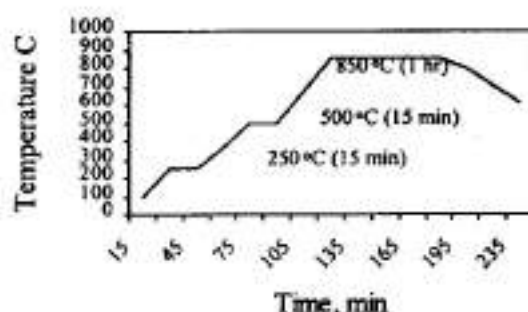


Fig. 1 Heating pattern of the degassing treatment

TABLE 3 Processing routes of the various samples

Sample #	A	B	C	D	E	F
Composition	$\text{Fe}_3\text{Al}$ : $\text{Ni}_3\text{Al}$ 100 : 0	$\text{Fe}_3\text{Al}$ : $\text{Ni}_3\text{Al}$ 100 : 0	$\text{Fe}_3\text{Al}$ : $\text{Ni}_3\text{Al}$ 100 : 0	$\text{Fe}_3\text{Al}$ : $\text{Ni}_3\text{Al}$ 90 : 10	$\text{Fe}_3\text{Al}$ : $\text{Ni}_3\text{Al}$ 90: 10	$\text{Fe}_3\text{Al}$ : $\text{Ni}_3\text{Al}$ 90: 10
Processing route	Direct hot pressing of the green compact	Sintering followed by hot pressing	Sintering and hot pressing followed by homogenization.	Direct hot pressing of the green compact	Sintering followed by hot pressing	Sintering and hot pressing followed by homogenization

### 2.1 Reactive sintering (pressure less)

Sample # B and # E were produced through reactive sintering route with the purpose of comparing the same with RHP technique. Reactive sintering was carried out in tube type resistance furnace (fused Quartz tube) at temperature of 850°C in vacuum at a heating rate of 10° C/min. **Figure 1** shows the heating pattern adopted for sintering incorporating a degassing step which reduces voids and cracks considerably. After sintering, the product was cooled in the furnace. The samples were next hot pressed at 1000°C.

**Figure 2** shows the effect of compacting pressure on the green density and sintered density of the reaction synthesized product. The product density increases with increasing pressure. The density of the green compact affects the density of the product. **Figure 3** shows the effect of Ni content on the sintered density of the samples. For sample # C and # F the homogenization after reactive sintering and hot pressing was carried out at 1000 °C for 1 hour. The density measurement, the microstructure observation and the phase analysis were performed. Vickers hardness of the samples was also measured.

### 2.2 Direct hot pressing of the green compact

Sample # A and # D were produced through RHP technique. An indigenously designed hot press was used for this process. **Figure 4** shows the schematic diagram of the hot press. The pressing was carried out using graphite die and punch system. The required temperatures were obtained through resistance heating by passing high amperage current through the heating element, which also acted as the die. Pure graphite electrodes were used as upper and lower punches. This heating element is connected to the power supply through water-cooled copper electrodes. The lower copper electrode is fixed and the upper one is movable. The copper electrodes have a central hole for the insertion of the upper and lower punches. A DC transformer was used to step down the input voltage of 230V to output voltage of 0-24V.

Green compact was placed inside the graphite-heating element coated with boron nitride. The upper and lower graphite punches were also coated with boron nitride to prevent the reaction between compact and the graphite. The heating rate of the compact was 300 °C/min up to 700 °C and 150 °C/min up to 1000 °C. As the temperature approaches 600 °C, application of pressure was started gradually and reached maximum of 20MPa at 1000 °C. At 1000°C compact was kept for 15 min under the same pressure. After this, power was switched off and the compacted was allowed to cool to room temperature.

## 3.RESULTS

**Table 4** shows the green and sintered/hot pressed densities of the samples produced through various techniques, with and without the addition of Ni. Samples that were reaction sintered and hot pressed followed by homogenization at 1000°C showed highest densities among all the samples. Increased compacting pressure yields higher sintered density at all stages of processing (fig. 5 b). XRD, SEM-EDS analysis has been carried out to determine the formation of phases and analysis of the reaction product.

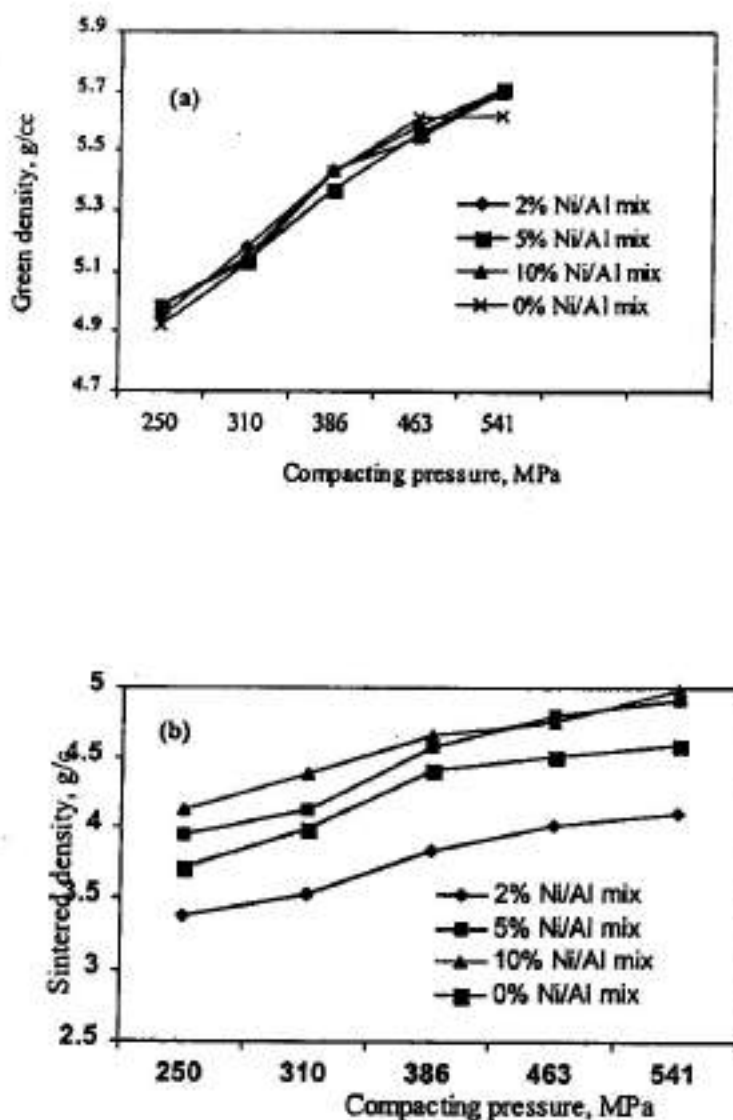


Fig. 2 (a) The green density as a function of compacting pressure  
(b) The sintered density as a function of compacting pressure.

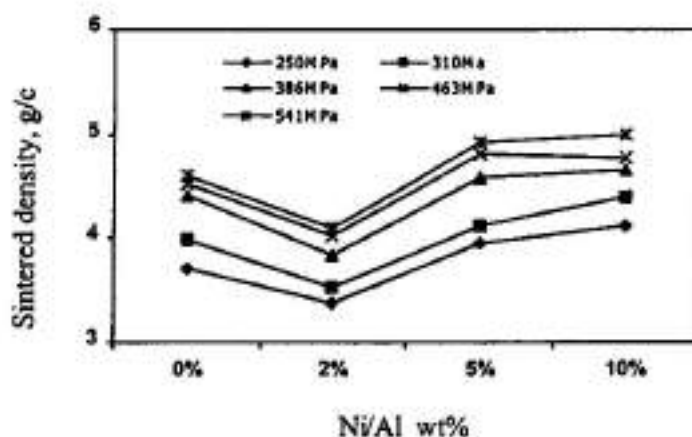


Fig 3 Effect of Ni/Al addition on the sintered density.

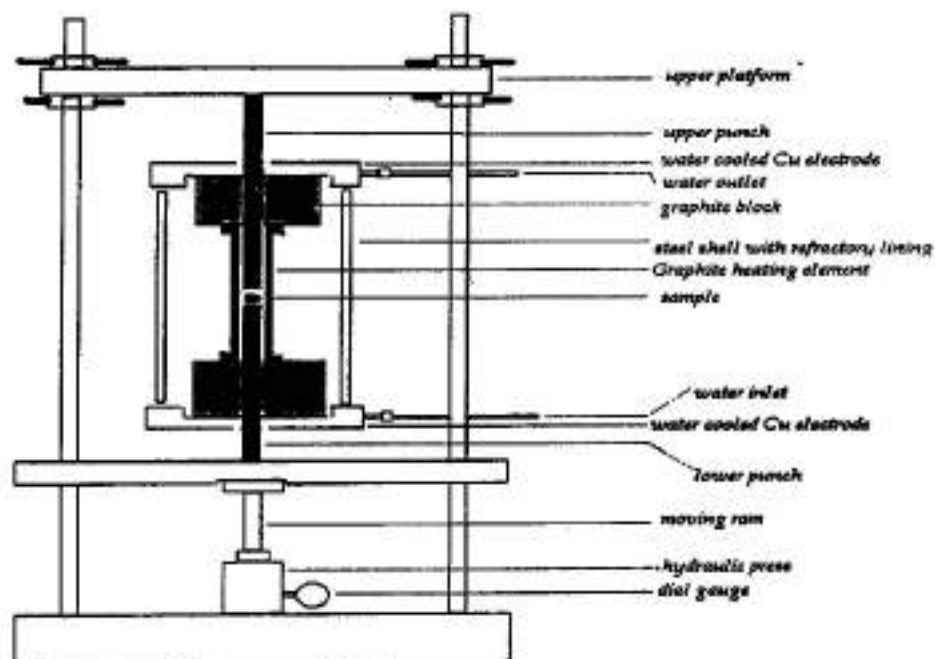


Fig. 4 Schematic diagram of the indigenously designed hot press



TABLE 4. Densities of samples before and after sintering/hot pressing.

Sample #	A	B	C	D	E	F
Green density g/cc	5.74	5.71	5.69	5.69	5.62	5.67
Density g/cc	4.69 (after direct hot pressing of the green compact)	4.99 (after reactive sintering) 5.03 (after sintering followed by hot pressing)	5.05 (after sintering and hot pressing followed by homogenization)	4.98 (after direct hot pressing of the green compact)	4.89 (after reactive sintering) 5.25 (after sintering followed by hot pressing)	5.27 (after sintering and hot pressing followed by homogenization)

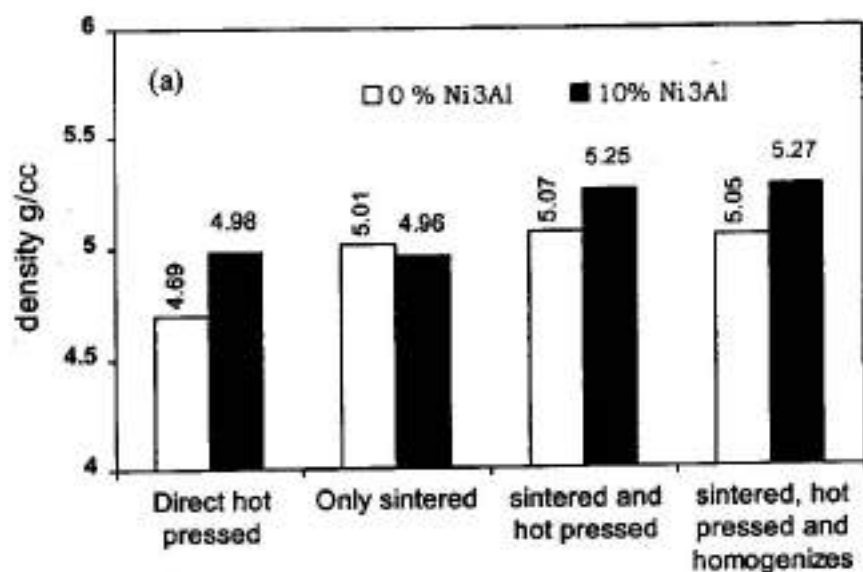
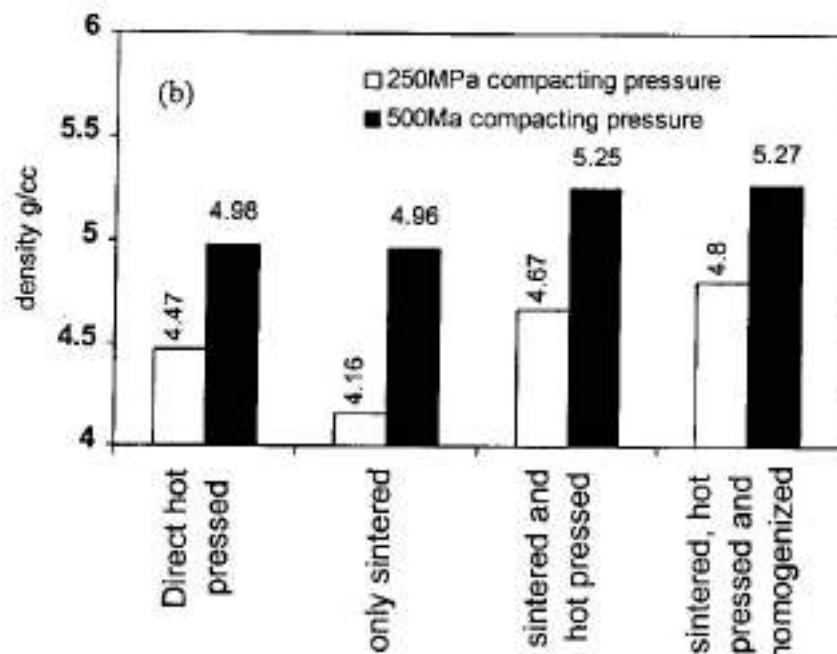


Fig. 5 a) Densification of the compacts through various processes



**Fig. 5** b) Effect of compacting pressure on densification

#### 4. EFFECT OF Ni/Al ADDITION ON THE REACTIVE HOT PRESSING

With the addition of Ni, the density was found to increase, reaching maximum at 8.6wt % Ni content. The porosity in the product is reduced by the addition of the Ni/Al powders. Samples with Ni content have finer grain size compared to the samples free from Ni. Preliminary experiments earlier have indicated that Ni additions when varied from 0 to 8.6 wt% indicated that increasing Ni content gave continuously better results. The Vickers hardness of the samples is increased with the addition of Ni. Fig. 6 shows the microstructures of the samples produced through various techniques, with and without Ni contents.

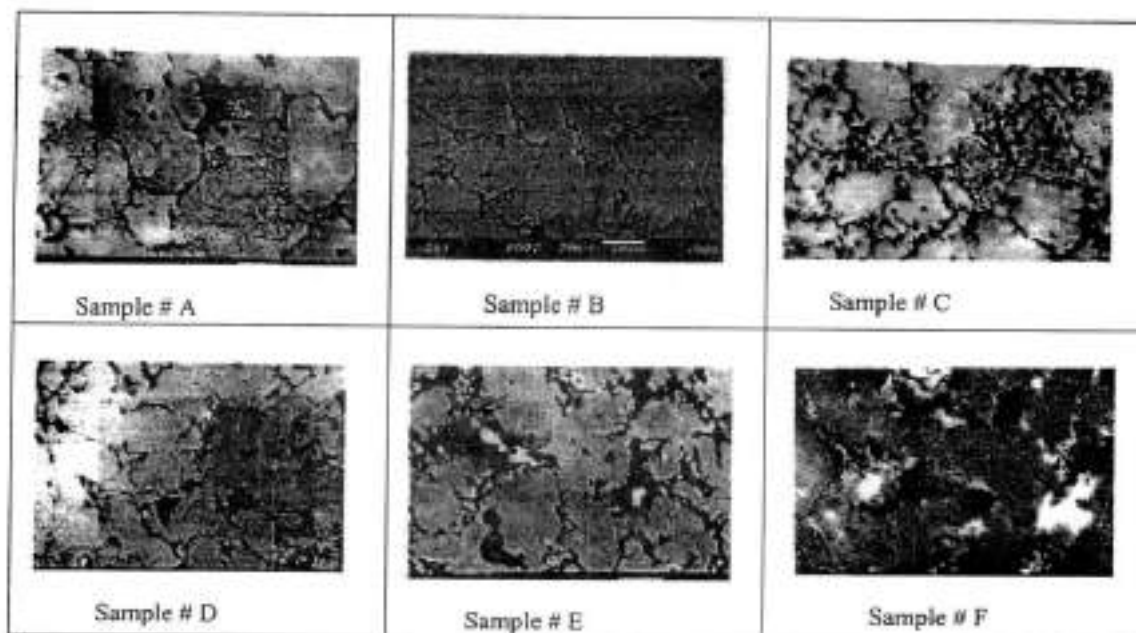


**Fig. 6** Microstructures of samples produced through various routes

## 5.DISCUSSION

Samples that are without Ni and directly hot pressed from green compact (sample # A) showed porosity inside the grains. Samples with Ni content of 8.6 wt% and directly hot pressed from green compact (sample # D) showed considerable increase in density. Reaction synthesized samples and reaction synthesized & hot pressed samples showed good densities and the pores are located at the grain boundaries. Grain size of these samples was found to be finer ( $25\mu\text{m}$ ) compared to the RHP samples. Samples that were reactive sintered, hot pressed and homogenized showed only slight increase in density but the Vickers hardness of these samples was found to be high compared to the other samples. Table 5 shows the SEM-EDS analysis of the various samples and it was found that in all the samples, the synthesized phase is  $\text{Fe}_3\text{Al}$ . Figure 7 shows the XRD profile of the product that consists of mainly  $\text{Fe}_3\text{Al}$ . Figure 8 shows the Vickers hardness values of various samples. From the hardness values, it is clear that hardness is increasing with the homogeneity of the samples.

**TABLE 5.** SEM-EDS analysis of various samples (spot analysis at various points)

Sample	A	B	C	D	E	F
At % Fe	76.4	70.34	76.4	74.8	81.0	72.53
At % Al	23.6	29.01	22.7	25	17.7	18.4
At % Ni	----	----	----	0.2	1.3	9.06

Studies have also been carried out on the wear characteristics of these samples and sample# C shows the best results i.e. wear rate of  $2.43 \times 10^{-4} \text{ mm}^3/\text{m}$  with a friction force of 30 N.

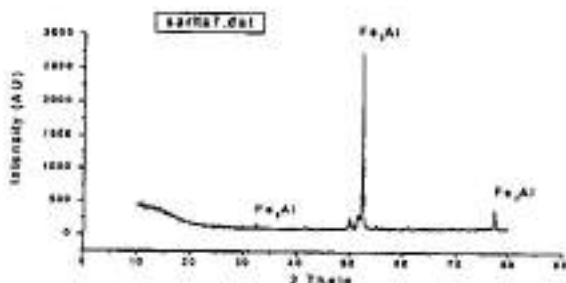
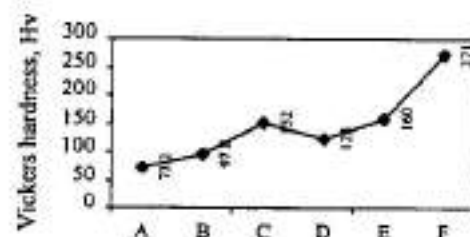


Fig. 7 XRD pattern of the synthesized product (sample # F).



Load: 5 kg, time 20 sec

Figure 8 Vickers hardness of the samples.

## 6. CONCLUSIONS

(1) Reactive hot pressing process for the production of iron aluminides samples has been investigated in order to optimize process parameters. While pure  $\text{Fe}_3\text{Al}$  mixture could not be sintered to full density, addition of nickel helped in achieving high density (low porosity).

(2) The optimal conditions that yielded best results (free from porosity and distortion) are:

Composition: 77.7 wt % Fe, 13.7 wt % Al and 8.6wt % Ni ( $\text{Fe}_3\text{Al}:\text{Ni}_3\text{Al} = 90:10$ )  
 Mixing time: 1 hour  
 Compacting pressure: 500MPa  
 Reaction hot pressing temperature: 1000°C  
 Reaction hot pressing pressure: 20MPa  
 Reaction hot pressing atmosphere: Air

(3) XRD, SEM- EDS and hardness data all indicated complete homogeneity of the product after reactive hot pressing.

(4) Homogenization treatment of the hot pressed samples has given rise to a very large increase in the hardness values though very little increase in density was observed. Marked increase in the hardness values upon addition of Ni.

## REFERENCES

- (1) <http://www.hr.doe.gov/energy100/business/08.html>
- (2) Materials Technology: A Strategic Industry Report on the Synthesis, Processing and Applications of Advanced Materials, Vol. 10 No. 3/4 p. 48-51, 1995.
- (3) M.M Godkhindi, P.G Mukunda, S Das and D. Srinivas: Reaction Synthesis of Iron Aluminides with the Addition of Ni, at Int. Conference of materials and material processing, IIT, Kharagpur on Feb 1-3, 2002.
- (4) A. Hibino, and M. Kiuchi: Material Transactions, JIM, Vol. 40, No. 2 (1999), pp. 92 to 99.
- (5) Hand book of Binary Metallic Systems, structure and property, vol. 2, p. no 140

## SYNTHESIS OF TITANIUM NITRIDES BY DIRECT NITRIDATION OF TITANIUM POWDERS

V.V Dabhade, R. Baijal, T.R.Rama Mohan and P. Ramakrishnan,  
Department of Metallurgical Engineering and Materials Science,  
Indian Institute of Technology, Mumbai- 400 076, India.

### ABSTRACT:

In the present investigation, titanium nitrides were synthesized by the direct reaction (nitridation) of titanium powder compacts with nitrogen. The gas-solid reaction under atmospheric pressure between nitrogen and titanium powders has been studied with respect to the initial titanium powder particle size, nitridation temperature and soaking time. Titanium powders of average particle size of 8.8 $\mu$ m, 3.8 $\mu$ m and 62nm were used in the present investigation. The 8.8 $\mu$ m and 3.8 $\mu$ m Ti powders were as procured whereas the 62nm Ti powder was synthesized by the attrition milling of the 3.8 $\mu$ m Ti powder in argon atmosphere for 40 hrs. The titanium powders (of three different particle sizes) were then compacted at different compaction pressures to obtain approximately similar amount of porosity in all the compacts. The Ti compacts were then nitrided at four different temperatures in the range of 400°C-1000°C for different soaking times of 1, 30, 60, and 120 min in flowing nitrogen atmosphere. The initial Ti powders were characterized by SEM, TEM and XRD whereas the green and nitrided Ti compacts were characterized by SEM and XRD. The extent of nitridation has been derived from the % change in weight between the nitrided and green Ti compacts.

### INTRODUCTION:

Titanium Nitride possesses unique properties such as high strength at high temperatures, high hardness, high wear resistance, high chemical resistance, high thermal conductivity, low thermal expansion, high thermal shock resistance, and low density. Due to these properties it has found applications for cutting tools, tool coatings, solar-control films, and microelectronics applications [1,2].

The various methods employed for synthesizing titanium nitrides are:

- (1) Chemical vapour deposition: In which the reaction of titanium tetrachloride with a mixture of hydrogen and nitrogen is used to deposit thin coatings of titanium nitride on substrates heated to > 1000°C.
- (2) Nitridation of titanium hydride: Here high purity titanium nitride is produced from the reaction of titanium hydride with ammonia.
- (3) Carbothermal reduction of titanium oxide: Involves reduction of titanium oxide by heating with carbon powder in a nitrogen atmosphere which simultaneously nitrides the reaction product [3].
- (4) Mechanical alloying: This process involves the high - energy milling of titanium powder in nitrogen or ammonia atmosphere. Crystalline TiN is formed in-situ at ambient temperature from the solid state reaction [4,5].
- (5) Direct nitridation of titanium: This process involves the direct nitridation of titanium powder with nitrogen at elevated temperatures. The process takes place according to the following overall reaction:  $2\text{Ti(s)} + \text{N}_2\text{(g)} \rightarrow 2\text{TiN(s)}$ .

The chemical vapour deposition and nitridation of titanium hydride processes involve high production costs and toxic raw materials [1]. The carbothermal reduction process leads to titanium nitride of low purity [3]. Mechanical alloying leads to contamination from wear of the milling media and also increases the cost of the material due to the low energy efficiency

of the high energy milling process [4,5]. The direct nitridation of titanium is an attractive route because of the simplicity of the process and because no side products are produced in the process [1].

Previous reports have focused on the kinetics of the direct nitridation reaction [1], morphological study of the directly nitrided pellets [6], modeling of the direct nitridation reaction [7] and on the nitridation reaction during sintering of micron sized and nano sized titanium powder [8]. In the present investigation an attempt has been made to study the gas-solid reaction under atmospheric pressure between nitrogen and titanium powders with respect to the initial titanium particle size, nitridation temperature and soaking time.

#### EXPERIMENTAL:

Titanium powders of average particle size of 8.8  $\mu\text{m}$ , 3.8  $\mu\text{m}$  and 62 nm were used in the present experiment. The 8.8  $\mu\text{m}$  and 3.8  $\mu\text{m}$  Ti powders were as procured whereas the 62 nm was produced by the attrition milling of the 3.8  $\mu\text{m}$  Ti powder. In the attrition milling, stearic acid was used as the process-controlling agent while high purity argon gas was used as the milling atmosphere. Nano sized Ti powder (avg. particle size 62 nm) was obtained after 40 hrs of milling.

The attrition mill used for milling consists of a double-jacketed stainless steel cylinder with cooling arrangement and equipped with double ball bearing and oil sealing. The speed of mill is automatically controlled by using a microprocessor-based circuit. Hardened steel balls of 8 mm diameter were used as milling media. The ratio of weight of charge to grinding media was kept at 1:10. Attrition milling was carried out at around 400 rpm at room temperature.

Table 1: Values of parameters / variables.

Sr. no.	Parameters / Variables	Value
1.	Gas flow rate ( $\text{m}^3 / \text{s}$ )	$65.5 \times 10^{-5}$
2.	Titanium grain size ( $\mu\text{m}$ )	8.8, 3.8 and 0.062
3.	Porosity (%)	20 - 26
4.	Compaction pressure (MPa) (for 8.8 $\mu\text{m}$ 3.8 $\mu\text{m}$ and 62nm)	109, 435, 652
5.	Nitridation temperature ( $^{\circ}\text{C}$ )	400, 600, 800, 1000.
6.	Soaking time (min)	1, 30, 60, 120
7.	Heating rate ( $^{\circ}\text{C} / \text{min}$ )	20

The values of the parameters / variables used in the present investigation are given in table 1. The Ti powders of varying particle size i.e. 8.8 $\mu\text{m}$ , 3.8 $\mu\text{m}$  and 62 nm were compacted at different pressures of 109 MPa, 435 MPa, 652 MPa respectively so as to obtain similar levels of porosity in the range of 20-26% in each compact. The compacts of varying particle size were then nitrided at different temperatures of 400, 600, 800 and 1000 $^{\circ}\text{C}$  for different soaking intervals of 1, 30, 60 and 120 min. The furnace was first evacuated to a pressure of  $10^{-3}$  torr after which the nitrogen gas was back filled in the furnace. This procedure was repeated twice before starting the experiment. A constant heating rate of 20 $^{\circ}\text{C}/\text{min}$  was used while heating to the nitridation temperature. Nitridation was carried out in flowing nitrogen (constant flow rate of  $65.5 \times 10^{-6}$ ). The nitrided compacts were then analyzed for change in weight and dimensions.



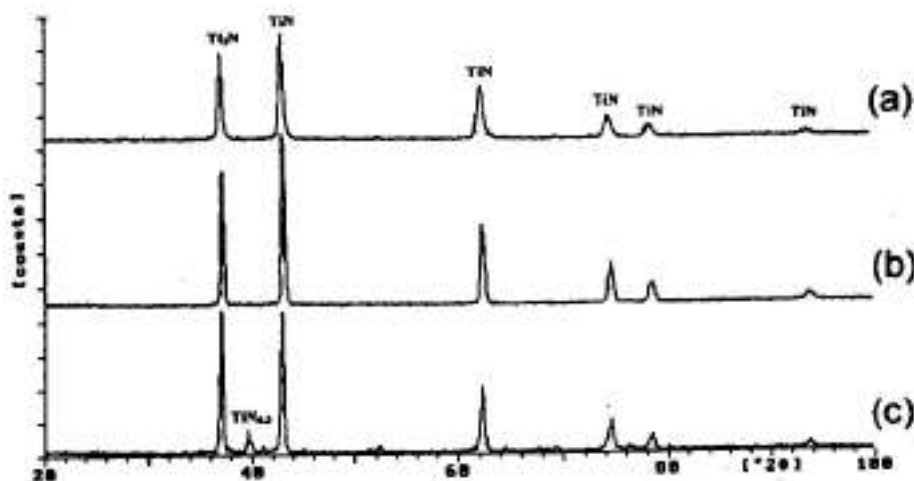


Figure 1: XRD patterns of the (a) 62nm, (b) 3.8 $\mu$ m, and (c) 8.8  $\mu$ m Ti powder nitrided at 1000°C for 30 min.

#### RESULTS AND DISCUSSION:

The particle size of the as procured Ti powder i.e. Ti powders of particle size 3.8 $\mu$ m and 8.8 $\mu$ m were measured by scanning electron microscopy (SEM) whereas the particle size of the attrition milled Ti powder i.e. 62 nm Ti powder was measured by transmission electron microscopy (TEM). The measured particle size is the average of at least 20 readings. The Ti powders of different particle sizes were subjected to X-ray diffraction (XRD) analysis and revealed that titanium was in  $\alpha$  form and no other peak (corresponding to any titanium oxide or nitride) was observed.

Figure 1 shows the XRD pattern of the (a) 62nm, (b) 3.8 $\mu$ m, and (c) 8.8  $\mu$ m Ti powder nitrided at 1000°C for 30 min. The XRD patterns reveal the formation of TiN, Ti<sub>2</sub>N and TiN<sub>0.5</sub> nitride phases at the surface of the nitrided compacts. The absence of the  $\alpha$ Ti phase in the XRD pattern indicates the complete transformation of titanium into titanium nitrides at the surface of the nitrided compacts. Figure 2. shows the SEM photographs of the green compacts of the (a) 62 nm, (b) 3.8 $\mu$ m and (c) 8.8  $\mu$ m Ti powder and the nitrided compacts of the (d) 62 nm, (e) 3.8 $\mu$ m and (f) 8.8  $\mu$ m Ti powder. All the green compacts show approximately a porosity level of 25%. The pores in the green compact of 62 nm powder are smaller and more in number than those in the green compact of 3.8 $\mu$ m powder which in turn are smaller and more in number than those in the green compact of 8.8 $\mu$ m powder. The total open pore area is the same for all the green compacts. The nitrided compacts show nearly the same level of porosity after the nitridation. The particles in the nitrided compacts show a white nitrided layer around the particle boundary.

Figure 3(a)-3(d) show the % change in weight as a function of nitridation temperature for different soaking times of 1,30, 60 and 120 min. From the figures it is clearly seen that the extent of nitridation (as derived from the % change in weight) increases with the nitridation temperature.



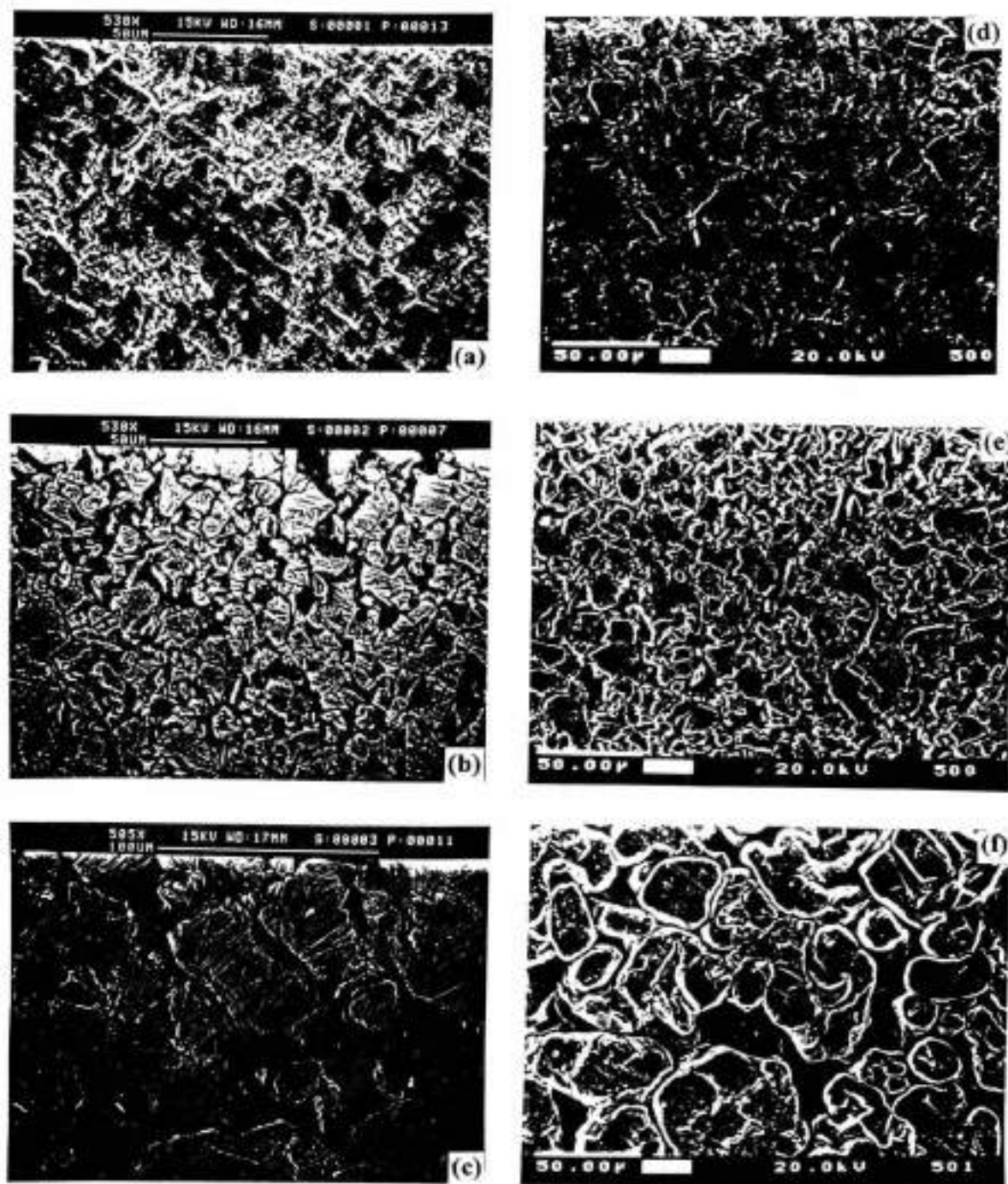
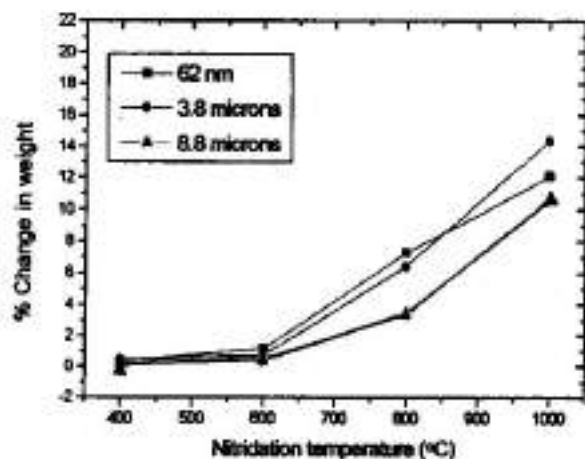
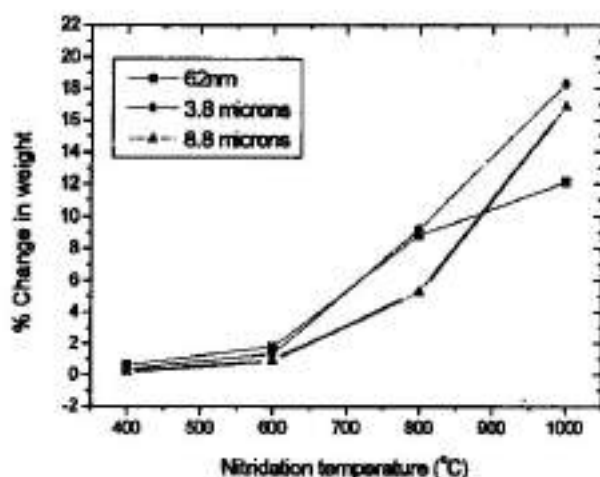


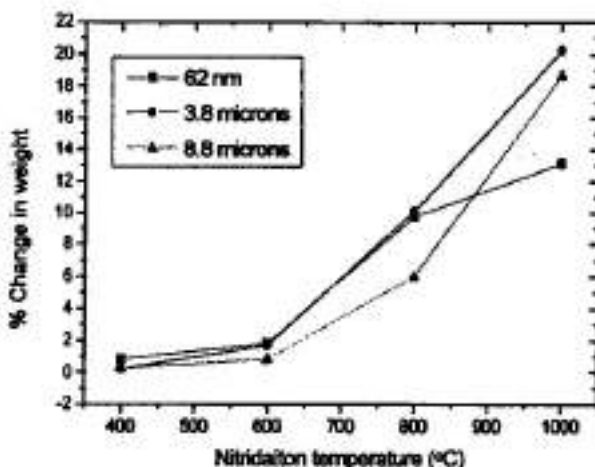
Figure 2. SEM photographs of the green compacts of the (a) 62 nm, (b) 3.8 μm and (c) 8.8 μm Ti powder and the nitrified compacts of the (d) 62 nm, (e) 3.8 μm and (f) 8.8 μm Ti powder.



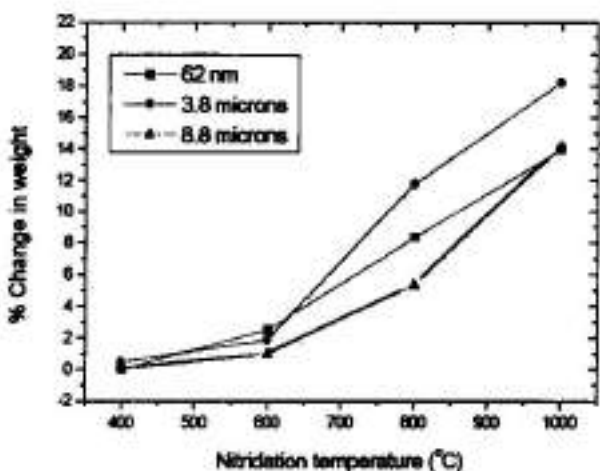
(a)



(b)

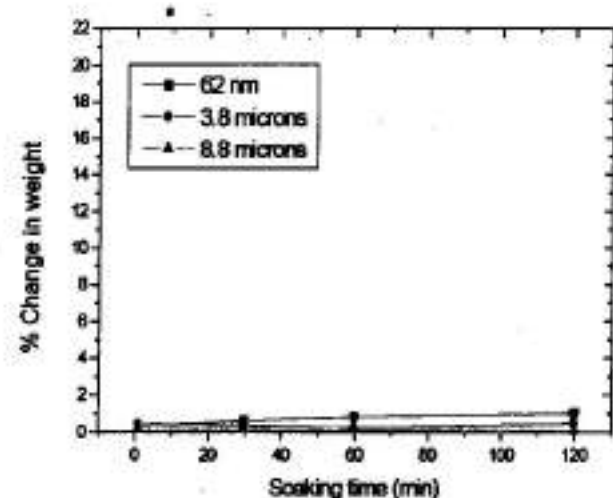


(c)

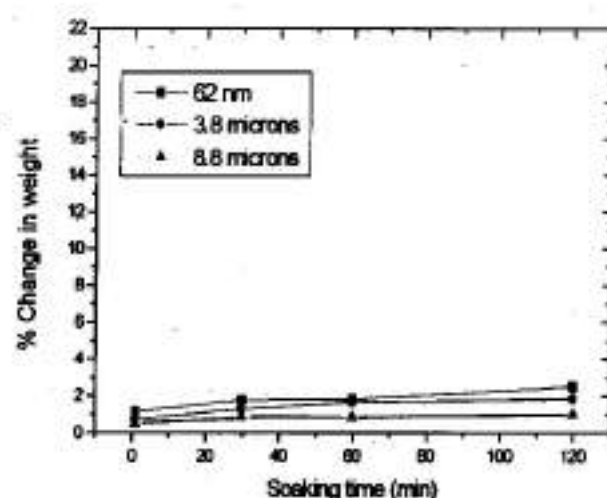


(d)

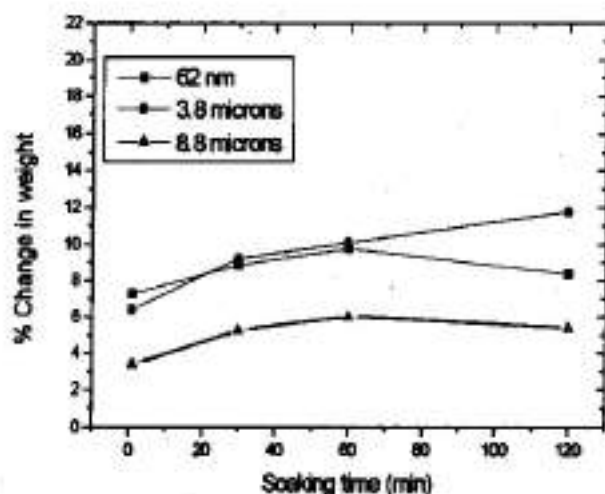
Figure 3: % Change in weight as a function of nitridation temperature for soaking time of (a) 1 min, (b) 30 min, (c) 60 min, and (d) 120 min.



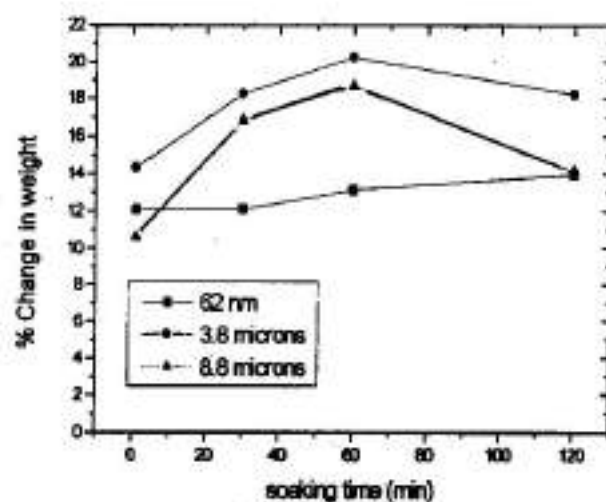
(a)



(b)

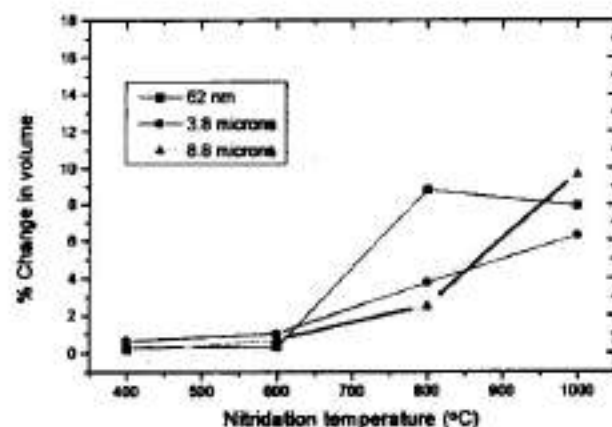


(c)

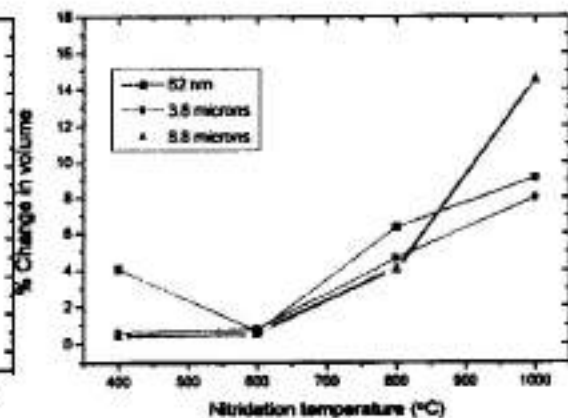


(d)

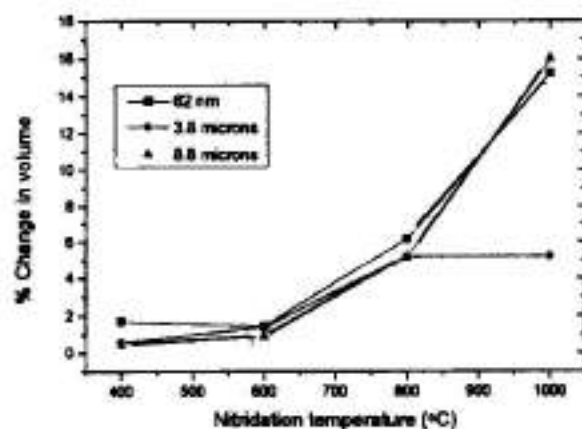
Figure 4: % Change in weight as a function of soaking time for samples nitrided at (a) 400 °C, (b) 600 °C, (c) 800 °C, and (d) 1000 °C.



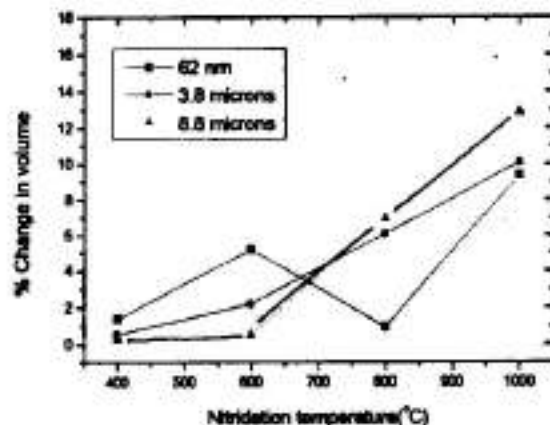
(a)



(b)



(c)



(d)

Figure .5: % Change in volume as a function of nitridation temperature for soaking time of (a) 1 min, (b) 30 min, (c) 60 min, and (d) 120 min.

In general it is observed that at lower nitridation temperatures (400°C-600°C) the extent of nitridation is more for the 62 nm Ti powder compacts which is not the case at higher nitridation temperatures (800°C-1000°C). The larger extent of nitridation for the 62 nm Ti powder compacts at lower nitridation temperatures can be attributed to the larger surface area of the 62 nm Ti powder which leads to larger amount of nitridation. The 62 nm Ti powder due to their larger surface area form a nitride layer at the initial stages which hinders further nitridation at the later stages. This can be one reason why the extent of nitridation is lower for the 62 nm Ti powder at higher nitridation temperatures. At higher nitridation temperatures (800°C-1000°C) the 3.8µm Ti powder compacts show a larger extent of nitridation than the 62 nm Ti powder compacts and the 8.8µm Ti powder compacts. The larger extent of nitridation of the 3.8µm Ti powder compared to the 8.8µm Ti powder can be attributed to the larger surface area of the 3.8µm Ti powder. A powder compact of fine particles will have a larger number of open pores compared to a powder compact of coarse particles with similar porosity level. But the diameter of the pores in the compact of fine particles will be far smaller than the diameter of the open pores in a compact of coarse particles. When such two compacts react with a gas, they will form a product, which will tend to close the open pores, which will restrict the gas to penetrate the compact leading to a restriction to the reaction between the compact and the gas. This will take place earlier in compacts with finer particle size, which have open pores of smaller diameters. This can be another reason why at higher nitridation temperatures the extent of nitridation was larger in the 3.8 µm Ti powder compacts as compared to the 62 nm Ti powder compacts.

Figure 4. show the % change in weight as a function of soaking time for samples nitrided in the temperature range of 400°C-1000°C. The figures indicate that in general the extent of nitridation (% change in weight) increases with the soaking time. It can again be seen here that at lower nitridation temperature (400-600°C) the extent of nitridation is more in the 62 nm Ti compacts whereas at higher nitridation temperature (800-1000°C) the extent of nitridation is more in the 3.8 µm and 8.8 µm Ti compacts.

Figure 5. show the % change in volume as a function of soaking temperature for different soaking times of 1,30,60 and 120 min. It can be seen that the % change in volume is positive, indicating an expansion in all the Ti powder compacts due to nitridation. The % change in volume increases with the nitridation temperature as well as the soaking time. A clear trend was not observed for the change in volume with respect to the Ti powder particle size.

The Arrhenius plots, i.e.,  $\ln(w_f/w_i)$  as a function of  $1/T$  for Ti powders of various particle sizes of 62 nm, 3.8 µm and 8.8 µm were plotted to calculate the activation energy. The activation energies for nitridation was calculated from the graphs which were 1.30 KJ/mol, 1.44 KJ/mol and 1.04 KJ/mol for the Ti powder compacts of particle sizes of 62 nm, 3.8 µm and 8.8 µm respectively. The obtained activation energies are less than those reported in literature i.e. 52.10 KJ/mol and 68.99 KJ/mol [9]. It can be seen that the activation energy of nitridation was larger for Ti powder of particle size 3.8 µm followed by Ti powder of particle size 62 nm and the least for Ti powder of particle size 8.8 µm. One would expect that the Ti powder of particle size of 62 nm would exhibit the largest activation energy but this was not the case. This may be due to the closure of the open pores (smaller in size than those in the 3.8µm and 8.8µm Ti powder) which restrict further nitridation in the 62 nm Ti powder compacts.

## CONCLUSION

- (1) XRD analysis confirmed the formation of nitrides such as TiN, Ti<sub>2</sub>N and TiN<sub>0.3</sub> whereas the SEM of the nitrided compacts revealed nitrides in the form of white layer around the particle boundary.
- (2) The extent of nitridation (% change in weight) was found to increase with the nitridation temperature. At lower nitridation temperature (400-600°C) the extent of nitridation was larger in the 62 nm Ti powder whereas at higher nitridation temperature (800-1000°C) the extent of nitridation was larger in the 3.8 µm Ti powder.
- (3) The extent of nitridation (as observed from the % change in weight) was also found to increase with the soaking time.
- (4) The % change in volume of the compacts due to nitridation was found to increase with the nitridation temperature. A clear trend was not observed for the change in volume with respect to initial Ti particle size.
- (5) The activation energy of nitridation was larger for Ti powder of particle size 3.8 µm i.e. 1.438 KJ/mol followed by Ti powder of particle size 62 nm i.e. 1.298 KJ/mol and the least for Ti powder of particle size 8.8 µm i.e. 1.038 KJ/mol.

## REFERENCES:

- (1) Ying-Hwa Hwang and Chun-I Lin, "Preparation of titanium nitride from direct nitridation of titanium," *Journal of Chemical Engineering of Japan*, Vol.31, No.2, pp. 214-219, (1998).
- (2) Shierif M. El-Eskandarany, Omari, M., Konno T.J., Sumiyama K., Hirai T. and Suzuki, K., "Synthesis of full-density nanocrystalline titanium nitride compacts by plasma-activated sintering of mechanically reacted powder", *Metallurgical and Materials Transactions A*, Vol. 29A, July 1998, pp.1973-1981, (1998).
- (3) G.V. White, K.J.D. Mackenzie and J.H Johnston, "Carbothermal synthesis of titanium nitride," *Journal of Materials Science*, 27, pp. 4287-4293, (1992).
- (4) Y.Ogino, T.Yamasaki, N. Atzumi and K. Yoshioka, "Nitriding of transition metal powders by ball milling in nitrogen gas, *Materials Transactions, JIM*, Vol.34, No.12, pp.1212 - 1216. (1993).
- (5) A.Calka and J.S. Williams, "Synthesis of nitrides by mechanical alloying," *Materials Science Forum*, Vols. 88-90, pp. 787-794, (1992).
- (6) Ching-Hua Meng, Chun-I Lin and Hsi-Kuei Chen, "Morphological Study on Direct Nitridation of Titanium Pellet," *Journal of Chemical Engineering of Japan*, Vol. 33, No.5, pp.808-810, (2000).
- (7) Ying-Hwa Hwang, Chun-I Lin and Hsi-Kuei Chen, "A Model for Direct Nitridation of Titanium Pellet," *J. Chin. Inst. Chem. Engrs.*, Vol. 29, No.3, pp. 201-209, (1998).
- (8) V.V Dabhade, M.M Godkhindi, T.R. Rama Mohan and P. Ramakrishnan, "Nitridation reaction during sintering of mechanically milled titanium powders," National Conference on Powder Metallurgy for the 21<sup>st</sup> century (NCPM), I.I.T Madras, (2000).
- (9) Ying-Hwa Hwang, Chun-I Lin and Hsi-Kuei Chen, "Determination of rate constants of the reaction between titanium pellet and nitrogen," *J. Chin. Inst. Chem Engrs.*, Vol. 29, No. 4, pp.257-263, (1998).



## **Si<sub>3</sub>N<sub>4</sub> Composite by insitu Foramtion of MoSi<sub>2</sub>**

**R.V.Krishnarao, J.Subrahmanyam and M.Srinivasarao**

Defence Metallurgical Research Laboratory,

Kanchanbagh, Hyderabad-500058 India

**Abstract:** MoSi<sub>2</sub> reinforced Si<sub>3</sub>N<sub>4</sub> matrix composite was fabricated by dry blending molybdenum powder and Si<sub>3</sub>N<sub>4</sub> powder, followed by vacuum hot-pressing in grafoil lined graphite die at 1675°C and 26MPa. Five weight percent MgO was used as densification aid for Si<sub>3</sub>N<sub>4</sub>. MoSi<sub>2</sub> was formed by reaction between Mo and Si<sub>3</sub>N<sub>4</sub>. The composite contained about 40 volume percent of MoSi<sub>2</sub>. The MoSi<sub>2</sub> particles were well distributed within the dense Si<sub>3</sub>N<sub>4</sub> matrix. No extraneous reaction phases associated with MgO densification aid were detected by X-ray diffraction and electron probe micro analysis. The composite achieved a hot-pressed density of 97.9% theoretical. Vickers micro hardness indentation testing was carried out to investigate micro hardness and indentation fracture toughness. An average room-temperature indentation fracture toughness of 7MPa.m<sup>1/2</sup> was achieved. Crack morphology of indentation cracks revealed the occurrence of both transphase fracture of the MoSi<sub>2</sub> as well as interphase fracture along the MoSi<sub>2</sub>-Si<sub>3</sub>N<sub>4</sub> phase boundaries. [key words: MoSi<sub>2</sub>, Si<sub>3</sub>N<sub>4</sub>, composite, synthesis, processing]

### **1. Introduction**

Silicon nitride (Si<sub>3</sub>N<sub>4</sub>) is an important structural ceramic material because of its attractive combination of properties: low density, high strength, low thermal co-efficient of expansion, high temperature refractoriness, high temperature oxidation resistance and good creep resistance. However, the wide spread use of Si<sub>3</sub>N<sub>4</sub> is hindered because of its brittle behavior and low fracture toughness in comparison to metals. The second and the most important factor is the cost of machining. Since Si<sub>3</sub>N<sub>4</sub> is an electrical insulator and a hard material, diamond machining is typically required and limits the complexity of machined shapes. Even with near-net shape fabrication methods for Si<sub>3</sub>N<sub>4</sub> components, some final diamond machining is usually required. In an attempt to decrease the cost of machining electrically conductive Si<sub>3</sub>N<sub>4</sub> composites were fabricated by introducing TiN or TiB<sub>2</sub> phases in the matrix [1,2].

Intermetallic compound MoSi<sub>2</sub> has long been known as a high temperature material that has excellent oxidation resistance and electrical/thermal conductivity, low cost, high melting point (2023°C), relatively low density (6.2 g Cm<sup>-3</sup>). Its ease of machining, makes it an attractive structural material. MoSi<sub>2</sub> is thermodynamically stable with structural ceramics SiC and Si<sub>3</sub>N<sub>4</sub> at elevated temperatures. The addition of MoSi<sub>2</sub> phase to a Si<sub>3</sub>N<sub>4</sub> matrix has the potential to produce composites with both improved fracture toughness and improved machinability, as well as improved oxidation resistance [3].

The composite containing both MoSi<sub>2</sub> and Si<sub>3</sub>N<sub>4</sub> is an interesting and important system [4]. Hebsur *et al* [5-8] have studied MoSi<sub>2</sub> matrix Si<sub>3</sub>N<sub>4</sub> reinforced composites. They observed that Si<sub>3</sub>N<sub>4</sub> additions to MoSi<sub>2</sub> completely eliminate the pest oxidation behavior of MoSi<sub>2</sub>. The fracture toughness of the composite containing 30-50 vol.% Si<sub>3</sub>N<sub>4</sub> phase increases significantly with increasing temperature, reaching values as high as 15 MPa m<sup>1/2</sup> at 1300°C. Si<sub>3</sub>N<sub>4</sub> matrix MoSi<sub>2</sub> reinforced composites have been investigated by Petrovic *et al* [9]. MoSi<sub>2</sub> additions significantly increase the fracture toughness of Si<sub>3</sub>N<sub>4</sub>, with a maximum room temperature



toughness of  $8.5 \text{ MPa m}^{1/2}$  observed with a 40 vol.%  $\text{MoSi}_2$  addition [10]. The creep resistance of composite is similar to that of pure  $\text{Si}_3\text{N}_4$  for fine  $\text{MoSi}_2$  particulate additions. Importantly, composites containing greater than 30 vol.%  $\text{MoSi}_2$  phase can be electro discharge machined [11]. Petrovic *et al* [9,10] used  $\text{MoSi}_2$  and  $\text{Si}_3\text{N}_4$  powders with or without  $\text{MgO}$  densification aid. Zhang *et al* [12,13] prepared  $\text{Si}_3\text{N}_4$ - $\text{MoSi}_2$  composite by reaction bonding of (Si-Mo) powder compacts in  $\text{N}_2 + \text{H}_2$  atmosphere.

$\text{Si}_3\text{N}_4$  reacts with Mo to form  $\text{MoSi}_2$ ,  $\text{Mo}_3\text{Si}_2$  and  $\text{Mo}_5\text{Si}_3$  [14]. Krishnarao *et al* [15-18] studied the formation of  $\text{MoSi}_2$ -SiC/ $\text{Si}_3\text{N}_4$  composites by reacting Mo powder with  $\text{Si}_3\text{N}_4$  powder. In the present investigation  $\text{MoSi}_2$  is formed within  $\text{Si}_3\text{N}_4$  matrix by reaction of (Mo+ $\text{Si}_3\text{N}_4$ ) and the mechanical properties of the composites are studied.  $\text{MgO}$  sintering aid was used for densification of  $\text{Si}_3\text{N}_4$ .



## 2. Materials

Mo powder was supplied by New Metals and Chemicals Ltd., Essex, U.K..  $\text{Si}_3\text{N}_4$  powder of grade LC12, was obtained from H.C.Starck, Germany.  $\text{MgO}$  was supplied by Loba Chemie, Mumbai, India.

## 3. Experimental

Molybdenum and  $\text{Si}_3\text{N}_4$  powders were taken in a molar ratio of (1:1). The mixture of powders was prepared by dry ball milling for 50h. Plastic containers and  $\text{Al}_2\text{O}_3$  grinding media were used. The mixture of powder was vacuum hot pressed using grafoil-lined graphite dies. The hot pressing was carried out at a temperature of 1600, 1630, and  $1650^\circ\text{C}/2\text{h}$ , and pressure of 26 MPa. The densities of the hot pressed billets were 85-88% of theoretical density. Then 5 wt% of  $\text{MgO}$  sintering additive for  $\text{Si}_3\text{N}_4$  was added to the initial powder mixture and ball milling was continued for another 40h. The powder mixture was vacuum hot pressed using grafoil-lined graphite dies at a temperature of  $1675^\circ\text{C}/2\text{h}$ , and pressure of 26 MPa. The hot pressed disc was 75 mm in diameter and 8mm thick. This sample was used for further investigation in the present work.

A piece of hot pressed billet was ground in an agate mortar and analysed by X-ray diffraction (XRD). A Philips X-ray diffractometer, Model PW3710, with  $\text{Cu K}_\alpha$  radiation through Ni filter was used. The microstructure, morphology and indentation crack path of the composite billet was examined with a Leo 440i, SEM and an optical microscope. Scanning Electron Probe Microanalysis (SEPM) was carried out with CAMECA (model CAMEBAX-MICRO, France) equipment. An elastosonic tester was used to determine the Young's modulus of the sample.

Vickers microhardness indentation test was used to investigate microhardness and indentation fracture toughness of the composite. A 30 kg indentation load was selected so that the indentation size would be large with respect to the two phase micro structural features. Indentation work was carried out at room temperature. Indentation fracture toughness measurements were made using the equation proposed by Anstis *et al* [19] for median cracks. The expression for indentation fracture toughness according to Anstis *et al* is:

$$K_{\text{IQ}} = 0.016.(E/H)^{1/2}.P/c^{3/2}$$

Where E is the Young's modulus, H is the hardness, c is the crack length and P is the indentation load applied. A number of Vickers indentations were used for the measurement of fracture toughness.

#### 4. Results and Discussion

XRD analysis revealed the presence of  $\text{MoSi}_2$  and  $\text{Si}_3\text{N}_4$  phases in the hot pressed billet. Neither lower silicides of molybdenum nor phases associated with  $\text{MgO}$  sintering additive were observed in XRD pattern. Schuster [20] showed that in the absence of external nitrogen pressure,  $\text{Si}_3\text{N}_4$  co-exist with  $\text{MoSi}_2$  and  $\text{Mo}_5\text{Si}_3$  but not  $\text{Mo}_5\text{Si}$  and  $\text{Mo}$ . The density of hot pressed billet was measured by water displacement method. The composite achieved a hot pressed average density of  $4.27 \text{ g.cm}^{-3}$ . The BSE image of the composite is shown in Fig. 1(a). The in situ formed  $\text{MoSi}_2$  is well distributed in the  $\text{Si}_3\text{N}_4$  matrix. The average particle size of  $\text{MoSi}_2$  could be  $10 \mu\text{m}$ .

The vol.% of  $\text{MoSi}_2$  phase was determined to be 40%. From rule of mixtures the above measured density was corresponding to 97.9% theoretical density. According to reaction (1) the sintered billet should contain 63 vol.% of  $\text{MoSi}_2$  and 37 vol.% of  $\text{Si}_3\text{N}_4$ . After hot pressing a weight loss of  $(194-148.45=45.55\text{g})$  was observed. This could be due to the volatilisation of  $\text{Mo}$  as  $\text{MoO}_3$  under experimental conditions of vacuum hot pressing.

The SEM micrograph of the hot pressed billet is shown in Fig. 1(b). The inter face of  $\text{MoSi}_2$ - $\text{Si}_3\text{N}_4$  is very clean. No precipitates or reaction phases were observed in  $\text{Si}_3\text{N}_4$  matrix. Results of the EPMA analysis are shown Fig. 2. The magnesium X-ray map clearly shows that  $\text{MgO}$  is present with in  $\text{Si}_3\text{N}_4$  matrix. No reaction of  $\text{MoSi}_2$  with  $\text{MgO}$  or  $\text{Si}_3\text{N}_4$  was observed. An average value of vickers hardness was found to be 14.53 GPa. The Young's modulus (365GPa) of the composite was determined by an elastosonic tester. The room temperature Indentation fracture toughness of the  $\text{Si}_3\text{N}_4$ - $\text{MoSi}_2$  composite was determined according to Anstis *et al* [19]. An average indentation fracture toughness value of  $7 \text{ MPa m}^{1/2}$  was obtained.

The optical photomicrograph of the vickers indentation is shown Fig. 3. This micrograph show that the fracture morphology involved both transphase fracture of the  $\text{MoSi}_2$  (Fig. 3(a)) as well as interphase fracture along the  $\text{MoSi}_2$ - $\text{Si}_3\text{N}_4$  phase boundaries. The crack propagation through the interface of  $\text{MoSi}_2$ - $\text{Si}_3\text{N}_4$  is clearly shown in Fig. 3(b).

Petrovic *et al* [10] studied the mechanical behaviour of  $\text{Si}_3\text{N}_4$ - $\text{MoSi}_2$  composites. They studied the effect of  $\text{MgO}$  content and  $\text{MoSi}_2$  particle size on hardness and indentation fracture toughness. Increased  $\text{MgO}$  levels were shown to be deleterious to mechanical properties of composites. On comparing with literature data (40 vol.% of  $10 \mu\text{m}$  size  $\text{MoSi}_2$  particle reinforced  $\text{Si}_3\text{N}_4$  composite with 5 wt%  $\text{MgO}$  [10]), the room temperature hardness (14.53GPa) in the present work is higher than that reported in literature ( $\approx 12 \text{ GPa}$ ). Similarly the room temperature indentation fracture toughness value ( $7 \text{ MPa m}^{1/2}$ ) in the present work is higher than that ( $\approx 6 \text{ MPa m}^{1/2}$ ) reported by Petrovic *et al* [10]. This could be due to the in situ formation of  $\text{MoSi}_2$  in the  $\text{Si}_3\text{N}_4$  matrix during sintering. This work demonstrated the possibility of fabrication of  $\text{MoSi}_2$  reinforced  $\text{Si}_3\text{N}_4$  composites by in situ formation of  $\text{MoSi}_2$ .

#### 5. Conclusions

- (i)  $\text{MoSi}_2$  reinforced  $\text{Si}_3\text{N}_4$  matrix composite was fabricated by reactive hot pressing of molybdenum and  $\text{Si}_3\text{N}_4$  powders in molar ratio of 1:1.
- (ii) About 40 vol% of  $\text{MoSi}_2$  has formed in situ in  $\text{Si}_3\text{N}_4$  matrix by reaction between  $\text{Mo}$  and  $\text{Si}_3\text{N}_4$ . No extraneous reaction phases associated with  $\text{MgO}$  sintering additive were detected by X-ray diffraction and electron probe micro analysis
- (iii) The in situ formed  $\text{MoSi}_2$  particles were well distributed within the dense  $\text{Si}_3\text{N}_4$  matrix and the composite achieved a hot-pressed density of 97.9% theoretical.
- (iv) A vickers micro hardness of 14.53GPa and an average room-temperature indentation fracture toughness of  $7 \text{ MPa.m}^{1/2}$  were achieved.

- (v) Crack morphology of indentation cracks revealed the occurrence of both transphase fracture of the  $\text{MoSi}_2$  as well as interphase fracture along the  $\text{MoSi}_2$ - $\text{Si}_3\text{N}_4$  phase boundaries.

### Acknowledgements

The authors thankfully acknowledge the financial support received from the Defence Research & Development Organisation, Govt. of India in order to carry out the present research study.

### References

1. A. Bellosi, A. Fiegna, A. Giachello, and P. Demaestri, *Advanced Structural Inorganic Composites*, Elsevier, Amsterdam, pp 225-234 (1991).
2. A. Tampieri, A. bellosi, and V. Biasini, *Advanced Structural Inorganic Composites*, Elsevier, Amsterdam, pp409-420 (1991).
3. J.J. Petrovic, M.I. Pena, and H. Harriet Kung, "Fabrication and Microstructures of  $\text{MoSi}_2$  reinforced- $\text{Si}_3\text{N}_4$  Matrix Composites", *J.Am.Ceram.Soc.* Vol.80 pp1111-1116 (1997).
4. J.J. Petrovic, and A.K. Vasudevan, "Key Developments in high Temperature Structural Silicides", *Mater.Sci.Eng. A*, Vol.261, pp1-5 (1999).
5. M.G. Hebsur, "Pest Resistant and Low CTE  $\text{MoSi}_2$  Matrix for High temperature Structural Applications", *Mat.Res.Soc.Symp.Proc.*, Vol.350, pp177-182 (1994).
6. M.G. Hebsur, and M.V. Nathal, "Strong, Tough, and Pest resistant  $\text{MoSi}_2$  -base Hybrid composite for Structural applications", *Structural Intermetallics 1997*, The Minerals, Metals & Materials Society, pp949-957 (1997).
7. R.W. Kowalik, M.G. Hebsur, "Cyclic Oxidation study of  $\text{MoSi}_2$ - $\text{Si}_3\text{N}_4$  base Composites", *Mater.Sci.Eng. A*, Vol.261, pp300-303 (1999).
8. M.G. Hebsur, "Development and Characterization of  $\text{SiC}_{10}/\text{MoSi}_2$ - $\text{Si}_3\text{N}_{4.99}$  Hybrid Composites", *Mater.Sci.Eng. A*, Vol.261, pp24-37 (1999).
9. J.J. Petrovic, R.E. Honnell, "MoSi<sub>2</sub> particle Reinforced-SiC and Si<sub>3</sub>N<sub>4</sub> Matrix Composites", *J.Mater.Sci.Lett.*, Vol.9, pp1083-1084 (1990).
10. J.J. Petrovic, M.I. Pena, I.E. Reimanis, M.S. Sandlin, S.D. Conzane, H. Harriet Kung, and D.P. Butt, "Mechanical Behavior of  $\text{MoSi}_2$  Reinforced - $\text{Si}_3\text{N}_4$  Matrix Composites", *J.Am.Ceram.Soc.* Vol.80 pp3070-3076 (1997).
11. K. Yamada, N. Kamiya, "High temperature Mechanical Properties of  $\text{Si}_3\text{N}_4$  - $\text{MoSi}_2$  and  $\text{Si}_3\text{N}_4$  -SiC composites with network structures of second phases", *Mater.Sci.Eng. A*, Vol.261, pp270-277 (1999).
12. B.R. Zhang, F. Marino, "Reaction Bonding Preparation of  $\text{Si}_3\text{N}_4$  /  $\text{MoSi}_2$  and  $\text{Si}_3\text{N}_4$  /  $\text{WSi}_2$  Composites from Elemental Powders", *J.Am.Ceram.Soc.* Vol.80 pp269-272 (1996).
13. B.R. Zhang, F. Marino, V.M. Sglavo, S. Gialanella, "Insitu Formation and High-temperature Reinforcing Effect of  $\text{MoSi}_2$  and  $\text{WSi}_2$  on Reaction-bonded  $\text{Si}_3\text{N}_4$ ", *Mater.Sci.Eng. A*, Vol.261, pp503-506 (1999).
14. E. Heikinheimo, A. Kodentsov, J. A. Van Beek, J. T. Klomp and F. J. J. Van Loo, *Acta Metall.Mater.* Vol.40 ppS111-119 (1992).
15. R.V. Krishnarao, Y.R. Mahajan, "Studies on the Formation of  $\text{MoSi}_2$ -SiC through reaction of  $\text{Si}_3\text{N}_4$  with Molybdenum and Carbon", *Mater. Sci. and Engng. A*, Vol.214 pp161-166 (1996).
16. R.V. Krishnarao, Y.R. Mahajan, "Synthesis of Molybdenum Silicide-SiC composite powder by reacting silica with Molybdenum and Carbon", *J. Mater.Synth. Process.* Vol.4 pp89-96 (1996).
17. R.V. Krishnarao, Y. R. Mahajan, "Synthesis of  $\text{MoSi}_2$ -SiC Composite Powder by reacting  $\text{Si}_3\text{N}_4$  with Molybdenum and Carbon", *J. Mater. Sci. Lett.* Vol.16 pp350-353 (1997).
18. R.V. Krishnarao, V.V. Ramarao, and Y.R. Mahajan, "Insitu formation of  $\text{MoSi}_2$  -SiC through reaction of  $\text{SiO}_2$  or  $\text{Si}_3\text{N}_4$  with Mo and Carbon", *J. Mater. Res.* Vol.12 pp3322-3327 (1997).
19. G.R. Anstis, P. Chantilul, B.R. Lawn, D.B. Marshall, "A Critical Evaluation of Indentation Technique for Measuring Fracture Toughness: Direct Crack measurement", *J.Am.Ceram.Soc.* Vol.64 pp533-538 (1981).
20. J.C. Schuster, "J.Mater.Sci.", Vol.23, pp2792-2796 (1988).

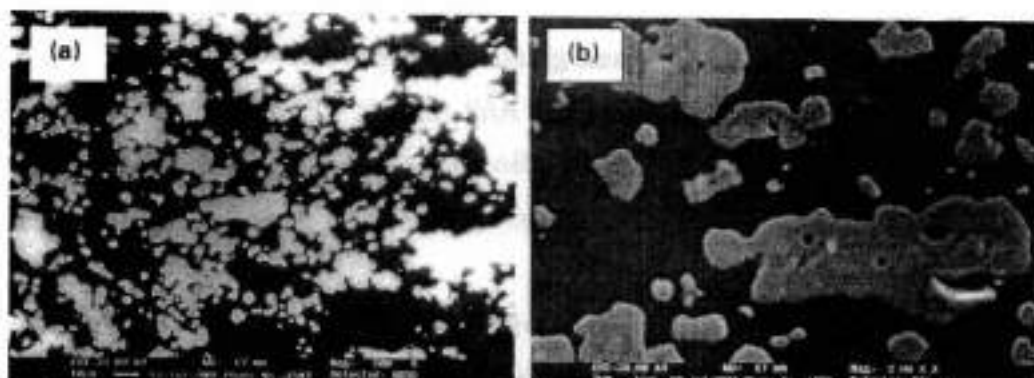


Figure. 1.  $\text{Si}_3\text{N}_4$ -insitu formed  $\text{MoSi}_2$  composite obtained by vacuum hot pressing at  $1675^\circ\text{C}/2\text{h}$ , and 26 MPa. (a) BSE image, 500X, and (b) SEM image, 2K X.

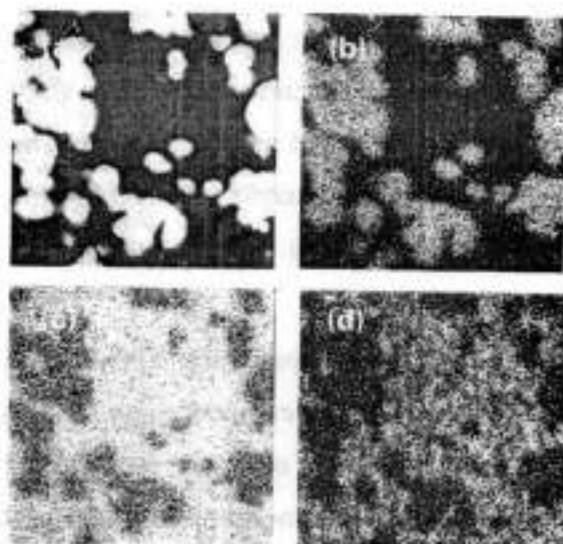


Figure. 2. EPMA of the  $\text{Si}_3\text{N}_4$ - $\text{MoSi}_2$  composite (a) BSE at 2K X, (b) Mo X-ray map, (c) Si X-ray map, and (d) Mg X-ray map



Figure. 3. Optical micrograph showing indentation cracks. (a) transphase fracture of  $\text{MoSi}_2$ , 200X, and (b) interphase ( $\text{MoSi}_2$ - $\text{Si}_3\text{N}_4$ ) fracture, 500X

## Synthesis of Silicon pentacoordinate complex as a precursor for processing glass and glass ceramics

G.V.Ramana Reddy, Debasis Bera, Anil Anal, B.T.Rao, T.R.Rama Mohan

IIT Bombay

### Abstract

Sodium pentacoordinated ethylene-glycolato-silicate ( $\text{Na}_2\text{Si}_2(\text{O}_2\text{C}_2\text{H}_4)_3$ ) has been synthesized using NaOH and silica-gel (1:1 mole) in excess ethylene glycol under nitrogen atmosphere with constant mechanical stirring and heating  $\sim 180^\circ\text{C}$  for 2hrs. Using this pentacoordinated silicon complex, bioglass composites and ceramers have been prepared. The bioglass has been prepared through sol-gel method, using pentacoordinated silicon complex as a precursor, as well as through dispersion method, where pentacoordinated complex was used as a dispersant. Then Bioglass composites have been made using polymethyl methacrylate (PMMA) through hot-pressing at a temperature  $\sim 130^\circ\text{C}$  at 100 MPa and 200 MPa. The modulus of rupture (MOR) of composites was evaluated.

Two types of ceramer have been prepared using pentacoordinated silicon complex and polymethyl methacrylate (PMMA); One was through physical mixing route, which contained only silica (free from NaCl) and other one was through solution route which contained both silica and NaCl. These ceramer powders were processed into rectangular specimens by hot-pressing. An increase in the density, glass transition temperature, MOR and the elastic modulus has been observed with increase in silica content in both ceramers.

**Key words:** *Pentacoordinate Silicon complex, bioglass, ceramer, bioactive glass composite, ( $\text{Na}_2\text{Si}_2(\text{O}_2\text{C}_2\text{H}_4)_3$ ).*

### Introduction:

Advanced materials have always played a vital role in the development of new technologies. The requirements of material properties have become more specific. It is difficult to find a naturally occurring material meeting all the requirements. As a result



There has been increasing interest in the development of new materials consisting of an organic polymer and a ceramic material [1]. The resulting new materials are as for example ceramers, composites. These materials exhibit some characteristics and properties of both ceramics (heat resistance, retention of mechanical properties at high temperatures and low thermal expansion) and organic polymers (e.g. toughness, ductility and processability).

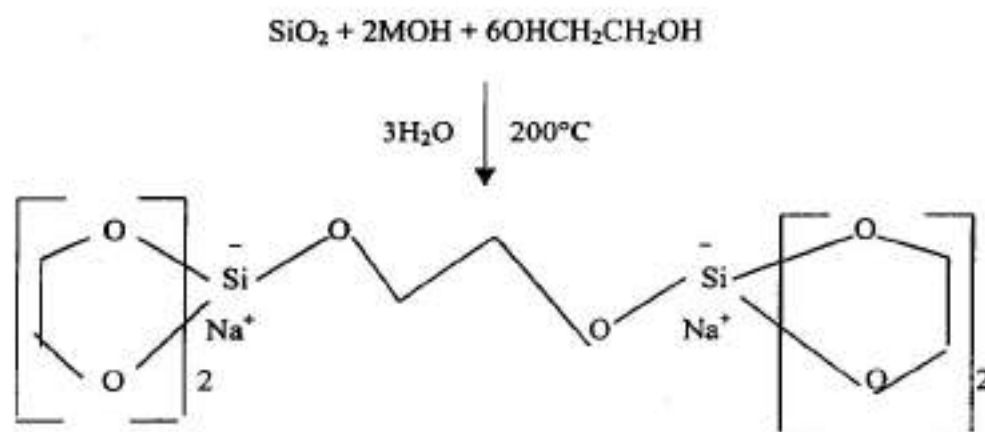
To prepare these types of compounds precursor is very important. In this present work pentacoordinated Silicon complex has been prepared to synthesize these types of materials. Two types of materials have been prepared using this complex: bioglass and ceramer. The bioglass later has been used to make composites.

Anionic pentacoordinated and dianionic hexacoordinated organosilicates were first reported more than 60 years ago. Pentacoordinate silicon complexes have recently received considerable attention because of their role in sol-gel processing of silicate glasses, their utility in organic synthesis and polymerisation, and their use as precursors to organosilicon compounds. Pentacoordinate silicates have been prepared from compounds with tetra substituted Si-centers by Fyre [2], Holmes et al [3,4] rather than directly from silica. R.M. Laine et al. [5] have described synthesis of Pentacoordinate silicon complex directly from  $\text{SiO}_2$  and ethylene glycol and base under controlled conditions. The same reaction was done under ambient conditions in our laboratory [6]. The resulting glycolato silicates are very reactive and offer unique opportunities for an inexpensive synthesis of a wide variety of silicon-containing compounds such as bioglasses, ceramers etc. Using this complex most bioactive bioglass [7] 45S5 bioglass has been made. The present studies aim at preparing a novel bioglass composites composed of polymethyl methacrylate (PMMA) and bioglass.

#### **Preparation of Pentacoordinated Silicon Complex:**

A mixture of 1:1 mole ratio of NaOH and  $\text{SiO}_2$  and excess of ethylene glycol in a flask was heated to  $-180^\circ\text{C}$  under  $\text{N}_2$  atmosphere with constant stirring. The silica and the alkali hydroxide readily dissolved with continuous distillation of ethylene glycol.

Water formed as a byproduct was removed out going  $N_2$  gas. When 60% of glycol had distilled off, the solution became increasingly viscous along with simultaneous precipitation. On cooling for about 12 hr, the large mass formed was broken up and the product (glycolato silicate) was filtered and stored in desiccators.



#### Characterization of the Complex:

The dried complex was characterized by using *XRD*, *DTA* and *FTIR*.

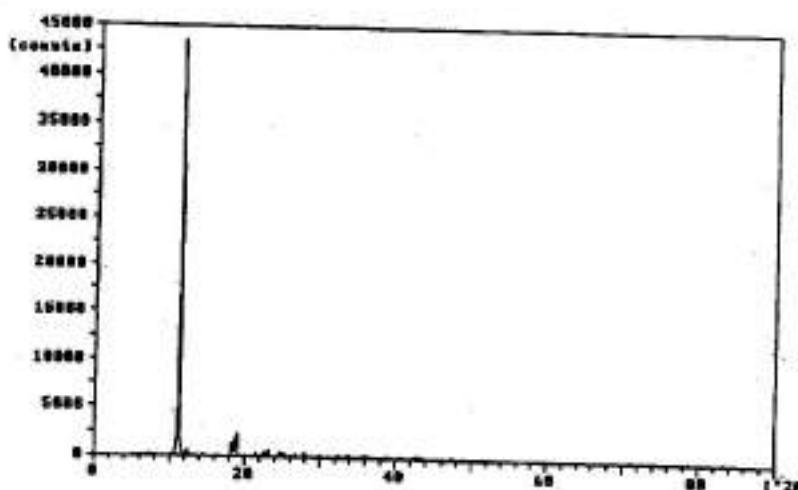


Fig-16 XRD pattern of pentacoordinate sodium ethylene glycolato silicate prepared under controlled conditions.

*Figure 1: XRD pattern of pentacoordinated silicon complex*



### 1. X-Ray Diffraction (XRD):

The precipitates were analyzed by X-ray diffractometer (PW 1820 PHILIPS, Netherlands) using Cu K $\alpha$  radiation. Figure 1 shows the XRD pattern of the sodium glycolato silicate. The crystalline nature of the complex is shown by the sharp peaks at  $2\theta=11^\circ$ ,  $18.8^\circ$ . The comparisons of d-values of this compound with literature values are shown in Table 1. The values exactly matched with previous studies conducted in our laboratory. Negligible deviation from the standard pattern given in literature shows the greater stability of the sodium glycolato silicate complex under ambient conditions.

Table 1: Comparison of d-values of experimental data with literature values

d-values		Relative intensities	
Exp. data	Literature	Exp. data	Literature
7.8936	8.1852	100	100
4.6811	4.7539	5.8	4.09
4.8295	4.8179	3.5	2.41
4.1183	4.0370	1.1	1.17

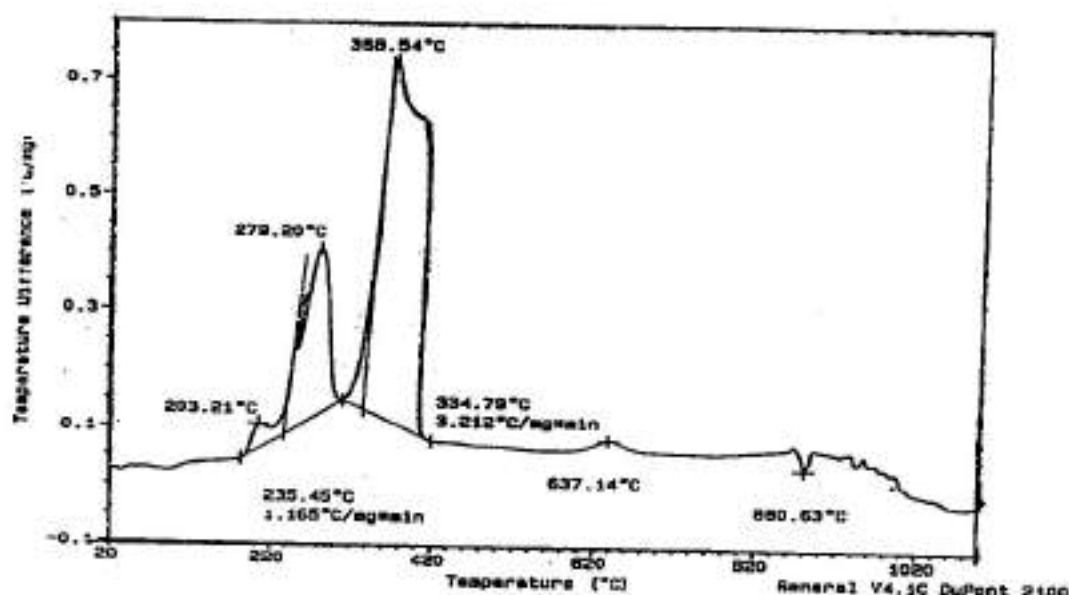


Figure 2: DTA of Pentacoordinated sodium ethylene glycolato silicate prepared under controlled condition.

### 2. Differential Thermal Analysis (DTA):

The DTA for this compound exhibited an exothermic peak at 368.54°C (365°C), which is mostly due to the oxidative removal of the glycolate ligands. The exothermic peak at the 637°C (660°C) is due to crystallization of  $\text{Na}_2\text{O} \cdot 2\text{SiO}_2$ . An endothermic peak at 880°C (875°C) results from melting of  $\text{Na}_2\text{Si}_2\text{O}_5$ . These observations are in agreement with standard values, which are shown in the brackets. The DTA curve is shown in *Figure 2*.

### 3. Fourier Transform Infrared Spectroscopy (FTIR):

FTIR spectrum is shown in *Figure 3*. The peaks in the  $\nu(\text{OH})$  ( $3200\text{--}3300\text{cm}^{-1}$ ) confirm the formation of ethylene glycol molecules by hydrolysis using moisture content in atmosphere. The crystalline dimer exhibits the  $\nu(\text{C-H})$  vibrations  $2800\text{--}3000\text{ cm}^{-1}$ . The peaks at  $\sim 1090\text{cm}^{-1}$  correspond to a combination of  $\nu(\text{Si-O})$  and  $\nu(\text{C-O})$  asymmetric vibrations.

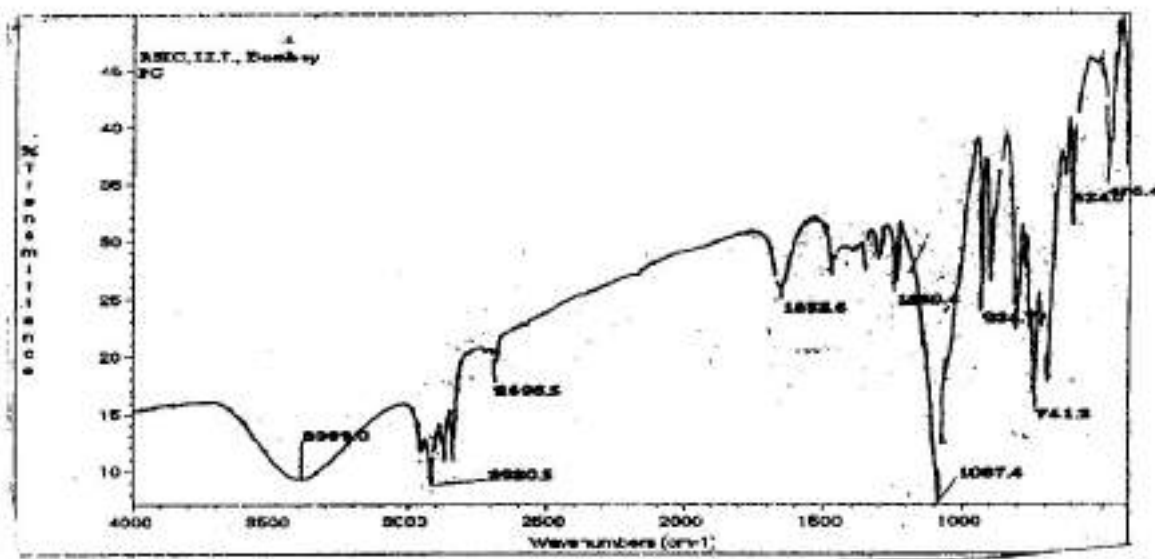


*Figure-3: FTIR of pentacoordinated ethylene glycolato silicate prepared under controlled condition.*

### Preparation of 45S5 Bioglass:

Preparation of 45S5 bioglass was carried out through two processes using pentacoordinated complex as a precursor. The weight percent of various constituents in the 45S5 bioglass is shown in *Table 1*.

**Table 1: Composition of 45S5 bioglass**

Composition	Percentage
SiO <sub>2</sub>	45%
CaO	24.5%
Na <sub>2</sub> O	24.5%
P <sub>2</sub> O <sub>5</sub>	6%

The two methods employed to synthesize bioglass were the sol-gel combined with dispersion method and sol-gel method.

#### 1. Sol-gel Combined with Dispersion Method:

*Table 2* gives the various constituents used for preparing 50g batch of bioglass.

**Table 2: Constituents required to make 50g bioglass**

Constituents	Amount
Sodium-pentacoordinate-ethylene-glycolato- silicate ( $(\text{Na}_2\text{Si}_2(\text{C}_{10}\text{H}_{16}\text{O}_{10}))$ )	70 g
Calcium Nitrate ( $\text{Ca}(\text{NO}_3)_2$ )	51.6 g
Ortho Phosphoric Acid ( $\text{H}_3\text{PO}_4$ )	2.07 ml

Initially aqueous solution of calcium nitrate was made in a beaker. Then 70g of pentacoordinate complex was taken in a sol-gel reactor. After that the aqueous solution of calcium nitrate was added slowly to the reactor with continuous stirring. Some amount of nitric acid was then added as a catalyst. and refluxing was done at  $\sim 90^\circ\text{C}$ - $100^\circ\text{C}$  for 2 hrs. The solution was kept undisturbed for overnight. The resulting precipitate was filtered, dried, and heated in an oven for 2hrs at  $150^\circ\text{C}$ .

## 2. Sol-gel Method:

The second batch of bioglass was prepared using exclusively the sol-gel route. For this 1:1 mole ratio of NaOH and SiO<sub>2</sub> was taken in a sol-gel reactor. Then 400ml of ethylene glycol was added and the solution was heated to 180°C under nitrogen gas atmosphere with continuous mechanical stirring. After 2hrs of continuous distillation of glycol, a solid precipitate was formed. This was aged overnight. Calcium nitrate solution and ortho-phosphoric acid were then added to it in such a way that the liquid-to-solid ratio was ~9:1 and the distillation was further carried out at 90°C with continuous stirring. A white precipitate had appeared which was filtered, dried in an oven at 150°C for 2 hrs.

## Preparation of Bioglass-PMMA Composites:

The 45S5 bioglass-polymethyl-methacrylate composites were made through hot-pressing at 130°C. The pressures used to make the rectangular-shaped composites were 100MPa and 200MPa. Five types of composites were made with varying amounts of PMMA and bioglass powders. For each composition three specimens were made. The PMMA weight percentages were 30%, 40%, 50%, 60% and 70%. Table 3 gives the notation followed for various composites prepared at different pressures. Densities of the hot-pressed composites were measured.

*Table 3: Various composites made at different pressures*

Pressure	Polymer Weight Percentage				
	30	40	50	60	70
100MPa	301BP	401BP	501BP	601BP	701BP
200MPa	302BP	402BP	502BP	602BP	702BP

## Evaluation of Modulus of Rupture of Composites:

The composites were tested for modulus of rupture (MOR) by three-point bend technique. The MOR values of composites are given in Table 4. The reported values of MOR for the Bioglass and PMMA are ~215 MPa and 140 MPa respectively. It is expected that as the PMMA percentage in the composite increases, the corresponding

MOR decreases. However, the results of the present study show that MOR decreases with increasing PMMA percentage only upto a certain PMMA content in the composites and beyond that it increases with increase in PMMA content. This is likely due to a dispersion **b**ordering effect. Bioglass behaves as dispersant in the polymer matrix (PMMA).

**Table 4: MOR and density of composite**

Bioglass	Polymer %	Composites Name	MOR (MPa)	Percentage Relative Density ( $\rho_s/\rho_{theo}$ )X 100
BD850	30	301BP	50.26	59.2
	40	401BP	30.64	60.56
	50	501BP	41.26	61.97
	60	601BP	45.90	67.01
	70	701BP	49.84	71.53
BS850	30	302BP	37.86	60.85
	40	402BP	49.57	63.47
	50	502BP	36.55	63.19
	60	602BP	38.45	77.01
	70	702BP	34.66	74.21

#### **Preparation of Ceramic Powders:**

sodium glycolate silicate was dissolved in water. To this diluted hydrochloric acid was added until pH of the solution reached to 2.5 for getting required fine particles. The clear solution was allowed to age for 25hrs. A clear transparent gel was observed. This gel was dried at 200°C to remove the solvent present in it. On evaporating the solvent white powder (nano-size particles of silica along with sodium chloride) formed. The later was calcined for 2hrs at 600°C to remove the residual solvents.

#### **Preparation of Ceramers:**

Ceramers with varying compositions of polymer and silica content were prepared by two methods:

**1. Solution Route:**

Ceramers with varying compositions of polymer and pentacoordinated silicon complexes were prepared, which are shown in Table 3. Required amount of pentacoordinated silicon complex was dissolved in small quantity of water, and acetone was added as a solvent, followed by hydrochloric acid till the pH reached to ~2.5 (isoelectric point of pentacoordinated complex). This mixture was allowed to age in atmospheric conditions for 5 minutes for effective sol formation. This sol was then added slowly to the polymer solution prepared by dissolving the PMMA in acetone at 60°C with continuous mechanical stirring. A viscous solution was observed. On cooling overnight, a formation of solid mass was observed. This solid mass was crushed and dried for 2hrs at 150°C. After complete evaporation of the solvent, ceramer was milled in a zirconia vessel with zirconia grinding media, using a centrifugal ball mill. A constant speed of 250 rpm was maintained.

*Table 5: Ceramers prepared based on pentacoordinated complex and PMMA through solution route*

Ceramer	Polymer (g)	Pentacoordinated complex (g)	Wt% of Silica	Wt% of NaCl
SC1	10	4	9.7	9.38
SC2	10	6	13.29	12.85
SC3	10	8	16.30	15.76
SC4	10	10	18.86	18.23

**2. Physical Mixing:**

Ceramic powder was added slowly to the polymer solution prepared by dissolving the PMMA in acetone at 60°C with continuous mechanical stirring. The homogeneous viscous solution formed was heated at 100°C till the semi solid formation was observed. This semi solid mass was crushed and dried for 2hrs at 150°C. After complete evaporation of the solvent, ceramer was milled in a zirconia vessel with zirconia grinding

media, using a centrifugal ball mill. A constant speed of 250 rpm was maintained. The powders were subsequently hot pressed at 110°C by applying 100 MPa pressure for one minute to obtain rectangular solid ceramers of size 10mm width and 50 mm length.

#### **Evaluation Of Modulus of Rupture of Ceramer:**

The results of the three-point bend test were used to compute MOR of the ceramers prepared by both solution route and physical mixing method.

##### **Solution Route:**

From Table.4 it can be noticed that the MOR in generally increased from 17.4 MPa for SC1 sample to 24.7MPa for SC4 sample and the increase is directly proportional to increase in silica content of the ceramers.

**Table 6: Mechanical properties of ceramers prepared through solution route**

<b>Ceramer</b>	<b>Wt% of silica</b>	<b>MOR(MPa)</b>
SC1	9.7	17.43
SC2	13.29	21.89
SC3	16.2	20.24
SC4	18.86	24.66

##### **Physical mixing route:**

Table 10 shows that the MOR increased as silica content increases but the results show a considerable scatter.

**Table 6: Mechanical properties of ceramers prepared through physical mixing route**

<b>Ceramers</b>	<b>Wt% of Silica</b>	<b>MOR(MPa)</b>
PC1	20.07	34.1
PC2	33.33	33.0
PC3	41.8	38.3



**Conclusions:**

MOR is found to decrease with increasing PMMA content in PMMA-bioglass composites only upto a certain extent followed by an increase. This can be attributed to the dispersion hardening effect in the composite at high polymer percentages and to interfacial porosity at high ceramic percentages.

The observed MOR values of the composites are less than the expected ones because of porosity in the samples.

The modulus of rupture (MOR) had increased with increase in silica content in creamers prepared by both the methods. The change in MOR in the ceramers prepared through solution route is from ~17.4MPa to ~25MPa, where as in ceramers prepared by physical mixing the MOR increased from 32MPa to 38Mpa.

**References:**

1. H.H. Haung, B. Order and G.L.wilks, *Macromolecules*, 20,1322 (1987).
2. C.L. Frey, *J.Amer.Chem.Soc.*, 92, 1205 (1970).
3. R. Holems, R.O. Day, J.J. Harland, et al. *Organometalics*, 3, 341 (1984).
4. R. Holems, R.O. Day, J.J. Harland, et al. *Organometalics*, 3, 347 (1984).
5. R.M. Luine, K.Y.Blohowiak, T.R.Robinson, M.L.Hoppe, P. Nardi, J. Kampf and J.Uhm, *Nature* (London), 353, 642 (1991)
6. N.R.Reddy. M.Tech Dissertation, "Synthesis of pentacoordinate silicon complexes and silicon precursors",IIT.Bombay. (2000).
7. Neo M, Ohtsuki C, Kokabu T, Katani S, Saga N, Bando Y, Nakamura T & Yamamura T, *J. of Biomed. Matls. Research*, 26, 1419-1432, (1992).

## Synthesis and characterization of Yttria fully stabilized Zirconia powders

<sup>1</sup>Nikhil Deo, <sup>1</sup>N V N Ramakrishna, <sup>1</sup>Anil Anal, <sup>1</sup>B T Rao,  
<sup>1</sup>T R Rama Mohan, <sup>2</sup>Ramji Lal

<sup>1</sup> Indian Institute of Technology, Bombay

<sup>2</sup> Naval Materials Research Laboratory, Ambernath

### Abstract

yttria-fully stabilized-Zirconia powders containing 8 mol% Yttria were prepared by Spray-drying & co-precipitation methods. The co-precipitated gel was subjected to water washing and Propanol-washing. The powders obtained were characterized for composition, particle shape, particle size and size distribution by XRD, SEM, TEM and laser particle size analyser. The Yttria-Zirconia powders obtained from the different processing routes were compacted at different pressures and sintered at 1400 °C, 1500 °C and 1600 °C to assess their sinterability. The electrical conductivity of the sintered specimens measured by a. c. Impedance Spectroscopy is also presented.

*Key words:* Yttria, Zirconia, spray drying, co-precipitation, Propanol-2, conductivity

### Introduction:

Zirconia whose cubic form is fully stabilized by Yttria addition (YSZ) has been a potential candidate as solid electrolyte for fuel cells and oxygen sensors. The electrical conductivity in these ceramics can be enhanced by increasing their density. Currently, research has been going on[1-4] in the synthesis of tailor made powders with electrical conductivity in the range of 0.1-0.2 S/cm. Achieving high sintered densities has always been a major problem for powders prepared through wet chemical routes, the reason being the presence of agglomerates.[5-7] Co-precipitation has always been a well-known technique for synthesizing high purity and fine ceramic powders. However, the produced powders show poor sintering behavior due to the presence of agglomerates.[8] It is argued that alcohol washing of the co-precipitated gel eliminates agglomeration, by substitution of organic -OR groups for the hydroxyl groups in the gel.[9-10]

In the present work, 8 mol% Ytria stabilized Zirconia powders are synthesized through Co-precipitation and also through Spray drying. Propanol washing of the co-precipitated gel was carried out and its effect on the sintered density and thereby on the conductivity was studied. The powders prepared were characterized using Thermal analysis, XRD, SEM, TEM and particle size analysis. The powders were compacted at various pressures and their sinterability was studied. Electrical conductivity of the pellets was measured using Impedance Spectroscopy.

## Experimental:

8 mol% Ytria stabilized Zirconia (YSZ) was synthesized through two routes – spray drying and co-precipitation. Zirconium nitrate solution and Yttrium oxide (99.9%) supplies by Indian Rare Earths Ltd. Were used for spray drying. Amount of Zirconia in the Zirconium nitrate solution was estimated using Mandelic acid method and the corresponding amount of Yttrium oxide was taken and converted into nitrate solution. These two solutions were vigorously mixed and spray dried. The flow chart of spray drying is given in Fig 1. The spray dried nitrates were calcined at 550 °C, 600 °C, 700 °C, 800 °C and 900 °C, each for 2 hours.

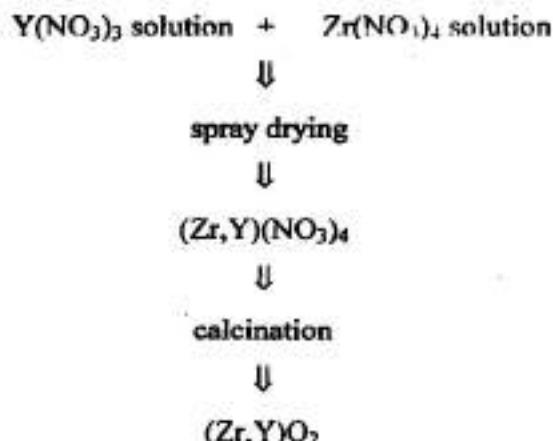


Fig 1. flow chart of spray drying

Synthesis of YSZ powders through co-precipitation consisted the hydrous gel preparation followed by drying and calcinations steps. The starting materials used were Zirconyl nitrate (Laboratory reagent, Thomas Baker Chemicals Ltd.) and Yttrium oxide (99.9%) (Indian Rare Earths Ltd.). Aqueous solution of Zirconyl nitrate was prepared and the required amount of Yttrium oxide was taken and was converted into nitrate solution. These two solutions after mixing vigorously, were added drop-wise to Ammonium hydroxide. The pH of the precipitating media was maintained between 9.0 and 10.0. Washing of the gel was done, in one case by water and in another case by 2-Propanol. In

the second case, 2-Propanol was added to the gel and using a mechanical stirrer the gel was stirred vigorously for 6 hours. The dried gels were calcined at 400 °C for 2 hours.

The spray dried and co-precipitated powders were ball milled at 200 rpm for 10 hours.

TGA of the spray dried powder, DTA of the co-precipitated gel, XRD, SEM, TEM and particle size analysis of the calcined powders were carried out. The powders were compacted at 100, 150, 250, 350, 450 and 550 Mpa and were sintered at 1600 °C for 2 hours. Pellets of highest density prepared from each processing technique were chosen for conductivity measurement, and, using Impedance Spectroscopy, conductivity of the pellets was measured.

## Results and Discussions:

TGA of the spray dried powder (Fig 2.) was carried out using Dupont TGA 2100. It can be observed that there was no more weight loss after 525 °C and so the spray dried powder was calcined at 550 °C, 600 °C, 700 °C, 800 °C and 900 °C, each for 2 hours. DTA of the co-precipitated powders was carried out using General V 4.1C Dupont 2100. DTA of the water washed co-precipitated gel is given in Fig 3 and that washed in Propanol is in Fig 4. The co-precipitated powders were calcined at 400 °C for 2 hours.

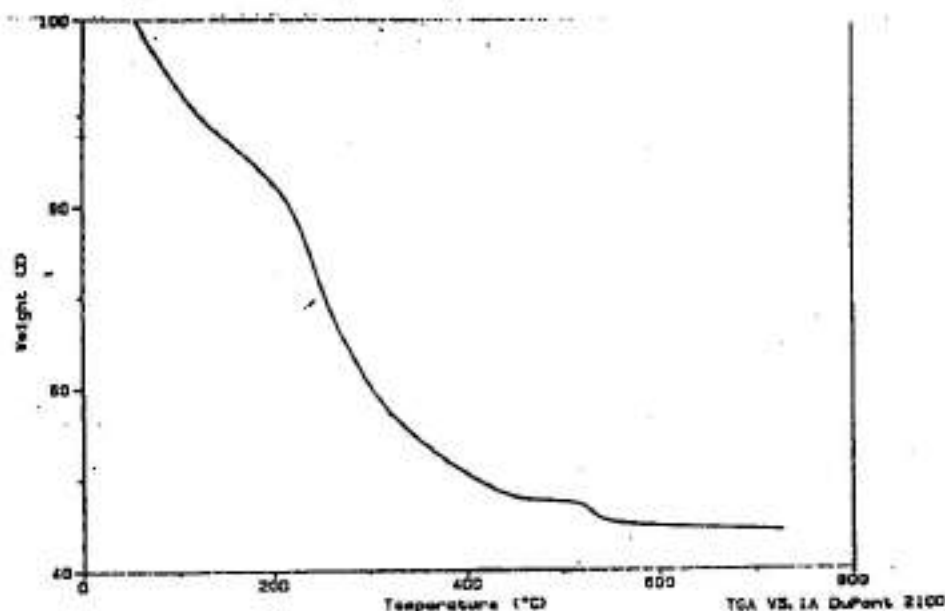


Fig 2. TGA of spray dried powder

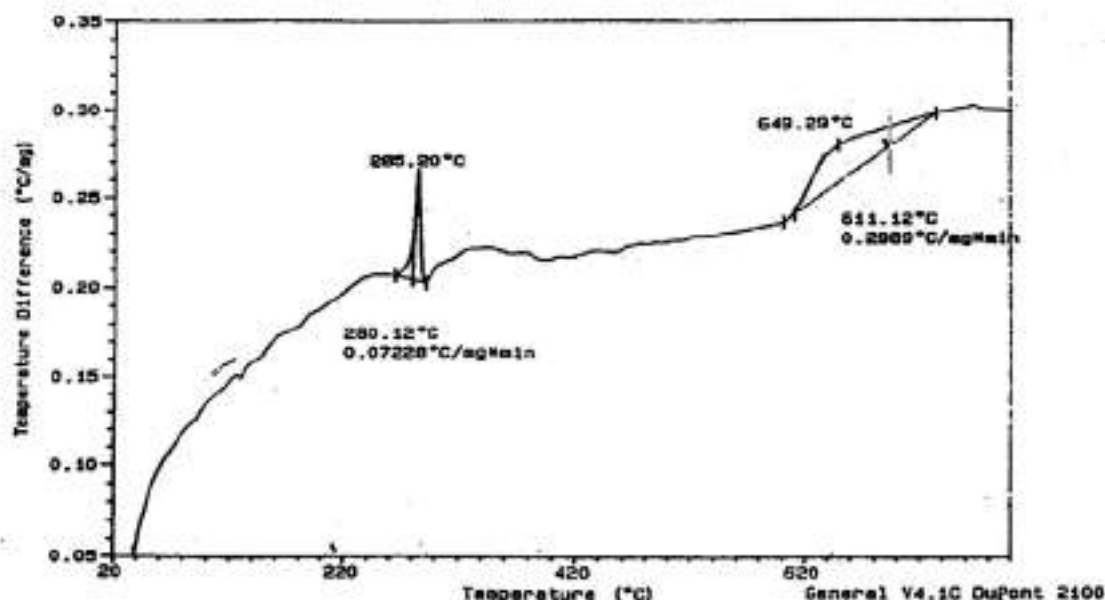


Fig 3. DTA of water washed co-precipitated gel

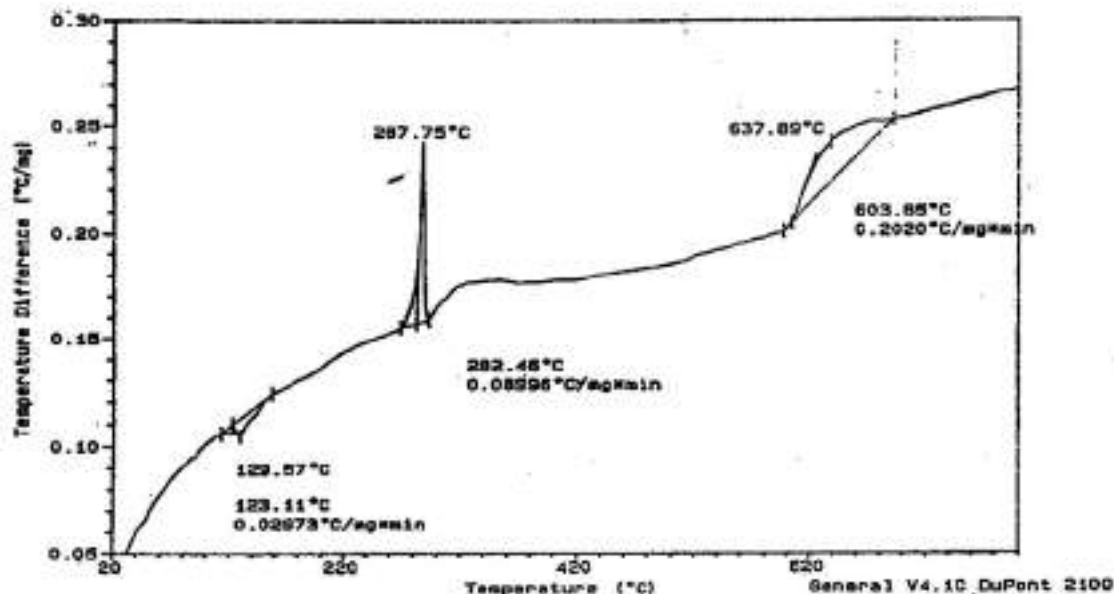


Fig 4. DTA of propanol washed co-precipitated gel

XRD of the calcined powders was carried out using Philips X-ray diffractometer. Cubic phase was found in powders calcined at 550 °C for spray dried powders and at 400 °C for co-precipitated powders.

The agglomerate size of the powders were 6.16  $\mu\text{m}$ , 1.02  $\mu\text{m}$  and 1.16  $\mu\text{m}$  for spray dried, water washed co-precipitated and propanol washed co-precipitated powders respectively. After ball milling at 200 rpm for 10 hours, these were reduced to 1.20  $\mu\text{m}$ , 0.66  $\mu\text{m}$  and 0.64  $\mu\text{m}$  respectively.

SEM (Cambridge Stereoscan S-9013 SEM) photographs of even ball milled powders showed the particles to be agglomerated. TEM (Philips CM200) of the powders indicated the particle sizes to be 100-450 nm in case of ball milled spray dried powders and 70-250 nm in case of ball milled co-precipitated powders.

The powders were compacted at 100, 150, 250, 350, 450 and 550 MPa and sintered at 1600 °C for 2 hours. Sintered density of compacts made from ball milled spray dried powders reached 90% whereas that from ball milled co-precipitated powders reached 80% (Fig 5). In case of co-precipitated powders, rather low sintered densities are due to the poor sinterability of the hard agglomerates formed, which could not be destroyed during ball milling. Densification in propanol washed gel was found to be similar to that in water washed gel. Propanol washing of the co-precipitated gel was carried out to minimize agglomeration, but without success.

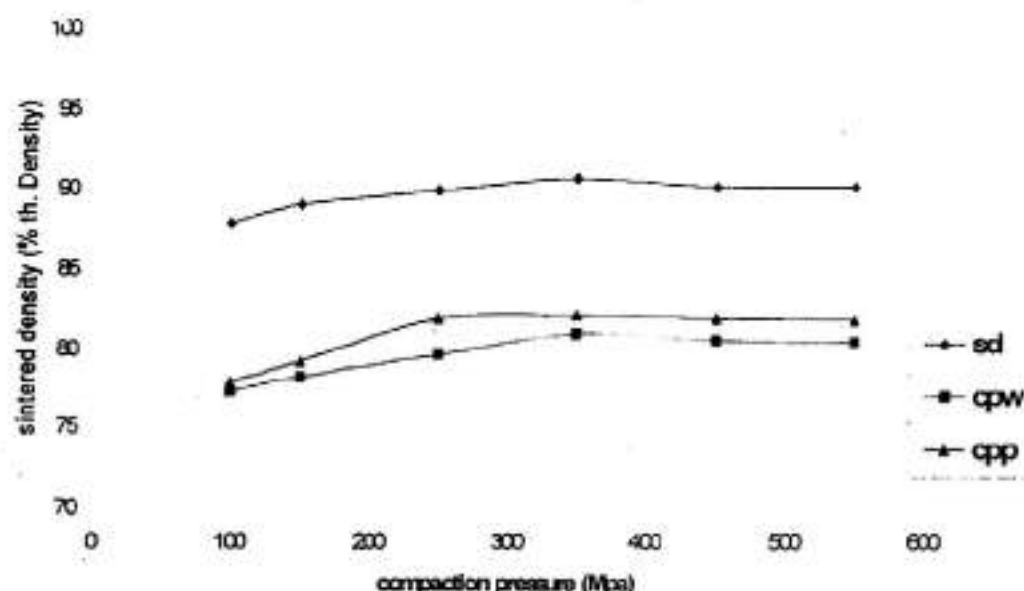


Fig 5. Sintered density for samples sintered at 1600 °C, 2hr

Conductivity of platinum coated pellets was measured as a function of temperature. Typical conductivity plots for the sintered samples made from the three powders are shown in Fig 6. The conductivity obtained at 950 °C for ball milled spray dried powders

was 0.051 S/cm whereas for ball milled water washed co-precipitated powders it was 0.018 S/cm and for ball milled propanol washed co-precipitated powders it was 0.019 S/cm. The activation energy for conduction was calculated and the obtained values are 127 kJ/mol for spray dried powders and 156 kJ/mol for co-precipitated powders.

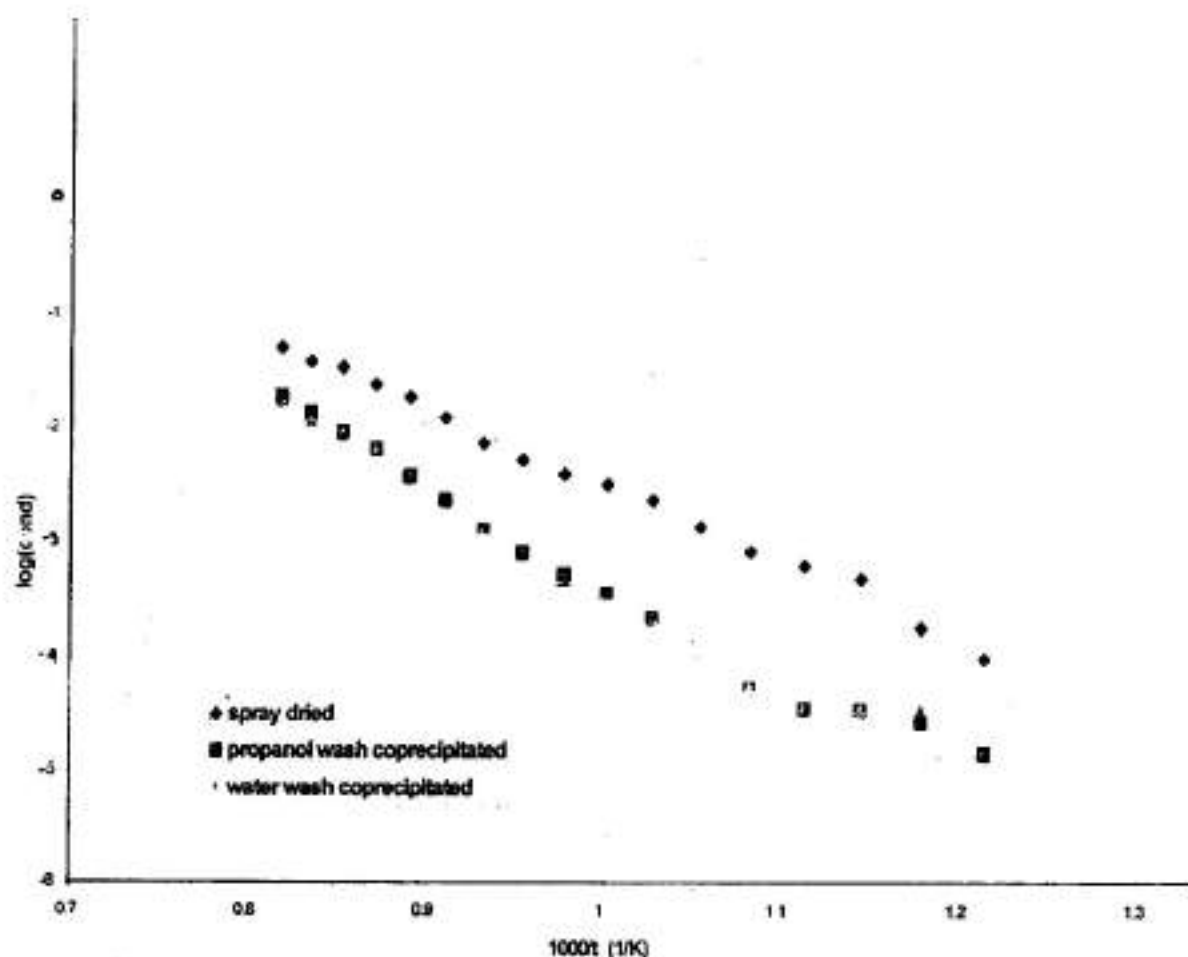


Fig 6.  $\log(\text{conductivity})$  vs.  $1000/\text{Temperature}$



### Summary:

8 mol% Ytria stabilized Zirconia powders were synthesized by spray drying and co-precipitation. Effect of propanol washing on the co-precipitated gel was studied. The spray dried powders calcined at 550 °C and co-precipitated powders calcined at 400 °C were found to be cubic. The electrical conductivity extrapolated to 1000 °C for spray-dried samples was found to be 0.08 S/cm as against the often reported 0.1-0.2 S/cm. The activation energy values obtained in the current experiment are somewhat higher (often reported value is 96 kJ/mol) possibly due to the presence of entrapped gases opposing the sintering process. Further studies are in progress to achieve higher sintered densities.

### Acknowledgements:

The authors thank the Director, IIT Bombay and the Director, Naval Materials Research Laboratory, Ambernath for funding the project.

## References:

1. R Gibson, G P Dransfield, J T S Irvine; *Journal of Materials Science*; 33, pp 4297-4305 (1998)
2. Osamu Yamamoto, Yoshinori Arati, Yasuo Takeda, Nobuyuki Imanishi, Yasumobu Mizutani, Masayaki Kawai, Yasuhisa Nakamura; *Solid State Ionics*; 79, pp 137-142 (1995)
3. Y Arachi, H Sakai, O Yamamoto, Y Takeda, N Imanishi; *Solid State Ionics*; 121, pp 133-139 (1999)
4. Jianghong Gong, Ying Li, Zilong Tang, Zhongtai Zhang; *Materials Letters*; 46, pp 115-119 (2000)
5. Jian-Lin Shi, Jian-Hua Gao, Zu-Xiang Lin and Tung-Sheng Yen; *Journal of American Ceramic Society*; 74 (5), pp 994-997 (1991)
6. Jiang Xing-Xiang, Huang Dong-Shan, Weng Luquian; *Journal of Materials Science*; 29, pp 121-124 (1994)
7. W H Rhodes; *Journal of the American Ceramic Society*; 64 (1), pp19-22 (1981)
8. Rajiv Dayal, N M Gokhale, S C Sharma, Ranji Lal; *Transactions of Indian Ceramic Society*; 48 (4) July-Aug, pp 58-62 (1989)
9. M A C G Vandegraaf, J H H Ternaat, A J Burggraaf; *Journal of Materials Science*; 20, pp 1407-1418 (1985)
10. J L Shi, J H Gao, Z X Lin, D S Yan; *Journal of Materials Science* 28, pp 342-348, (1993)

## **Synthesis of Titanium-Bioglass Composites**

Vivek Mathur, Anil Anal, B.T Rao, T.R Rama Mohan  
I.I.T Bombay

### **Abstract**

Ceramics, such as bioglass ceramics and hydroxyapatite have similar compositions to that of bone and thus are extensively used as coatings on surgical and dental implants. It is often found that the implants fail at the implant-coating interface, while the coating tissue interface remains strong. The current project aims at solving this problem by developing a composite of titanium and bioglass ceramic. It is expected that such composites exhibit good mechanical properties as well as improved bonding to the tissue. The present paper reports the preliminary investigations on the synthesis of apatite-wollastonite compositions by sol-gel process and their subsequent processing into titanium-bioglass composites. The sol gel powders are calcined at 600°C to form bioglass ceramic composition. After characterization, these powders are mixed with titanium powders in a high-energy centrifugal ball mill. The composite powders, thus obtained are compacted into cylindrical specimen and sintered in argon and partial hydrogen (argon:hydrogen:5:1) atmospheres at temperatures in the range of 1000°C to 1200°C. The properties of the sintered samples are discussed.

**Keywords:** Bioglass, Hydroxyapatite, Apatite-Wollastonite, Composite, Sintering

## 1. Introduction

A revolution has occurred in the use of ceramics during the past four decades to improve the quality of life. This revolution is the innovative use of specially designed ceramics for the repair, reconstruction, and replacement of diseased or damaged parts of the body. Ceramics used for this purpose are termed as "bioceramics". Bioceramics could be polycrystalline (alumina or hydroxyapatite), bioactive glasses, bioactive glass-ceramic (A/W), or bioactive composites. Applications include replacements for hips, knees, disease, maxillofacial reconstruction, augmentation and stabilization of the jawbone, spinal fusion, and bone repair after tumor surgery. [1].

An understanding of the mechanisms of tissue bonding to bioactive ceramics has resulted in molecular design of bioceramics for interfacial bonding with hard and soft tissue. Clinical success requires the simultaneous achievement of a stable interface with connective tissue and a match of the mechanical behavior of the implant with the tissue to be replaced. Ceramics used for the repair and reconstruction of diseased or damaged parts of the musculo-skeletal system, termed bioceramics, may be bioinert (e.g., alumina and zirconia), resorbable (e.g., tricalcium phosphate), bioactive (e.g., Hydroxyapatite, bioactive glasses, and glass ceramics), or porous for tissue in growth (e.g., Hydroxyapatite-coated metals). [2].

The clinically most important bioactive glass-ceramic is the three phase silica-phosphate material composed of apatite  $\text{Ca}_{10}(\text{PO}_4)_6(\text{OH},\text{F}_2)$  and Wollastonite ( $\text{CaO-SiO}_2$ ) crystals and a residual  $\text{CaO-SiO}_2$  rich glassy matrix, termed as A/W glass ceramic. It has excellent mechanical properties and forms a bond with bone that has very high interfacial bond strength. The stable phases of calcium phosphate ceramics depend considerably upon temperature and the presence of water, either during processing or in the use environment. At body temperature, only two calcium phosphates are stable in contact with aqueous media, such as body fluids: at  $\text{pH} < 4.2$ , the stable phase is  $\text{CaHPO}_4 \cdot 2\text{H}_2\text{O}$  (dicalcium phosphate, brushite,  $\text{C}_2\text{P}$ ), whereas, at  $\text{pH} > 4.2$ , the stable phase is  $\text{Ca}_{10}(\text{PO}_4)_6(\text{OH})_2$  (HA). At higher temperature, other phases, such as  $\text{Ca}_3(\text{PO}_4)_2$  ( $\beta$ -tricalcium phosphate,  $\text{C}_3\text{P}$ , TCP) and  $\text{Ca}_4\text{P}_2\text{O}_9$  (tetracalcium phosphate,  $\text{C}_4\text{P}$ ) are present. The unhydrated, high temperature calcium phosphate phases interact with water, or body fluids, at  $37^\circ\text{C}$  to form HA. [3], [4], [5].

Titanium is the metal most commonly used for implants because of its good biocompatibility, ready availability and sufficient strength for low specific gravity. The main problem with ceramics is that they lack in strength, so in order to make biomaterials having high strength as well as good biocompatibility, use of composites may be a better solution. As titanium has good mechanical properties as well as high strength, it is a natural choice to make composites. [6], [7], [8].

The Bioglass used in this study is the Apatite Wollastonite (AW) bioglass, it is made by sol-gel method. The sol-gel route has the unique advantage of producing homogenous bioglass with high purity and greater control over the process. The composite is produced by mechanical alloying and the compacts made from powders are sintered in different atmospheres.

## 2. Experimental Work

### 2.1 Preparation of A/W Bioglass by Sol-Gel Method

#### 2.1.1 Preparation of Sol

The sol-gel route has unique advantage of producing homogenous bioglass with high purity and greater control over the process. The resulting powders have higher surface area and hence can be sintered at relatively lower temperatures. Bioglass was prepared by sol-gel technique using both organic and inorganic pre-cursors. The weight percent of the various constituents in the bioglass ceramic composition are given in table1.

*Table1 : Composition Of A.W. Bioglass*

Compound	Composition (wt %)
SiO <sub>2</sub>	34.2%
CaO	44.9%
P <sub>2</sub> O <sub>5</sub>	16.3%
MgO	4.6%
CaF <sub>2</sub>	0.5%

- Initially aqueous solutions of  $\text{Ca}(\text{NO}_3)_2$  and  $\text{Mg}(\text{NO}_3)_2$  are made in separate beakers. These are mixed to form the ionic solution.
- Methanol and Tetra Ethoxy Ortho Silane (TEOS) are mixed in a beaker and  $\text{CaF}_2$  particles are then dispersed in this organic solution by constant stirring.
- Ionic Solution is added drop wise to the organic solution with continuous stirring.
- This is followed by addition of HCl and Ortho Phosphoric Acid.
- The solution is heated to  $80^\circ\text{C}$  along with constant stirring for 30 minutes, resulting in formation of a clear viscous transparent sol.

### 2.1.2 Gelation and Drying

- The sol is kept for 24 hours without disturbing for natural evaporation and a clear transparent gel is obtained.
- Gel is dried over the hot plate to get dry powder
- The powder is Calcined at  $600^\circ\text{C}$  for two hours. The powder is loosely compacted (without binder) into cylindrical pellets of diameter 3 cm for calcination.

## 2.2 Preparation of Titanium-Bioglass Composites

Bioglass powder and titanium powder are mixed in the appropriate amounts and are milled in the centrifugal ball mill at a constant speed of 200 rpm. Steel container and steel balls are used for milling.

*Table 2: Amounts of Ti and Bioglass powders used in ball milling*

Material	Percentage by weight
Titanium powder	80%
Bioglass powder	20%

### 2.3 Compaction of Bioglass Composites

Pellets 3mm thick and having 1.5 cm diameter are made using a cylindrical die. A hydraulic press is used to apply the required pressure. PVA is used as a binder. Debinding is done afterwards to remove the binder by heating the pellets to 450 °C. To facilitate the removal of sample pellets from the die walls, the upper punch and the lower punch are lubricated with stearic acid dissolved in acetone. The compaction pressures used are 550 MPa and 800 MPa.

### 2.4 Sintering

The compacts are sintered at different temperatures from 1100 – 1200°C and in different atmospheres, such as argon and partial H<sub>2</sub> (Argon:H<sub>2</sub>:5:1). The sintered samples are analyzed by XRD.

## 3. Results & Discussion

The bioglass powder after calcining at 600 °C showed calcium phosphate silicate and magnesium silicate phases. These on ion exchange with body fluids are expected to nucleate hydroxyapatite. The average particle size was around 2.4 µm, which is similar to the 2.35 µm observed for α-Titanium powder used in present investigation.

Centrifugal ball milling of both the powders resulted in a composite powder with average particle size 3.74 µm. This increase is possible only when the Ti particles expand during milling and the bioglass particles are dispersed in them. An interesting observation is that the calcium phosphate silicate and magnesium silicate present in the original bioglass powder have now changed to calcium silicate, magnesium silicate and titanium phosphide in the composite powders. This is likely to be due to the stress concentration and heat generated during milling causing chemical reactions between both titanium and bioglass powders.

Sintering in Argon atmosphere at 1100 and 1200 °C showed decrease in sintered density as shown in Table.3. Further, the phase composition obtained was different from the starting powders. Sintering in Partial H<sub>2</sub> at 1200 °C resulted in slight increase in sintered density. The phase composition once again was different.



*Table 3: Sintering Data.*

S. No.	Sintering Temperature	Sintering Atmosphere	Green Density $\text{gm/cm}^3$	Sintered Density $\text{gm/cm}^3$
1.	1000 °C	Argon	2.72	2.71
2.	1000 °C	Argon	2.74	2.73
3.	1000 °C	Argon	2.72	2.71
4.	1100 °C	Argon	2.72	2.69
5.	1100 °C	Argon	2.82	2.65
6.	1100 °C	Argon	2.79	2.70
7.	1200 °C	Argon	2.85	2.74
8.	1200 °C	Argon	2.81	2.70
9.	1200 °C	Argon	2.79	2.69
10.	1200 °C	Partial $\text{H}_2$	2.73	2.81
11.	1200 °C	Partial $\text{H}_2$	2.83	2.90
12.	1200 °C	Partial $\text{H}_2$	2.75	2.88
13.	1200 °C	Partial $\text{H}_2$	2.73	2.94
14.	1200 °C	Partial $\text{H}_2$	2.75	2.87
15.	1200 °C	Partial $\text{H}_2$	2.62	2.66

X-Ray Diffraction of the pellets sintered in argon atmosphere at 1100°C indicated the major peak to be titanium and with other phases  $\text{Ti}_2\text{O}$  and  $\text{Mg}_2(\text{SiO}_4)(\text{OH})_2$  and a minor amount of  $\text{Ca}_3(\text{PO}_4)_2\text{SiO}_4$ . An increase in sintering temperature to 1200°C in addition to titanium major peak surprisingly showed minor peaks of  $\text{Ti}_3\text{SiC}_2$  and  $\text{TiP}_2$ .

The pellets sintered in partial hydrogen atmosphere at 1200°C indicated the major phase to be  $\text{TiO}_2$ , followed by  $\text{MgSiO}_3$  and  $\text{Ca}_3(\text{PO}_4)_2(\text{SiO}_4)_6$ .

When the composites are heated in argon atmosphere in order to maintain the oxygen partial pressure some amount of oxygen has to go in to the vapour phase to maintain equilibrium, this phenomenon will be much more in the case of partial hydrogen atmosphere, where oxygen is likely to be reacting with the continuously flowing

hydrogen and carried away from the system. It is also possible for the smaller hydrogen molecule to diffuse in to the pores and react with oxygen, thereby creating fresh metallic surfaces. The later readily sinter resulting in increase in sintering density. This perhaps is the reason for increase in densities of samples sintered in partial hydrogen. Probably optimizing the percentage of hydrogen in the sintering atmosphere to give a maximum sintered density followed by controlled oxidation might result in a better composite. Currently work is in progress in this direction.

#### 4. Conclusions

The experimental work has demonstrated that it is possible to sinter titanium-bioglass composites in partial hydrogen atmosphere. Sintering in neutral atmosphere such as argon did not help possibly due to the absence of titanium-titanium particle contacts.

#### References

- [1] Joon B.Park, "Introduction to biomaterials", CRC handbook of Biomedical Engineering, CRC Press, Boca Raton, FL, 2000.
- [2] Joon Bu Park, Biomaterials Science and Engineering. Plenum Press, New York, 1984.
- [3] Donald L.Wise, Debra J.Trantolo, David E.Altobelli, Michael J.Yaszemski, Joseph D. Gresser, Edith R. Schwartz. Encyclopedic Handbook of Biomaterials and Bioengineering. Part A: Materials, Vol 2, Marcel Dekker , New York, 1995.
- [4] Donald L.Wise, Debra J.Trantolo, David E.Altobelli, Michael J.Yaszemski, Joseph D. Gresser, Edith R. Schwartz. Encyclopedic Handbook of Biomaterials and Bioengineering Part B: Applications, Vol 1, Marcel Dekker , New York, 1995.
- [5] Larry L. Hench, Bioceramics. Journal of the American Ceramics Society, 81[7] Pages 1705-28, 1998.
- [6] Hironobu Matsuno, Atsuro Yokoyama, Fumio Watari, Motohiro Uo, Takao Kawasaki, Biocompatibility and osteogenesis of refractory metal implants, titanium, hafnium, niobium, tantalum and rhenium, Biomaterials 22, Pages 1253-1262, 2001.

- [7] Marc long, H.J.Rack, Titanium alloys in total joint replacement- a materials science perspective. Biomaterials 19, Pages 1621-1639, 1998.
- [8] David F. Williams, Biocompatibility of Clinical Implant Materials. Vol. 1, CRC series in Biocompatibility, CRC Press, Boca Raton, Florida, 1981

## Effect of Sintering Temperature and $Y_2O_3$ Addition on the Microstructural Evolution of P/M Stainless Steels

Shankar, J\* and A. Upadhyaya\*\*

\*Graduate Student

\*\*Assistant Professor

*Materials and Metallurgical Engineering  
Indian Institute of Technology, Kanpur 208016, INDIA*

### Abstract

The present study aims at investigating the microstructural evolution and sintering behavior of P/M 316L (austenitic) and 434L (ferritic) stainless steels with oxide dispersions of yttria. The reinforced stainless steels can be named as oxide dispersion strengthened (ODS) stainless steel. In the present study, two sintering processes namely, solid state sintering at 1250°C and supersolidus liquid phase sintering at 1400°C were used to prepare the samples. The pure P/M stainless steel samples sintered through supersolidus liquid phase sintering was found to exhibit better densification. In the case of P/M stainless steel composites, the composites sintered through solid state sintering exhibited better density due to the rare earth effect of the oxide. The SEM microstructures of the stainless steel samples and composites reveal the effect of sintering temperature and rare earth addition in detail.

### Introduction

Despite its application in various fields, processing of wrought stainless steel suffers from several limitations. Wrought stainless steels are normally processed by the casting route and require machining to achieve the desired dimensional precision in the final products. Therefore, there is a continued thrust for seeking an alternative method for processing stainless steel in order to obtain near net shaped products. Powder metallurgy (P/M) route is one of the best processing technique to obtain near net shape products. P/M stainless steels are a relatively small, but rapidly growing, segment of the P/M market. However its application is limited due to their poor density, corrosion resistance and mechanical properties. Nowadays, P/M Stainless steels with improved mechanical properties, corrosion properties and densities are gaining wide popularity, compared to the wrought stainless steels. The aim of the present work was to produce novel stainless steel through P/M route by adding  $Y_2O_3$  oxide dispersoids. The ODS stainless steels possesses better mechanical properties and corrosion resistance than the straight P/M stainless steels [1,2]. The better mechanical properties can be attributed to the oxide dispersoids, which act as pinning centers for dislocation motion and grain boundary sliding [1,2]. The oxide dispersoids have been proposed to act as initiating sites for the formation of protective chromium oxide layer and as pinning centers between the surface oxide layer and the metal surface, thereby giving better mechanical strength to the surface oxide layer [2]. Moreover, the work was carried out at two different sintering temperatures of 1250°C and 1400°C corresponding to solid-state sintering and Supersolidus liquid phase sintering respectively. The supersolidus liquid phase sintering is a novel method for producing stainless steels as this process imparts better mechanical properties, density and corrosion resistance to the sample than liquid phase sintering.  $Y_2O_3$  dispersoids retain their mechanical strength at high temperatures. Moreover, the

rare earth oxides form a garnet with the protective  $\text{Cr}_2\text{O}_3$  oxide. This leads to better corrosion properties in the samples. The effect of oxide dispersions in P/M stainless steel was studied in detail for solid state sintering [1,2]. However, there was no work reported on the SLPS of particulate composites.

### Supersolidus Liquid Phase Sintering

The use of prealloyed powders led to the new process in liquid phase sintering called as supersolidus liquid phase sintering (SLPS). SLPS is a novel method for sintering components. As the name suggests, SLPS involves heating a prealloyed powder between the solidus and liquidus temperature to form liquid phase [4,5]. This process should be used with precise control because the conditions of the prealloyed approach are very close to compact distortion. During SLPS the liquid phase forms within the particles, causing each particle to split into individual grains [6]. The fragmented particles undergo repacking, giving a homogenous distribution of liquid. The resulting sintering rate is rapid once the liquid is formed due to capillary action. The various stages of densification during SLPS of a prealloyed polycrystalline powder are shown in Fig 1. The steps of SLPS are liquid formation, particle fragmentation, fragment rearrangement, grain packing and sliding, coarsening, and eventual pore elimination by solution-precipitation. The mechanism of SLPS was explained by Lund and Bala [7]. They suggested that mechanisms responsible for densification included,

- (i) redistribution of liquid formed due to melting at particle contacts
- (ii) flattening of the wetted particle contacts by a solution-precipitation mechanism
- (iii) grain growth due to solution-precipitation leading to release of intergranular liquid
- (iv) pore elimination due to the escape of the entrapped gas by diffusion.

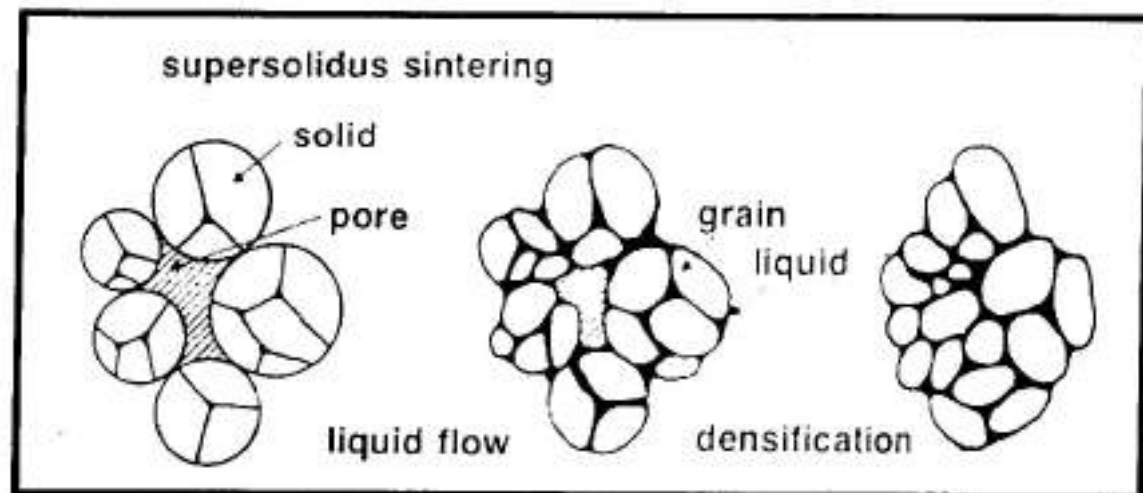


Figure 1. SLPS of a prealloyed polycrystalline powder [6].

Extensive work on densification mechanisms and microstructural evolution during SLPS of prealloyed powders was carried out by Tandon [8], who studied the sintering behavior of a wide range of alloys including, Ni-based super alloys, austenitic stainless steel and bronze powders. Lal worked on mechanisms and mechanics of shape loss during SLPS on various prealloyed powders, including bronze, 316L stainless steel and T15 tool steel. He investigated the shape loss during SLPS and rationalized the processing and material factors with regard to distortion [9]. Lal *et al.* [10] examined densification during SLPS of a mixture of two Ni-base superalloys. To one of the mixtures boron is added and it was observed that it had a lower melting temperature. This enhanced the densification of the sintered component. Ghosh [11] examined SLPS of prealloyed and premixed bronze (copper-10% Tin) powders. The author found that the compacts prepared from prealloyed powders were having better densities than the compacts from premixed powders. The work on supersolidus liquid phase sintering of stainless steel composites is carried out for the first time in the present study. Moreover, a detailed comparison of the sintered behavior of austenitic and ferritic stainless steels was carried out in the present experiments.

### Experimental Procedure

The austenitic 316L and ferritic 434L stainless steel samples produced by gas atomization were supplied by AMETEK. The apparent density of the 434L ferritic stainless steel powder was  $2.72 \text{ g/cm}^3$ . The apparent density of 316L austenitic stainless powders was  $2.72 \text{ g/cm}^3$ . Both the powders were free flowing and had a flow rate of 29 s (for 50 g). The  $\text{Y}_2\text{O}_3$  oxide powders supplied by RE Acton, UK and were 99.9% pure. The compositions of the stainless steel powders are tabulated in Table 1. The composites were mixed in a tubular mixer for 30 mins in order to obtain a homogenous mixture. A die of 12.7 mm inner diameter was used to make the green compacts of approximately 5 mm in height. The pressure was applied uniaxially i.e. in one direction using a manually operated hydraulic press machine (Apex Construction Ltd., UK) of 20 T capacity. All the stainless steel samples were compressed at pressures from 200 to 600 MPa. The stainless steel composites were pressed at 600 MPa. The nominal green densities of the sample were  $5.79 \text{ g/cm}^3$  for pure stainless steel samples and  $5.72 \text{ g/cm}^3$  for the composites. Sintering was performed in a laboratory furnace at two temperature,  $1250^\circ\text{C}$  and  $1400^\circ\text{C}$  using hydrogen as the atmosphere. The hydrogen atmosphere acts as a reducing environment for the surface oxides formed in the powders during atomization. Moreover, the atmosphere prevents oxidation of the samples during sintering. The heating rate was  $5^\circ\text{C/min}$  and the samples were held at the sintering temperatures for 60min. The samples were allowed to cool the furnace at a slow rate. The various experimental variables used for the preparation of the sample are shown in Table 2. The surfaces of the samples were characterized by optical and scanning electron microscopy.



**Table 1.** Composition for 316L and 434L powders.

Grade	Chemical Composition, wt %									
	Fe	Cr	Ni	Mn	S	Si	C	P	Mo	( )
316L	Bal	16.51	12.97	0.21	0.008	0.93	0.025	<0.01	2.48	-
434L	Bal	15.93	-	0.24	0.710	0.71	0.023	0.02	1.00	0.27

**Table 2.** Experimental variables used for the preparation of the P/M samples.

Sample	Y <sub>2</sub> O <sub>3</sub> (Weight %)	Temperature (°C)	Compaction Pressure (MPa)	Holding Time (mins)	Sintering Atmosphere
Austenitic (316L) Stainless steel	0	1250 (solid state) and 1400 (SLPS)	200 to 600	60	Hydrogen
	2.5		600		
	5		600		
	7.5		600		
	10		600		
Ferritic (434L) Stainless steel	0	1250 (solid state) and 1400 (SLPS)	200 to 600	60	Hydrogen
	2.5		600		
	5		600		
	7.5		600		
	10		600		

## Results and Discussions

### Densification results

Figure 2 shows the variation of sintered densities for the 316L stainless steel samples with compaction pressure. Figure 2 also shows the effect of sintering temperature on the samples. From the figure it was observed that the sintered density of the compacts increases with increase in pressure and the maximum sintered density was obtained for the sample compacted at 600 MPa. This can be attributed to the higher green density of the sample. Moreover, the samples sintered at 1400°C (SLPS) were having higher sintered densities than the samples sintered at 1250°C (Solid state sintering). The higher sintered density due to SLPS can be attributed to the liquid formation that increases the sintering rate. Figure 3 represents the variation in sintered densities of 434L stainless steel samples with compaction pressure. It was observed that the sintered densities were maximum for the samples compacted at 600MPa at both the sintering temperatures. This can be attributed to the higher green density of the sample compacted at 600 MPa. This is why the future compaction experiments with Y<sub>2</sub>O<sub>3</sub> composite stainless steels were prepared at 600 MPa pressure. The samples sintered by SLPS were having higher densities than the samples sintered by solid state sintering similar to that of



$Y_2O_3$  dispersoids for 316L stainless steel composites. The graph shows decrease in the sintered density with addition of  $Y_2O_3$  at both the temperatures. The addition of second phase particles reduce the interparticle bonding leading to decreased density in the composites. Figure 5 compares the variation of density with addition of  $Y_2O_3$  for 434L stainless steel composites. It was noticed that the densities of the composites decreases with addition of  $Y_2O_3$  when sintered at  $1400^\circ C$ . But when sintered at  $1250^\circ C$ , the densities show a typical behavior with the density of the composite containing 10%  $Y_2O_3$  increasing drastically. The density of the sample reaches that of the straight 434L stainless steel sample. In the case of the sample sintered at  $1250^\circ C$ , the oxide dispersoids are distributed at the grain boundaries, when compared to samples sintered at  $1400^\circ C$ , where the  $Y_2O_3$  particles get distributed uniformly in the sample.

Figure 5 shows the densification behavior of pure stainless steel samples of 316L and 434L along with 10%  $Y_2O_3$  composites. When the samples were sintered at  $1250^\circ C$ , the 434L with 10%  $Y_2O_3$  composite showed enhanced densification when compared with 316L with 10%  $Y_2O_3$  composite. This can be attributed to the faster diffusion in 434L when compared to 316L. Moreover, we believe that when the critical limit of 10%  $Y_2O_3$  is reached the rare earth oxides forms garnet with the chromium oxide layer leading to enhanced densification and corrosion resistance of the sample. In the case of the samples sintered at  $1400^\circ C$ , the  $Y_2O_3$  particles are distributed uniformly in the liquid phase and hence the enhanced densification is not seen.

### Microstructural results

#### *a) Optical microscopy*

The micrographs capture the microstructural evolution trajectory of the samples as a function of sintering temperature and effect of  $Y_2O_3$ . The samples of 316L and 434L stainless steel and the composites with 10%  $Y_2O_3$  were considered. Figure 6 reveals the microstructure of 316L P/M stainless steel samples sintered at  $1250^\circ C$  and  $1400^\circ C$ . It can be noticed that the sample sintered at  $1400^\circ C$  has higher grain growth and lower porosity. This can be attributed to the higher sintering temperature, which results in grain growth. Moreover, the pores tend to become more rounded because of higher driving force to attain minimum energy at the interface. Figure 7 shows the microstructure of 434L stainless steel samples sintered at  $1250^\circ C$  and  $1400^\circ C$ . It was observed from the micrographs that the sample sintered at  $1400^\circ C$  was having higher grain growth. The grain boundaries were clearly distinguished and the pores were rounded. In the sample sintered at  $1250^\circ C$ , pores were preferentially segregated at the grain boundaries and there were no clear grain boundaries. The pores were also irregular in shape and the porosity was higher.

#### *b) SEM Micrographs*

The SEM micrographs were used to explain the effect of  $Y_2O_3$  addition on the microstructure. Hence only the extreme case of the composite with 10%  $Y_2O_3$  was considered. Micrograph 316L + 10%  $Y_2O_3$  is shown in Fig 8 in both secondary electron (SE) mode and back scattered electron (BSE) mode. In the BSE mode the  $Y_2O_3$

dispersoids were not revealed as the density of the dispersoids are similar to that of surface. Hence the BSE mode depicts the surface morphology of the sample more clearly and reveals the pores network on the surface. Pores visible on the surface of the sample were irregular in shape. Figure 9 shows the SEM micrograph of the composite sintered by SLPS. Pores were regular on the grain boundaries and the grain growth was higher than the solid state sintered sample, due to the higher temperature sintering. 316L + 10%  $Y_2O_3$  sample sintered at 1250°C and 1400°C are shown in Fig 10. The micrographs elucidate that the grain growth was more in the sample sintered at 1400°C. Moreover, in the sample sintered at 1400°C, the oxide dispersoids are distributed uniformly throughout the grain surface. In the case of the sample sintered at 1250°C, the  $Y_2O_3$  agglomerates are seen at the grain boundaries. Figure 11 (a) and 11 (b) compare the SEM micrographs of 434L + 10%  $Y_2O_3$  composites sintered at 1250°C and 1400°C respectively. In the sample sintered at 1250°C, the  $Y_2O_3$  dispersoids were distributed along the grain boundaries. Moreover, the pores are also concentrated at the grain boundaries. In the sample sintered at 1400°C, the oxide dispersoids are distributed uniformly on the surface of the sample. The same set of samples was observed in BSE mode and SE mode in Fig 12. The left side of the Figure shows the SE mode and the right side of the Figure shows the BSE mode. The pores are more rounded during SLPS as shown in Fig 12 (b).

## Conclusions

The sintered density of the stainless steel samples sintered by SLPS is higher than compared to the samples sintered by solid state sintering. During SLPS melt formation occurs within the particles leading to increased sintered density. Moreover, the liquid phase lead to the rounding of pores in the sample. But in the case of the stainless steel composites the condition was reversed. The composites sintered at 1250°C were having better sintered densities due to the rare earth effect of the  $Y_2O_3$  dispersoids. This was observed in the sintered microstructure of the samples. In future, work is planned to study the electrochemical behavior and oxidation properties of the sintered stainless steel composites. It is hypothesized that the 434L sample containing 10%  $Y_2O_3$  will result in better corrosion resistance and oxidation resistance than the other composites.

## Acknowledgement

The authors gratefully acknowledge the funding from All India Council for Technical Education (AICTE) for the present research.

## References

- 1) S. Lal, "Sintering of 316L Austenitic Stainless Steel- $Y_2O_3$  Particulate Composites," Ph.D. Thesis, Indian Institute of Technology, Kanpur, India, 1988.
- 2) S.K. Mukherjee, "Sintering of 434L Ferritic Stainless Steel- $Al_2O_3$  Particulate Composites," Ph.D. Thesis, Indian Institute of Technology, Kanpur, India, 1984.
- 3) J. S. Hirschhorn, Introduction to Powder Metallurgy, American Powder Metallurgy Institute, Princeton, NJ, USA.

- 4) R.M. German, "Quantitative Theory for Supersolidus Liquid Phase Sintering," *Powder Metallurgy*, 1991, vol. 34, pp. 101-107.
- 5) R.M. German, "Supersolidus Liquid Phase Sintering; Part I: Process Review," *International Journal of Powder Metallurgy*, 1990, vol. 26, pp. 23-33.
- 6) R. M. German, Sintering Theory and Practice, John Wiley and Sons, Inc., New York, USA, 1996.
- 7) J.A. Lund and S.R. Bala, "Supersolidus Sintering," *Modern Developments in Powder Metallurgy*, H.H. Hausner and W.E. Smith (eds.), Metal Powder Industries Federation, Princeton, NJ, USA, 1974, vol. 6, pp. 409-421.
- 8) R. Tandon, "Densification Mechanisms and Microstructural Evolution Leading to High Density Processing of Prealloyed Powders in Supersolidus Liquid Phase Sintering," Ph.D. Thesis, The Pennsylvania State University, University Park, USA, 1995.
- 9) A. Lal, "Mechanisms and Mechanics of Shape Loss During Supersolidus Liquid Phase Sintering," Ph.D. Thesis, The Pennsylvania State University, University Park, USA, 1999.
- 10) A. Lal, R. Iacocca and R.M. German, "Densification During Supersolidus Liquid Phase Sintering of Nickel-base Prealloyed Powder Mixtures," *Materials and Metallurgical Transactions A: Physical Metallurgy and Material Science*, 1999, vol. 30, n. 8, pp. 2201-2208.
- 11) S. Ghosh, "Processing of Premixed and Prealloyed Bronze Through Transient and Supersolidus Liquid Phase Sintering," M.Tech Thesis, Indian Institute of Technology, Kanpur, India, 2001.

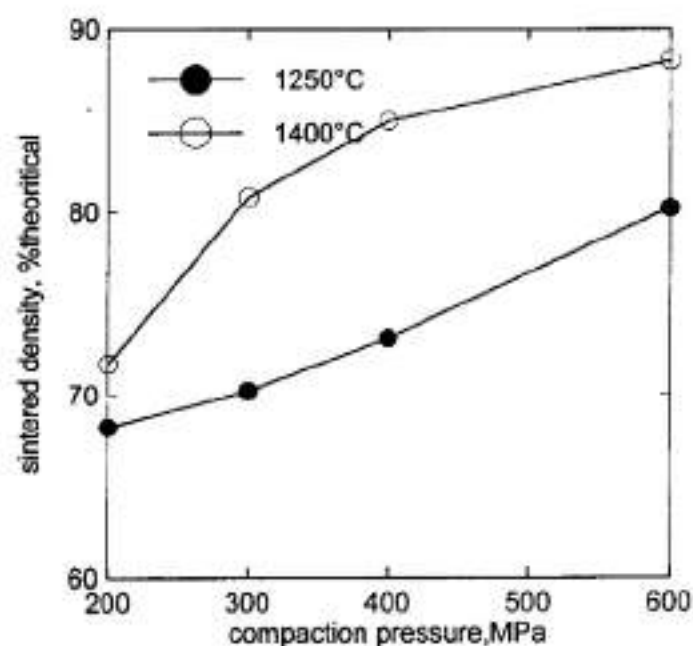


Figure 2. Variation of sintered density of 316L stainless steel with compaction pressure and sintering temperature.

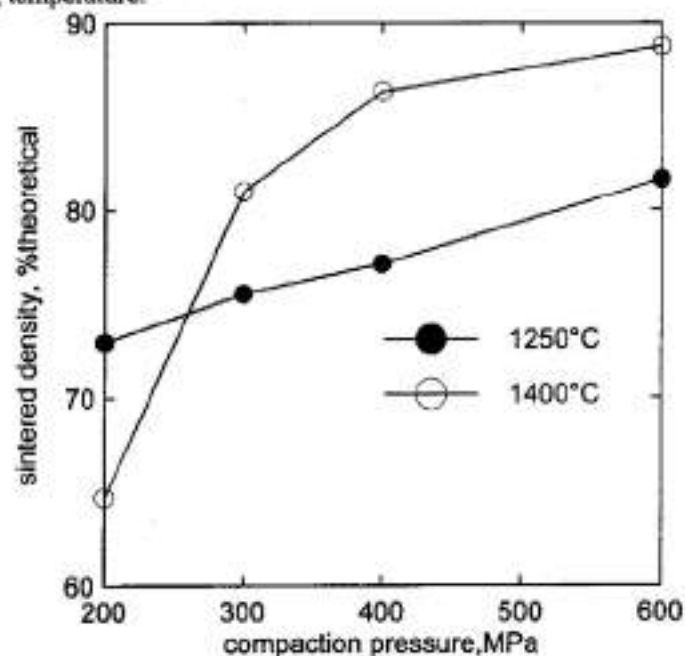


Figure 3. Variation of sintered density of 434L stainless steel samples with compaction pressure and sintering temperature.

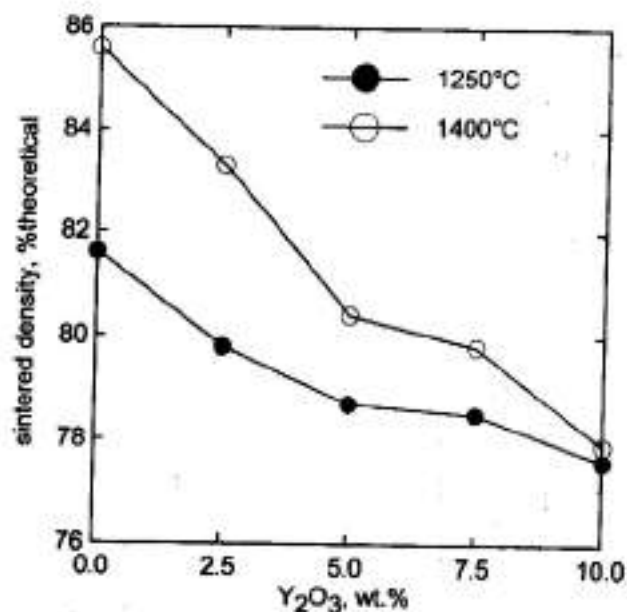


Figure 4. Variation of sintered density of 434L stainless steel samples with compaction pressure and sintering temperature.

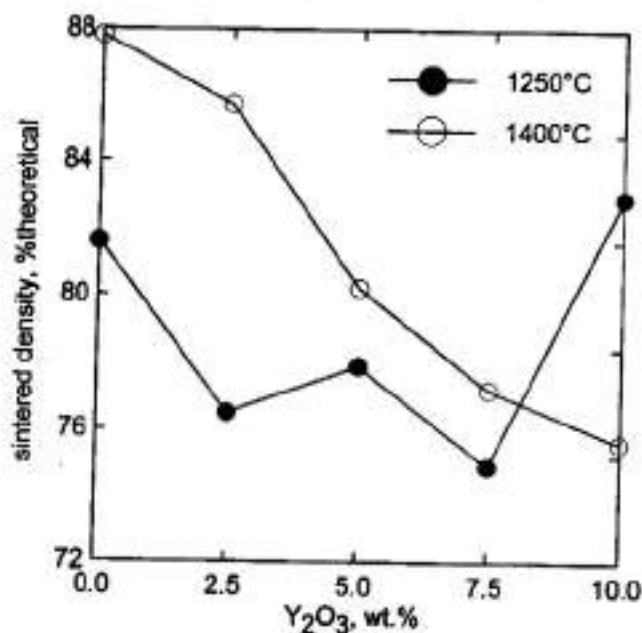


Figure 5. Variation of sintered density for 316L composites with addition of  $Y_2O_3$  and change in sintering temperature.

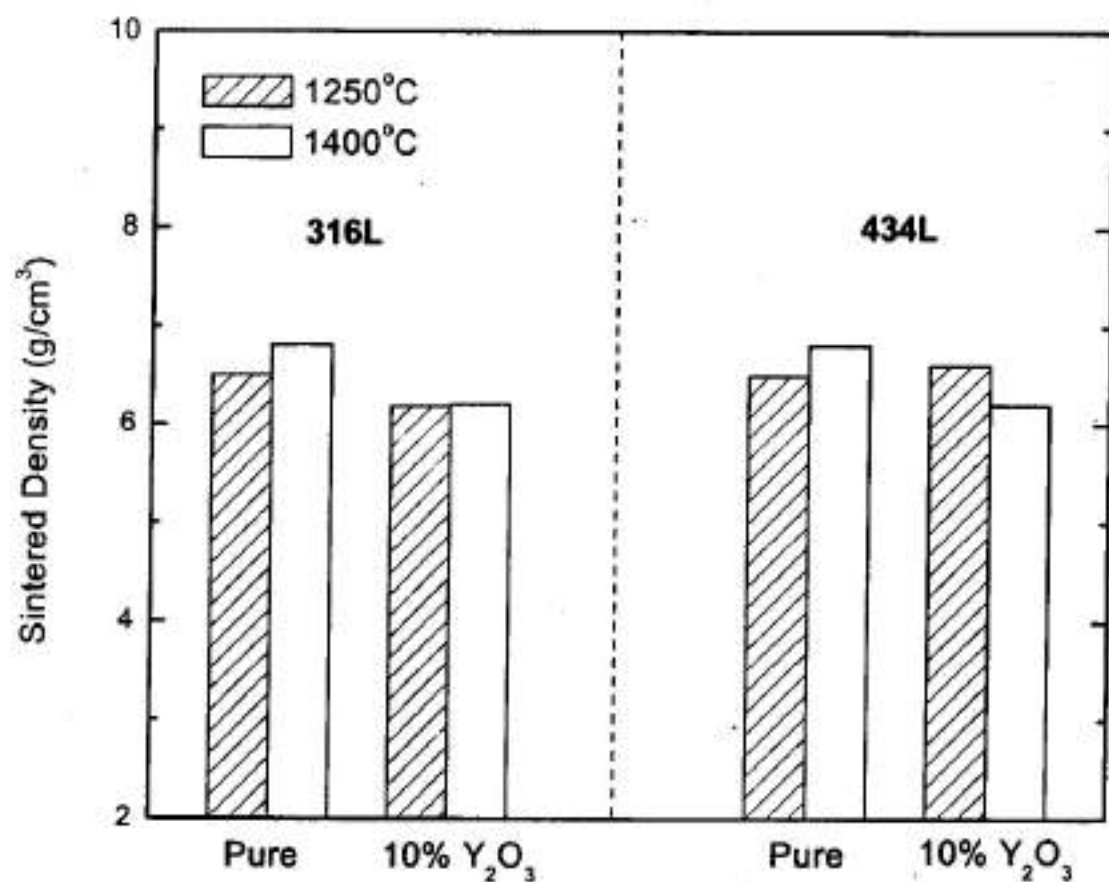
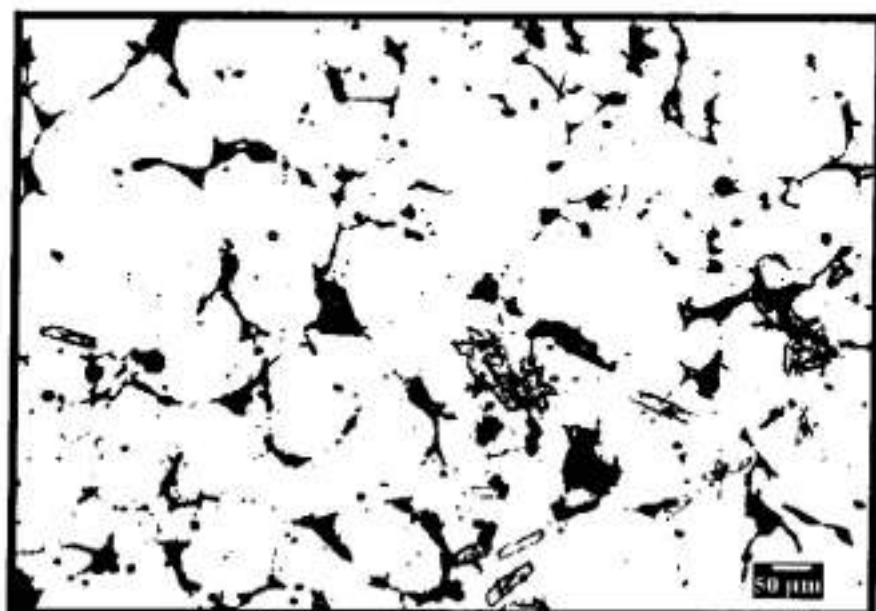
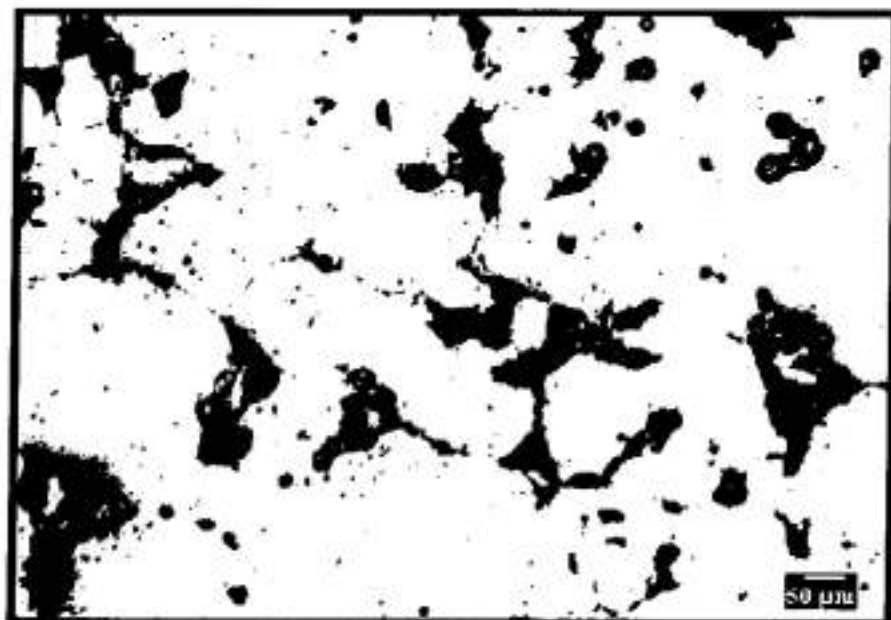


Figure 6. Comparison of sintered density with addition of Y<sub>2</sub>O<sub>3</sub> and sintering temperature in 316L and 434L stainless steels.



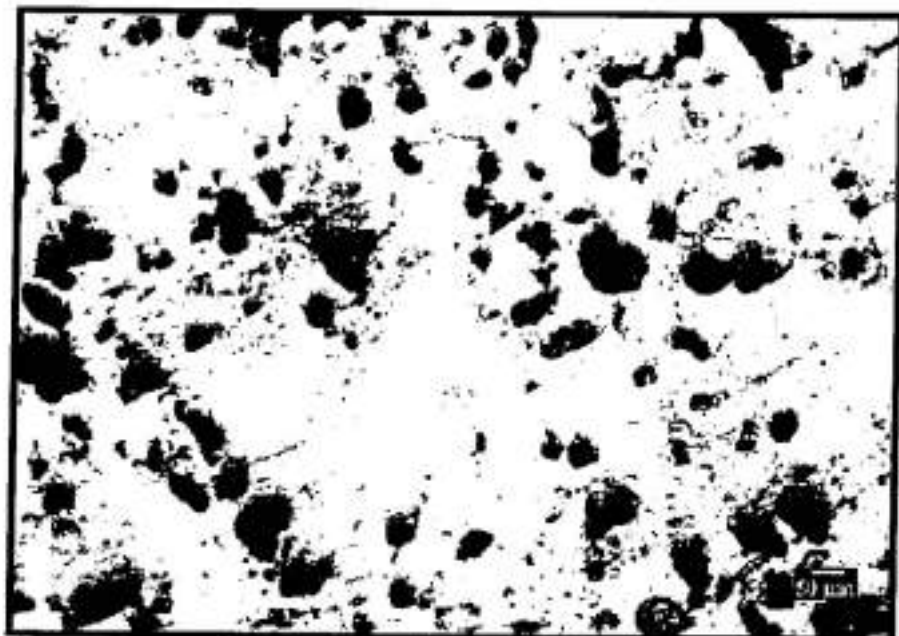
(a)



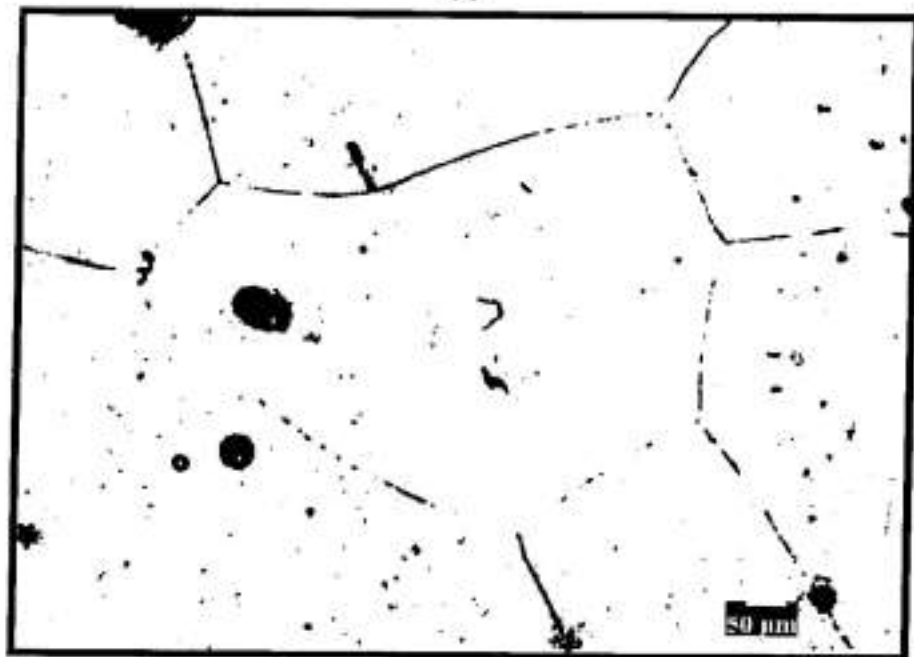
(b)

**Figure 6.** Optical micrograph of 316L P/M stainless steels sintered at (a) 1250°C and (b) 1400°C. The samples were compacted at 600MPa.



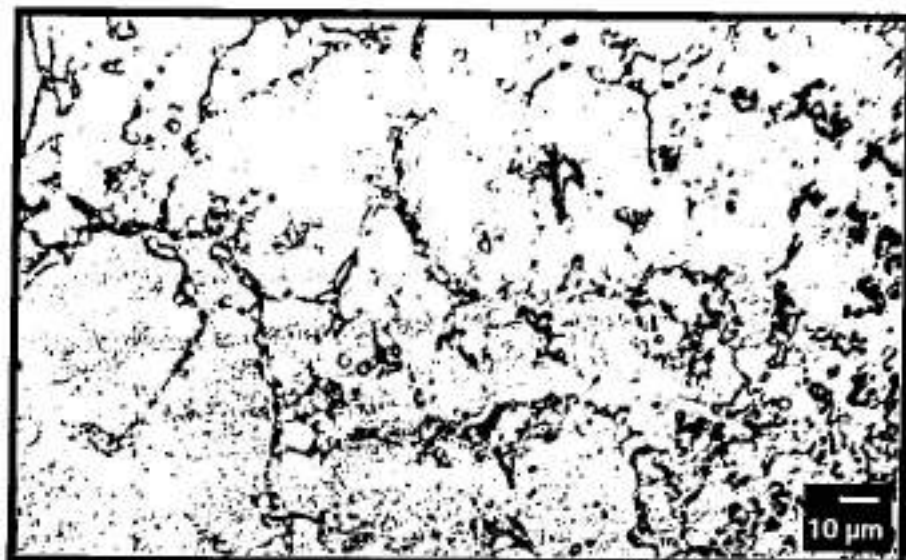


(a)

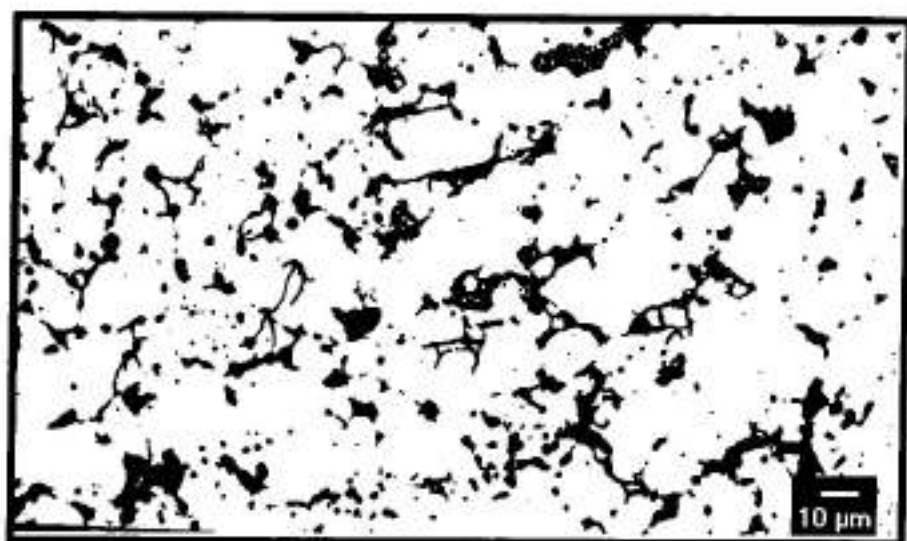


(b)

**Figure 7.** Optical micrographs of 434L stainless steels sintered at (a) 1250°C and (b) 1400°C. The samples were compacted at 600 MPa pressure.

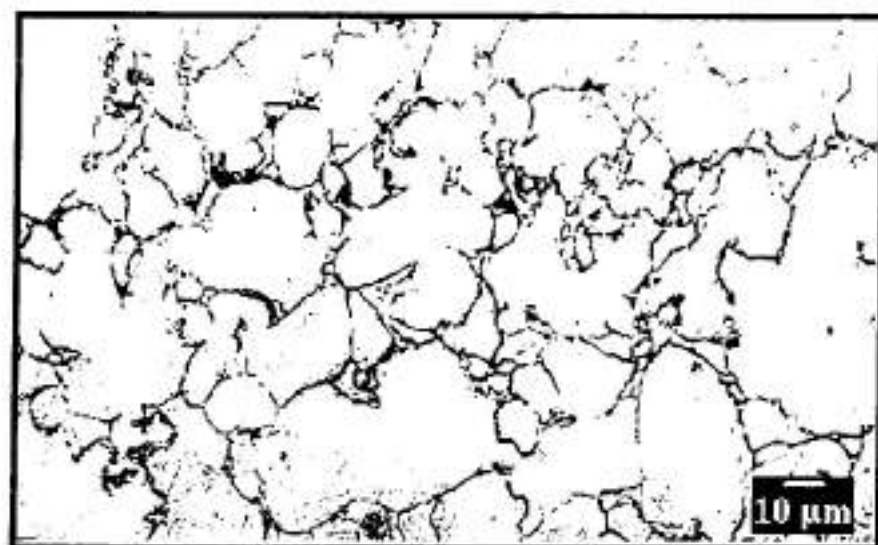


(a)

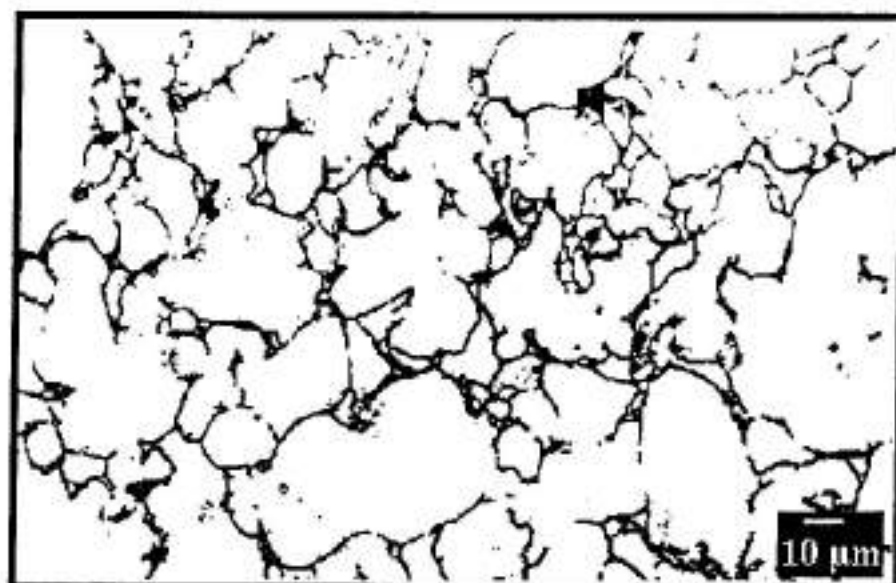


(b)

**Figure 8.** SEM micrograph of 316L+10% Y<sub>2</sub>O<sub>3</sub> stainless steel composite sintered at 1250°C in (a) SE mode and (b) BSE mode showing the surface porosity.

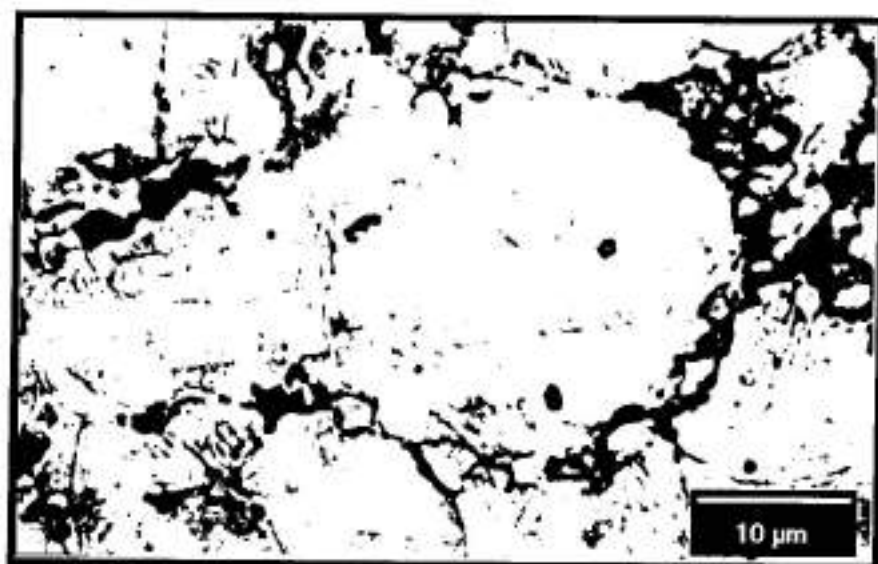


(a)



(b)

**Figure 9.** SEM micrograph of 316L+10% Y<sub>2</sub>O<sub>3</sub> stainless steel composite sintered at 1400°C in (a) SE mode and (b) BSE mode showing the surface porosity.



(a)



(b)

**Figure 10.** SEM micrograph of 316L+10% Y<sub>2</sub>O<sub>3</sub> stainless steel composite sintered at (a) 1250°C and (b) 1400°C showing arrangement of Y<sub>2</sub>O<sub>3</sub> at the surface.

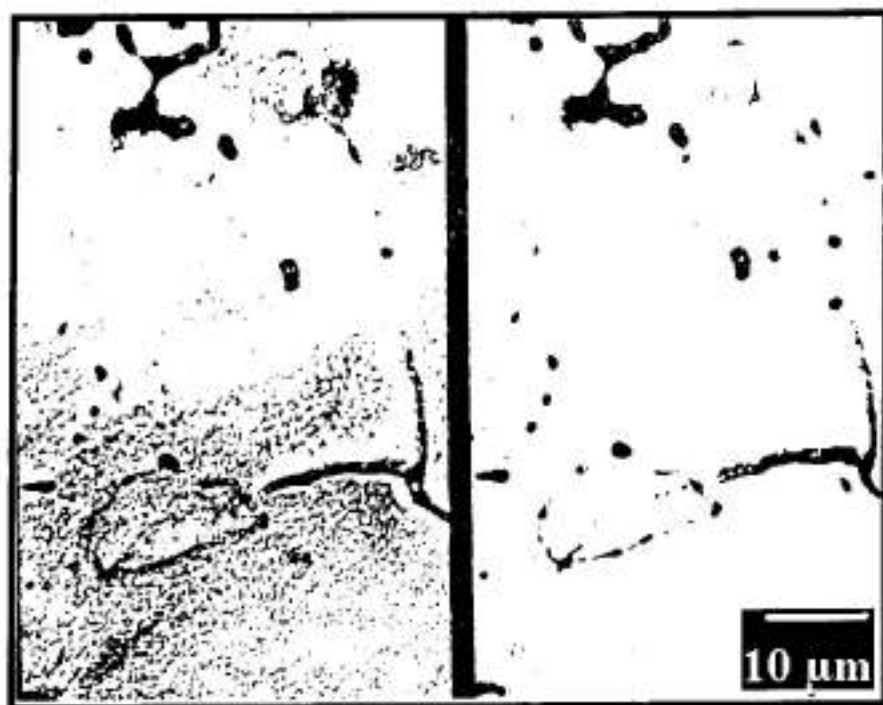


(a)



(b)

Figure 11. SEM micrographs of 434L + 10% Y<sub>2</sub>O<sub>3</sub> composites sintered at (a) 1250°C and (b) 1400°C.



(a)



(b)

**Figure 12.** SEM micrograph of 434L + 10% Y<sub>2</sub>O<sub>3</sub> composites sintered at (a) 1250°C and (b) 1400°C.

## **CORRELATION BETWEEN THERMAL SHOCK RESISTANCE AND THE SALIENT PARAMETERS OF ALUMINA BASED SELF-FLOW CASTABLES**

**K.Sankaranarayanan and Paramanand Singh**

Department of Metallurgical Engineering

IIT Madras, Chennai-600 036, India

Email: ps@iitm.ac.in

### **Abstract**

The refractories are subjected to thermal shock frequently during operation, which affects the life of the refractory structures. The effect of three important parameters such as grain size, temperature difference and number of thermal cycles on the retained modulus of rupture of alumina based ultra-low cement self-flow castable has been correlated and optimized using response surface design. Among the three parameters, the temperature difference has shown dominating effect compared to grain size and number of thermal cycles. The grain size distribution has shown considerable effect on retained modulus of rupture.

**Keywords:** Self-flow castables, Thermal shock resistance parameter, Thermal shock damage resistance parameter, Alumina based self-flow castable

### **Introduction**

A refractory castable is a combination of refractory grain and a suitable amount of bonding agent that, after the addition of a proper liquid, is generally poured into place to form a refractory shape or structure, which becomes rigid because of chemical action [1]. Self-flow castables (SFC) are characterized by a consistency after mixing which allow them to flow and de-air without application of vibration. SFC can be low-cement castable (LCC) or ultra-low cement castable (ULCC) or no cement castable (NCC) [2]. The free-flow behaviour of a SFC which is a predominant property required for installation of castable structure is strongly dependent on particle size (PSD) distribution as well as particle size [3-5]. Apart from free-flow, which defines the quality of SFC at room temperature, there are other properties directly related to refractory grain size at high temperature. Thermal shock resistance is one among them that determines the life of the refractory structure at application i.e., at high temperature.

Degradation of refractories and ceramics due to thermal shock is an important area of research since many years (6-18). Under operation, fluctuation of temperature leads to thermal stress



generation and damages the refractory structure. Thermal shock resistance of a refractory structure is generally evaluated using  $R$  parameters. These parameters can be broadly classified into two categories [6-8]

- a) Thermal shock fracture resistance parameter (Kingery's parameter,  $R$ )
- b) Thermal shock damage resistance parameters (Hasselmann parameter,  $R^{III}$  and  $R_d$ )

$$R_{th} = \sigma (1 - \nu) / \alpha E \quad [1]$$

$$R^{III} = E \gamma_{wg} / \sigma_f^2 (1 - \nu) \quad [2]$$

$$R_d = (\gamma_{wg} / \alpha^2 E)^{1/2} \quad [3]$$

where  $\sigma$  is the modulus of rupture in  $MPa$ ,  $\nu$  is the Poisson's ratio,  $\alpha$  is the thermal expansion coefficient,  $E$  is the modulus of elasticity and  $\gamma_{wg}$  is the work of fracture.

The parameter  $R$  represents the resistance of the refractories to the fracture initiation by very severe thermal shock and is calculated by equation (1).  $R^{III}$  and  $R_d$  represent the resistance of the refractory to thermal shock damage by kinetic crack growth and resistance of the refractory to quasistatic crack growth (equation 2 and 3) respectively.

There has been many experimental work carried out to evaluate the thermal shock resistance parameters for refractory brick and castables for various alumina content, aggregate distribution, aggregate size, aggregate shape and aggregate strength etc. [11-19]. Now a day's ultrasonic velocity method is also used to predict the thermal shock resistance behaviour of refractory castable [20].

The present investigation attempts to correlate, amount of coarse grain content, temperature difference and number of thermal cycles on the thermal shock resistance of ultra-low cement self-flow castable through design of experiments.

## EXPERIMENTAL WORK

### Design of Experiment

In the present investigation three important variables, such as amount of coarse grain content, temperature difference and number of thermal cycles which affect the thermal shock resistance were chosen at five levels and experiments were conducted using central composite design (CCD) and analysis were carried out using response surface methodology. Central composite design (CCD) basically consists of full or fractional factorial design of 2 level factors with center points and star points (also called as axial points). The details of CCD can be found elsewhere [21-24]. This can be written as:

$$\text{Total number of design points} = 2^k + 2k + n_0 \quad [4]$$

where,  $k$  is the number of variables.

$2^k$  is the complete or fraction of a  $2^k$  factorial design, where the factor levels are coded to the usual  $-1$  and  $+1$  values. This is called the fractional portion of the design.  $n_0$  is the center points ( $n_0 \geq 1$ ) in this case 6,  $2k$  axial points on the axis of each design variable at a distance of  $\alpha$  from the design center. This portion of design is called the axial portion.

The variables  $X_i$  were coded as  $x_i$  according to the following equation.

$$x_i = [(X_i - X_0) / \Delta X_i] \quad [5]$$

Where  $x_i$  = code value,  $X_0$  = central value,  $\Delta X_i$  = step change and  $X_i$  = actual value

In this investigation, the design with three important variables consists of 20 experiments. Among them 8 experiments are designed with combination of two level factorial design i.e., high (+1) and low level (-1) of factors, 6 center points (0,0) and 6 star points with the combinations of  $-\alpha$ ,  $+\alpha$  and 0 levels. The  $\alpha$  value is 1.682. Table 1 shows the factors and their levels chosen in the current study. The design matrix is given in Table 2.

**TABLE 1 Selection of Factors and Level**

Factors	Level				
	-1.682	-1	0	+1	+1.682
3/6 Mesh (G)	2	6	12	18	22
Temperature (T)	565	700	900	1100	1240
Cycles (N)	1	3	6	9	11

### Particle Size Distribution

The particle size distribution of SFC was calculated using LISA (Elkem India Private Limited) particle size analyzer. The particle size distribution for the castable containing 22 wt% and 2wt% coarse grain content is shown in Fig.1 and 2 respectively.

TABLE 2 Design Matrix

Expt.No	Coarse grain content	Temperature	Number of cycles
1	-1	-1	-1
2	+1	-1	-1
3	-1	+1	-1
4	+1	+1	-1
5	-1	-1	+1
6	+1	-1	+1
7	-1	+1	+1
8	+1	+1	+1
9	-1.682	0	0
10	+1.682	0	0
11	0	-1.682	0
12	0	+1.682	0
13	0	0	-1.682
14	0	0	+1.682
15	0	0	0
16	0	0	0
17	0	0	0
18	0	0	0
19	0	0	0
20	0	0	0

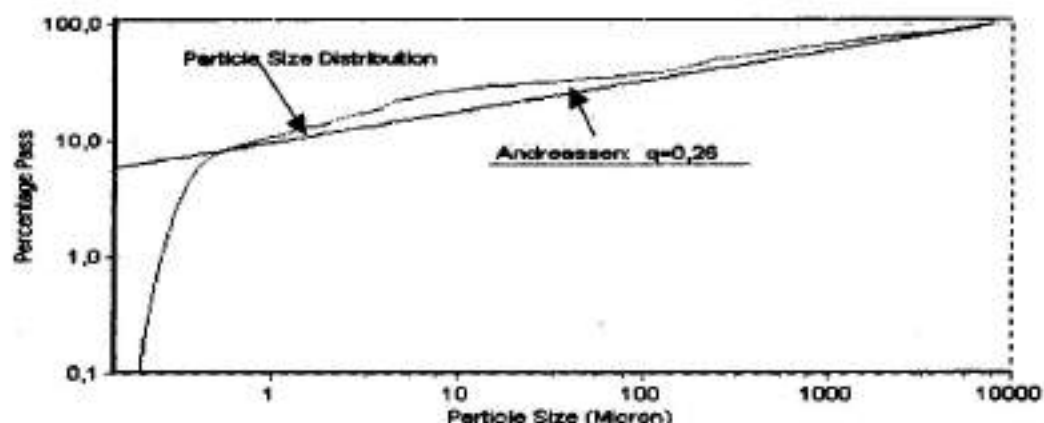


Fig.1 Particle size distribution of SFC containing 22 wt% coarse grain content

The Andreassen exponent changes from 0.26 to 0.30 when the coarse aggregate (3/6#) content varies from 22 wt% to 2 wt%. The Andreassen formula representing the continuous particle size distribution is given by

$$CPFT = (d/D)^q \quad [6]$$

where,  $CPFT$  is the cumulative % finer than,  $d$  is the particle size ( $\mu\text{m}$ ),  $D$  is the maximum particle size ( $\mu\text{m}$ ) and  $q$  is the Andreassen exponent.

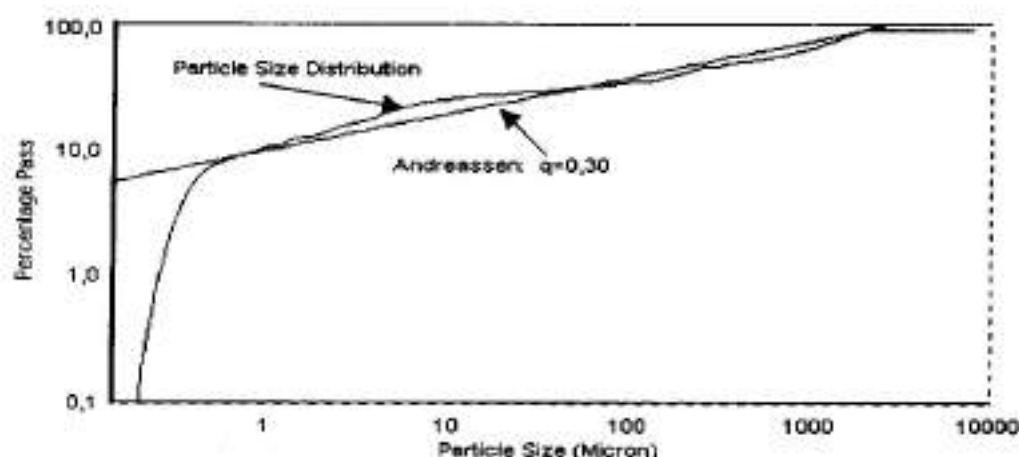


Fig.2 Particle size distribution of SFC containing 2 wt% coarse grain content

### Castable Mixing and Sample Preparation

The ingredients including water were kept in a climate chamber (Weiss Umwelttechnik, GmbH model SBI<sup>500</sup>) at the required temperature for 24 hrs. Then they were dry mixed in a mixer machine for 4 min followed by wet mixing for 3 min with the required water. The free-flow of the mix was measured as per ASTM C-230 and the % free-flow was calculated using the formula given below [19].

$$\% \text{ Free flow} = [(D_{av} - D_c) / D_c] \times 100 \quad [7]$$

where,  $D_{av}$  is the average diameter after flow test (mm) and  $D_c$  is the diameter of the flow cone ( $100 \pm 1/2$  mm). The free-flow reduced from 100% to 50% when the coarse grain content varied from 24 to 0 wt%. Samples of  $150 \times 25 \times 25 \text{ mm}^3$  were cast into a wooden mould for five different

composition containing coarse fraction varying from 2 wt% to 22 wt%, cured for 24 hrs at 25°C. The samples were demoulded, dried at 110°C followed by firing at 1370°C and cooled to room temperature.

### Apparent Porosity and Bulk Density

The apparent porosity and bulk density of fired castable were carried out as per ASTM C201.

### Modulus of Rupture ( $\sigma$ ) and Modulus of Elasticity (E)

The modulus of rupture was tested by three point bending test using NESTCH apparatus, using three-point bending test. The MOR was calculated using the formula

$$\sigma = 3PL / 2BD^2 \quad [8]$$

where,  $\sigma$  = Modulus of rupture in MPa,  $P$  = Load in Newton,  $L$  = Span length, m  $B$  = Breadth, m and  $D$  = Thickness, m

The *MOE* of the samples were measured by ultrasonic velocity method (Pandit, C.N.C Electronics Ltd., London, England). *MOE* and ultrasonic velocity are related to *MOE* by the following formula;

$$E = V_L^2 \rho [(1+\mu) (1-2\mu) / (1-\mu)] \quad [9]$$

where  $V_L$  - ultrasonic velocity m/s,  $\rho$  - bulk density in kg/m<sup>3</sup> and  $\mu$  - Poisson's ratio (In this case  $\mu=0.2$  was adopted).

### Work of Fracture ( $\gamma_{wof}$ )

The 25.4 mm × 25.4 mm × 150 mm specimens were center notched with a 0.8 mm thick diamond saw to form a chevron-shaped notch. Specimens were tested at a crosshead speed of 0.05cm/min with a span length of 12mm. The area under the load-displacement curve was determined to calculate the energy required to create the new crack surfaces. The following equation was used to calculate the work of fracture.

$$\gamma_{wof} = [Fdx / 2A] \quad [10]$$

where,  $\int Fdx$  is the work required for the formation of new surfaces and  $A$  is the cross-sectional area of the fracture surface.

### Thermal Shock Test

The samples were inserted in furnace, preheated at 560, 700, 900, 1100 and 1240°C and soaked for 30 minutes. Then they were removed from furnace and air quenched under forced air for 30 minutes. The no of cycles for thermal shock were as per design matrix as shown in Table.2. The MOR and MOE of the samples were measured before and after the thermal shock test.

### Results and Discussion

Fig.3 shows the apparent porosity and bulk density of the castable after firing at 1370°C. The apparent porosity increases from 12 to 15% as top grain size decreases. The bulk density has shown the reverse trend.

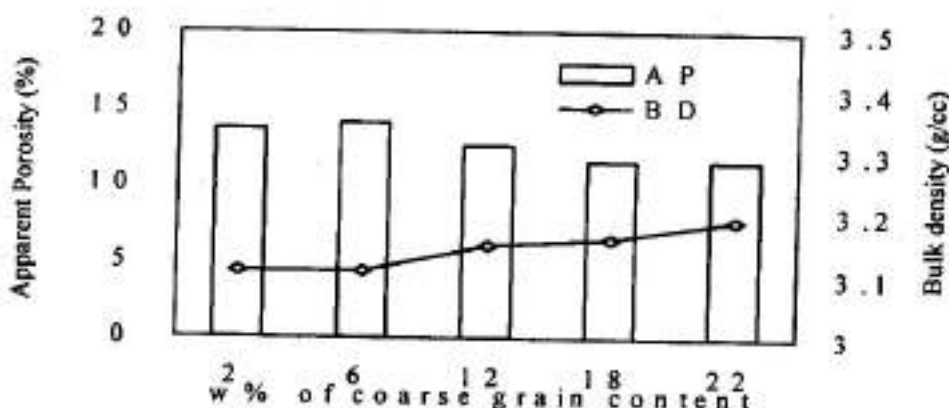


Fig.3 Apparent porosity and bulk density as a function of wt% coarse grain content.

The *MOR* of the samples decreases with increasing coarse grain content whereas the *MOE* remains almost constant and independent (Fig.4) of grain size. The slight reduction in *MOE* for fine grain structure may be because of the increase in the casting water and increase in apparent porosity.

The  $\gamma_{wef}$  increases with coarse grain content (Fig.5). It is known that within the main cracks, following wake region, extensive aggregate grain interlocking and frictional effects are predominant, especially for large aggregate such as those in refractory concretes. When a crack passes these aggregates, severe wedging of grains within the following wake region may be expected. This might be the primary reason for refractories to have large work of fracture (9). Since the crack takes a tortuous path around coarse grain the crack path increases with increase in the amount of coarse grain in the castable leading to increase in the work of fracture. The increasing trend of work of fracture with grain size clearly indicates that the energy required for crack propagation is high for the coarse grained structure.

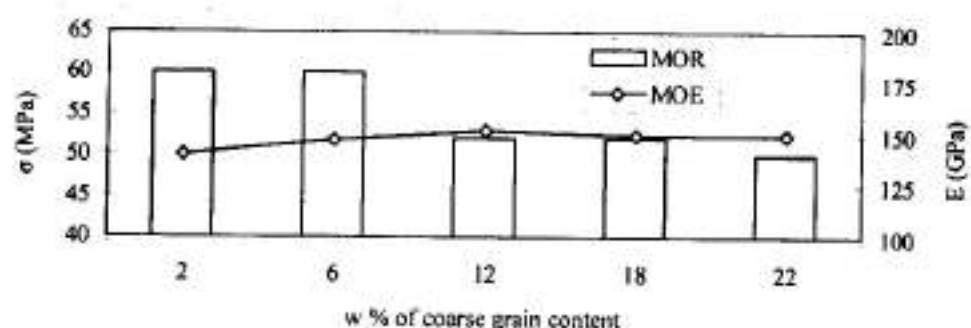


Fig.4 MOR and MOE as a function of coarse grain content

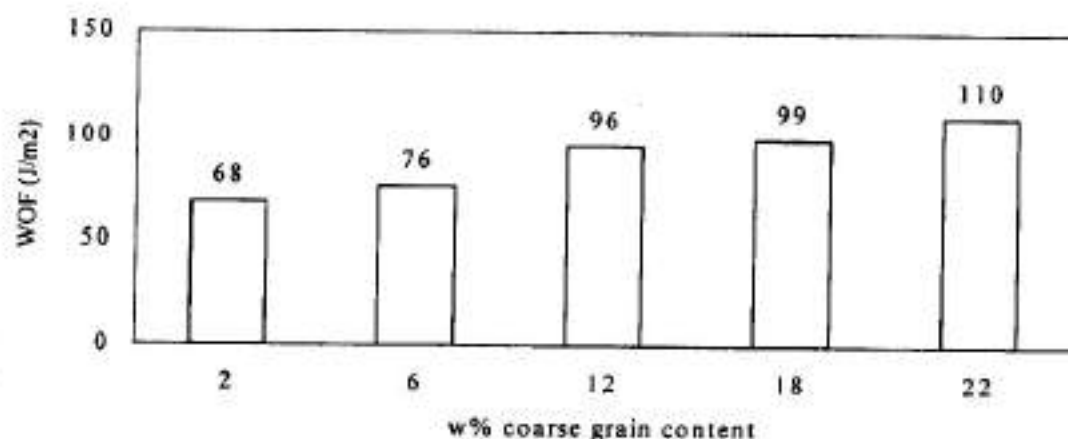


Fig.5 Work of fracture as a function of coarse grain content.

The calculated values of  $R$ ,  $R^{III}$  and  $R_{SY}$  parameters values are given in the Table.3. The  $R$  value is decreasing because the value of  $\sigma$  decreases and  $E$  increases with grain size. The  $R^{III}$  value is increasing with grain size whereas the  $R_{SY}$  value is maximum for 18 wt% coarse grain content and remains the same with further addition. This means addition of coarse grain content beyond a level does not bring any improvement in the damage resistant parameter.



TABLE 3 Calculated values of parameters  $R_{90}$ ,  $R^{III}$  and  $R_{ST}$ 

% coarse grain content	$R_{90}$ ( $^{\circ}\text{C}$ )	$R^{III}$ ( $\text{m}\times 10^{-3}$ )	$R_{ST}$ ( $\text{m}^{1/2}\times\text{C}$ )
2	42.328042	3.30	2.72
6	42.406573	3.88	2.95
12	39.653929	5.90	3.40
18	36.017316	6.86	3.33
22	32.921811	8.25	3.34

The SEM photographs of the fracture surface of samples containing 0 wt%, 12 wt% and 24 wt% are shown in Fig.5(a) and (b) respectively. The mixed mode fracture observed in the fracture surface.

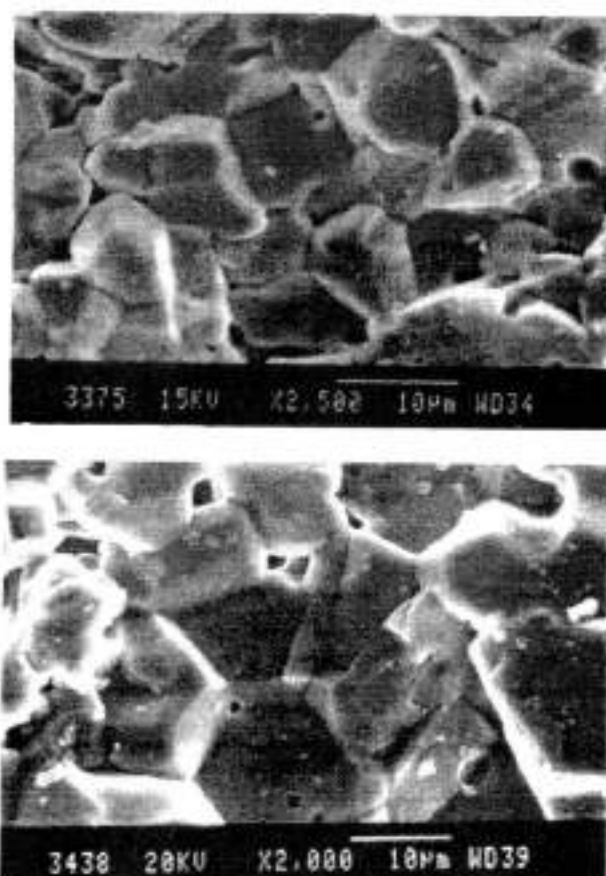


Fig. 5 Fracture surface of sample with (a) 12 wt% and (b) 22% coarse grain content

## Analysis of Variance (ANOVA)

### Retained MOR

The measured values of response i.e., the retained MOR are subjected to analysis of variance (ANOVA) as shown in Table 4. For the current analysis the Design-Expert® version 6, software for experiment design (developed by Stat-Ease, Inc. 2021 East Hennepin Avenue, Suite 191, Minneapolis, MN 55413) is used.

Table 4. ANOVA for retained MOR

Source	Sum of square, SS	DF	Mean square $S^2 = SS/DF$	F Value $= S_m^2 / S_e^2$	Prob>F
Model, m	8334	9	926	4.57	0.013
Error, e	2024	10	202.4		
Total, t	10358	19			

The mean squares are obtained by dividing the sum of squares of each of the two sources of variation (model and error variance) by the respective degrees of freedom. The F value, known as Fisher variance ratio ( $= S_m^2 / S_e^2$ ) provides the information on how well the factors describe the statistical variation in the data from its mean. It is generally calculated by dividing mean square due to model variance ( $S_m^2$ ) by that due to error variance ( $S_e^2$ ). The higher the F value from unity the greater is the certainty of the factors in explaining the variation in the data about its mean. The correlation coefficient,  $R^2$  is generally used to provide correlation measures for the estimation of the regression model. The closer the  $R^2$  value to unity the better is the correlation between the observed and predicted values. The value of  $R^2=0.81$  indicates the high degree of correlation between the observed and predicted value.

The individual effect of factors on retained MOR is shown in Fig.6 as perturbation plot. The perturbation plot helps to compare the effect of all the factors at a particular point in the design space. The response is plotted by changing only one factor over its range while holding of the other factors constant at center level. The increase in temperature difference and number of thermal cycle is reducing the retained MOR whereas the increase of grain size increases the retained MOR.

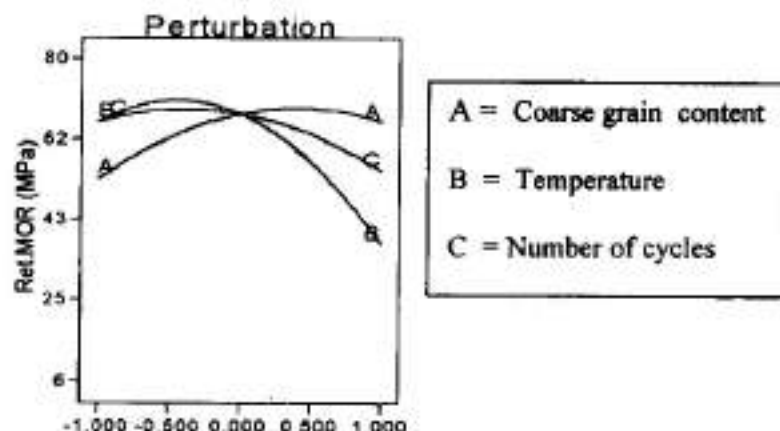


Fig.6 Perturbation plot for factors showing individual effect of factors.

### Interactions

The interactions between the factors are given in Fig.7a-c. The interaction between coarse grain content and temperature shows that the maximum MOR is achieved in the grain content of 18% in the castable. The interactions between the temperature and number of cycles reveals the fact that the retained MOR will be more as the temperature difference is less. It is observed from Fig 7c, the interaction between coarse grain content and number of cycles, the retained MOR is maximum when the coarse grain content approaches the middle value of around 15 wt%. It is clear from the interactions that the retained MOR is always less, when there is no coarse grain in the structure.

Based on the interactions and single factor effects from ANOVA the retained MOR is correlated with the factors as follows:

$$\text{Ret.MOR} = 67.23 + 6.56 \cdot A - 14.07 \cdot B - 5.57 \cdot C - 8.15 \cdot A^2 - 15.75 \cdot B^2 - 7.26 \cdot C^2 - 1.12 \cdot A \cdot B + 0.13 \cdot A \cdot C - 1.62 \cdot B \cdot C \quad [11]$$

Based on this relationship the calculated values of retained MOR are plotted against actual values as shown in Fig.8. The higher value of correlation coefficient  $R^2$  indicates close resemblance between the experimental value and predicted values



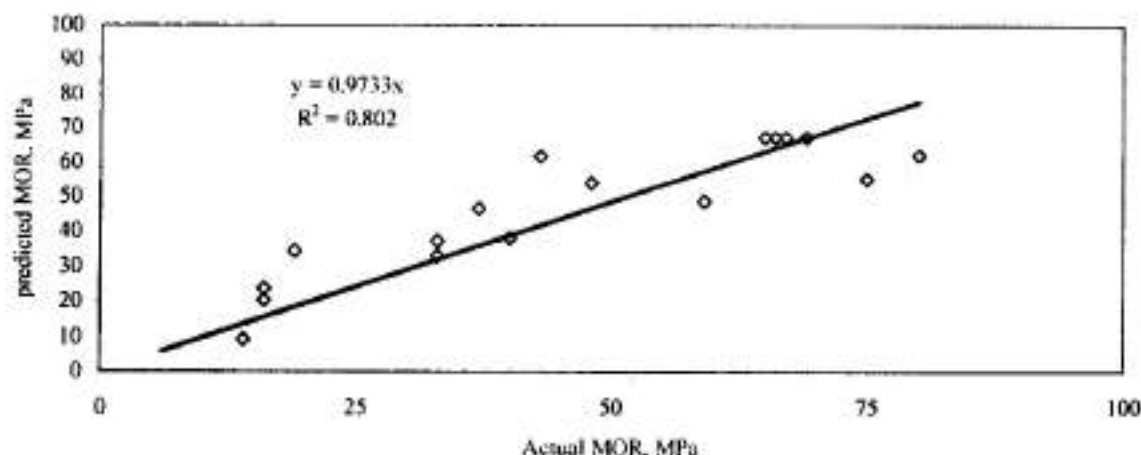


Fig.8 Predicted Vs Actual % retained MOR

## Conclusions

Increasing the amount of coarse grain content decrease the apparent porosity, increases the bulk density, decreases MOR, increases work of fracture whereas the MOE remains almost constant and is independent of grain size. The increase of coarse grain content decreases  $R$  while increases  $R_{III}$   $R_{ST}$  values. The ANOVA studies indicate that the influences of factors are in the order temperature difference followed coarse grain content and number of thermal cycles. The retained MOR is maximum for around 15-18 wt% coarse grain content.

## References:

1. Annual Book of ASTM Standards, Vol. 15.01. Standard Terminology Relating to Refractories, C71-97 pp14-18 (1988).
2. F. -G. Brachet, R. Avis, B. Clavaud, P. de Lafarge and P. Meunier, "Self-Flowing Refractory Castables", *Proceedings of UNITECR '91*, Aachen, Germany, pp186-188 (1991)

3. B.Myhre and K.Sunde, "Alumina based castable with very low contents of hydraulic compound. Part-I The effect of binder and particle size distribution on flow and set", *Proceedings of UNITECR95* Kyoto, Japan, Nov19-22 (1995).
4. B.Myhre, "The effect of particle size distribution on flow of refractory concrete", *The Am.Cer.Soc 30<sup>th</sup> Annual refractories symposium*, St.Louis, (1994).
5. B.Myhre, "particle size distribution and its relevance in refractory castable", *Proceedings of 2<sup>nd</sup> India international refractories congress*, ppl/147-1/156(1996).
6. W.D.Kingery, "Factors affecting thermal shock resistance of ceramic materials" *J.Am.Cer.Soc.* Vol.38 (1) 1, pp3-15 (1955).
7. D.D.H. Hasselman, "Elastic energy at fracture and surface energy as design criteria for thermal shock" *J.Am.Cer.Soc.* vol.38(11),pp535-540 (1955).
8. D.D.H. Hasselman, "Unified theory of thermal shock fracture initiation and crack propagation in brittle ceramics", *J.Am.Cer.Soc.* Vol.52 (11), pp600-604 (1969).
9. R.C.Bradt, "Fracture testing of refractories, past present and future", *Proceedings of the 2<sup>nd</sup> International conference on refractories*, Nov 10-13, Tokyo, Japan, pp61-68 (1987).
10. J.Nakayama and M.Ishisuka, "Experimental evidence for thermal shock damage resistance", *Am.Cer.Soc. Bull.*, vol.45 (7), pp666-669 (1966).
11. C.E.Semler, Jr and T.H.Hauisher and R.C.Bradt, "Thermal shock of alumina refractories damage resistance parameters and the Ribbon test", *Am.Cer.Soc.Bull.*, vol.60 (7), pp724-729 (1981).
12. J.Horney, "Aggregate distribution effects on the mechanical properties and thermal shock behaviour of model monolithic refractory systems", *New developments in monolithic refractories The Am.Cer.Soc. Inc.*, pp46-66 (1985).
13. McIntyre,S.E.L. and R.C. Bradt, "Elevated temperature fracture of a tabular alumina refractory aggregate", *UNITECR89*, ppl471-1480 (1989).
14. B.Mohammed, "Role of aggregates on properties and performance of ULCC based products", *In.proc.UNITECR '97*, 1, pp657-665. Am. Ceram. Soc., Louisiana. USA (1997).
15. S.N.Mamahonina and N.M.Permikina, " Corundum-Chromite refractories with improved thermal -shock resistance", *Ogneupory*, 32(11), ppl80-184 (1991).

16. G.A.Gogotsi, " Thermal shock resistance of heterogeneous ceramics and refractories", *Ogneupory*, 34 (11), pp539-547 (1993).
17. D.S.Whittemore and S.R.Pavlica, "Thermal shock resistance of 60-80% alumina brick", *Proceedings of UNITECR '97*, pp909-918(1997).
18. T.D.Volkov-Husovic, R.M.Jancic, Z.V.Popovic, K.T.Raic, " Comparison of critical  $\Delta T$ -values with the R-parameters of thermally shocked alumina refractories", *Interceram*, 46(1),pp13-15(1997).
19. M.Ishikawa, " The effect of shape of aggregates on fracture mechanical properties of monolithic refractories", *Taikubutsu overseas*, 13(2), pp35-38 (1993).
20. Niyogi,S.K. and A.C.Das, "Prediction of thermal shock behaviour of castable refractories by sonic measurements", 43(6) pp453-457 (1994).
21. Box and Wilson, "*Experimental Design*", Ann. of. Math. Statistics, 28,pp195-241(1957).
22. Opera,G. T.Troczynski and F.Esanu," Rheology studies on binding systems for self-flow refractory castable", *UNITECR97*, pp613-624 (1997).
23. Douglas C.Montgomery, *Design and Analysis of experiments*, Third edition, John Wiley & Sons (1991).
24. Keki.R.Bhote and Adi K.Bhote, *Word Class Quality, Using Design of Experiments to Make it Happen*, Second Edition,AMACOM, American Management Association, (2000).



## **STUDY OF PRODUCTION AND PROPERTIES OF COPPER-MICA COMPOSITE BY POWDER METALLURGY TECHNIQUE**

\*Vishal Arora

\*Gaurav Verma

\*Manisha Taneja

\*\*N.C.Upadhyay

### **Abstract**

Solid lubricants dispersed in metal matrices result in self-lubricating composites suitable for bearing and electrical contact application. Copper is a comparatively inexpensive elemental material used as electrical contacts and graphite is the most common solid lubricant. Copper graphite and silver graphite are the materials used for sliding or brush contacts under normal service conditions. Graphite dispersed in these composites is supposed to form a film between the mating surfaces, which imparts antiwear and antiseizure properties.

However under conditions of high temperature, low pressure, low humidity and oxygen generally present at high altitude, the film may disappear and metal-graphite composites may show rapid wear. It was reported that the wear rate of metal-graphite Composites above 100°C is twice that at a temperature below 95°C. It was also reported that graphite undergoes rapid oxidation under arcing conditions leaving to a higher wear rate of the copper-graphite contact strip. The arc and wear resistance of this material have been found to improve by substituting MoS<sub>2</sub> and matte for (A mixture of Cu<sub>2</sub>S and FeS) for graphite. Attempts have been made by a number of research workers to develop metal-mica composites as substitute materials for metal-graphite composites. It has been found that mica is a solid lubricant, which is superior to graphite under dry friction conditions because of its high oxidation resistance and chemical inertness. Nickel-mica composite is reported to be far superior to nickel-graphite composite under dry condition. Nickel-mica, silver-mica and aluminium alloy-mica

## COPPER-GRAPHITE COMPOSITES

Mixing copper powder and graphite powder manually made the following materials.

1. Pins
2. Journal Bearings

The pins and bearing were made by

- (i) Pure copper and by mixing
- (ii) 10% graphite powder and remainder copper powder
- (iii) 20% graphite powder and remainder copper powder
- (iv) 30% graphite powder and remainder copper powder

### Production of Pins and Bearings

Due to manual mixing of copper and graphite powder, there is no uniform distribution of graphite powder in the copper powder matrix.

When we apply a load more than 15 tons i.e. a pressure of 16.6 Kg. Per  $\text{mm}^2$ , the pins are broken which may be due to:

- (a) Improper bounding of graphite particles with copper particles.
- (b) Improper design of the die.

Similar problems were associated with bearings. After the compaction, the bearings were ejected from the die at a load of 500-1000 Kg. After removal from die, some expansion of dimensions of compacts also takes place. It is about 2-2.5 %. To obtain microstructure, the bearing samples were polished and pure bearing were etched with ferric chloride solution to reveal microstructure.

### Wear Test Results

Tests were carried to study the wear rates for all four samples (specimen). The results are summarized in table (1-2). The composition of the samples, the wear rate for each sample is shown in respective columns of the tables. The result is being plotted in fig. (1-3). It can be seen from the figures that

- (a) Wear rate decreases up to 20 % graphite and then increases almost linearly. This may be due to the squeezing of graphite from matrix.
- (b) As the load increases, the wear increases almost linearly. The wear rate is not uniform with applied load, which may be due to the smearing of graphite between the disc and

TABLE - I

Room temp. =  $28^{\circ}\text{C}$  -  $34^{\circ}\text{C}$ 

Radius = 0.0375 m

RPM = 1050

Weight = 100 gm.

Time = 30 min.

Circumference = 0.2357 m

Distance travelled =  $0.2357 \times 1050 \times 30 = 7425 \text{ m}$ 

S.N.	Sample No. (Pins)	Initial Weight (gms)	Weight after wear (gms)	Loss in weight (gms)	Wear Rate gm/m
1.	1. (3A) Pure Cu 15 T, 16.6 Kg/mm <sup>2</sup>	8.1446	8.1429	0.0017	$2.28 \times 10^{-7}$
2.	2. (2B) 10% gr. 15 T, 16.6 Kg/mm <sup>2</sup>	6.1802	6.1790	0.0012	$1.61 \times 10^{-7}$
3.	3. (5A) 20% gr. 15 T, 16.6 Kg/mm <sup>2</sup>	5.2374	5.2367	0.0007	$0.9 \times 10^{-7}$
4.	4. (6A) 30% gr. 15 T, 16.6 Kg/mm <sup>2</sup> (Broken during test)	2.8750	2.8731	0.0019	$2.55 \times 10^{-7}$

TABLE - 2

Room temp. = 28°C - 34°C

Radius = 0.0375 m

RPM = 700

Weight = 500 gm.

Time = 60 min.

Circumference = 0.2357 m

Distance travelled = 0.2357 x 700 x 60 = 9900 m

S.N.	Sample No. (Pins)	Initial Weight (gms)	Weight after wear (gms)	Loss in weight (gms)	Wear Rate gm/m
1.	1. (3A) Pure Cu 15 T, 16.6 Kg/mm <sup>2</sup>	8.1464	8.1446	0.0018	$1.81 \times 10^{-7}$
2.	2. (2B) 10% gr. 15 T, 16.6 Kg/mm <sup>2</sup>	6.1819	6.1802	0.0017	$1.71 \times 10^{-7}$
3.	3. (5A) 20% gr. 15 T, 16.6 Kg/mm <sup>2</sup>	5.2389	5.2374	0.0015	$1.51 \times 10^{-7}$
4.	4. (6A) 30% gr. 15 T, 16.6 Kg/mm <sup>2</sup>	4.7544	4.7524	0.0020	$2.02 \times 10^{-7}$

tip of the pin. Although wear rate is not uniform but increases as load increases (from 100 gms. to 500 gms in the present experiment).

### **Bearing Tests Results**

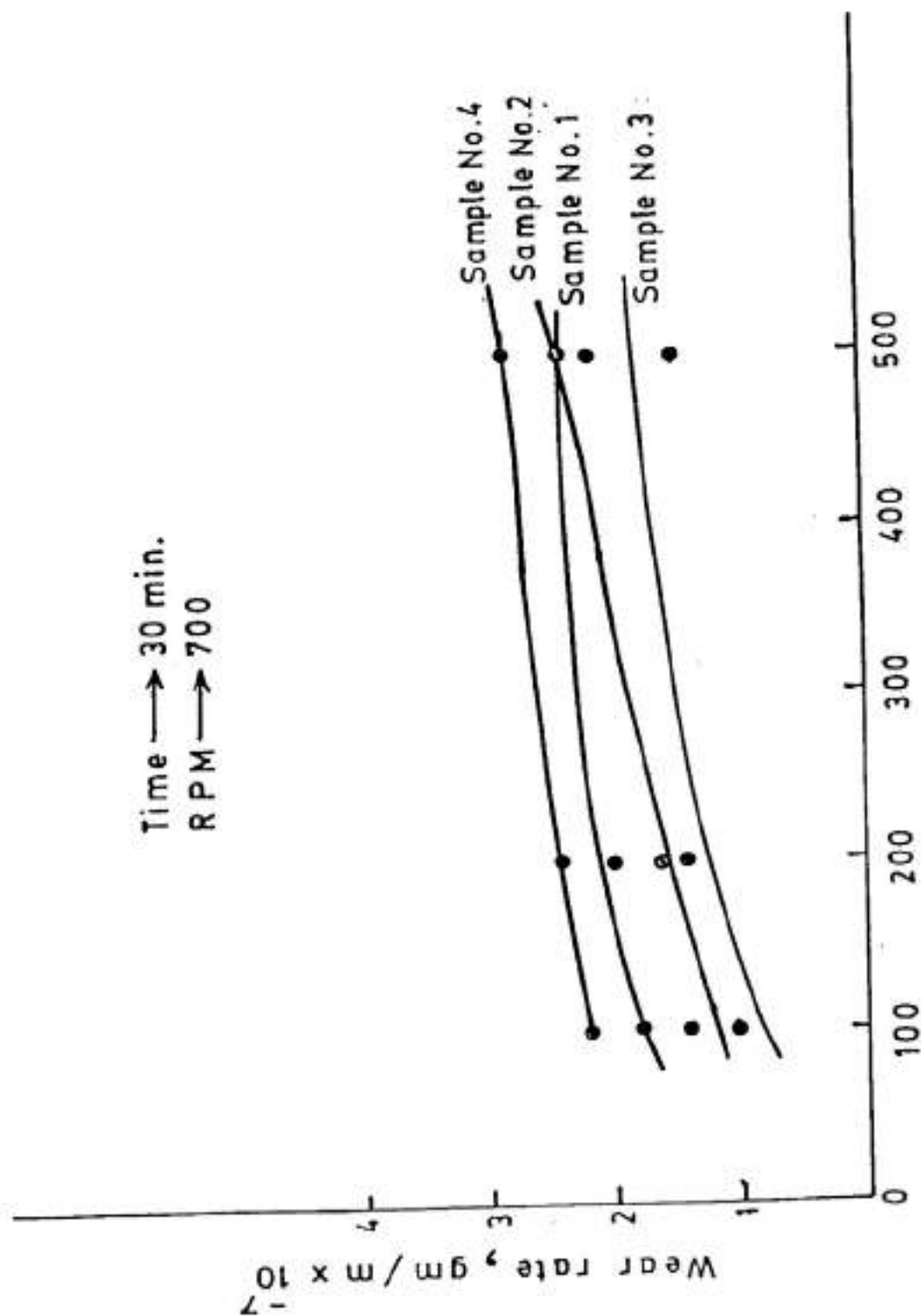
Bearing tests were carried out to measure coefficient of friction and bearing characteristic number (ZN/P) for all four samples (specimen). The composition of various samples is given in table (1). The results are summarized in table (1). The calculated values of coefficient of friction and bearing parameter for each load –speed combination have been shown in their respective columns of the tables. The test results are plotted in fig (5), which is similar to ideal curve shown in fig. 1.

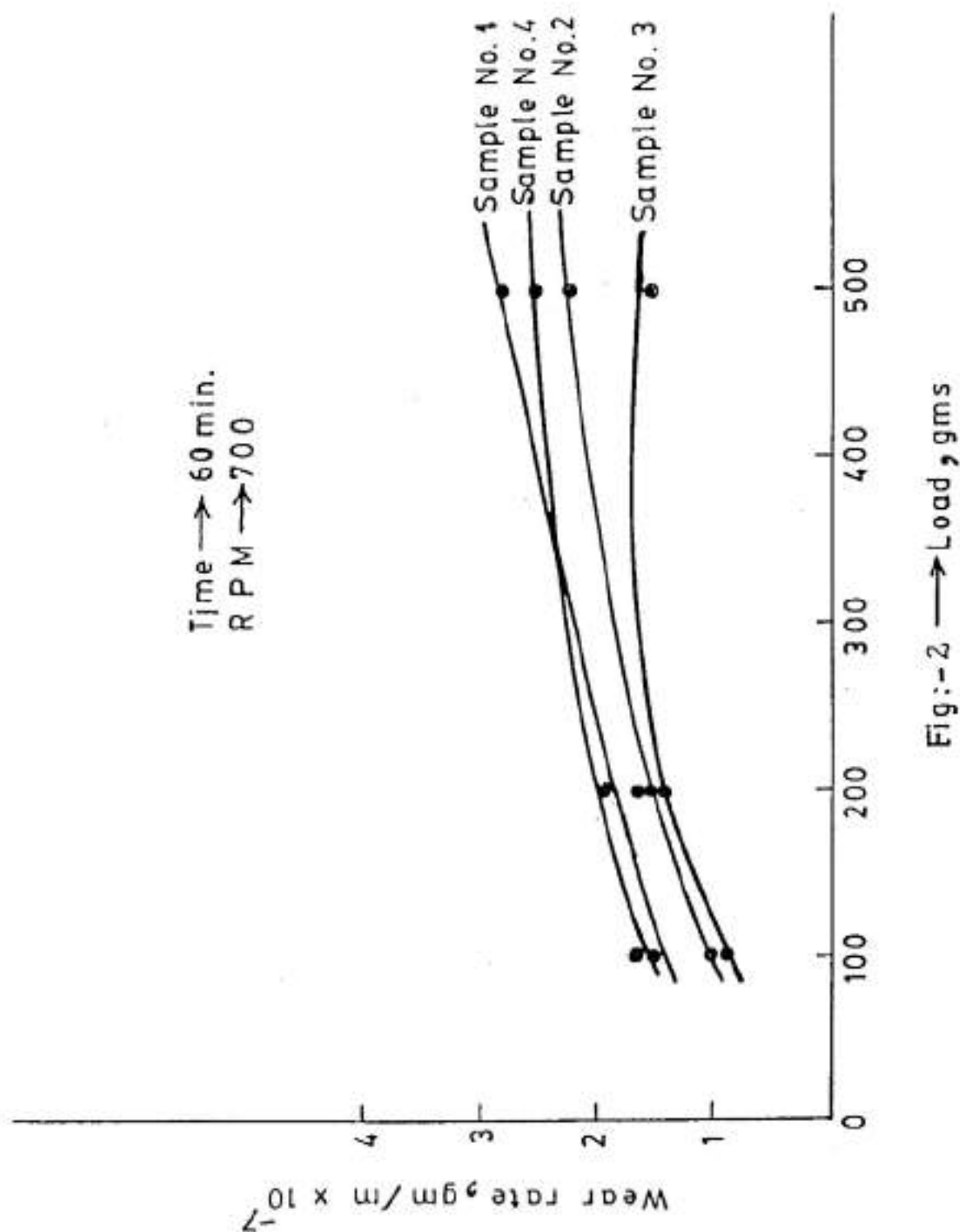
In figure (5) it can be seen that coefficient of friction decreases as the percentage of graphite in sample increases. For specimen no. 4 with 30 % graphite, there is no further appreciable decrease in coefficient of friction. Also there is no appreciable change in values of (ZN/P), for sample no 2, 3 and 4. The values of coefficient of friction almost coincide for sample no 3 and 4. This shows that there are appreciable decreases in coefficient of friction by addition of more amounts of graphite.

### **COPPER MICA COMPOSITES**

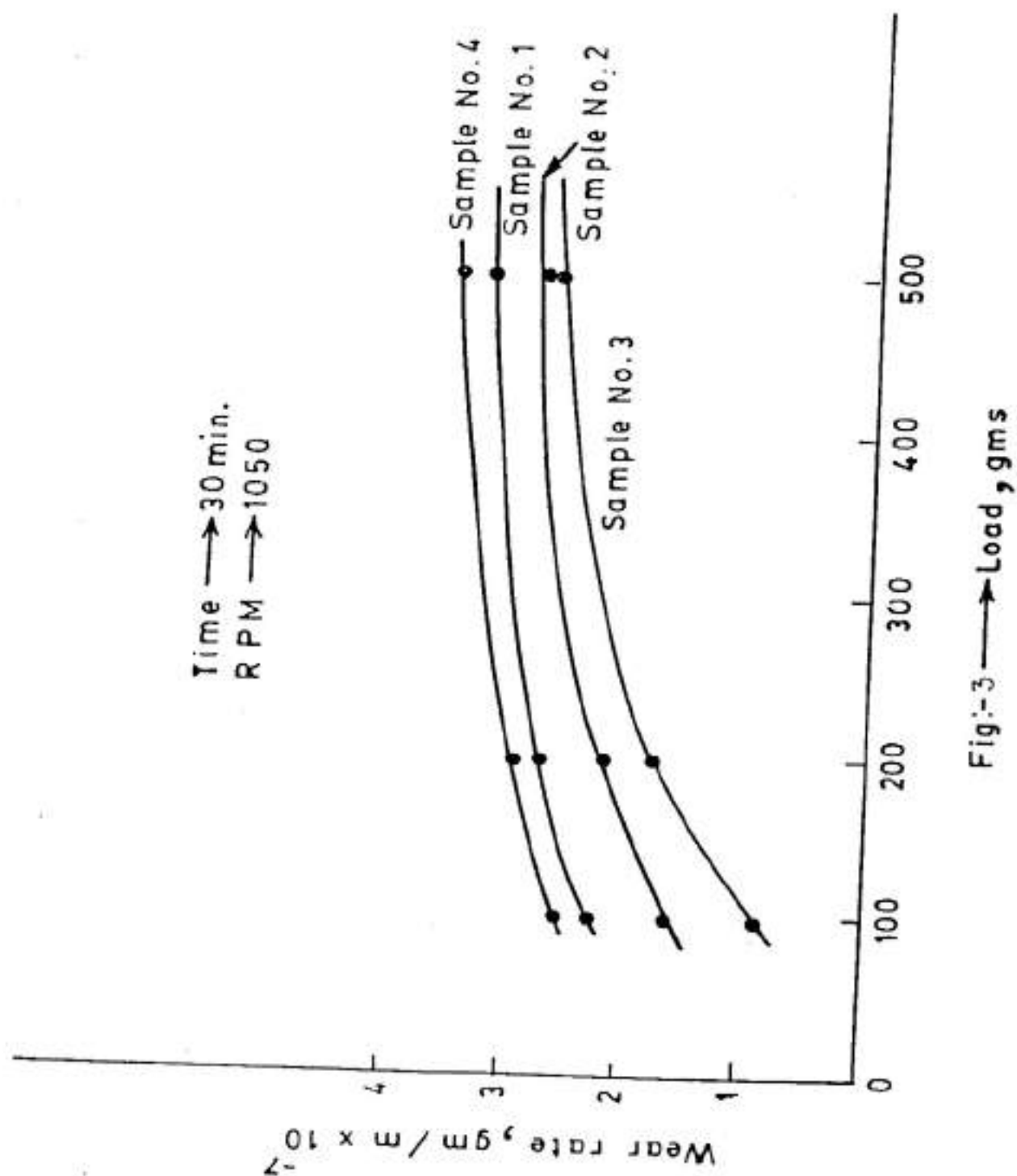
Deo nath, Prem Shyam and Anand Shankar studied characteristics of copper-mica particulate composites prepared by Powder Metallurgy Technique. The details of which are given below:

Electrolytic grade copper powder and flake shape ground mica powder were subjected to sieve analysis. SEM studies were made for determining size distribution and morphology of the particles. Required proportions of these powders were blended. The apparent density of the blends was determined. The powder blends containing different proportions of copper and mica were compacted on a 50 ton universal testing machine at three different pressures i.e. 269, 377 and 539 Mpa respectively, under lubricated and dry die wall conditions. Stearic acid was used as a lubricant. Green density, Compressibility, ejection force and spring back of the powder compacts were determined. Green compression strength of the compacts was determined on a universal-testing machine. A Vickers's pyramid hardness tester with 10 kg load was used for determining the hardness. Copper-mica composites compacts were sealed in a transparent silica tube under vacuum

Fig:-1  $\rightarrow$  Load, gms

Fig:-2  $\rightarrow$  Load, gms





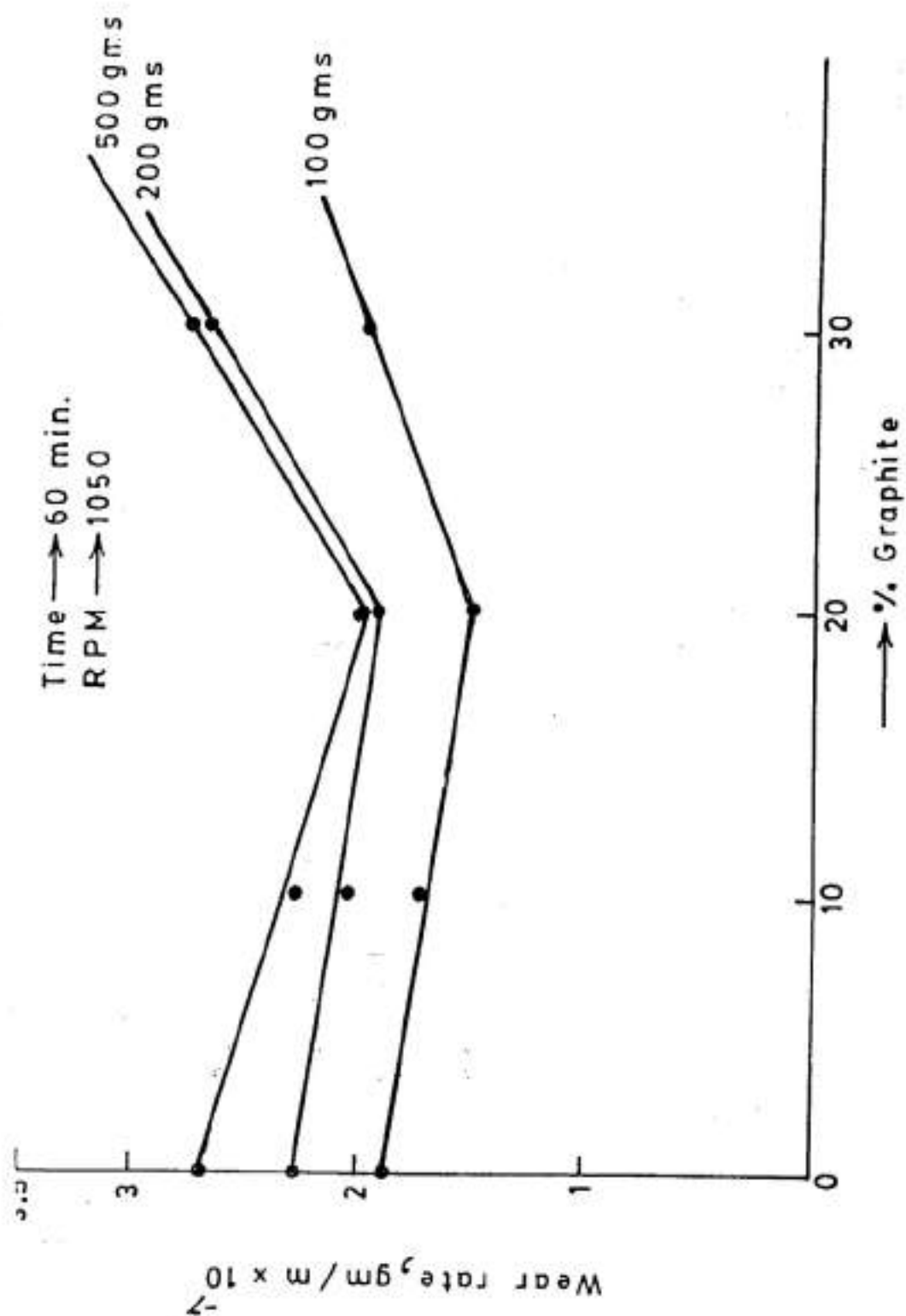


Fig:-4

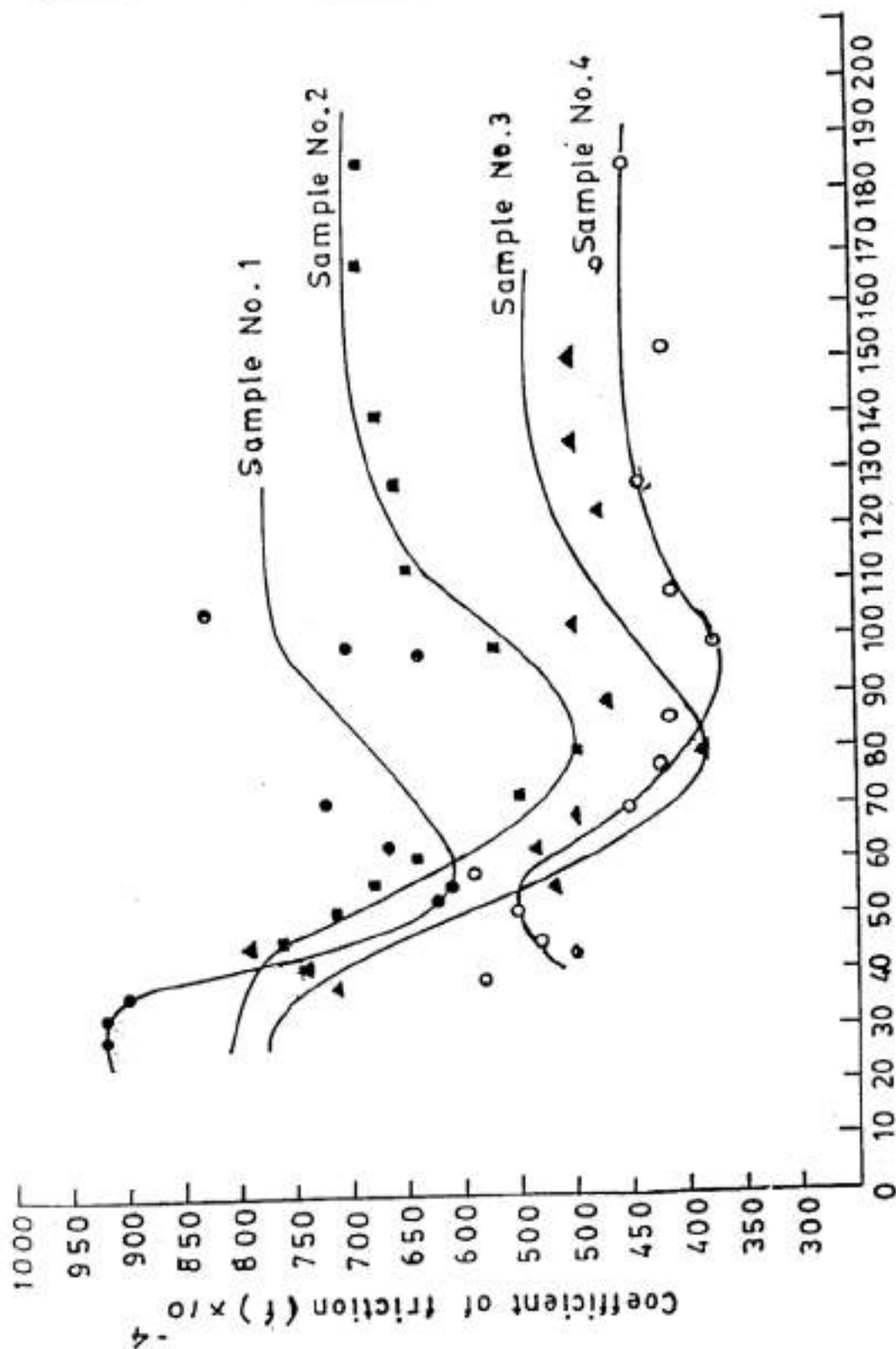


Fig:-5 - Bearing characteristic number  $(\frac{ZN}{P})$

(1,33 Pa) and sintered at  $840 \pm 10$  °C. Density, compressive strength and shrinkage of the compact after sintering were also determined. The load corresponding to 50 % deformation was used in calculation of sintered compressive strength.

### **Powder Characteristics**

Size distribution of copper and mica as determined by sieve analysis are shown in Fig. 1 and Fig. 2 respectively. This figure indicates that about 80% of the copper powder has a particles size less than  $37 \mu\text{m}$  (-400 mesh), the larger fraction of mica falls within 105 and  $53 \mu\text{m}$  (140 and 325 mesh).

Figs. 3 and 4 are Scanning Electron Micrographs of Copper and Mica particles respectively. They indicate the dendritic and flaky morphology of copper and mica particles. Figure 5 shows that a decrease of certain copper-mica blends goes along with as increase in mica content which is due to lower density of mica as compared to copper.

### **Compacting Characteristics**

The results of compressibility tests of copper-mica composite compacts containing different amounts of mica pressed under dry and stearic acid lubricated die wall conditions at different compactions pressure are presented as densification parameter in fig. 6. The densification parameter decreases with increases in mica content of the compacts. This may be attributed to a decrease in apparent density of copper mica powder blends with mica contents (Fig. 5). Fig. 6 is also indicates that for a fixed mica content the lubricated die wall result in a better flow of particles and give higher densification as compared to dry wall conditions. The effect of compaction pressure on green density for different mica content. The effects of mica content on the ejection force shown in fig.8. Under dry die wall conditions, the ejection force increases with increases in mica content. However, the ejection force decreases in case of a lubricated die wall. Fig. 9 shows the effect of mica percentage on spring back of copper mica compacts of different compacting pressures under lubricated and dry wall conditions. It is reported that the higher the yield stress, the lower the elongation modulus and greater the plastic strain, the greater the spring back will be. Fig. 9 indicates that for pure copper the spring back, under lubricated conditions, increases with increasing compaction pressure. This may be attributed to higher plastic strain. However, this behaviour is not observed under dry die wall conditions. For copper mica compacts containing different amounts of mica,

the spring back is always higher than for a pure copper at all compaction pressure used in investigation. Fig. 10 and 11 show the effect of the mica content on the compressive strength and hardness of the compacts produced at different compaction pressures under lubricated die wall conditions. The increase in the mica content is observed to reduce the compressive strength and hardness of the compacts. The strength of the green compacts results mainly from mechanical interlocking of the irregularities on the surfaces and the bonding between matrix and second phase particles on the one hand and between matrix and second phase particles on the other hand. The reduction in strength and hardness with increasing mica content may be attributed to the reduction of the mechanical interlocking of irregularities on the surface of copper particles.

### **Sintering Characteristics**

The green and sintered densities decreases with increasing mica content, the later were being always higher than the former (Fig. 13). The increase in density is due to the shrinkage resulting during sintering (Fig. 14)

Fig. 15 shows the variation of the compressive strength of sintered copper mica composites with mica content. The sintered compacts when deformed up to 50 % did not show fracture except some edge cracking. A SEM photograph of composite after about 50% deformation is shown in Fig. 16 indicates that the voids presents around the mica particles get reduced after sintering (Fig. 12 & 16). Partially accounting for the higher strength of the sintered product as compared to the green compacts (Fig.10). Most of the higher strength of the sintered compacts as compared to the green ones is due to the development of metallic bonding and recrystallization of copper particles during sintering evident from Figs. 17 and 18.

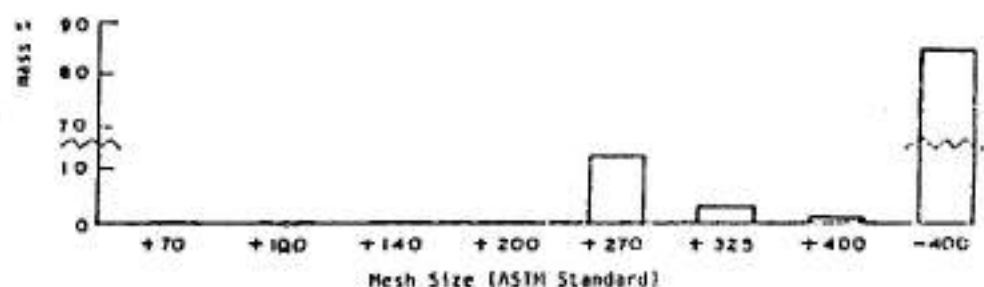


Fig. 1 Histogram showing particle size distribution in copper powder

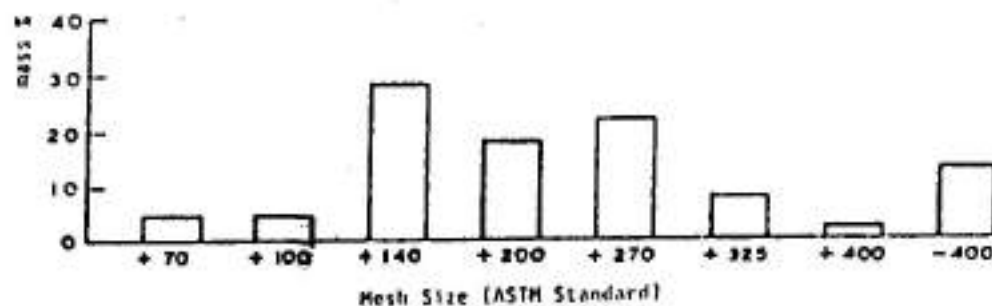


Fig. 2 Histogram showing particle size distribution in mica powder



Fig. 3 SEM photo of copper particles



Fig. 4 SEM photo of mica particles

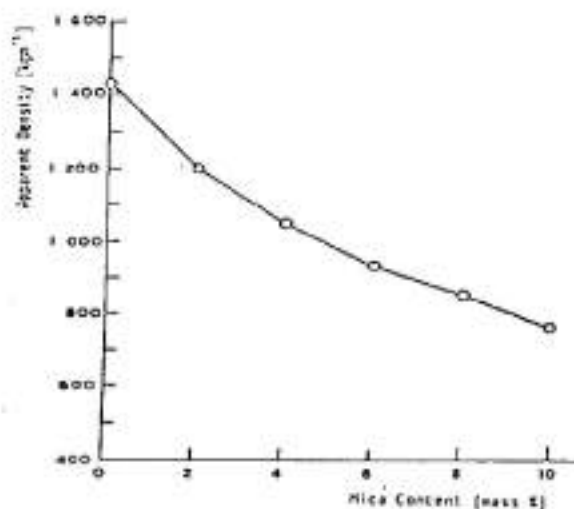


Fig. 5 Effect of mica percentage on the apparent density of copper-mica powder blend



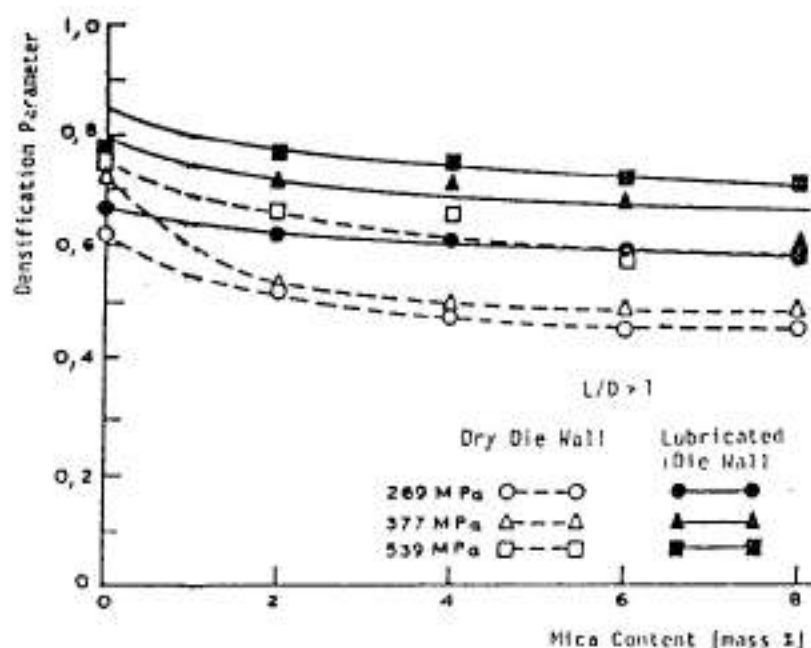


Fig. 6 Effect of mica percentage on the densification parameter of the copper-mica compacts

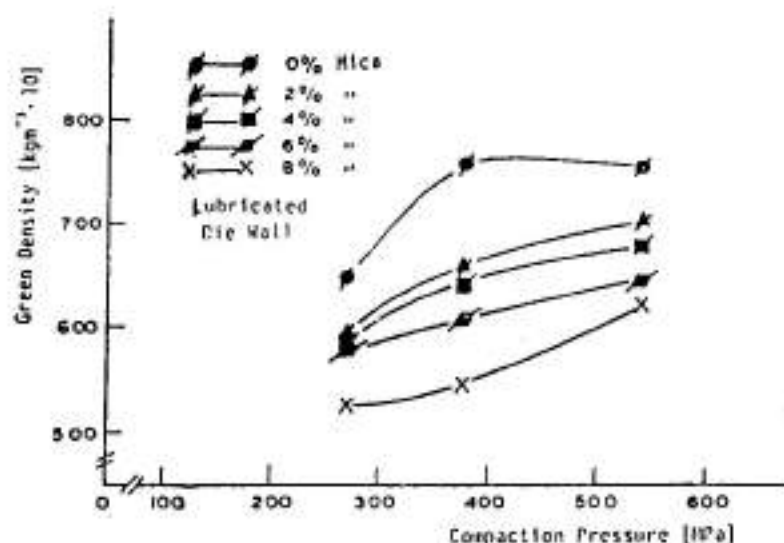


Fig. 7 Effect of compaction pressure on the green density of copper-mica compacts

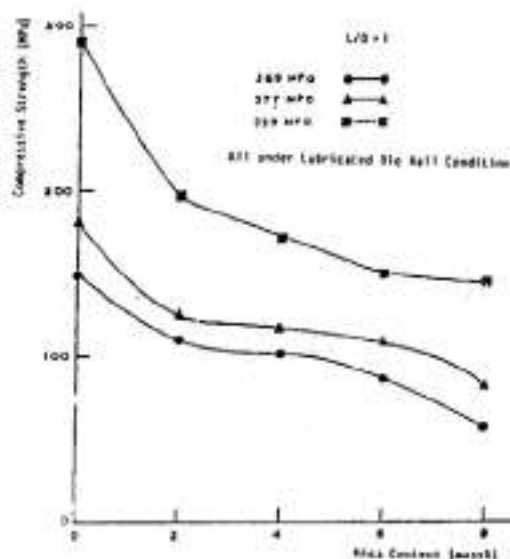


Fig. 10 Effect of mica percentage on the compressive strength of copper-mica compacts

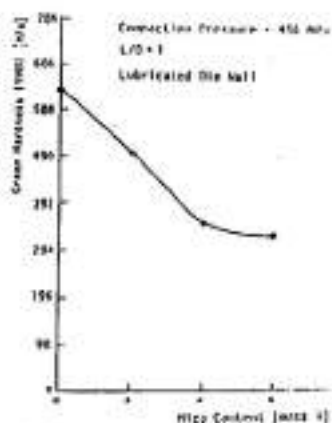


Fig. 11 Effect of mica percentage on the hardness of copper-mica compacts



Fig. 12 SEM photo of the fractured surface of green (copper-1% mica) compacts

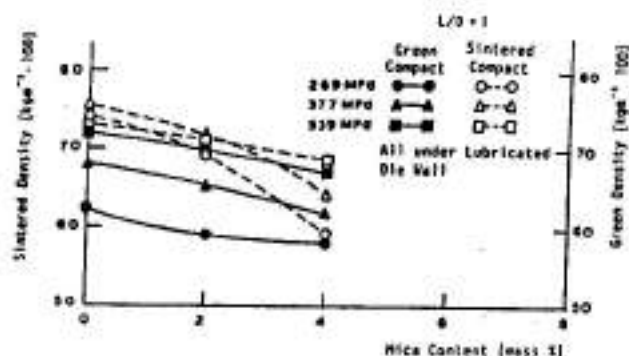


Fig. 13 Effect of mica percentage on the green and sintered density of copper-mica compacts

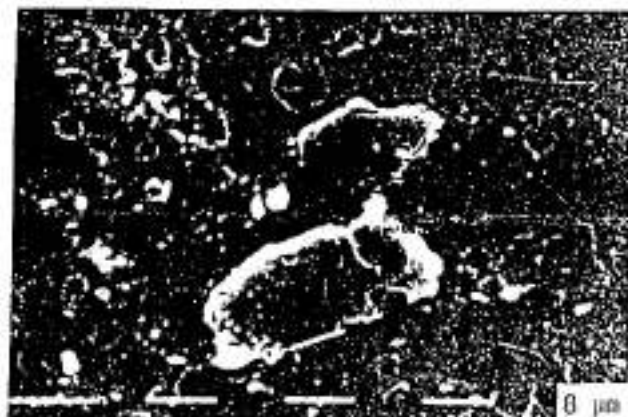


Fig. 16 SEM photo of 50%-deformed sintered copper-2% mica composite

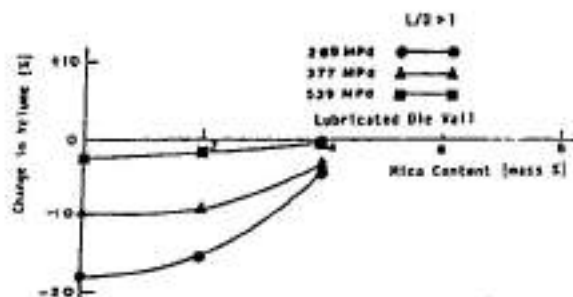


Fig. 14 Effect of mica percentage on the percentage change in volume during sintering of copper-mica composites

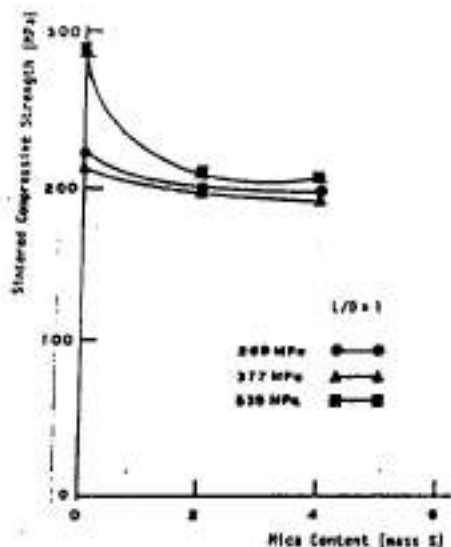


Fig. 15 Effect of mica percentage on the compressive strength of sintered copper-mica composites

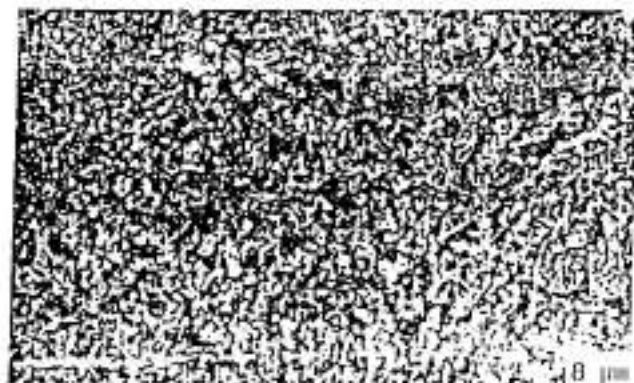


Fig. 17 SEM photo of green copper compacts

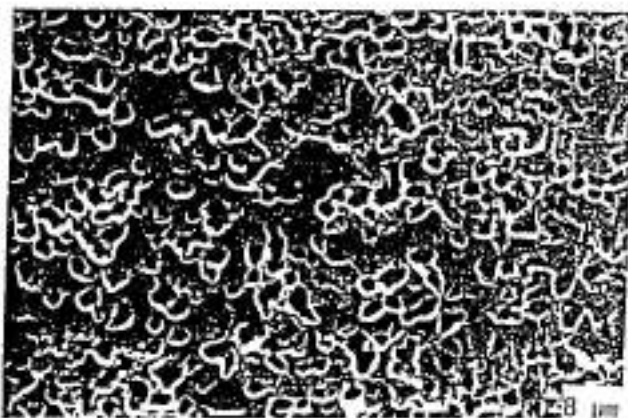


Fig. 18 SEM photo of sintered copper compacts

## **EXPERIMENTAL DETAILS**

The experiment performed by Sanjeev Kumar Soudhani and Santaosh V.N. Under the guidance of Dr. N.K. Jain of Malaviya Regional Engineering College Jaipur. The experiment conducted in order to study the characteristics of copper-mica particulate composites prepared by powder metallurgy technique. The characteristics studied were hardness and porosity of the composite. The samples were prepared from copper powder and mica powders have the following specifications: -

1. Apparent density = 1.4 %
2. Particle size
  - (a) 60 microns = 1.5 %
  - (b) 40-45 microns = 85 %
3. Oxygen content = 0.3% max.
4. Purity of copper = 99.7%

The size of the mica particles was very coarse. So the mica powder was subjected to sieve analysis (~ 400 mesh). Then these two powder were mixed thoroughly for a weight of 165 gm in the following proportions:-

1. 100% Cu
2. Copper with 2 % mica.
3. Copper with 4 % mica.
4. Copper with 6 % mica.
5. Copper with 8 % mica.
6. Copper with 10 % mica.

Then the samples of the above mentioned proportioned were made in a circular die of internal diameter 28mm and depth 72 mm. With addition of lubrication to allow easy compaction. 15-ton load was applied on each sample for making compacts. The capacity of the press through which the load was applied manually for pressing or compaction of each sample. After compaction these samples were sintered in a suitable environment. After the samples were removed from furnace they were polished with emery paper 0, 1, 2, 3, 4 and then followed by polishing on a polishing wheel by using Brasso. The hardness is determined with the help of Vickers Hardness Tests at 10-kg load. The hardness of the samples are given in table 1. A graph of hardness v/s percentage of mica

is plotted. The porosity of the samples were given in Table 2. Again the samples were subjected to polishing wheel by using Brasso for observing of microstructures.

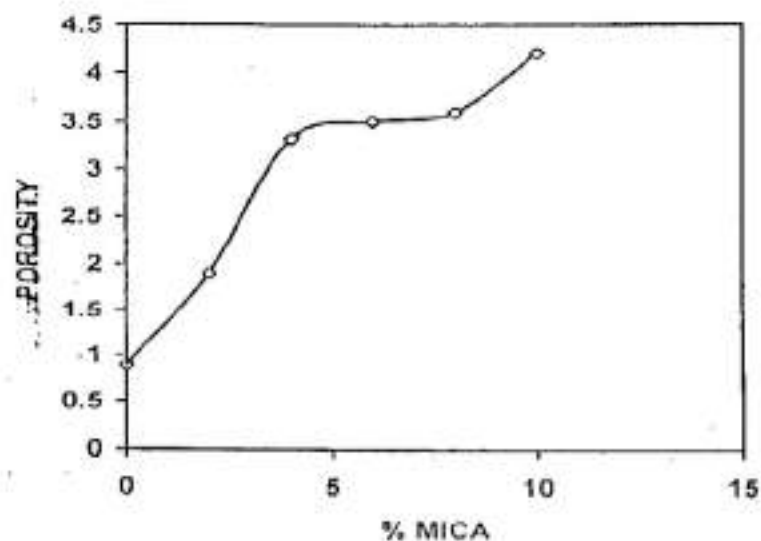
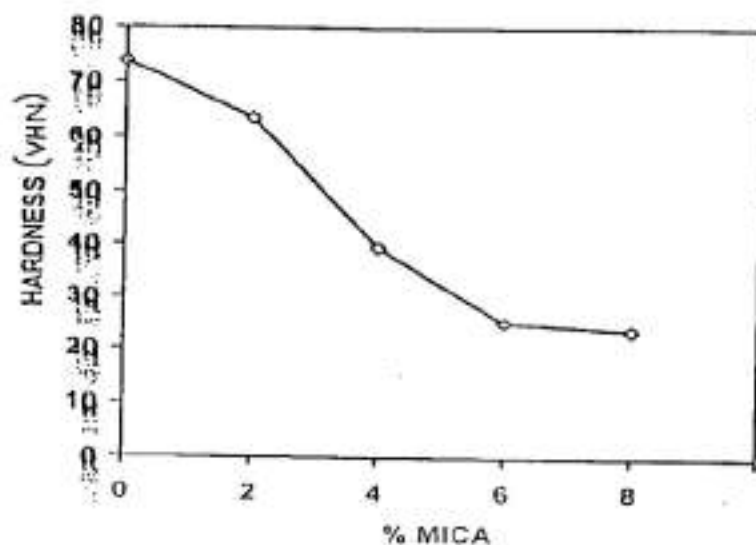
**Table no: 1**

S.NO.	SPECIMEN	LENGTH OF DIAGONAL	HARDNESS (VHN)
1.	100% Cu	0.501	73.864
2.	Cu with 2% mica	0.540	63.580
3.	Cu with 4% mica	0.687	39.282
4.	Cu with 6% mica	0.860	25.068
5.	Cu with 8% mica	0.890	23.406

**Table No: 2**

**STANDARD COPPER DENSITY = 8.94 g/cc**

S.NO.	SPECIMEN	DENSITY (g/cc)	POROSITY
1.	100% Cu	8.0412	0.8988
2.	Cu with 2% mica	7.0423	1.8977
3.	Cu with 4% mica	5.6103	3.3297
4.	Cu with 6% mica	5.3620	3.578
5.	Cu with 8% mica	5.2987	3.6433
6.	Cu with 10% mica	4.6500	4.2900

1. GRAPH OF POROSITY V/S PERCENTAGE MICA2. GRAPH OF HARDNESS V/S PERCENTAGE MICA

## **CONCLUSION**

1. Density decreases with increase in Mica content.
2. Porosity increases with increase in Mica content.
3. Volume of the compacts increases with increase in Mica content.
4. Hardness decreases with increase in Mica content.

## **SUGGESTIONS FOR FUTURE WORK**

1. Wear studies can be carried out.
2. Bearing test studies can be carried out.
3. Mechanical properties after compaction can be tested.
4. More loads may be used.

## **REFERENCES**

1. Powder Metallurgy International, Vol.20, No.5,198 Characteristics of Cu-Mica particulate composites prepared by Powder Metallurgy technique by Mr. Deo Nath, Prem Shyam & Anand Shanker.
2. Tribiological study of Cu-Graphite composites - A Dissertation submitted by Mr. H.C.Agarwal.



## Synthesis and Mechanical Property Evaluation of Yttria Partially Stabilized Zirconia Ceramics

Soumen Biswas, Anil Anal , B.T.Rao,T.R.Rama Mohan  
Indian Institute of Technology , Bombay  
And  
Ramji Lal  
Naval Material Research Laboratory  
Ambernath

The present work reports on the synthesis and mechanical properties of yttria partially stabilized zirconia ceramics obtained through the spray drying route. The zirconia -5 mol% yttria composite powder was prepared in the laboratory from a solution of zirconium and yttrium nitrates. The composite powder so obtained was characterized for its composition, shape, size and size distribution using x-ray diffraction , and particle size analyzer. The composite powder was then compacted at different pressures starting from 50MPa to 350MPa and sintered at various temperatures in the 1200-1600 °C region. The sintered specimens were characterized for their densities and mechanical properties like hardness, modulus of rupture, wear resistance and fracture toughness, which are presented and discussed here. The effect of aging treatment (at 1300°C) of the sintered specimens on the mechanical properties has also been reported.

### Introduction:

Zirconia ceramics have received considerable attention because of the feasibility to obtain relatively high fracture toughness values through induced microstructural and phase assemblage changes. This possibility is related to the stress induced phase transformation that tetragonal zirconia may undergo to monoclinic symmetry(t->m). Such phase transformation involves a volumetric increase (~4%)that may induce compressive stresses in the crack wake[1-5]. Beside the mechanical properties much study has been made in the last years on the sinterability of the PSZ powder compacts and the parameters affecting it . [8-11]

In the present investigation zirconia -5 mol% yttria powder has been synthesized through the spray drying technique. The powders prepared were characterized using Thermal analysis, XRD, SEM and particle size analysis. The powder was then compacted at various pressures and a study of their sinterability was carried out. The sintered compact was then examined for mechanical properties such as MOR, fracture toughness, hardness and wear resistance. A study on the effect of aging treatment over the mechanical properties of sintered compacts have also been made by aging the sintered compact at 1300° C for 25 -100 hours.

## EXPERIMENTAL WORK:

### 1) *Preparation of zirconium nitrate -yttrium nitrate solution and spray drying*

Zirconium nitrate solution was obtained from zirconium oxychloride. Yttrium nitrate was added to it to produce a solution of zirconium and yttrium nitrate. 30 liters of the solution was spray dried and calcined to produce  $ZrO_2 - 5 \text{ mol \% } Y_2O_3$  powder

### 2) *Characterization*

The TGA of the powder was carried out and the calcination temperature was determined. The particle size was measured by the mastersizer with the help of the data obtained from the percent obscuration of the laser beam by the particles. The phase analysis was done by the X-Ray diffraction methods. The powder produced after the spray drying was calcined at different temperatures so as to analyze the variation of particle size with the calcination temperature.

### 3) *Compaction:*

After the calcination, the powder was compacted at different pressures starting from 50Mpa to 350Mpa in steps of 50 MPa. The green densities of the samples thus compacted at different pressures were determined.

### 4) *Sintering:*

The powders that were compacted at different pressures were subjected to different sintering temperatures starting from 1200°C to 1600°C in steps of 100°C. Sintering was carried out with a slower heating rate (5°C/min) up to 450°C, followed by 10°C/min till the sintering temperature was attained. A dwell time of 30mins was given between each step.

After soaking time of 2 hours at the sintering temperature, the samples were cooled at a rate of 10°C/min till 500°C and furnace cooled to room temperature.

#### 5) SEM of the calcined and the sintered specimens

The SEM of the calcined powder and the sintered specimen was carried out at different magnifications.

#### 6) Hardness measurement

Hardness was calculated by Vickers indentation method using the following formulae:

$$H_v = (1854 \text{ kgf} \cdot \mu\text{m}^2 / \text{gf} \cdot \text{mm}^2) \cdot F / d^2$$

Where, F is the test load in grams, d is the mean diagonal length of the indentation expressed in micrometers. The hardness test was done with a test load of 18 kg.

The hardness values were corrected for SI units

#### 7) Fracture toughness determination

The Fracture toughness of the samples was determined by the Vickers indentation method. From the hardness data generated and by measuring the crack length produced by the diamond indenter the fracture toughness values were obtained for the sintered samples using the following formula.

$$K_{IC} = 0.15 K (c/a)^{3/2} H a^{1/2} / c_f$$

Where,

K is a correlation factor equal to 3.2,  $c_f$  is a constraint factor of 3, c is the average crack length from the center of the indentation, a is the average distance from the center of the indentation to the corner, and H is the hardness corrected for SI units.

#### 8) Determination of Modulus of rupture (MOR)

The MOR from three-point bend test is given by,

$$\text{MOR} = \frac{\frac{P}{2} \times \frac{L}{2} \times \frac{d}{2}}{\frac{bd^3}{12}} = \frac{3PL}{2bd^3}$$

Here, P is the load in Newton and L, the span length in mm, b and d are breadth and thickness of the sample, also measured in mm. The modulus of rupture of the sintered

specimens was calculated from the load required to rupture the specimen in the three point bend test.

#### 9) *Wear resistance*

Abrasive testing of PSZ was carried out on a Pin-On-Disc wear testing machine. Silicon carbide wheels were used as the disc material. Volumetric wear rate was studied from the test. All the wear tests were carried out at room temperature under unlubricated dry condition. Wear resistance was calculated under different sliding distances.

#### 10) *Aging of the sintered specimen*

A study of the effect of isothermal aging on the mechanical properties had been carried out. The aging treatment was carried out at 1300°C for 25-100 hours for specimens that were compacted at 350 MPa and sintered at 1600°C.

### **Results and discussions:**

The particle size showed an initial decrease, followed by a steady increase with increase in calcination temperature (Fig. 1). The decrease in the particle size at 650°C is most likely due to the total decomposition of the precursors into the zirconia solid solution. The subsequent increase in particle size is due to particle growth.

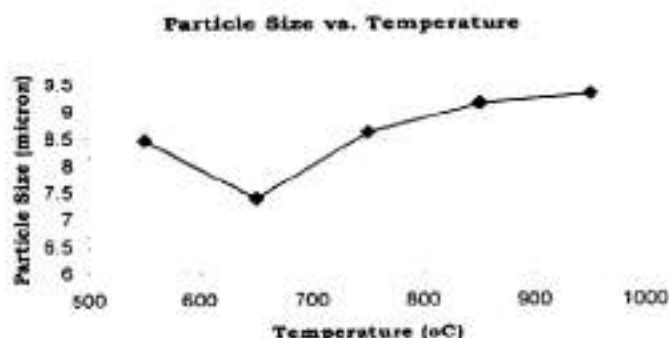


Fig1. The variation of particle size with the calcination temperature

From the X-Ray diffraction data, the  $d$  values of the peaks were compared with the standard JCPDS data file, and the presence of both the cubic and the tetragonal phases of zirconia were confirmed, as it should be the case with the partially stabilized zirconia. From the half peak width, the crystallite size was found to be 80-130 nm.

The green density of the samples increased with increase in compaction pressure but at higher compaction pressure the variation in green density was almost negligible

(Fig.2). The sintered density data also showed ( Fig. 3) the same trend for samples compacted at higher pressures at any given temperature of sintering . It has also been observed that the sintered density showed an increasing trend with increase in the sintering temperature for a particular compaction pressure as shown in Fig. 4.

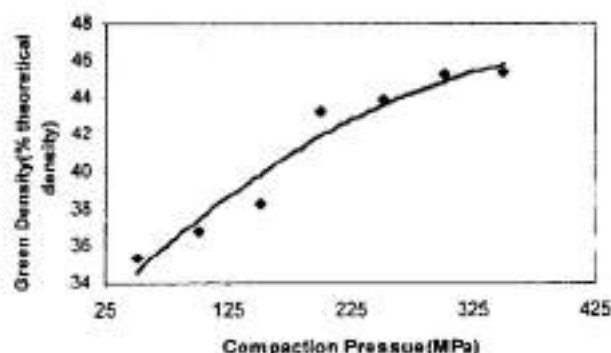


Fig2: The variation of green density with compaction pressure

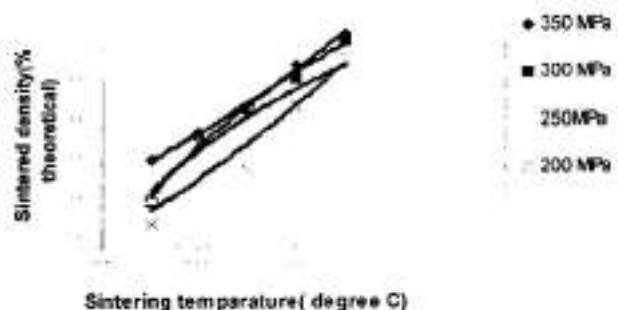


Fig 3. The variation of sintered density with sintering temperature at various compaction pressures

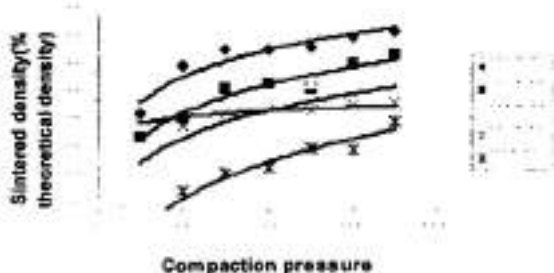


Fig4: The variation of sintered density with compaction pressure for different sintering temperatures

The Vickers hardness values obtained showed an increasing trend with increase in compaction pressure as well as with the increase in the sintering temperature. The maximum value of hardness was obtained for the samples ( Fig. 5) which had been compacted at 300MPa and subsequently sintered at 1600°C as shown in Fig. 6. This can be attributed to the higher sintered density of the samples that had been initially compacted at high pressure and subsequently sintered at higher temperature.

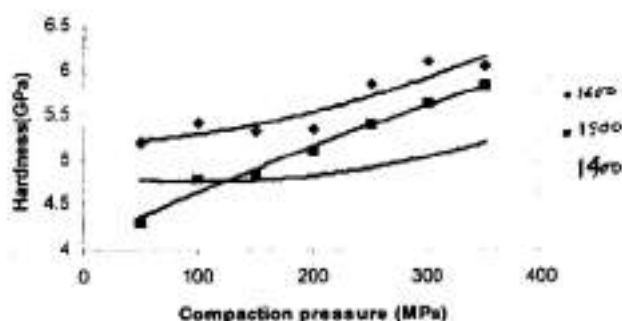


Fig5: The variation of hardness with compaction pressure for different sintering temperatures

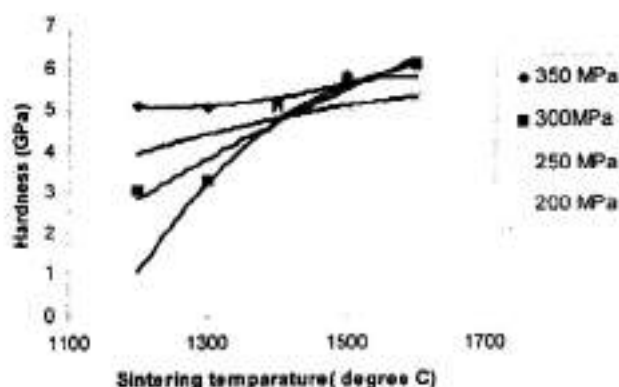


Fig6: The variation of hardness with sintering temperature for different compaction pressure

The over all fracture toughness and the modulus of rupture of the samples obtained were low as compared to the standard fracture toughness and MOR values of YPSZ (fig 8 -10). This can be due to the presence of pores (around 8% for samples

compacted and sintered at 350MPa and 1600°C respectively, and still higher for other samples).

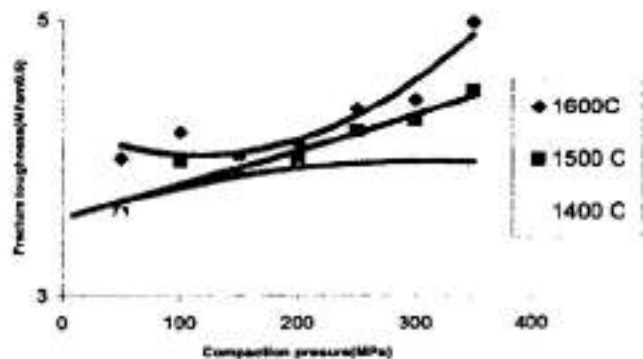


Fig7: The variation of fracture toughness with compaction pressure at constant sintering temperatures

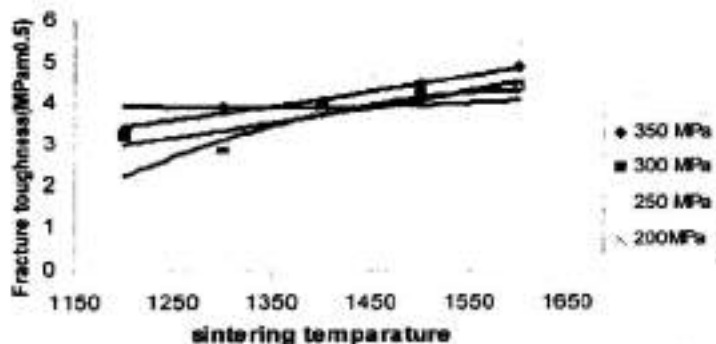


Fig8: The variation of fracture toughness with sintering temperature at different values of compaction pressure

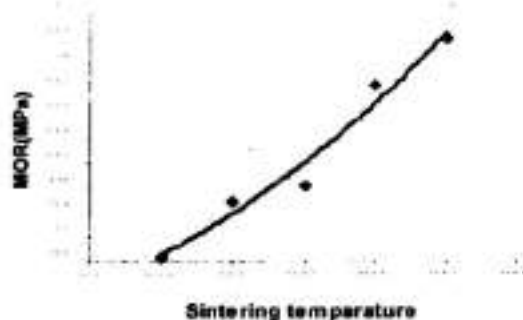




Fig9. The variation of MOR with sintering temperature

Form the wear resistance tests it is evident that with the increase in compaction pressure the wear rate decreases as depicted from fig 10.

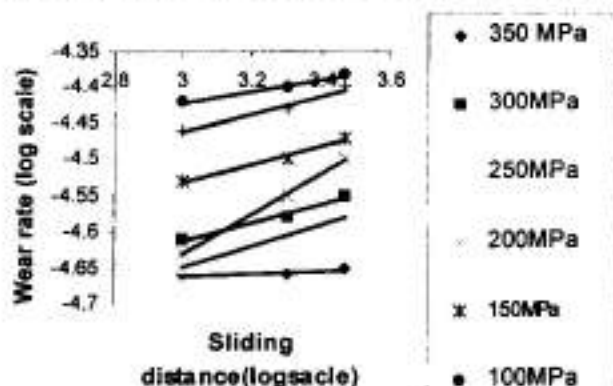


Fig10: The variation of wear rate and sliding distance for the sintered samples under a constant weight

The aged samples showed an increase in the MOR value during the initial stages of aging. After which the MOR value dropped drastically with increase in the aging time. This may be due to the presence of more of monoclinic phase at higher aging temperature which is formed due to the transformation of coarse tetragonal particles on prolonged aging. The fracture toughness values also varied accordingly. (fig 11-13)



Fig11: Indentation fracture toughness as a function of aging time



Fig12: Plot showing the variation of modulus of rupture with aging time

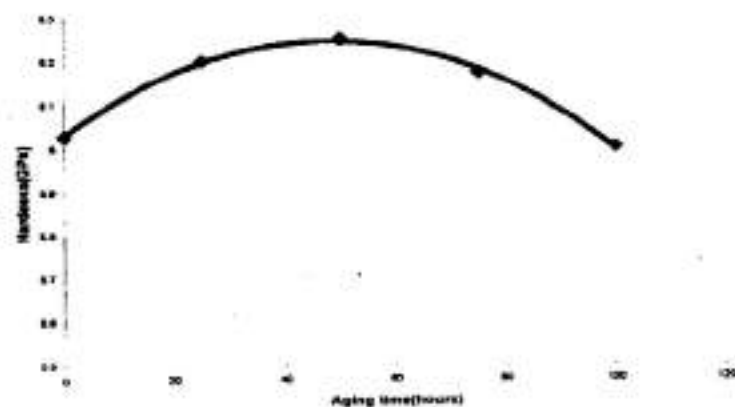


Fig13: Plot showing the variation of hardness with aging time

#### CONCLUSIONS:-

1. Zirconia -5 mol% Yttria powder was synthesized by spray drying of the zirconium nitrate -yttrium nitrate solution. The particle size of the resultant powder was found to be around 80- 130 nm.
2. The particles, however are agglomerated, and agglomerate size was found to increase from 6.2  $\mu\text{m}$  to 9.3  $\mu\text{m}$  with increase in the calcination temperature.
3. Increase in compaction pressure and sintering temperature in general had sintered density, and hence the hardness, MOR and fracture toughness. The best combination of compaction pressure and sintering temperature that led to the

best mechanical properties (hardness 6.03 , MOR 332 MPa, fracture toughness  $4.98\text{MPa}\sqrt{\text{m}}$  ) was found to be 350 MPa and  $1600^{\circ}\text{C}$ .

4. Aging of the sintered sample for a moderate period of time (approximately 50 hrs) increased the MOR from 330 MPa to 381 MPa .

### **Acknowledgements**

We profusely thank and express our deepest gratitude to the **Director** of Naval Materials Research Laboratory, Ambernath for providing the experimental facilities.

## REFERENCES:

- [1] Garvie R.C. ,Hannik.R.C. and Pascoe.R.T." Ceramic steel", *Nature(London)* **vol.258**,pp 703-704(1975).
- [2] Heuer.A.H., "Transformation toughening in zirconia containing ceramics", *Journal of American ceramic society*,**vol 70**[10],pp 690-698(1987).
- [3] Behrens.G, Heuer.H.A, "Thermally activated martensitic transformations in Mg-PSZ" *Journal of American ceramic society*, **vol79** [4], pp 895-905(1996).
- [4] Porter.D.L,Heuer.A.H," Mechanisms of toughening partially stabilized zirconia"*Journal of American ceramic society*,**vol 60**[3-4], pp 183-185(1977).
- [5] Hannik.H.J.R, Patrick.M.K, Barry.C.M," Transformation toughening in zirconia-containing ceramics", *Journal of American ceramic society*, **vol 83**[3],pp461-487(2000).
- [6] Scott.H.G, "Phase relationship in the zirconia -yttria system", *Journal of material science* , **vol 10**,pp 1527-1535(1975).
- [7] Ramamurthy.S,Xu.Z,Payne.D." Preparation of powders for structural ceramics" *Journal of American ceramic society*,**vol 73**[9], pp 2760-2766 (1990).
- [8]Olmo.D.L,Duran.p,Moure.C. "Sintering behaviour of an yttria stabilized zirconia", *Sintering theory and practice*,pp 401-406(1981).
- [9]Rhodes.W.H,"Agglomerate and particle size effects on sintering yttria stabilized zirconia", *Journal of American ceramic society*,**vol 64**[1],pp 19-22(1981).
- [10] Chen.Da Jiang,Merrilea J.Mary, "Rapid rate sintering of nanocrystalline  $ZrO_2$ -3 mol%  $Y_2O_3$ -", *Journal of American ceramic society*, **vol 79**[4], pp 906-912(1996).
- [11] Shi.J.L, Jian.G, Lin Z," Sintering behaviour of fully agglomerated zirconia compacts" *Journal of American ceramic society*, **vol 74**[ 5], pp 994-997(1991).
- [12] Lukasiewicz, S. J., "Spray-drying ceramic powders." *Journal of American ceramic society*" , **vol 72**(4), pp 617-624 (1989)
- [13] Armor, J. N., Fanelli, A. J., Marsh, G. M. and Zambri, P. M.Nonaqueous, "spray-drying as a route to ultrafine ceramic powders." *Journal of. American Ceramic Society*, **vol 71**(11), pp938-942 (1988).

## DEVELOPMENT OF INDIRECTLY HEATED FUEL ROD SIMULATOR FOR THERMO HYDRAULIC SAFETY EXPERIMENT

S.K.Srivastava, P.SundaraRajan, S.V.Paibhale, V.G.Date \*

\* Atomic Fuels Division, B.A.R.C., Trombay, Mumbai 400 085

### ABSTRACT

Investigations of the thermodynamic behaviour of reactor fuel elements require out-of-pile experiments on electrically heated fuel rod simulators. The results of these experiments depend strongly on the similarity of thermodynamic behaviour between fuel rod simulators and nuclear fuel rods. Requirements also depend on the type of experiments, where fast transients are involved. Work for the development of indirectly heated FRS was taken up to simulate fuel rods of Advanced Heavy Water Reactor. A heater assembly, the key component of the FRS rod with adequate heat rating has successfully been developed by employing powder metallurgical technique such as vibratory compaction. This paper deals with the development and fabrication of Fuel Rod Heater Assembly.

### 1.0. INTRODUCTION

The safety of Nuclear Reactor is to be ensured not only under normal operating conditions, but also under transient and accident conditions. Loss of Coolant Accident (LOCA) is one of the postulated accident, the course of which is strongly dependent on thermal, hydraulic characteristics of the reactor core, comprising of fuel rods. The complex nature of the phenomena occurring during accidents calls for extensive experimental investigations. Electrically heated fuel rods (FRS) are extensively used to simulate nuclear heating (particularly decay heat) in out-of-pile experiments. Different designs of FRS to simulate fuel rod behaviour have been proposed. These can mainly be categorised into directly heated fuel rod simulators and indirectly heated fuel rod simulators. In directly heated type FRS, current is passed directly through the tube which geometrically simulates the cladding of nuclear fuel rod. This type of FRS finds applications in experiments related to steady state heat transfer in single and two phase flow of fluids which are non conductors of electricity. Very high heat flux can be achieved in this type of FRS. However, for unsteady state test simulation of

stored heat is extremely difficult in such design. For safety related experiments, where fast transients are involved, the stored energy and transfer of stored energy in fuel play an important role. Indirectly heated FRS which simulates stored energy better, is preferred for such applications.

It is proposed to conduct safety related experiments on FRS of Advanced Heavy Water Reactor (AHWR) being designed in India. A cross section of the fuel cluster containing 52 numbers of fuel rods and 8 water rods. The heated length of the fuel rods is 3.5 meters. The outer diameter of the fuel rod clad is 11.2 mm and clad thickness is 0.4 mm. The average linear heat rating of the fuel rod is about 100 w/cm. Work on the development of indirectly heated FRS was taken up in BARC. This paper gives the development and fabrication of the FRS in Atomic Fuels Division, BARC.

### 2.0. REQUIREMENTS OF FRS

Some important design criteria of heater assembly are given below.

- Electrical resistivity of heating elements should not change with temperature to any significant extent
- Thermal storage capacity of heating element

should be comparable with that of fuel rod

- c) Heating element is to be electrically insulated with sheath (but for one end) by providing insulating material in between.
- d) Thickness and density of insulating material should be uniform all through out the gap.
- e) Insulating material should have good thermal conductivity.
- f) Outer tube should have exact geometrical similarity with prototype fuel clad.

### 3.0. DESCRIPTION OF FRS

The fuel rod simulator mainly consists of the outer tube simulating the clad and a heater assembly concentrically located inside the outer tube. The gap between outer tube and heater assembly is filled by alumina pellets. During the differential expansion between heater sheath and clad, a incoel spring provided in the annular space keeps alumina pellets in their respective locations. A copper flexible wire allows relative movement between the clad and the heater assembly. The heater assembly (Figure 1) consists of a tubular heating element concentrically housed inside the tubular sheath with electric insulating material in between. Incoel X-600 is selected for the heating element and tubular sheath because it has good oxidation resistance at higher temperature and low coefficient of resistivity. The melting point of incoel is in the range of 1354 °C to 1413 °C. It has also got good cold workability. Up to 20% elongation can be achieved with incoel X-600 with out intermediate annealing operation. The temperature of the heating element can be reduced if the insulating material between the heating element and the heater sheath and the ceramic pellets in between the heater sheath and the clad have good thermal conductivity. The annulus between the heating element and the heater sheath is filled with Boron Nitride powder. The thermal conductivity of BN powder is reported to be as good as incoel tube if the powder is compacted to a value of more than 93% of theoretical density. The relative thermal conductivity of BN with BN packing density is shown in Figure 2. Magnesia powder is used to fill the inner space of tubular heater element to improve heat storage capacity. The MgO powder is compacted to 85% of its theoretical density to achieve the desired thermal and physical properties. The physical and thermal properties of the materials used in FRS and UO<sub>2</sub> (for comparison) are given in table 1. At one end of the FRS the outer tube (simulating the clad) heater sheath and heating element are all electrically connected to each other. This end forms the grounded end, the outer end being the live end. The electrical power supply will be connected to the grounded end and Nickel connector rod of heating element at the other end.

### 4.0 EXPERIMENTAL WORK

Initial experiments were performed to ascertain the problems associated with the vibro packing of MgO powder in incoel tube to the required packing density and to determine the percentage elongation of

magnesia powder filled rod after swaging. As received MgO powder was having poor flowability. It was found to contain about 5% moisture in the powder. The powder was dried at 300°C for 2 hours in nitrogen atmosphere to remove the moisture. One heater element was fabricated using following procedure.

Incoel X-600 tube of 6 mm OD, 4.6 mm ID and 765 mm length was taken and one end was TIG welded with nickel plug. Tube with one end welded was vibro filled with dried MgO powder to a initial packing density of 23% of T.D. and second end was welded with nickel plug. The hardness level of the MgO powder filled tube was measured to be 50 to 53 RB. This rod was swaged in three stages, each time limiting the elongation to 13 % and followed by intermediate annealing at 982°C for 15 minutes. It was observed that after first stage swaging, the hardness of the tube was measured to be about 87 RB which was reduced to 56 RB after annealing. After second step swaging the hardness was measured to be 84 to 87 RB. The rod was again annealed and the hardness was found to be 50 to 53 RB. After final stage of swaging the hardness was measured to be 87 RB which was reduced to 53 RB after annealing. Final dimensions achieved were 3.6 mm OD, 1327 mm length and final packing density was only 60 % TD.

Subsequent experiment was carried out with fused MgO powder to avoid moisture pick up. Intermediate annealing also was eliminated and the observed packing density of MgO powder was 93% TD. Problem was observed in vibro filling of BN powder in the annular space between the heater element and outer incoel sheath up to required packing density. Number of trials were carried out to improve the tap density by pre-compaction, pre-sintering and granulation of the powder. The pre-compacts were pre-sintered at 800°C for 30 minutes and crushed to required size. It improved the flowability and vibro filled density. We could achieve by this process the density of 62 % TD. After swaging the packing density improved further to > 93% TD which was very essential for good thermal conductance.

### 5.0. FABRICATION OF HEATER ASSEMBLY

The incoel X-600 tubes 6 mm OD 4.6 mm ID and 1911 mm length was taken and one end was TIG welded with nickel plug (fig 3). the tube with one end welded was vibro-filled with MgO powder to a packing density of 64% T.D. and second end was welded with nickel plug. The MgO filled rod was swaged to 3.52 mm OD. The length of the MgO filled rod after swaging was about 4820 mm and the hardness was 91 to 92 RB. The swaged rod was segment wise annealed in a tube furnace at 982°C for 15 minutes with each segment length of 150 mm. Hardness of the rod after annealing was 56 to 59 RB. The annealed rod was straightened, second end plug was drilled to accommodate the connecting plug which was then welded to the end plug.

Outer incoel X-600 tube of 7.5 mm OD, 6.1 mm ID and length of 3910 was TIG welded to the nickel connecting plug. The annular space between the central heater rod and outer incoel tube was filled with BN powder by distributing the powder manually and then vibrating the assembly. The initial packing density of BN powder was

49% TD. Other end of the annulus was closed with copper plug. This assembly was swaged to 6 mm OD and length of 4840 mm of outer tube. The final packing density of BN is calculated to be more than 93%TD. The swaged assembly was annealed segment wise as a mentioned earlier. The swaged and annealed assembly was subjected to X-ray radiography in segments ( 1,2 and 3 with 2 as the central segment) and also after rotating by 90° at each of these three segments ( fig 5) for checking the conductivity of central rod with respect to outer tube. From X-ray radiographs, it was observed that the maximum deviation of the longitudinal axis of central rod from the axis of heater assembly was about 0.13 mm. Flow sheet of fabrication of FRS is shown in appendix 1.

## 5.0. RESULTS OF TESTING

### 5.1. RADIOGRAPHY

Radiography test is carried out first on the weld between inconel tube and first end plug and then between magnesia filled tube & second end plug for finding the weld integrity. It is done in two mutually perpendicular directions using X-rays of 100 kv energy at about 1 meter distance between the job and the source. Film was in tight contact with the job. Next the integrity of weld between the connecting plug and second end welded rod was checked following the same procedure. Later the integrity of weld between connecting plug and outer tube was checked. Further, radiography is also employed to find the concentricity of the inner tube and the outer tube. Here the energy used is 120 Kv or more to get a rather low contrast. Profile of the tube wall was obtained in this technique. In order to find the concentricity the distance between the ID of the outer tube and OD of the inner tube is measured on both side of the inner tube. Same distances are taken after taking an x-ray in particular direction. This is to check concentricity in the perpendicular plane.

### 5.2. THERMAL TESTING

The performance of heater assembly can be improved if the temperature gradient in the radial

direction ( difference in central temperature and outer surface temperature of the heater assembly) is kept as low as possible for a given heat flux and geometry. This can be achieved if the thermal conductivity of insulating material is high. As stated earlier, if the packing density of boron nitride is more than 93%, the thermal conductivity of Boron increases to a large extent.

In view of above, thermal testing of heater assembly was carried out to determine thermal conductivity of BN. Bare Chromel-Alumel thermocouples (K-type) were spot welded on the surface of heater assembly as shown in fig. 4. An ungrounded thermocouples of 0.5 mm was also inserted about 70 mm longitudinally inside the heating element by cutting one end and removing magnesia powder from it. Test was conducted in air by supplying electrical power to the heating element and monitoring the temperatures. From the measured values of temperature, thermal conductivity of BN was evaluated.

## 6.0. CONCLUSIONS

The heater assembly developed, the linear heating rate of AHWR fuel rod simulator with coolant temperature was in conformity with the average linear heating rate of AHWR fuel rod. The fuel rod simulator can be used for experiments for normal operation and accidental conditions.

## 7.0. ACKNOWLEDGEMENT

Authors gratefully acknowledge the valuable guidance received Head RED, BARC. Thanks are due to Shri N.K.Maheshwari and Shri D.Saha, RED, BARC for designing the FRS. Thanks are also due to Shri P.R.Vaidhya, AFD for quality evaluation work and Sri P.T.trivedi, AFD for assisting in design & fabrication of fixtures.

### ✓ Reference

Valentin Casal, " Design of High-Performance Fuel Pin Simulators for Thermodynamics experiments with Nuclear Fuel Elements " Nuclear Technology, Vol, 47,Jan.1980



Table 1. Material properties at 770 K

Material	Density g/cc	Specific Heat (W-s/g-K)	Thermal conductivity W/cm-K
SS	7.98	0.35	0.230
Zr	6.50	0.38	0.199
Alumina(85%)	3.40	1.17	0.032
Alumina(95%)	3.80	1.17	0.104
BN	2.05	1.61	0.200
MgO	3.04	1.22	0.040
UO2	10.4	0.304	0.042

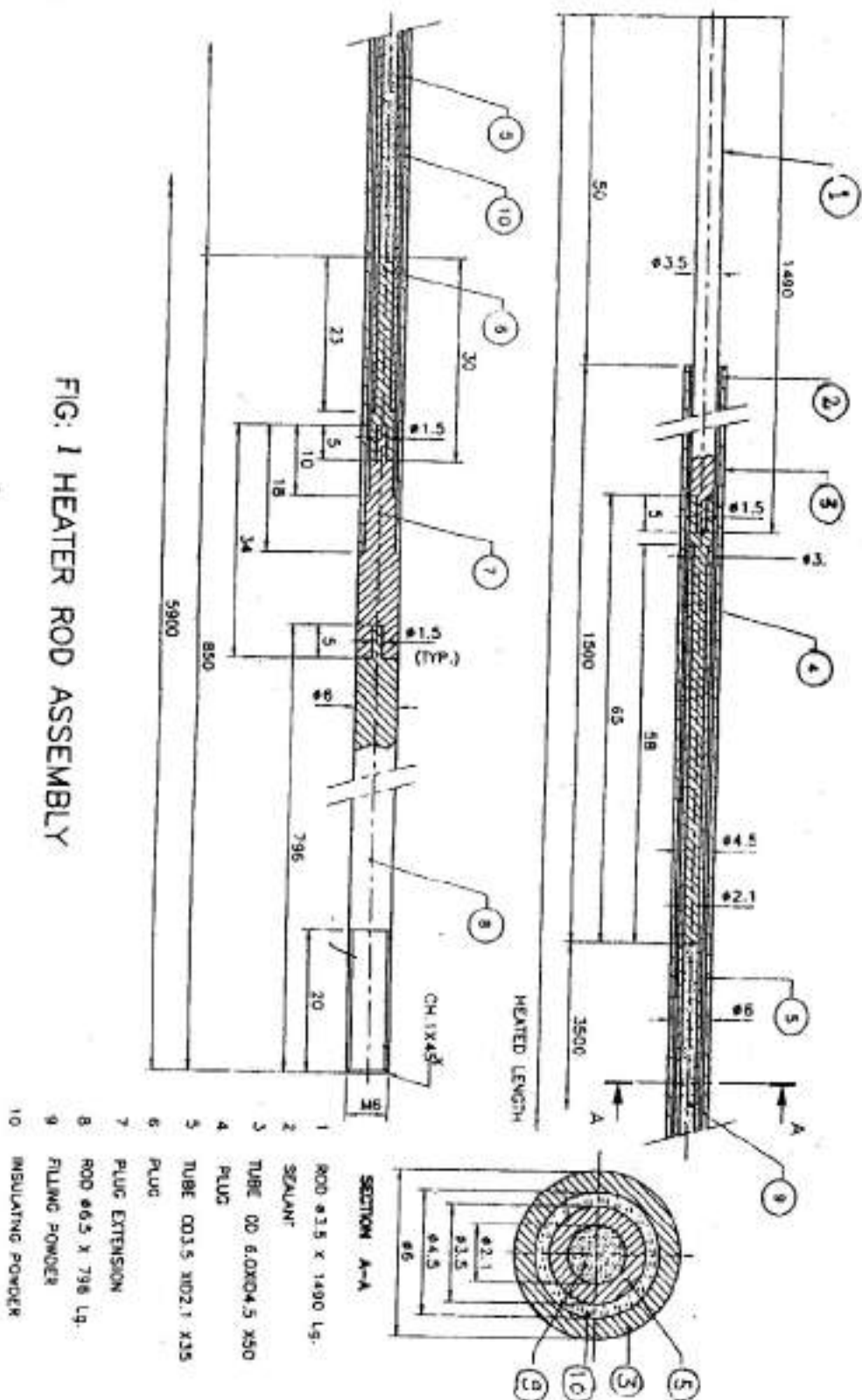


FIG. 1 HEATER ROD ASSEMBLY

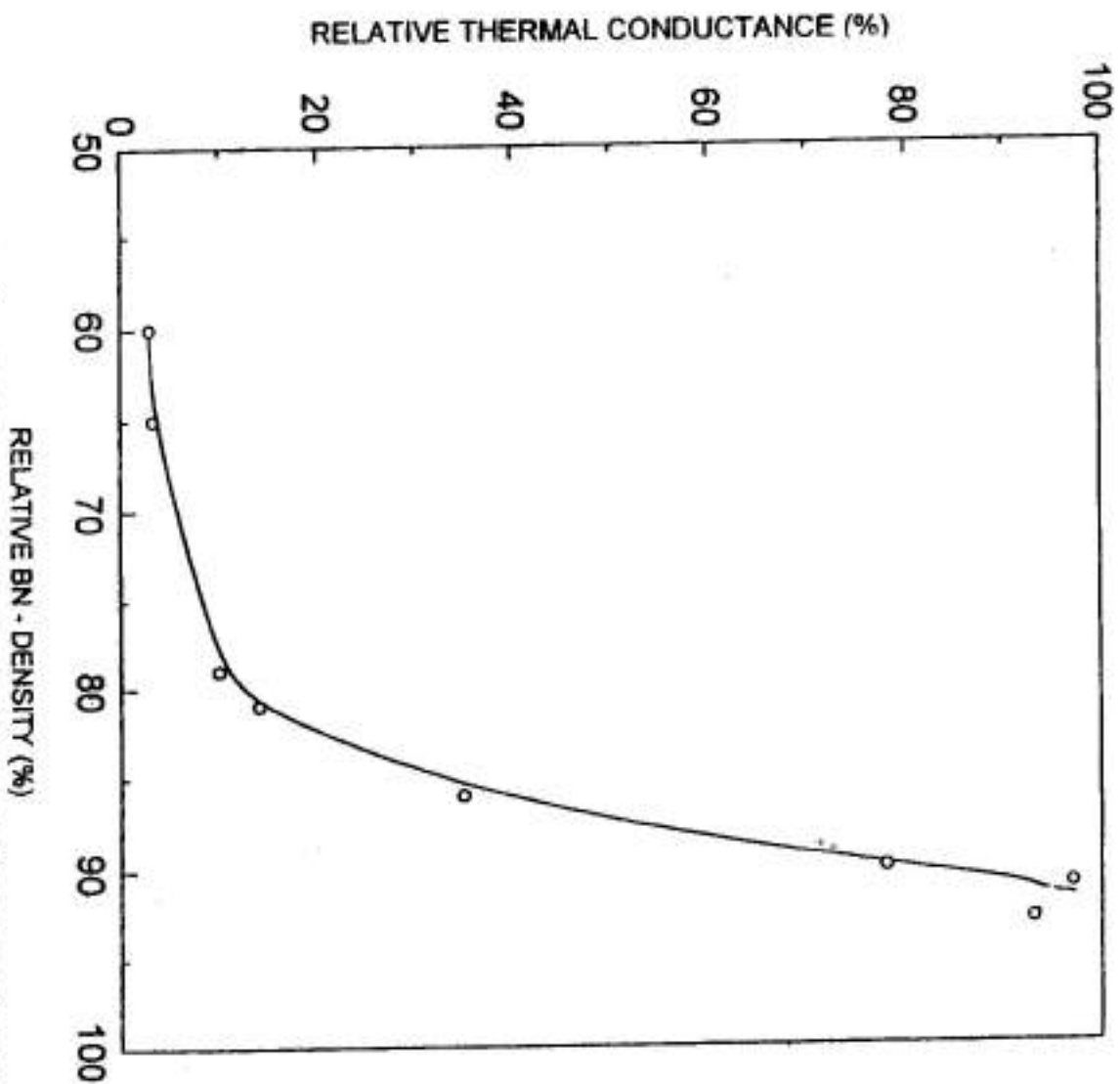


FIG. 2 RELATIVE OVERALL THERMAL CONDUCTANCE VS  
RELATIVE BN - DENSITY IN A HEATER ROD

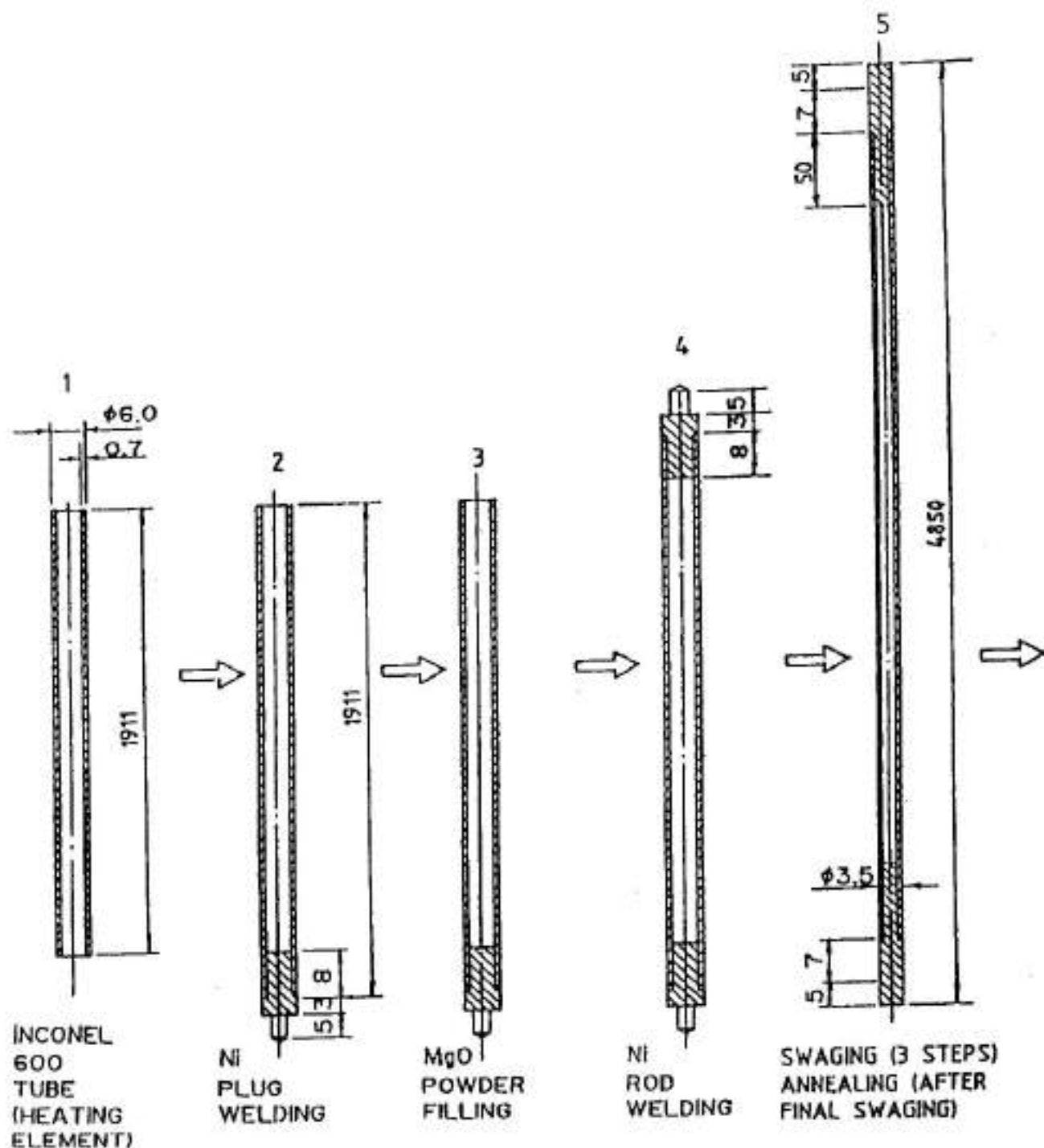


Fig 3 a. FABRICATION SEQUENCE OF HEATER ASSEMBLY

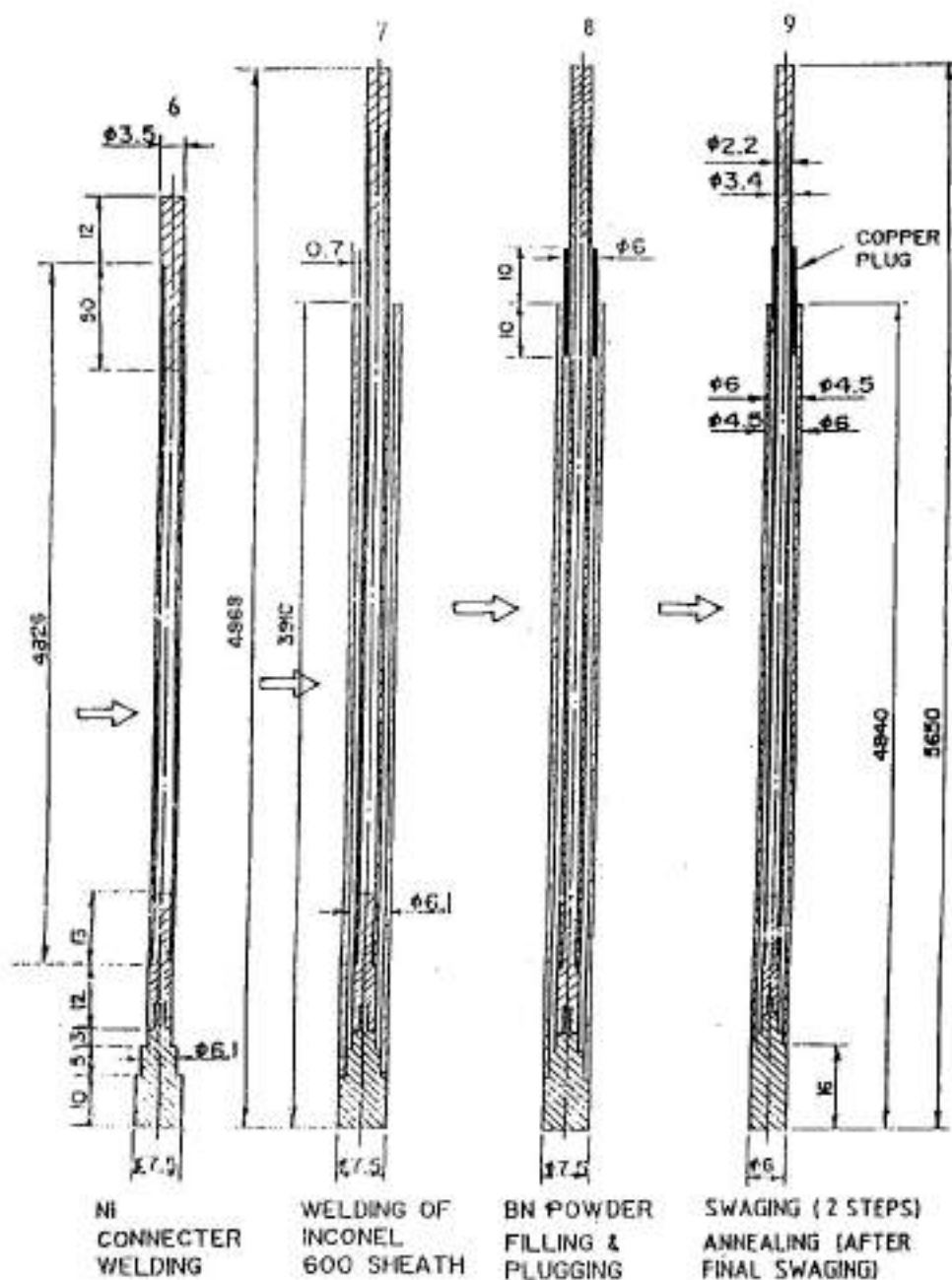


Fig. 3b. FABRIATION SEQUENCE OF HEATER ASSEMBLY

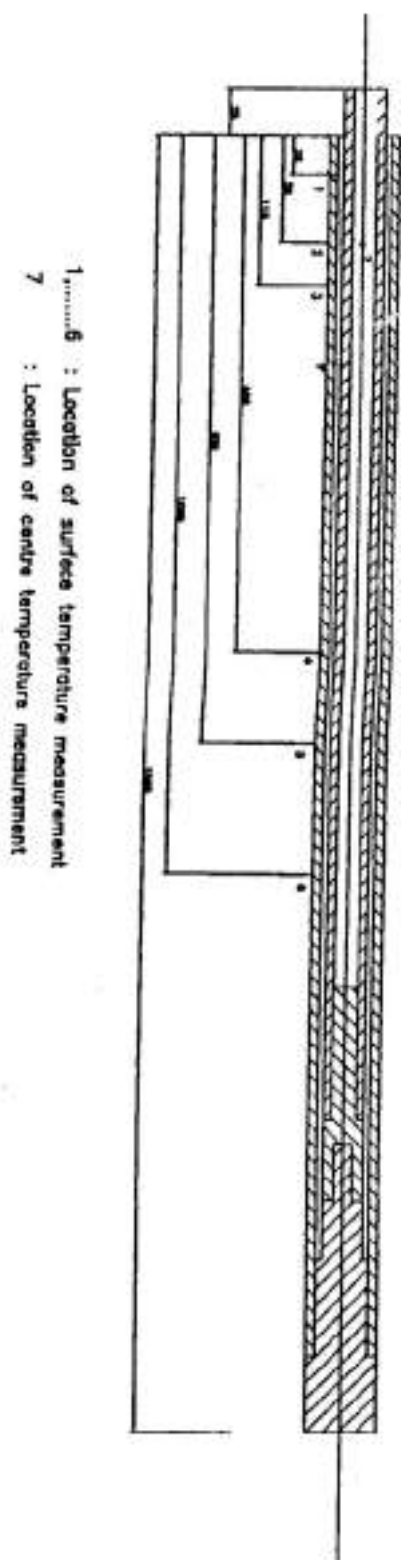
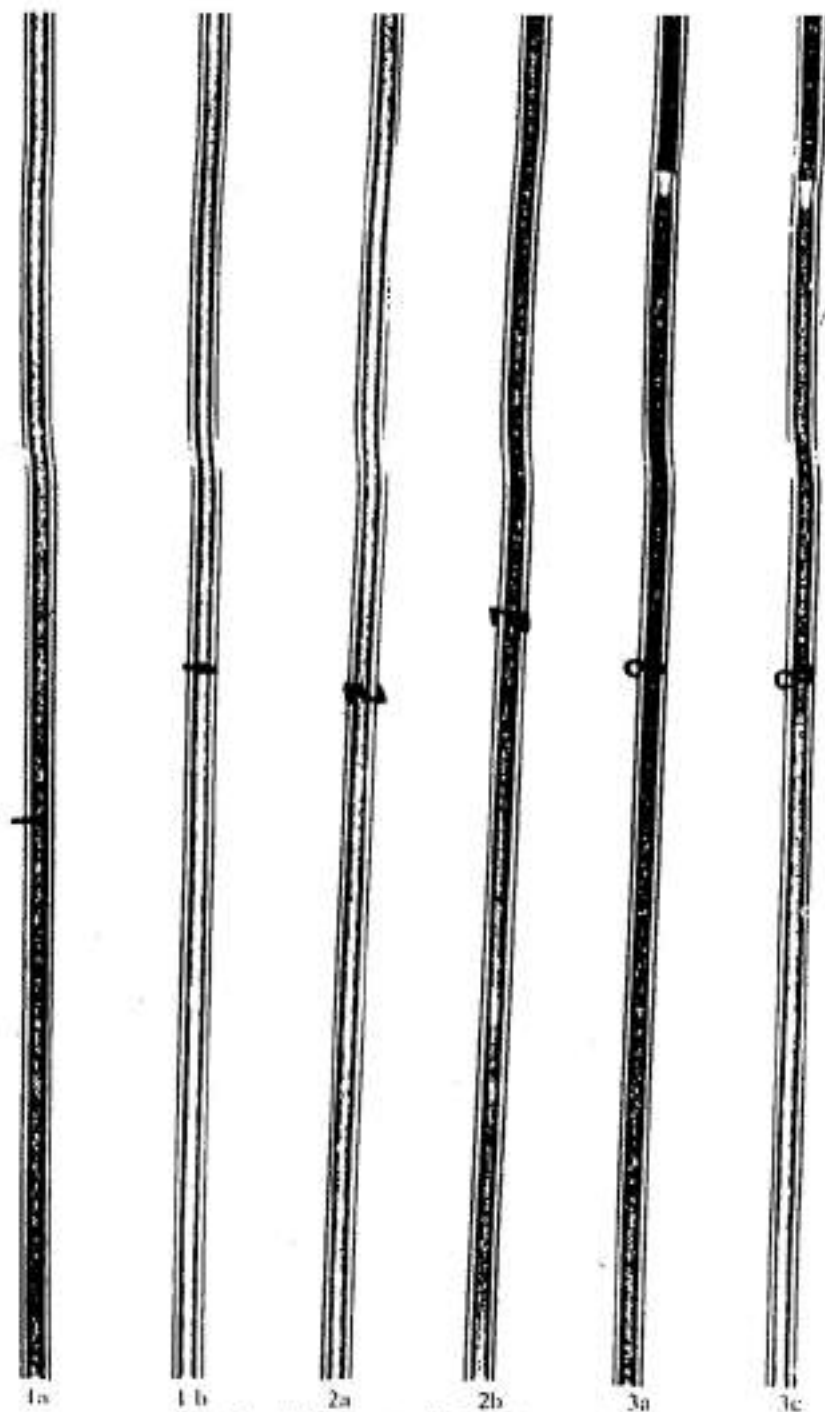


FIG 4 THERMAL TESTING OF HEATER ASSEMBLY - TEMPERATURE MEASUREMENT POINTS



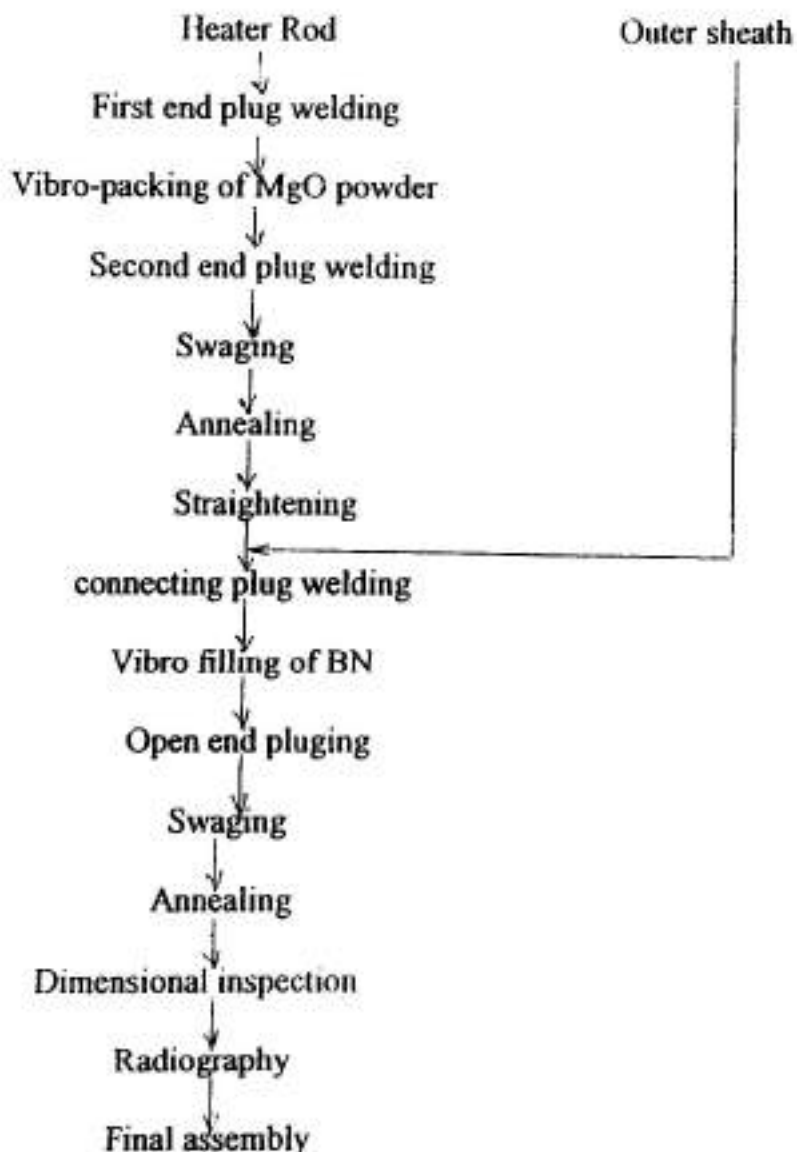
1, 2, 3 : axial segment with 2 as the central segment  
a, b : angular position with angle between a and b being  $90^\circ$

FIG. 5: RADIOGRAPHS OF LARGE LENGTH  
HEATER ASSEMBLY



## APPENDIX I

## Flow Sheet for fabrication of heater assembly



## MACHINABILITY OF S.G.IRON WITH ZIRCONIA TOUGHENED ALUMINA CUTTING TOOL

**T.Sornakumar \***, **R.Krishnamurthy \*\*** and **C.V.Gokularathnam \*\*\***

\* -Dept. of Mechanical Engg., Thiagarajar College of Engineering, Madurai - 625015.

\*\* -Dept. of Mechanical Engg., Indian Institute of Technology, Madras-600036.

\*\*\*-Dept. of Metallurgical Engg., Indian Institute of Technology, Madras-600036.

**Abstract:** The mechanical performance of brittle ceramics can be improved by increasing their fracture toughness. The mechanisms which can results in improved fracture toughness are phase transformation and associated stress induced transformation toughening and microcrack toughening; ductile reinforcement, twinning and fiber/whisker reinforcement. This has resulted in the development of ceramic-ceramic composites. The toughening mechanisms in zirconia toughened alumina (ZTA) are related to the volume expansion and shear strain associated with the tetragonal (t) to monoclinic (m) transformation of zirconia. The mechanisms of toughening in ZTA are stress induced transformation toughening, microcrack toughening, compressive stresses and crack deflection. Machining trials have been conducted on S.G.Iron workpiece in a high speed precision lathe. The machinability of S.G. Iron with ZTA cutting tool was evaluated in terms of surface finish of the turned workpiece, flank wear of the cutting tool insert and main cutting force during machining. The surface finish of the machined workpiece improves with cutting speed. The surface finish varies in a cyclic manner with machining time. The flank wear increases with machining time and cutting speed. The main cutting force continually varies with machining time.

### INTRODUCTION

The increasing interest in zirconia ceramics may be attributed to their unique set of properties, which includes high refractoriness and corrosion resistance, good mechanical strength, high fracture toughness and hardness, ionic conduction, high melting point, low thermal conductivity at high temperature and thermal stability and resistance to thermal shock. Zirconia is an important component in diverse structural ceramics with potential applications such as wear parts like bearings, shapes and seals; engine and machine components; cutting and abrasive tools; mill media; refractories etc. (1).

Zirconia toughened alumina (ZTA) is a ceramic-ceramic composite with good mechanical properties. The enhanced strength and toughness have made the ZTAs more widely applicable and more productive than plain ceramics and cermets in machining steels and cast irons. The presence of zirconia grains in the alumina matrix as a discrete second phase enables the zirconia to behave in an intrinsic manner, that is to undergo the tetragonal (t) to monoclinic (m) phase transformation or to be retained in a metastable t phase form during cooling of the composites from the fabrication temperatures. It is the volume expansion and shear strain associated with the t to m phase transformation that results in various toughening mechanisms in these composites, including stress induced transformation toughening, microcrack toughening, compressive surface stresses and crack deflection (2).

Zirconia ( $\text{ZrO}_2$ ) exists in three well-defined polymorphs: cubic(c) (above 2370 °C), tetragonal (t) (between 2370 and 1150 °C) and monoclinic (m) (below 1150 °C) (3). The high temperature phases can be stabilised to room temperature by the addition of dopants like yttria, ceria, or magnesia (4). Since this t to m transformation absorbs energy, and since the ability of a material to absorb energy is its toughness (5), this t to m transformation leads to an increase in the toughness of the material. Hence, the material is said to be toughened and this phenomenon is termed transformation toughening. Introduction of adequate quantity of zirconia in traditional alumina matrix has led to the development of zirconia toughened alumina (ZTA) with improved toughness. In ZTA the  $\text{ZrO}_2$  experiences a constrained transformation, the constraining matrix is  $\text{Al}_2\text{O}_3$  which has a higher elastic modulus and lower thermal expansion than zirconia.

## EXPERIMENTAL PROCEDURE

Machining trials have been conducted on S.G. Iron workpiece of Hardness 225  $H_v$  in a high speed precision Lathe using the Zirconia Toughened Alumina (ZTA) ( 95.5 % wt  $\text{Al}_2\text{O}_3$  + 4.2 % wt  $\text{ZrO}_2$  + 0.3 % wt MgO) (Pressureless sintered + Hot Isostatic Pressed) cutting tool inserts. The Feed is 0.063 mm/rev and the Depth of Cut is 0.75 mm. The Properties of Zirconia Toughened Alumina (ZTA) is presented in Table 1. The Tool Geometry is presented in Table 2. The performance of the cutting tool was evaluated by measurement of surface finish of turned workpieces, flank wear and main cutting force during machining. The surface finish values of the turned workpieces were measured with the help of Perthometer; the flank wear of the cutting tool inserts were measured in a tool makers microscope and the main cutting force during machining was measured using a Kistler Dynamometer. The variation of surface roughness with machining time is presented in Tables 3 and 4. The variation of flank wear with machining time is presented in Table 5. The variation of main cutting force with machining time is presented in Table 6. The type of chips produced from the S.G. Iron workpiece in all machining conditions is discontinuous chips.

TABLE.1.Properties of Zirconia Toughened Alumina (ZTA)

Property	Notation	Value	Units
Young's Modulus	$E$	380	GPa
Fracture Toughness	$K_{Ic}$	4.0	$\text{MPa.m}^{1/2}$
Transverse Rupture Strength	$\sigma$	550	MPa
Hardness	$H_v$	16.5	GPa
Density	$\rho$	4.00	$\text{g/cm}^3$

TABLE.2.Tool Geometry

## Tool geometry

$\gamma$	$\alpha$	$\lambda$	$\kappa$	$\theta$	$r$
-6	5	-5	75	90	1.6

where  $\gamma$  is the side (main) rake angle ;  $\alpha$  is the side (main) relief angle;  $\lambda$  is the angle of inclination of the side (main) cutting edge;  $\kappa$  is the plan approach angle;  $\theta$  is the included angle between the cutting edges; and  $r$  is the nose radius.

The angles are in degrees and the nose radius is in mm

## RESULTS AND DISCUSSION

## Surface finish

In turning it is necessary to maintain both dimension and surface quality. While dimensional accuracy is controlled by flank wear of turning tools, the surface quality largely depends upon the form stability of the cutting nose. An ideal tool in turning is one which replicates its nose well on the work surface. Hence, the surface quality of turned work surfaces will be largely dependent on the form stability of the cutting tool.

The role of transformation toughening on surface texture control can be seen in the influence of cutting speed on surface roughness (Table 3). With increasing cutting speed the cutting temperature will usually increase, thereby resulting in higher order thermal (quenching) stress; this results in greater amount of t to m transformation, producing more toughening and deformation around the cutting nose (in the cutting plane) resulting in observed reduction in surface roughness. The improvement of surface finish values with increasing cutting speed may also be attributed to the possibility that the machined surface texture could have been partially burnished due to deformation of the toughened cutting nose.

The surface roughness Parameters of the machined workpiece varies in a cyclic manner with machining time (Table 4). This is an indication of the possible cyclic t-m-t phase transformation of  $ZrO_2$  taking place at the tool tip during cutting. For understanding the status of the tool material over the nose portion, X-ray diffraction (XRD) patterns of each tool material before and after a certain amount of machining time were recorded. It was observed that all the tools exhibited a certain amount of m phase and t phase after machining, indicating phase transformation and associated toughening. This is possible because the temperature at the tool tip interface may be as high as 1000-1200 °C (6). Machining involves both stress and temperature. The transformation of  $ZrO_2$  is very much dependent on the combined effects of stress and temperature. The mechanical stress or thermal stress in machining can induce the tetragonal (t) to monoclinic (m) transformation. The frictional heat in machining can induce the monoclinic (m) to tetragonal (t) transformation (7).

TABLE.3.The variation of Surface roughness  $R_a$  in microns with machining time

Cutting speed, m/min	Machining time, minutes				
	1	2	3	4	5
200	0.49	0.60	0.57	0.60	0.70
300	0.50	0.65	0.61	0.53	0.57
400	0.47	0.52	0.57	0.42	0.68
500	0.42	0.46	0.61	0.53	0.65
600	0.40	0.41	0.38	0.36	0.51

TABLE.4.The variation of Surface Roughness Parameters in microns with machining time- Cutting Speed 200 m/min

Machining Time, Minutes	Surface Roughness Parameters, Microns			
	$R_a$	$R_z$	$R_y$	$R_{max}$
1	4.56	6.42	0.49	6.42
2	4.49	7.62	0.60	7.62
3	3.88	5.18	0.57	5.18
4	4.20	5.90	0.60	5.50
5	5.20	8.00	0.70	7.50
6	5.00	7.20	0.80	6.40
7	3.90	5.70	0.60	5.70
8	4.90	5.70	0.70	5.70
9	5.60	8.40	0.70	7.80
10	4.90	6.60	0.80	5.70

**Flank wear**

Apart from surface finish of turned workpieces, flank wear of the cutting tool can also be considered as a criterion for tool performance. Among the different forms of tool wear, flank wear will be a significant measure in that it affects the dimensional tolerance of the workpiece. Flank wear of cutting tools is largely due to intense adhesion between the tool flank and the just machined work surface sliding over it. During the sliding, depending upon the hardness gradient and the tool composition, the flank wear will be of adhesive and/or abrasive type. The flank wear increases with machining time and cutting speed (Table 5).

TABLE.5.The variation of Flank wear VB in mm with machining time

Cutting speed, m/min	Machining time, minutes				
	1	2	3	4	5
200	0.12	0.18	0.19	0.23	0.245
300	0.14	0.19	0.22	0.23	0.25
400	0.16	0.20	0.24	0.25	0.26
500	0.17	0.22	0.26	0.275	0.28
600	0.19	0.23	0.28	0.29	0.30

### Main cutting Force

The main cutting force continually varies with machining time (Table 6). Because of the discontinuous nature of chip formation, forces continually vary during metal cutting. It may also be attributed to the possible cyclic t-m-t phase transformation of  $ZrO_2$  taking place at the tool tip during cutting (7).

**TABLE.6.**The variation of Main Cutting Force in Newtons, with machining time – Cutting Speed 200 m/min

Machining Time, Minutes	Main Cutting Force, N
1	10
2	20
3	10
4	15
5	15
6	15
7	20
8	20
9	15
10	25

### CONCLUSIONS

The machinability of S.G Iron with ZTA cutting tool is very good, in terms of precision surface finish of the machined workpiece, lower flank wear of the cutting tool insert and lower main cutting force. The surface finish of the machined workpiece improves with cutting speed. The surface finish varies in a cyclic manner with machining time. The flank wear increases with machining time and cutting speed. The main cutting force continually varies with machining time.

### REFERENCES

1. Michael, Z.C. Hu, Rodney D. Hunt, E. Andrew Payzant and Camden R. Hubbard, "Nano crystallization and phase transformation in mono dispersed ultrafine zirconia particles from various homogeneous precipitation methods", *J. Amer. Ceram. Soc.*, Vol. 82[9], pp. 2313-2320 (1999).
2. J. Wang and R. Stevens, "Review - Zirconia Toughened Alumina (ZTA) ceramics", *J. Mater. Sci.*, Vol. 24, pp. 3421-3440 (1989).
3. E.C. Subba Rao, H.S. Maiti and K.K. Srivastava, "Martensitic transformation in zirconia", *Phys. Stat. Solidi (a)*, Vol. 21, pp. 9-40 (1974).
4. R.H.J. Hannink, "Significance of microstructure in transformation toughening zirconia ceramics", *Mater. Forum*, Vol. 11, pp. 43-60 (1988).
5. G.E. Dieter, *Mechanical Metallurgy*, McGraw Hill, Singapore., p. 282 (1986).
6. M. Trent, *Metal cutting*, Butterworths, London., p. 68 (1984).
7. V.E. Annamalai, T. Sornakumar, C.V. Gokularathnam and R. Krishnamurthy, "Transformations during grinding of ceria stabilized tetragonal zirconia polycrystals", *J. Amer. Ceram. Soc.*, Vol. 75[9], pp. 2559-2564 (1992).



## Synthesis and Evaluation of Mechanical Properties of Zirconia Toughened Alumina (ZTA).

R.Mehreja, N.Bhargava, Praveen G. Nair, G.V. Prabhu Gaunkar,  
B.T.Rao and T.R.Rama Mohan.  
Indian Institute of Technology, Bombay.  
Ramji Lal.  
Naval Materials Research Laboratory, Ambernath.

### ABSTRACT

Zirconia toughened alumina (ZTA) ceramics have been prepared from zirconia powders containing 3 mol% yttria, which was synthesized by spray drying and calcinations of mixed nitride solutions. Two compositions of ZTA (80-20 ZTA and 85-15 ZTA) were pressed at various compacting pressures and sintered in the temperature range of 1300°C - 1700°C. Mechanical properties such as Modulus of Rupture (MOR), hardness, fracture toughness and impact strength have been evaluated and discussed in terms of various processing parameters.

*Keywords: Alumina, zirconia, toughening, spraydrying, Modulus of Rupture, hardness, fracture toughness, impact strength.*

### Introduction:

One of the main reasons for the restricted usage of ceramics in structural applications till now, is the fact that they fail in a brittle manner with little or no plastic deformation. Extensive work is going on all over the world to improve the toughness of ceramics so as to make them versatile particularly for structural applications. In the previous decade, a considerable amount of work has been done on the alumina-zirconia ceramic composite system with a particular emphasis on improving the mechanical properties, utilizing the recognized toughening mechanisms.

Zirconia Toughened Alumina showed a two-fold increase in strength and toughness, as shown in a review on ZTA ceramics by Wang and Stevens [1]. A combined effect of transformation toughening, microcrack toughening and crack deflection seems to be the main reason for the toughness improvement. Claussen [2] indicated that the toughness of ZTA is greatly increased with addition of monoclinic  $ZrO_2$  particles in



alumina while the strength showed a slight decrease. These results were contradicted by Heuer [3] who claimed that the strength along with the toughness had a direct relationship with the amount of tetragonal  $\text{ZrO}_2$  present in the matrix.

The stability of tetragonal  $\text{ZrO}_2$  particles in ceramics matrix, especially the size dependence, has been studied by Green [4], who indicated that the degree of transformation was dependent on the volume fraction of  $\text{ZrO}_2$  and also its size, of which the latter could be controlled by suitable heat treatments. He also observed that the critical transformation size of  $\text{ZrO}_2$  decreases with increasing amount of  $\text{ZrO}_2$  content.

The objective of the present investigation is to study the effect of 15 and 20 wt. percent  $\text{ZrO}_2$  (containing 3 mol%  $\text{Y}_2\text{O}_3$ ) dispersions on the mechanical properties of alumina ceramics. The other process variables studied include compaction pressure and sintering temperature.

### Experimental Procedure

Two ZTA compositions were studied with 15 and 20 wt.% additions of tetragonal zirconia (stabilized with 3 mol% of yttria) dispersed in an  $\alpha$ -alumina of 99.5% purity matrix. In the following sections these will be referred to as 85-15 ZTA and 80-20 ZTA respectively.

$\text{Zr}(\text{NO}_3)_4$  solution, prepared from zirconium oxychloride ( $\text{ZrOCl}_2 \cdot 8\text{H}_2\text{O}$ ) was recrystallized in hot concentrated HCl acid and then dissolved in water. This led to the formation of zirconium oxychloride ( $\text{ZrOCl}_2 \cdot 8\text{H}_2\text{O}$ ) solution. When this solution was treated with ammonium hydroxide,  $\text{Zr}(\text{OH})_4$  was precipitated. The latter was repeatedly washed in water till it became free from all chloride ions. This was followed by a final dissolution in dilute nitric acid to form  $\text{Zr}(\text{NO}_3)_4$  solution. Zirconium nitrate was then spray dried and calcined to form zirconia powder. Calculated amount of this  $\text{ZrO}_2$  powder in the form of its oxychloride solution was mixed with  $\alpha$ -alumina powder supplied by INDALCO in methanol medium. Yttria in required quantities was added and the resulting dispersion was simultaneously stirred and evaporated to dryness. The powder was then calcined at  $500^\circ\text{C}$ .

For comparison purposes 85-15 ZTA was also prepared from Condea alumina powder dispersed in zirconium and yttrium nitrate solutions. This method will be referred to as Partial Chemical Route (PCR). In this method, alumina powder was dispersed in methanol at a pH of 3 by the drop wise addition of dilute nitric acid. The solution was vigorously stirred for more than seventeen hours, while heating on a Rotamantle. Through out the dispersion, temperature was adjusted at 85°C. Zirconyl nitrate and yttrium nitrate in required quantities were dissolved in water and were then added to the dispersion. Further heating and stirring of the mixture was carried out for about two hours more till a uniform dispersion is obtained. The dispersion is then added dropwise into ammonia solution. A constant pH of about 8-9 was maintained while precipitating the dispersion. The precipitate thus obtained was washed thoroughly for about six hours with methanol over a boopner funnel to free the precipitate of all the hanging nitrates. The resulting wet precipitate was then dried as well as calcined for about 2 hours at temperature of 500°C.

The dried powder from both the processes were then wet ball milled in 2-propanol medium with 1:5 charge to ball ratio for 100hrs. The grinding media used was alumina balls. Both the ZTAs were characterized for finding out different phases, high temperature transformations, particle sizes and specific surface area. Qualitative phase analysis was carried out using the X-Ray Diffraction Technique. For this purpose, an X-Ray Diffractometer PW 1820, using Cu K $\alpha$  targets, manufactured by Philips, Netherlands was used. Particle size analysis was done on MASTERSIZER 2000 ver 2.00, manufactured by Malvern Instruments, UK. Thermal analysis was done on Dupont 2100 Thermal Analyzer was used. The heating rates employed were 5°C and 10°C per min.

The powders were mixed with a solution of 2% polyvinyl alcohol, dried, crushed and then sieved through 150 mesh size. These were subsequently pressed into ceramic tiles of 6cm X 6cm X 1cm size. The compaction was done under different compaction pressures (45 MPa, 50 MPa and 55 MPa for spray dried powders and 50-300MPa for powder prepared by PCR). The green samples were then sintered at three different temperatures, viz. 1300°C, 1500°C and 1600°C in air with 1 hour soaking time at the peak temperature. After sintering ZTA tiles were cut to 4.8cm X 0.8cm X 0.8cm size samples using a diamond wheel.

Green and sintered densities were calculated from dimensions and weight. Samples were subsequently polished to optical finish for hardness measurements. The measurements were made on a Vickers hardness tester with a load of 98N. To find out the Modulus of Rupture values, three-point bend test was carried out on an Instron machine while Fracture toughness was determined by Indentation method. [5].

## Results and discussion

The particle size analysis yielded the data shown in Table. 1

**Table. 1: Particle size and specific surface area of powders.**

S.No.	Material	Particle size ( $\mu\text{m}$ )	Specific surface area ( $\text{m}^2/\text{g}$ )
1	$\alpha$ -alumina	1.96	4.40
2	zirconia powder	3.55	2.53
3	80-15 ZTA	1.49	5.37
4	80-20 ZTA	1.15	6.46

Differential Thermal Analysis of  $\alpha$ -alumina, 85-15 ZTA and 80-20 ZTA powders was carried out with the heating rates of 5 and 10°C per minute. The temperature range up to which the powders heated varied from 800°C-1000°C. No significant phase change was observed.

XRD analysis for 85-15 ZTA and 80-20 ZTA, showed the presence of tetragonal zirconia and  $\alpha$ -alumina to be the major phases. 80-20 ZTA, in addition, showed presence of monoclinic zirconia. Yttria suppresses the tetragonal to monoclinic transformation of zirconia, making the zirconia phase to be present at room temperature in metastable tetragonal form.

The sintered densities of 85-15 ZTA are plotted against the compaction pressure at different sintering temperatures (Fig.1).

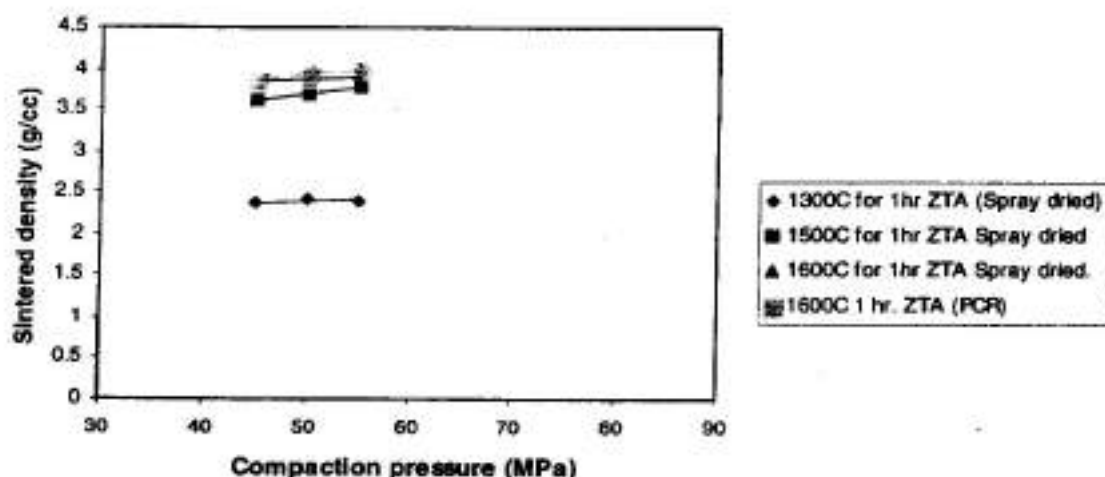


**Fig 1. Variation of Sintered density of 85-15 ZTA with compaction pressure at various sintering temperatures.**

When 85-15 ZTA was compacted at 200Mpa and sintered at 1600°C for 1hr. the sintered density increased to 4.11g/cc while 80-20 ZTA showed a higher density of 4.24g/cc. The sintered density of 85-15 ZTA prepared by PCR, sintered at 1600°C was found to be in the range of 3.86-3.98 g/cc.

In fig. 2, it can be seen that the modulus of rupture increased with sintering temperature for both 85-15 ZTA and 80-20 ZTA. This increase can be related to the increase in the sintered densities. The MOR also had increased with increase in zirconia content. This may be due to the transformation toughening of ZTA with increase in metastable zirconia content. Highest MOR recorded is 669 Mpa for 85-15 ZTA sintered at 1600°C.

Vickers hardness had increased with increase in sintering temperature till 1600°C (fig. 3). At higher temperatures the hardness decreased which is likely due to the abnormal grain growth. It can also be seen that with the increase in the zirconia content (80-20 ZTA), the hardness decreased. The reason may be the presence of monoclinic phase, which leads to micro cracking. The micro hardness of  $\alpha$ -alumina powder supplied

by INDALCO was found to be 19.2 GPa while that of tetragonal zirconia was 12.0 GPa and monoclinic zirconia was 8.0 GPa. So it is obvious that with the increase of zirconia content, the over all hardness of the matrix decreases. The powder prepared by PCR showed a comparatively low values.

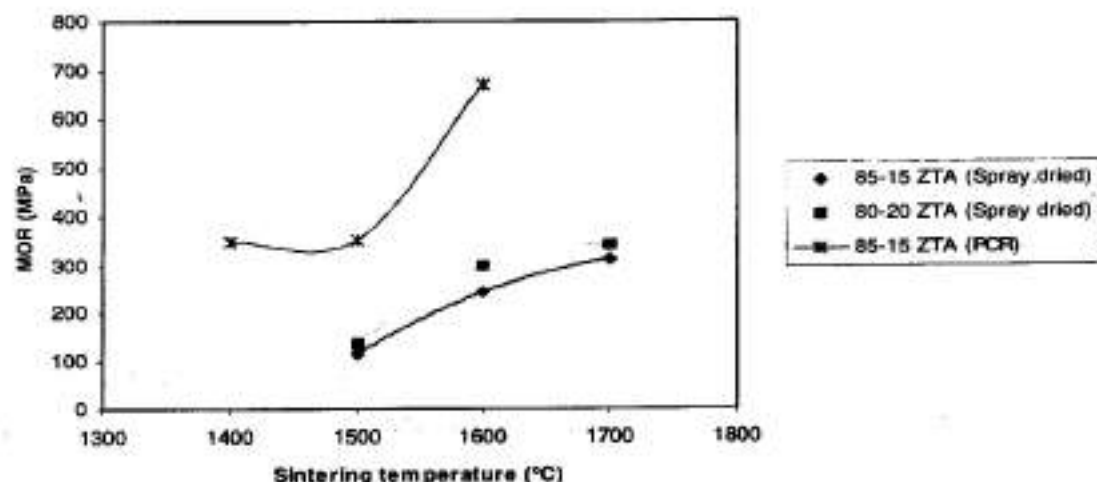


Fig 2. Effect of sintering temperature on MOR for 85-15 and 80-20 ZTAs compacted at 50MPa

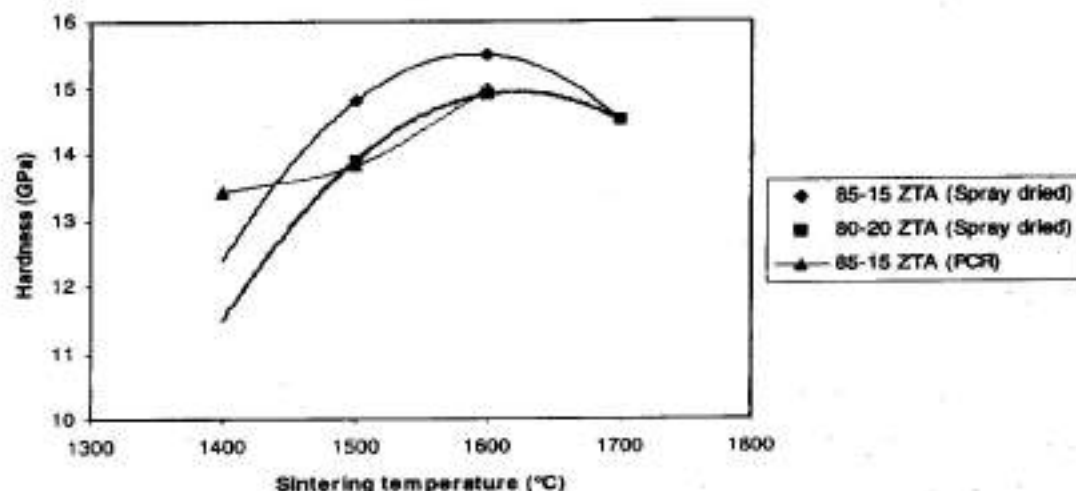
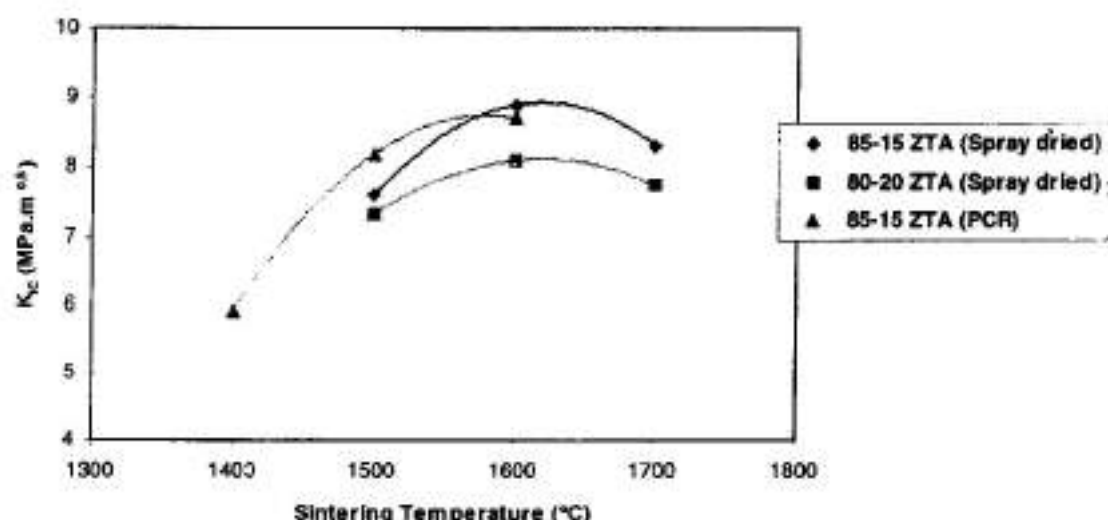


Fig 3. Variation of hardness with Sintering Temperature.

When fracture toughness ( $K_{IC}$ ) was plotted against sintering temperature (fig. 4) the curve decreased after 1600°C. This is due to the exaggerated grain growth of the matrix. And with the increase in the zirconia content the fracture toughness decreased. Though there is stress induced transformations and microcracking occurring at the same time, yet the toughness decreased with higher zirconia content. It can be predicted that with the increase in the zirconia content, the microcracks decreased the stiffness of the matrix. The fracture toughness of 85-15 ZTA produced by spray drying and by PCR have almost the same values.



**Fig 4. Variation of Fracture toughness with sintering temperature.**

Table 2 shows the impact test data obtained. Decrease in impact energy values with increase in sintering temperature, may be attributed to the grain coarsening. The decrease in impact strength with increase in the zirconia content is presumably due to the increase in the microcracks in the matrix.

Table 2: Impact strength data of 85-15 ZTA and 80-20 ZTA.

S.No.	Material	Impact Strength (Kg.cm)
1	85-15 ZTA (1500°C, 1hr)	41-42
2	85-15 ZTA (1600°C, 1hr)	39-40
3	80-20 ZTA (1600°C, 1hr)	36-38
4	80-20 ZTA (1700°C, 1hr)	31-37

### Conclusions

1. The maximum sintered density obtained for spray dried 85-15 ZTA was 3.92 g/cc and for 80-15 ZTA, which was prepared by PCR, was 3.98g/cc.
2. The MOR of spray dried 85-15 ZTA was 314 MPa while that for spray dried 80-20 ZTA was 341 MPa. The MOR for 85-15 ZTA prepared by PCR was found to be 669 MPa.
3. The hardness decreased with addition of zirconia from 15.5 GPa for 85-15 spray dried ZTA to 14.9 GPa for 80-20 spray dried ZTA. The hardness of 85-15 ZTA prepared by PCR was found to be 15 GPa.
4. The fracture toughness for spray dried 85-15 ZTA was found to be  $8.9 \text{ Mpa.m}^{0.5}$  where as for that of spray dried 80-20 ZTA it was found to be  $8.1 \text{ Mpa.m}^{0.5}$ . The fracture toughness for 85-15 ZTA prepared by PCR was found to be  $8.7 \text{ Mpa.m}^{0.5}$ .
5. The impact strength of 85-15 ZTA was found to be higher than 80-20 ZTA.

With the addition of zirconia mainly in tetragonal form, the mechanical properties of transformation toughened alumina improved considerably. At higher zirconia content part of the tetragonal phase would have transformed to the monoclinic phase, thus decreasing the toughness, impact strength and hardness. MOR on the other hand showed a continued increase with the addition of zirconia. Also the powder produced by Partial Chemical Route (PCR) was found to be more efficient than spray dried powder.



## References

1. Wang J. and Stevens R., " Review Zirconia Toughened Alumina (ZTA) Ceramics". *Journal of Material Science*, vol. 24, pp.3421-3440, 1989.
2. Claussen, N., " Fracture toughness of  $\text{Al}_2\text{O}_3$  with an unstabilised  $\text{ZrO}_2$  dispersed phase," *Journal of the American Ceramic Society*, 59 (1-2), pp. 49-51, 1976.
3. Heuer A.H., " Transformation toughening in  $\text{ZrO}_2$ - containing Ceramics", *Journal of the American Ceramic Society*, vol.70, no.10, pp. 689-698, Oct.1987.
4. Green D.J., "Critical microstructures for micro-cracking in  $\text{Al}_2\text{O}_3$ - $\text{ZrO}_2$  Composites", *Journal of the American Ceramic Society*, 65 (12), pp. 610-14, 1982.
5. Kim J., Uchida and Saito K., *Journal of the American Ceramic Society*, 73 pp. 1069, 1990.

## Acknowledgements

The authors profusely thank the Director of Naval Materials Research Laboratory, Ambarnath for funding the research programmes on zirconia ceramics and also, for providing the experimental facilities at NMRL.

## Author Index

Anil Anal 141, 152, 160, 221  
Arora Vishal 200

Baijal R. 127  
Bera Debasis 141  
Bhargava N. 249  
Bhattacharya Pritish 71  
Biswas Soumen 221

Dabhade V.V. 127  
Das K. 56  
Das S. 117  
Date V.G. 232  
Debata M. 92  
Deo Nikhil 152  
Desai P.R. 71

Fedorov D.N. 22, 64

Ghosh Chiradeep 84  
Godkhindi M.M. 56, 117  
Gokularathnam 243

Khovavko A.I. 64  
Krishnamurthy R. 243  
Krishnarao R.V. 136

Malhotra S.K. 43  
Malobika K. 22, 64  
Mathur Vivek 160  
Mehreja R. 249  
Mohanty O.N. 1, 5  
Mukunda P.G. 1, 56, 117

Nair Pravin G. 249

Paibhale S.V. 232  
Pani B.B. 1, 5  
Paramunand Singh 43, 185  
Prabhu Gaunkar G.V. 249  
Purohit Rajesh 31

Rama Mohan T.R. 127, 141, 152, 160, 221, 249  
Ramaji Lal 152, 221, 249  
Ramakrishna N.V.N. 152  
Ramakrishnan P.  
Ramana Reddy G.V. 141

Rao B.T. 141, 152, 160, 221, 249  
Rao Ramesh S. 71  
Ravi Kumar B. 5  
Rengarajan R. 71  
Rout S.K. 103

Sagar Rakesh 31  
Sahu Pramod 31  
Sangita Kumari 56  
Sankaranarayanan 185  
Shankar J. 168  
Shivashankar A. 71  
Sivakumar A. 22  
Sornakumar T. 243  
Srinivas D. 117  
Srinivasrao M. 136  
Srivastava S.K. 232  
Subrahmanyam J. 136  
Sundara Rajan P. 232  
Sundaresan R. 9

Taneja Manisha 200  
Thirunavukkarasu A. 43  
Tewari A. 103

Uma V. 9  
Upadhyay N.C. 200  
Upadhyaya Anish 84, 92, 103, 168

Verma Gaurav 200